Optical quantum memories with cold atomic ensembles : a free space implementation for multimode storage, or a nanofiber-based one for high collection efficiency

Adrien Nicolas

THÈSE DE DOCTORAT
DE L'UNIVERSITÉ PIERRE ET MARIE CURIE

Spécialité : Physique

école doctorale : « La physique, de la particule à la matière condensée »

réalisée

au Laboratoire Kastler Brossel

présentée par

Adrien NICOLAS

pour obtenir le grade de :

DOCTEUR DE L'UNIVERSITÉ PIERRE ET MARIE CURIE

Sujet de la thèse :

Optical quantum memories with cold atomic ensembles : a free space implementation for multimode storage, or a nanofiber-based one for high collection efficiency

soutenue le 30 septembre 2014

devant le jury composé de :

Mme	Laurence Pruvost	Rapporteur
M.	Barak Dayan	Rapporteur
Mme	Eleni Diamanti	Examinateur
M.	Fabio Sciarrino	Examinateur
M.	Jérôme Tignon	Examinateur
M.	Julien Laurat	Directeur de thèse

Contents

Acknowledgements

I would like to thank those who gave me the taste for science and constantly stimulated my curiosity and pushed me forward, which of course include my parents, my grandma and my godfather in a first place. I would not have gone here without them, and not only for biological reasons! Later in high school and especially in classes prépa, I had some wonderful science teachers who definitely had a great influence on me, in particular Emanuel Goldztejn, who gave me my liking for mathematics, Stéphane Mansuy, Jean-Claude Sifre and Jean-Pierre Lecardonnel.

I'm also thankful to the team who welcomed me in the lab: Julien and Elisabeth for their trust as they recruited me as a PhD student, Michaël, who guided my first steps in experimental optics. I appreciated very much the work with Dominik and I'm thankful to him for introducing me to Python and for sharing some late and friendly evenings in the lab. I also enjoyed every occasion he gave me to practice my german. Thanks to Baptiste with whom discussions were always pleasant and insightful. Thanks also to the rest of the team, past and present, whether I worked with them directly or indirectly, or merely enjoyed some chat during the pauses: Lambert, Lucile, Oxana, Sasha, Valentina, Christophe, Olivier, Anna, Kun, Josselin... Special thanks also to all the non-scientific or parascientific people in the lab: Monique, Thierry, Laëtitia, Michel and Delphine, Annick and Bintou, Corinne and Serge, Pascal, Jean-Michel, Gaël and Arnaud, Brigitte and Jean-Pierre, Florence... You make the lab a more humane place!

Thanks also to all my friends from out-of-the-lab, especially to Jean-Raphaël for the stimulating intellectual challenges in high school, which kind of include the numerous games we created and played in our younger days.

Most of all of course, I thank my beloved wife for patiently enduring "to have a student at home for three long years", and whose organizational skills were my most precious help during the writing of this manuscript.

Introduction

> *"He put his arms around his sons' shoulders.*
> *'Lads', he said proudly. 'It's looking really quantum' "*
>
> — Terry Pratchett, *Pyramids*, 1989 [1]

The amazingly apropos sentence by Terry Pratchett is only one of his many hilarious quotes involving science in general and quantum physics in particular. What Pratchett really makes fun of in these lines is the propension of many a science-fiction writer to invoke quantum physics as a kind of modern magic. "Don't ask, it's quantum" has become the sci-fi equivalent of "don't ask, it's magic" in fantasy. And indeed, the quantum wordage has even crossed the borders of sci-fi literature and has started to invade the language of plain commercials: I can go to my supermarket and buy a *quantum* detergent! Has it anything to do with something a physicist would call "quantum" ? Of course not! It's just the modern magic thing...

Are we, quantum physicists, modern wizards ? Some people would probably be affirmative, conjuring up the wonders of technique such as lasers, computer hardwares, ultrafast communications... I would prefer to attribute these wonders to a nature that generations of scientists and engineers have understood and tamed for their (and our) own purposes, and leave magic dwell in other realms. Wording quantum physics in terms of magic may be misleading. Leaving magic aside, a simple question for the quantum wizards-or-not is: how can you tell if something is quantum or not ? And ironically, it is a tough one. Most definitions of "quantum" use negative properties: "it can't be explained by a classical theory", "it cannot be measured simultaneously", "it cannot be factored as the product of two independant single-particle states"... Borrowing another line from Pratchett, "It's very hard to talk quantum using a language originally designed to tell other monkeys where the ripe fruit is." [2]. And it is precisely because they play with the limits of our intelligence that quantum phenomena fascinate so many of us even among experienced physicists. As if to illustrate that the quantumness question is a far from trivial one, a little part of the work presented here was focused on proving that what we were doing *was really quantum* (section 3.4.b). In fact, it would have no interest at all if it weren't quantum.

So, what have I been doing over the three last years (appart from getting married, getting a home, and getting a Terry Pratchett book collection) ? My intimate relationship with quantum physics, and quantum information in particular, began in my mid-teens with the reading of the popular science book *Alice in Quantumland* by Pr. Robert Gilmore [3]. The idea that manipulating quantum properties of objects can lead to a different way of conceiving (and handling) information itself held an incredible appeal to me, and I decided I wanted to play a part in the big game when I grew up. During my master's year, I came across the quantum memory laboratory of Pr. Julien Laurat, and this resulted in the aftermaths you're currently holding in your hands.

The general topic of this thesis is the study of (a particular kind of) *quantum memories* for light. A quantum memory means a device that can record faithfully the entire quantum state of a light field. In contrast, a classical memory for light is a device able to record a light field *without its quantum properties*, such as a standard camera, a photodiode, a wavefront analyzer... One of the characteristics of a *quantum state* of light is that some of its properties *cannot be measured at the same time* (again a negative definition). Consider for example the phase and amplitude patterns of a light beam, which you can respectively measure with a camera and a wavefront analyzer. By splitting a classical (bright) beam of light into two beams with a half-reflecting mirror, you can measure the beam phase and intensity simultaneously by putting the two detectors in different sub-beams. But imagine you have only a single photon. A single photon is the smallest possible amount of light. A single photon can be detected either *here*, or *there*, but not in the two places at the same time: there is *only one* photon to be detected. In this case, the photon will go either to the intensity detector *or* to the phase detector (let's not mention the fact that one would intrinsically need many photons to record a full intensity or phase *pattern*, the argument is just a hand-waving one [1], but it conveys the correct idea). What if we put the phase detector *after* (or before for that matter) the intensity detector ? Then the first measurement will randomly alter the photon's state, so that the second detector will not measure the state of the photon as it was before. The fact that a measurement changes the object being measured is an essential aspect of quantum physics, the weirdness of which contributes to quantum physics being temptingly qualified of "magical". Either way, only *one property out of two* can be measured. The fundamental reason behind this lies in the fact that physical quantities are (represented by) mathematical operators that do not necessarily commute, and hence cannot be simultaneously diagonalized [2].

So the characteristic feature of a quantum memory is that it records the *entire* quantum state of a light field, for example of a single photon as the case may be, something a classical camera cannot do. Of course, a quantum memory does not violate the laws of physics which means that it is *not* equivalent to measuring the light state. Indeed, another name for quantum memories underlines their fundamental difference with a classical measurement: "*stopped light*". I like the expression very much because light evokes something tremendously fast even to a non-physicist. Stopping the fastest thing in the universe pretty much looks like modern magic to me. As with magic, there is a trick here: light is not stopped, its state is merely transfered to something that doesn't move (a bunch of very cold gaseous atoms in our case).

But what is it good for ? Quantum memories are expected to find an application in what is known as quantum cryptography, a set of techniques for transmitting secret messages, in which the security of the message is guaranteed by the laws of quantum physics (like the impossibility to completely characterize a quantum state by classical measurements). Quantum cryptography typically relies on the exchange of single photons as information carriers. The challenge faced by these techniques is that the probability for a single photon to be sucessfully transmitted (e.g. through an optical fiber) decreases exponentially with the travel distance. Moreover, because of the quantum nature of the signal, classical repeaters (i.e. *amplificators*) are of no use for them. This can be intuitively understood in the following way. If a single photon arrives to the amplificator, then it needs not be

---

[1] It could be made rigorous for example by a more careful choice of parameters, such as the polarization of light.

[2] I.e. there are states of a physical system for which one parameter is well defined (the state is an eigenvector of the measurement operator) but the other one is not.

amplified. If the photon has been lost, then there is nothing left to amplify. It is just another hand-waving argument, but I believe it sort of conveys the idea.

An idea to overcome this issue is the concept of a quantum repeater, which proposes to divide the quantum communication line in a succession of smaller segments, over which so-called *entangled pairs* of photons are distributed. At the nodes between adjacent segments, photons from different pairs are combined together, which results in the other ends of the two pairs merging in a single entangled pair. When all segments have been connected in this fashion, only one entangled pair remains, which has one particle at one end of the line and the other particle at the other end. One feature of entangled pairs is that they allow to perform quantum cryptography. This protocole can be made more efficient than the direct transmission by the following trick, which critically requires quantum memories. Two pairs will be connected if and only if no photon has been lost. In the case of a photon being lost, then the other one will be stored in a quantum memory and wait there for a new partner to arrive on the other side. The time gained by this protocole makes all the difference between what's possible and what's not.

When I joined Julien's quantum memory group in 2011, a new free-space cold atom setup was being built there. I still remember vividly my first group meeting, everyone explaining me how everything fitted together and me trying to retain the funny nicknames of all the lasers: Zeus, Casper, Shadok... During my first six months, I learned a lot and participated in finalizing the construction of the experiment alongside Michael Scherman, Lambert Giner and Lucile Veissier. Former PhD student Sidney Burks had conceived a huge LABVIEW program to control the entire experiment, and I am thankful to Lucile (and later Dominik) for taking it over. I am also thankful to Michael who guided my first steps through the lab. We enjoyed the visits of Itay and Ben who worked with us on the magneto-optical trap construction and characterization. The theory part of the job was done by Oxana and Sasha. My main contribution to the experiment, which occupied me for the next one-and-a-half year, was focused on proving the spatial multimode capability of our quantum memory. This means proving that the memory can store (in a quantum fashion) light beams of different *shapes*, at the single-photon level. In this project, I mostly collaborated with Dominik, to whom I am being thankful for the impressive amount of work he did in computer programing and also for sharing late nights in the lab during the long measurements sessions. With Dominik and Lucile, we shaped photon wavefronts into various spiraling patterns to give them *orbital angular momentum*. We analyzed the orbital angular momentum state of our photon pulses and studied how it was preserved when the light was stored in our quantum memory. In parallel (and mostly over the course of my final year), I moved on with Dominik towards another project, which aims at interfacing a cold atom quantum memory with a nanowaveguide. The lead PhD student on this project, the passionate Baptiste, had been working already for one year on the topic, designing a home-made facility for the fabrication of the nanowaveguides. About that time also, our group was joined by Valentina and then Christophe, who took over the previous setup and conducted single-photon generation experiments. While I am completing this manuscript, Baptiste and Dominik are just getting the first "quantum" measurements with the nanowaveguide.

As for how this manuscript is organized, the first chapter introduces the concept of quantum memories, why they are required and what is expected from them. The second chapter describes stopped-light quantum memories and their underlying mechanism, electromagnetically induced transparency. Our experimental implementation of such sys-

tems is discussed. The third chapter then details everything we did in relation to the orbital angular momentum of light, from the theoretical description of orbital-angular-momentum-carrying beams, to the precise experimental characterization of the quantum storage of quantum bits encoded in this degree of freedom. The fourth chapter finally presents the goal of and our experimental progresses towards the interfacing of cold-atom-based quantum memories with nanowaveguides.

Some publications

Here follows a list of publications issued in relation with the work presented here:

- L. Giner, L. Veissier, B. Sparkes, A. S. Sheremet, A. Nicolas, O. S. Mishina, M. Scherman, S. Burks, I. Shomroni, D. V. Kupriyanov, P. K. Lam, E. Giacobino, and J. Laurat1. Experimental investigation of the transition between autler-townes splitting and electromagnetically-induced-transparency models. *Physical Review A*, 87:013823, 2013 [4]

- L. Veissier, A. Nicolas, L. Giner, D. Maxein, A. S. Sheremet, E. Giacobino, and J. Laurat. Reversible optical memory for twisted photons. *Optics Express*, 38:712, 2013 [5]

- A. Nicolas, L. Veissier, L. Giner, E. Giacobino, D. Maxein, and J. Laurat. A quantum memory for orbital angular momentum photonic qubits. *Nature Photonics*, 8:234, 2014 [6]

- Adrien Nicolas, Lucile Veissier, Elisabeth Giacobino, Dominik Maxein, and Julien Laurat. Quantum state tomography of orbital angular momentum photonic qubits via a projection-based technique. to be submitted, 2014 [7]

Notions and notations

As any quantum optics thesis, this manuscript deals with light and matter, and the relations between them. It is out of the scope of this work to rewrite the full derivations of the concepts involved, but I wish to make it as consistent as possible and therefore take some time to define the notations and concepts that will be encountered.

Space shall be parametrized using cartesian coordinates $\vec{x} = (x,\ y,\ z)$ or cylindrical coordinates $(\vec{r},\ z) = (r,\ \theta,\ z)$. Time is denoted t.

The usage of the ket notation $|\quad\rangle$ will be restricted to quantum states solely (whether of light or of matter).

Constants We shall use the standard notations for the physical constants:

$$
\begin{aligned}
c &= 299792458\ \mathrm{m \cdot s^{-1}} & &\text{light speed in vacuum} \\
\epsilon_0 &\sim 8.854187817620 \times 10^{-12}\ \mathrm{F \cdot m^{-1}} & &\text{vacuum permittivity} \\
\mu_0 &= 4\pi \times 10^{-7}\ \mathrm{H \cdot m^{-1}} & &\text{vacuum permeability} \\
h &\sim 6.626\ \mathrm{J \cdot s} & &\text{Planck's constant} \\
\hbar &\sim 1.055\ \mathrm{J \cdot s} & &\text{reduced Planck's constant}
\end{aligned}
\tag{1}
$$

In addition, we will often encounter the following ^{133}Cs constants:

$$\Gamma \sim 32.9 \times 10^6 \text{ s}^{-1} \qquad 6^2\text{P}_{3/2} \to 6^2\text{S}_{1/2} \text{ (D2 line) decay rate in } ^{133}\text{Cs}$$

$$\Gamma \sim 2\pi \times 5.234 \times 10^6 \text{ MHz} \qquad \text{and the associated homogeneous linewidth}$$
$$\text{(FWHM, angular frequency units)}$$

$$m = 2.207 \times 10^{-25} \text{ kg} \qquad \text{atomic mass}$$

$$\text{(2)}$$

On the description of light Light will be described either classically as a periodically varying electrical field $\vec{E}(\vec{x}, t)$, or quantum-mechanically as a train of photons. A mathematically complete derivation of the notion of a photon can be found in any textbook on quantum optics (for example [8]). Classical light will be typically a plane wave, given by its complex electric field $\vec{E}(\vec{x}, t) = \vec{E}_0 e^{i(\omega t - \vec{k} \cdot \vec{x})}$, or a gaussian beam like the fundamental TEM$_{00}$ beam (propagation direction z) given by its (complex) electric field:

$$\boxed{\vec{E}(r, \theta, z, t) = \vec{E}_0 \frac{w_0}{w(z)} e^{-\frac{r^2}{w(z)^2}} e^{i(\omega t - kz)} e^{-ik\frac{r^2}{2R(z)}} e^{i\zeta(z)}} \tag{3}$$

Following the usual notations, we call $\vec{E}_0$ the complex amplitude of the electric field (the real *physical* electric field being its real part) and we have:

$$
\begin{aligned}
\omega \qquad &\text{optical } \textit{angular} \text{ frequency} \\
\nu \text{ or } f \quad (\omega = 2\pi\nu) \qquad &\text{optical } \textit{real} \text{ frequency} \\
\lambda = \frac{c}{\nu} \qquad &\text{wavelength} \\
k = \frac{2\pi}{\lambda} = \frac{\omega}{c} \qquad &\text{wave vector}
\end{aligned}
\tag{4}
$$

For the gaussian beam, we have in addition:

$$
\begin{aligned}
w(z) = w_0 \sqrt{1 + \left(\frac{z}{z_R}\right)^2} \qquad &\text{radius at position } z \\
w_0 \qquad &\text{waist} \\
R(z) = z\left(1 + \left(\frac{z_R}{z}\right)^2\right) \qquad &\text{radius of curvature at position } z \\
z_R = \frac{\pi w_0^2}{\lambda} \qquad &\text{Rayleigh length} \\
\zeta(z) = \text{arctg}(z/z_R) \qquad &\text{Gouy phase}
\end{aligned}
\tag{5}
$$

Such a gaussian beam is the spatial shape of the output of an ideal laser. Putting aside the information relative to the spatial mode, the *quantum mechanical* description of such an ideal laser beam is given by a coherent state of amplitude α, defined by:

$$|\alpha\rangle = e^{-\frac{\alpha^2}{2}} \sum_{n \in \mathbb{N}} \frac{\alpha^n}{\sqrt{n!}} |n\rangle \tag{6}$$

where α is proportional to the electric field's amplitude and α^2 gives the mean photon number. We use the standard notation $|n\rangle$ for the Fock (photon number) state with $n \in \mathbb{N}$

photons. It is assumed that all photons in the above state are in the same spatial (and temporal) mode. Indeed, in order to be well defined, a photon state must be specified in a given spatiotemporal mode. In the case of the ideal gaussian beam, the spatial mode is given by the gaussian function of equation (3) and the temporal mode is an (also slightly ill-defined) infinitely extending envelope.

The action of a standard single-photon detector (such as an avalanche photodiode) is a projection over the Fock state $|1\rangle$ where the temporal mode is the discrete arrival time of the photon (with some spread given by the detector's time resolution). This gives another view of the coherent state: it is a flux of (temporally localised) photons with uncorrelated arrival times. Thus, over any time interval, the photon number statistics of a coherent states follows a Poisson probobility distribution (which can also be seen directly from equation (6)).

Frequency, decay rate and linewidth. Throughout this manuscript, we'll describe light's frequency using *angular* frequency ω, which is (in principle) expressed in radian per second [3].

The decay rate of an atomic excited level is denoted Γ and expressed in s^{-1}. It is the decay constant of the power of the light emitted by a decaying atom. By Fourier transforming the wavefunction of the emitted electric field $\mathcal{E}_0 e^{-\Gamma t/2} e^{-i\omega_0 t}$ into $\mathcal{E}_0 \frac{1}{\Gamma/2 - i(\omega - \omega_0)}$, the decay rate Γ appears to be also the natural linewidth (FWHM) of the atomic emission/absorption line. Following a widespread notation, we shall write $\Gamma \sim 2\pi \times 5.2\,\text{MHz}$ when we refer to the linewidth in angular frequency units (the 2π factor may be thought of as carrying the unit rad) and $\Gamma \sim 32.9 \times 10^6\,\text{s}^{-1}$ when we refer to the decay rate.
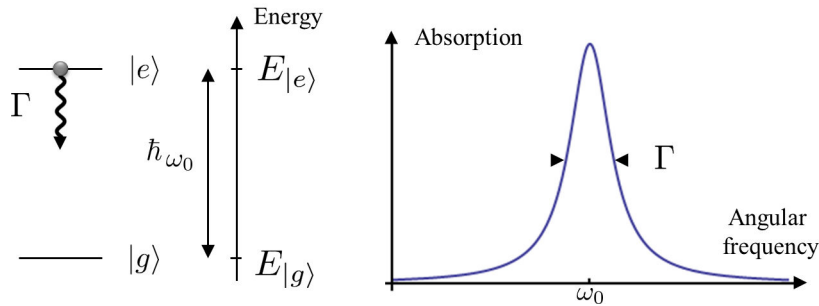
Figure 1: **The decay of a two-level atom and the Lorentzian shape of the emitted spectrum.** Quantum memories of the kind consedered here rely on a modification of this lineshape through a phenomenon called *Electromagnetically Induced Transparency* (EIT) to slow and trap light inside an atomic medium.

Entanglement. We will assume the reader to be familiar with the notion of entanglement [9], ie the fact that a pair of particles at spatially separated positions can be in a non-separable state, leading in particular in correlations that cannot be explained by local realistic assumptions. For particles a and b at positions A and B having possible states $|\mathbf{0}\rangle$ and $|\mathbf{1}\rangle$, the typical entangled wave function is (proportional to):

---

[3]Note that french people have a slight vocabulary advantage at distinguishing between frequency ("fréquence") and angular frequency ("pulsation").

$$|\Psi_{\mathrm{EPR}}\rangle_{ab} = |\mathbf{0}\rangle_a|\mathbf{1}\rangle_b + |\mathbf{1}\rangle_a|\mathbf{0}\rangle_b \tag{7}$$

Fock states, logical states and OAM states: avoiding confusions in various $|n\rangle$ notations. In order to have distinct notations for distinct notions, we shall use:

1. $|n\rangle$ with $n \in \mathbb{N}$ for the Fock state containing n photons (in a given spatio temporal mode).

2. $|\mathbf{0}\rangle$ and $|\mathbf{1}\rangle$ for the logical states in qubit space (bold font).

3. $|l = n\rangle$ with $n \in \mathbb{Z}$ for orbital angular momentum eigenstates.

Atom cooling and trapping We will assume the reader to be familiar with the physics and techniques of atom cooling and trapping, especially with the basics of magneto-optical trapping (MOT).

Some more notations and abbreviations

APD: avalanche photodiode (or SPD: single-photon detector),
VBG: volume Bragg grating,
FBG: fiber Bragg grating,
IF: interference filter,
UHV: ultra-high vacuum (pressures below 10^{-9} Torr),
OAM: orbital angular momentum,
SLM: spatial light modulator,
LC: liquid crystals,
LG, HG: Laguerre-Gaussian and Hermite-Gaussian beams,
DLCZ: quantum repeater protocole proposed in 2001 [10].

FWHM, HWHM: Full Width at Half Maximum, Half Width at Half Maximum,
SNR: Signal-to-Noise Ratio,
Tr: trace of a matrix or operator,
$\hat{\rho}$: atomic or photonic density matrix (operators are written with a hat).
$\hat{\mathbb{I}}$: identity matrix.
$\hat{\sigma}_1$, $\hat{\sigma}_2$, $\hat{\sigma}_3$: Pauli matrices.
$|\Psi\rangle$: quantum state. Typically, the state of a qubit:

$$\begin{aligned}|\Psi\rangle &= \alpha|\mathbf{0}\rangle + \beta|\mathbf{1}\rangle \\ &= a|\mathbf{0}\rangle + be^{i\phi}|\mathbf{1}\rangle \\ &= \cos(\vartheta/2)|\mathbf{0}\rangle + \sin(\vartheta/2)e^{i\phi}|\mathbf{1}\rangle\end{aligned}$$

with $a, b \in \mathbb{R}$ or $\vartheta \in [0, \pi[$, $\phi \in [0, 2\pi[$.

$F = \langle\Psi|\hat{\rho}|\Psi\rangle$: fidelity of a quantum state of density matrix $\hat{\rho}$ to a target state $|\Psi\rangle$.
S_1, S_1, S_1: Stokes parameters (see main text – section 3.3.1).
α: the angle between the signal and control beams in EIT experiments, or a complex number.
α_{d}: the angle of the dark axis in a HG mode.
η: quantum memory efficiency,

τ or τ_m: decay time of the quantum memory,

τ_s and $l_s = c \cdot \tau_s$: duration and free-space length of a signal pulse,

d_0: optical depth of an atomic ensemble.

Chapter 1

Quantum information and quantum memories

Contents

This thesis is about quantum memories, that are promised to be ubiquitous devices in future quantum information hardwares. In this chapter, we first introduce quantum information as a general framework, then we focus on quantum communications and highlight why quantum memories are the key element for them to become viable at long distances. We then give a short overview of the different physical substrates and protocols that can be used to implement such a quantum memory and finally detail their expected characteristics and the current state of the art.

1.1 Quantum information science

Quantum information and qubits. Quantum Information Science (QIS) has emerged over the last decades building over the idea that *information itself* can be manipulated as a quantum object. An extensive review on the state of the art of QIS in Europe can be found in [11].

To be a bit more specific, one can say that QIS is the research area that utilizes all quantum properties of the physical information carriers. To the notion of a classical bit of

information is thus substituted the notion of a quantum bit or *qubit*. While a classical bit is an object that can take two values, commonly denoted by 0 and 1, a qubit is an object that lives in a two-dimensional Hilbert space spaned by two basis states commonly denoted by $|\mathbf{0}\rangle$ and $|\mathbf{1}\rangle$. A quantum bit is the fundamental information quantity in QIS just as a classical bit is the elementary piece of information in classical information science. The main difference comes from the fact that the qubit can exist in any superposition of $|\mathbf{0}\rangle$ and $|\mathbf{1}\rangle$ – which has no equivalent in classical information science. A complete introduction to quantum information science can be found in [12].

Let us now examine briefly the *motivations* for QIS and the reasons why it has emerged as an active field of research over the last decades.

Moore's law up to the atomic scale. QIS was motivated on one side by the extrapolation of Moore's law (the observation that the size of transistors is reduced by half every two years) to the point where the computer's elementary circuits would become so small that they would reach the size of single atoms or molecules. In this extrapolated future, classical physics would fail to predict their behavior and computer designers would *de facto* have to work with *quantum* information carriers and processors. But this is not the main reason for the interest in QIS, since reducing the size of transistors is not the only way to ensure an exponential increase in computational power – at least for a few more decades.

Quantum simulation. A stronger motivation for the development of QIS was the fact that the behavior of large quantum systems is intrinsically *hard* to simulate on classical computers. A (slightly oversimplified) explanation for this is the following argument. In the simulation of a classical system, if the state of one particle is decribed by just one bit of information, then the state of N particles can be described with N bits. This can be already quite big, but it scales *linearly* with the number of particles. In the simulation of a quantum system, the quantum state of one particle is defined by one qubit (which is the smallest amount of information regarding a quantum system). Then, the state of N particles will have to be described by a vector living in a 2^N dimensional Hilbert space. This means that defining the system's state already requires 2^N real coefficients! Due to this exponential scaling, the information content of a quantum system is much much bigger than that of a classical one. One can find in popular science many picturesque descriptions of how the mere expression of the quantum state of a nanogram of matter would represents more information than could be stored on hard drives even if all the mass of Earth were used solely for this purpose.

Of course, *some* large quantum systems can be simulated given they are studied in a certain range of parameters. However, these are only exceptions and there *are* large quantum systems of interest that are *intrinsically hard* to simulate on a classical computer. However, the evolution of a large quantum system *does produce* the result of the simulation... of itself! While this is self evident, it was the origin of the idea of quantum simulation.

If a well controlled quantum system is created whose quantum evolution follows the same rules as that of another system, then the controlled evolution of the first system is a simulation of the second one. The second system may be a system of interest which is difficult to simulate on classical computers (as explained before) and not accessible to direct experimental control. This is the essence of quantum simulation.

A *universal* quantum simulator would be a device able to simulate the behavior of *any*

other quantum system. While no such universal simulator is likely to come to life in a close future, specific quantum simulators, designed to simulate given problems in many-body or high energy physics, are currently being developed (see [13] or [14] for reviews on this topic).

More futuristic versions of quantum simulators, relying on yet-to-be-developed universal quantum computers (see next) will require the development of quantum memories.

Quantum computers. The most ambitious goal in QIS, quantum computation, is the quantum manipulation of qubits with the purpose of performing the *same* tasks as a classical computer. In this respect, it complies with the Church-Turing thesis. The only difference may be in the *efficiency* with which a computation is performed. And indeed, a seminal discovery (and boost to the interest in quantum computing) came in 1993 with the finding of quantum algorithms able to outperform their classical counterparts. The efficiency of quantum algorithms is often explained intuitively as resulting from one of the properties of qubits mentionned earlier, namely that they can exist in a superposition of states $|0\rangle$ and $|1\rangle$, so they can be thought of as exploring multiple alternatives in parallel while a classical algorithm sometimes has to enumerate them all.

The efficiency of an algorithm is measured by its complexity class [15]. It describes how the ressources required for the computation (mainly computation time and possibly memory size) grow with the size of the input.

Shor's quantum algorithm [16, 17] allows to factor integers into primes in a time that grows "only" polynomially with the input size. The problem of integer factorization is well known in classical computing for being a "hard" problem, i.e. a problem for which the best known algorithm's complexity is exponential. It is even strongly believed to be intrinsically hard, meaning that not only no polynomial algorithm has been found yet, but that no such algorithm *exists*. The belief in the "hardness" of the factorizataion problem is so strong that it is the basis of virtually all modern cryptography through the RSA algorithm. Due to this fact, the quest for a quantum computer has been jokingly described as "solely motivated to create a market for quantum cryptography" (a set of QIS based cryptographic techniques, see next).

Heroic experimental implementations of Shor's algorithm have been performed over the past thirteen years, starting with the factorization of $15 = 3 \times 5$ in an NMR system [18], followed by several other implementations in different physical systems [19–21], and culminating with the factorization of $143 = 11 \times 13$ [22]. Other quantum algorithms have been theoretically shown to improve over classical ones and have known similar heroical experimental implementations using custom made hardware, such as Grover's algorithm for the search in an unordered database [23–26], or algorithms for linear solvers [27, 28] or data fitting [29].

Even if the various experimental demonstrations give proofs-of-concepts of the quantum algorithms, we are not even close today to having the basic buidling blocks of a universal quantum computer. Indeed, all the implementations up to date require a custom hardware and are not scalable. A real quantum computer should be able to perform any quantum factorization (even any quantum computation) on the same hardware.

Let us note that there is one company today claiming to produce and sell quantum computers (or rather quantum *annealers*, which is a weaker claim), but despite their recent mediatised broadcasting, their is a strong lack of agreement in the scientific world as to whether or not their device *is really quantum* [30].

There is no consensus today on which physical substrate to use for the implementation of qubits – let alone for a quantum computer. One thing however is pretty likely : future quantum computers will need to store (at least some) qubits in analogues of RAM memory during their calculations. And this is one of the reasons for the quest for quantum memories. Another reason, as will be detailed just next, is the development of long distance quantum communications.

1.2 Quantum communications

If the last section has depicted quantum computing as a somewhat far-away goal, QIS does have a shorter-term application in *quantum communications* and *quantum cryptography.*

Quantum communications can be defined as the art of transferring quantum states between remote places [31].

In this framework, quantum cryptography [1] is a set of techniques utilizing quantum communication to enable a secure (secret) communication between different parties.

We now give a general presentation of quantum communcations and explain why quantum memories are expected to play such a crucial role in their ability to operate at long distances.

1.2.1 Historical development and main features.

It was not long after the first experimental violation of Bell's inequalities [33–36] that the potential of quantum physics for secret communications was realized. The first *quantum key distribution* (QKD) protocol was proposed in 1984 [37]. It uses single photons as information carriers and the non-commutation of (polarization) observables to guarantee the generation of a secret key shared only by the trusted parties.

It was followed by several other proposals over the years. The first ones used single photons as quantum information carriers [38–40]. More recently, the use of *continuous variables*, ie coherent or squeezed states of light emerged as promising alternatives [41–45]. Some of them utilize *entanglement* explicitly as their primary source of privacy [38, 39, 41], while others rely on the *no-cloning theorem* [37, 40, 44] (see [46] for the no-cloning theorem). In all cases the source of privacy in QKD can be ultimately tracked down to the non-commutation of observables (or equivalently the uncertainty principle). In all cases also, the quantum information carriers are made of light because it travels fast and has little interaction with its environment. Moreover, in most cases it can benefit from the already existing fiber optics technologies and infrastructures.

To date, at least four companies already commercialize QKD devices, including the pioneering swiss ID Quantique and the french SeQureNet. Full scale prototypes of quantum networks have been developed in metropolitan areas like SECOCQ in Vienna in 2008 [47] or the QuantumCity in Durban in 2010 [48].

All QKD schemes use two channels: a *quantum* channel in which (secret) quantum information is transferred, and an open *classical* channel. Communication through the classical channel is required in order to extract a secret key from the quantum channel. Spying on the classical channel does not give any information to an eavesdropper because

---

[1]Although it is the main topic adressed here, quantum cryptography is not the only application of quantum communications. The more general concept of a quantum network ([32]) is another possible application of quantum communications, though probably a longer term one.

the key cannot be obtained without the quantum data. But the eavesdropper cannot copy or measure the quantum data without altering it – and hence revealing him- or herself.

Quantum information may be encoded in light pulses in many different ways. Polarization qubits are easily processed in local optical hardware, but they are limited to their fixed dimensionality and suffer from dispersion in optical fibers. They are therefore often converted to time-bin qubits [49, 50]. Ideally, polarization and time-bin qubits are carried by single-photons, but weak coherent states (with less than one photon per pulse in average) are more easily produced and they can prove sufficient in some useful cases. Ideally too, quantum states would be at telecom wavelength ($\lambda = 1550$ nm) where the attenuation in optical fibers is the smallest. There are however also proposals for free space QKD (such as satellite based QKD) [51, 52] in which the wavelength requirements are linked to atmospheric rather than glass transmission. Quantum information can be also encoded in a phase and/or amplitude modulation of a coherent state, or in its quantum fluctuations (squeezed states or Schrödinger cat states). In chapter 3, we shall study qubits encoded in the *spatial mode* of single photons, which can in principle give acces to higher dimensional states (called qu*dits*).

1.2.2 Current limitation of practical long distance QKD.

The assertion in the previous paragraph that conventional fiber optics technology can be used also for quantum communications was a little bit exaggerated because it neglects one very important issue: signal attenuation in fibers and optical repeaters. Although the glass out of which fibers are made is transparent, it's not perfectly transparent. Even at their maximum transmission, which is for $\lambda = 1550$ nm, the most widely used wavelength in standard fiber communications, their is a residual absorption of 0.2 dB/km or equivalently $\sim$ 4.6 %/km. Consequently, the energy of a signal travelling through a fiber undergoes an exponential decay with the propagation length (see focus).

While this is overcome with *optical repeaters* installed at regular intervals along the fiber in the case of classical communication, quantum signals cannot be handeled that easily. Indeed, the no-cloning theorem prevents noiseless amplification of a quantum signal. So optical repeaters, which are an essential asset of fiber communications are not re-usable for QKD.

> Imagine a source sending telecom wavelength single photon qubits at a rate of 1 Gbit $\cdot$ s^{-1}. The average time for transmitting a qubit would be: about 1 second for 500 km, about 300 years for 1000 km.

The world record for distant QKD, between 100 and 200 kilometers [53, 54] to date is limited by this exponential decay.

1.2.3 Quantum repeaters: the need for quantum memories for light.

To overcome the exponential attenuation of the quantum signal, architectures for *quantum repeaters* [55] have been proposed around the turn of the millenium. The concept of quantum repeaters is sumarized in figure 1.1. It consists in dividing the quantum channel of length L into N adjacent segments over which entangled pairs of particles are distributed. Not all QKD protocols use entanglement as their main ressource, but thanks to the quantum teleportation process [56–59], entanglement allows to transmit any desired quantum state. When two adjacent links are equipped with entangled pairs, an *entanglement swapping* operation is performed, projecting the state of the particles at the far ends of the

links onto an entangled state [60]. Thus, entanglement over two links of length L/N is transformed into entanglement over a single link of length $2L/N$.

All the subtility in the previous paragraph is hidden in the innocent-looking expression *"when two links are equipped"*. Imagine we are dealing with single photons here. If the quantum channel has a loss rate per unit of length α, then the probability to successfully equip a single link with an entangled pair is $\mathrm{e}^{-\alpha L/N}$. And consequently, if nothing else is done, the probability to have two adjacent links ready is $\mathrm{e}^{-2\alpha L/N}$... So that as the probabilities to have adjacent links ready multiply, the overall success probability drops back to the original exponential decay $\mathrm{e}^{-N\alpha L/N} = e^{-\alpha L}$. In order to overcome this, entanglement swapping operations must be done only *when adjacent links are ready*, i.e. the protocol must be *synchronized*. So photons must be told to "stop" at the link ends and wait for their partners to be ready. When doing so, the success probabilities do not multiply anymore. The detailed analysis shows that the initially exponential decay of the success probability is turned into a sub-exponential (polynomial) decay. This scheme lets long distance quantum communications step into the realm of feasible protocols.
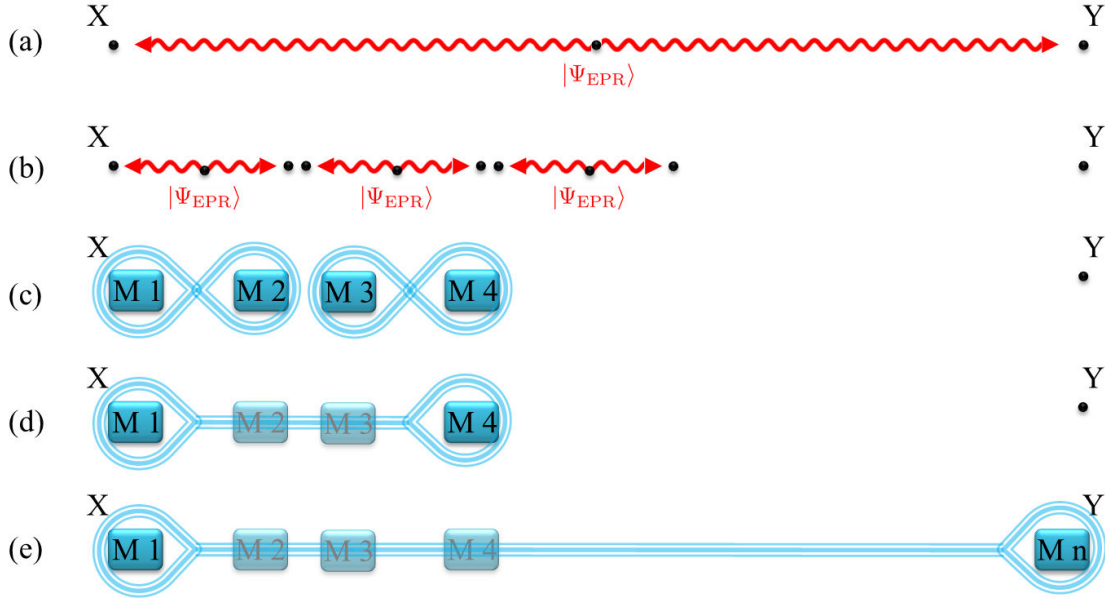
Figure 1.1: **Principle of a quantum repeater.** (a) The practical distribution of entanglement between far away parties X and Y cannot be performed by the direct transmission of an entangled pair because the success probability decreases exponentially with the distance between X and Y. (b) In a quantum repeater architecture, the quantum channel is split into many smaller segments over which entangled pairs are distributed. (c) Storing the entanglement in quantum memories (denoted M_i, $i \in \mathbb{N}$) and iterating the process allows to purify the entanglement [55] until it is ready for swapping. Blue lines linking two memories together symbolize their entanglement. (d) When adjacent links are ready (quantum memories are equipped with purified entanglement), entanglement is swapped between them, resulting in entanglement at a longer distance. (e) This process is iterated until the quantum memories at X and Y become entangled. Although this protocol is obviously much more complex than the direct transmission scheme, its success probability decreases polynomially with the X-Y distance instead of exponentially.

In order to stop the information carriers at the links' ends and synchronize the entangle-

ment swapping chain of operations, quantum memories for light are required, i.e. *devices able to store and recall arbitrary quantum states of light while preserving their quantum coherence.*

Let us now focus on quantum memories for light and review the characteristics expected from them, how they can be constructed and what achievements have been obtained so far.

1.3 Quantum memories

The last two sections presented why quantum memories are expected to be a key element in the future development of QIS in general, and how *photonic* quantum memories (i.e. for light) are the next step towards quantum repeaters and hence long-distance quantum communications. With this in mind, we now explore in more details what quantum memories should be, could be, and what they currently are.

1.3.1 Definition and requirements

As it has been hinted at before, a quantum memory is a device able to record faithfully and recall on demand the quantum state of a quantum information carrier as sketched on figure 1.2 . For quantum communications, which we are mainly interested in, the information carriers are made of light.

Obviously, a classical measurement device such as a CCD cannot fully record a quantum state because it projects (and thus alters) the state. A CCD camera for example would record the intensity at the expense of loosing the information on the phase. So a quantum memory must rely on the reversible and faithful mapping of a quantum state of light onto a (hopefully long-lived) quantum state of a piece of stationary matter.

Benchmarks for quantum memories. The following parameters are the main elements to assess the quality of a quantum memory.

- **Fidelity (F).** The fidelity measures quantitatively how closely the quantum state that is retrieved out of the memory after storage resembles the input state. The fidelity between two pure states $|\Phi\rangle$ and $|\Psi\rangle$ is given by the square modulus of their overlap: $F = |\langle\Phi|\Psi\rangle|^2$. The fidelity of a mixed state of density matrix $\hat{\rho}$ to a pure state $|\Psi\rangle$ is given by the analogous formula: $F = \langle\Psi|\hat{\rho}|\Psi\rangle$. The fidelity can be a good measure of *"how quantum"* a memory really is. For example if one tries to make a copy of an unknown single qubit using a classical measurement, then the fidelity of the copy will be bounded by 2/3 on average. Therefore, the ability to store a qubit (in any of its possible states) with a fidelity exeeding this threshold is a very strong indication of a quantum behavior, which we shall use explicitly in chapter 3. When the memory has a non-unit efficiency (see next point), the *conditionnal fidelity* is often used, which has the same definition but is computed only if the memory yields a non-empty output.

- **Efficiency (η).** Efficiency measures the energy ratio between the retrieved and input states. For single-photon input states, it translates into the success probability of the memory process. A less than unity efficiency counts as additionnal losses along the transmission line. It should therefore be as close as possible to 100 % .
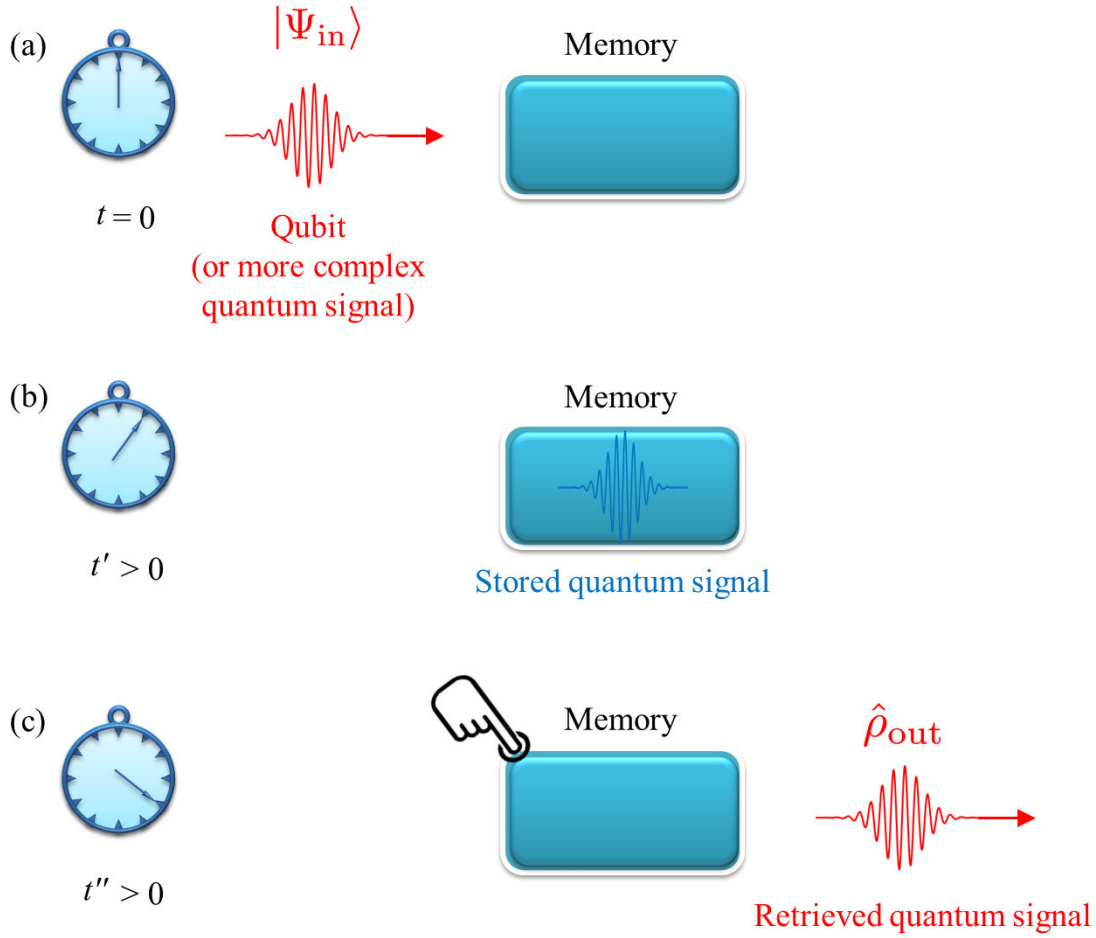
Figure 1.2: **Generic principle of a quantum memory.** (a) At time $t = 0$, a qubit $|\Psi_{\mathrm{in}}\rangle$ (or a more complex quantum state, as the case may be) arrives at the memory into which it is transferred. (b) The qubit remains stored in the memory for an arbitrary time. (c) At a later time t'', when the user pushes a button, the quantum state is released out of the memory. The fidelity of the retrieved state (of density matrix $\hat{\rho}_{\mathrm{out}}$) to the input state $F = \langle\Psi_{\mathrm{in}}|\hat{\rho}_{\mathrm{out}}|\Psi_{\mathrm{in}}\rangle$ measures the quality of the storage. The efficiency of the memory η is the probability to successfully retrieve the qubit. If the storage time t'' exceeds the memory lifetime τ, then these figures of merit start to decrease.

- **Memory time (τ or τ_m) or time-bandwidth product.** The memory time is the time over which the quantum state remains faithfully stored. A limited storage time results from decoherence inside the memory and affects both the fidelity and the efficiency of the storage. For a quantum memory to be useful in a real-world quantum communication scheme, it must have a long enough memory time. Depending on the protocol used and in the number of parallel channels available ([61, 62]), the requirements on the memory time vary between the time it takes to establish entanglement over an elementary link (of length L/N) to the time it takes to establish it over the full length L. For $L = 1000$ km and other realistic assumptions, it translates into storage times from a few tens of milliseconds to a few seconds. As the duration of input states may vary considerably from one implementation to the

other (from the picosecond to the microsecond range!), a more inclusive measure is the time-bandwidth product, where the bandwidth refers to the inverse of the input state duration. It describes qualitatively the number of quantum states that can undergo logical operations before the memory decoheres.

- **Multimode capacity.** Quite understandably, the speed (and in some cases the efficiency) of quantum communication protocols will increase with the number of quantum information carriers that can be prcessed in parallel, so the number of elementary states that can be stored in parallel inside the memory is also an important feature. Chapter 3 will show a proof-of-principle experiment indicating that our type of *ensemble-based* quantum memory (see 2.2.3) is well suited for mutlimode storage.

- **Wavelength (λ).** For fiber-optics-based quantum communications, memories should operate on a signal at telecom wavelength ($\lambda = 1.3$ to 1.5 μm). This is not an absolute necessity since quantum interfaces are being investigated that allow to transform telecom wavelength photons into memory compatible (visible) photons and vice versa [63, 64], but operating directly at the right frequency would be an undeniable advantage.

- **Signal-to-noise ratio.** Very often, quantum memories involve the use of auxilliary bright beams of light while the interesting signal is the smallest possible amount of light: a single photon! It is essential that these auxilliary beams do not pollute the quantum signal. Indeed, some very promising memory schemes have not been able to demonstrate their *"quantumness"* because the noise induced by the auxilliary light overwhelms the quantum signal. These issues will be given some considerations in sections 2.3.4 and 4.3.

These characteristics are hard to find all together in a single system. Indeed, no quantum memory to date is even close to meeting all the requirements. The next section illustrates how many different approaches are currently being investigated in the quest for quantum memories.

1.3.2 Physical substrates and protocols: many candidates

The variety of quantum memory candidates fall roughly into two categories, according to whether they rely on single quantum emitters or large ensembles of particles. They further differ in both the physical substrate onto which quantum information is mapped and the protocol used to realize this mapping.

Among the quantum memories based in single quanta one can find:

- **Single atoms in cavities.** Optically trapped single atoms in cavities have been used to demonstrate the storage of polarization qubits [65, 66] and the generation of matter-matter entanglement between remote places [67]. The best reported qubit storage showed an efficiency of $\eta = 9\%$, a fidelity of 93% and a decay time of $\tau = 180$ μs.

- **Individual trapped ions.** Electrically trapped ions in vacuum chambers are well controlled and individually adressable single quantum systems. Their applications to quantum networks have been reviewed in [68] and [69]. They have been shown to exhibit long coherence times [70]. Recent achievements with these systems include

the quantum teleportation of a qubit between remote ions [71] and the mapping of a single-photon polarization state onto a single ion [72]. In this last experiment, the storage fidelity was 95% and the low efficiency (below 1%) was compensated by a heralding mechanism. Müller and Eschner [73] have proposed to use single $^{40}Ca^+$ ions as a substrate for the storage of a polarization qubit at $\lambda = 854$ nm.

- **Nitrogen-vacancy centers in diamond.** Nitrogen-vacancy centers (NVC) are naturally occuring or engineered defects in bulk diamond exhibiting rich quantum properties. Entanglement between a single photon and the electronic spin of a NVC has been demonstrated [74] as well as the transfer of the electronic state of the NVC to its nuclear spin [75] – which has a much larger coherence time, on the order of the millisecond, and that can be further prolonged up to the scale of the second [76]. Long distance entanglement of two NVC has been reported recently in [77].

- **Quantum dots** have also been investigated as potential memory systems in recent experiments [78, 79].

Ensemble-based quantum memories are more versatile as their intrinsic multimode nature gives them the capacity to store not only "regular" (polarization) qubits but also various types of *continuous variable* quantum states such squeezed states or even Schrödinger cats. They also support a variety of different memory protocols. So far, they include:

- **Cold or ultra-cold atomic gases**, which are the earliest media used for light storage. Very pure gases of alkali atoms are prepared via laser cooling at various temperatures, from a few millikelvins in magneto-optical traps to microkelvins in dipole traps and even in the nanokelvin range in Bose-Einstein condensates (BEC). Once cooled and trapped, cold atoms can be used to implement various memory protocols. The first one ever demontrated relied on Electromagnetically Induced Transparency (EIT) and the associated ultraslow light effect [80, 81]. While being the oldest memory protocol, it has very promising features and is therefore still the subject of intense reserach. In particular, it is the one we will use in the rest of this thesis. Cold atomic ensembles in off-resonant EIT (Raman) conditions are also the medium of choice for the implementation of the DLCZ protocol (see 1.3.4 and [10, 82]). Other quantum storage protocols, such as the more recent Gradient Echo Memory (GEM) [83] have also known sucessful implementations with these systems.

- **Warm atomic vapors.** Hot gases support memory protocols that are very similar to the ones implemented in cold atomic ensembles (six orders of magnitude in temperature put aside). EIT based light storage was demonstrated in them almost at the same time as in cold atoms [84]. They have been used in several EIT or Raman-based optical storage experiments (some of which exhibited a quantum behavior) [85, 86], in GEM experiments [87] or in Faraday-interaction-based memory experiments [88].

- **Rare earth doped crystals.** These materials can experience extremely long coherence times at cryogenic temperatures. They are therefore studied as versatile light storage media. Following the demonstrations of EIT-based light storage in atomic gases, a similar experiment was performed in a crystal [89]. In addition to EIT, crystals are also well suited for photon echo protocols such as the Controlled Reversible Inhomogeneous Broadening (CRIB) [90] an equivalent of the Gradient Echo Memory or its discrete version, the Atomic Frequency Comb (AFC) [91–94]. Novel rephasing

protocols such as the poetically named Revival Of Silenced Echo (ROSE) [95] have also been successfully implemented in crystals.

- **Microcavity coupled NVC ensemble.** A recent theoretical proposal suggested that NV centers in diamond could also be used as a medium for an ensemble-based memory with very large time-bandwidth product [96].

1.3.3   The archenemy of quantum memories: decoherence

QIS as a whole is concerned with manipulating (complex) quantum states. While there are of course quantum states that are robust against external noise (they will not change significatively in the presence of a perturbation), they constitute but a small minority of all possible quantum states. Most states are indeed dreadfully fragile. And quantum information has to deal with them too. The eigenstates of common observables (often used as *basis* states) can be relatively stable. But in a superposition of such eigenstates, the *phase* (or coherence term) between them is often a very fragile element that gets blurred as time goes. This blurring of the phase or *decoherence* eventually destroys pure quantum states and turns them into classical (non-quantum) mixture states that are useless for quantum information purposes. It is recognised as the strongest obstacle to the development of quantum information technologies.

Quantum memories too have to cope with decoherence, and one of the essential issues of the research in this area is the fight against and control of its various sources.

Some people consider decoherence as a *characteristic trait of the quantumness* of a system. According to the most extreme version of this opinion, decoherence must forever prevent the emergence of quantum information technologies. In the quest for quantum memories, one needs of course to have faith in the existence of at least *some* systems in which interesting quantum states can live for long times!

We will examine the sources of decoherence that affect our type of quantum memory theoretically in section 2.2.5 and experimentally in section 2.3.2.

1.3.4   A closely related cousin: the DLCZ protocol

In our definition of a quantum memory it was implicitly assumed that a quantum memory has to be able to record the quantum state of a light pulse impinging on it. But in 2001, a protocol has been proposed for a quantum repeater involving a type of quantum memory where the quantum signal (a single photon) does not enter into the memory, but is created directly inside of it in a proabilistic (but heralded) process [10]. The DLCZ protocol, as it is commonly refered to, relies on ensemble-based memories intereacting with light in a configuration similar to the Raman (off resonant EIT) case. It is schematized in figure 1.3.

The memory unit consists in an ensemble of three-level atoms having two ground states $|g\rangle$ and $|s\rangle$ and one excited state $|e\rangle$. It is initialized by putting all atoms in the ground state $|g\rangle$. Light-matter entanglement can be created by shining a weak off-resonant *write* laser pulse on the ensemble. Being weak and off-resonant, this pulse has a strong probability to do nothing, and a weak probability to promote one of the atoms to the excited state, which can then decay either back into $|g\rangle$ or into $|s\rangle$. In this second case, a single photon, refered to as *field 1* (in blue in the figure), is emitted which heralds the transfer of one single atom from $|g\rangle$ to $|s\rangle$ (see top part of figure 1.3). Now if *two* nearby ensembles are being shined on by write pulses, and if their field 1 paths are interfered on a 50 : 50 beam splitter, then the detection of *one* photon after the beam splitter heralds the creation of one atomic

transfer in one of the two ensembles (but the *which ensemble* information is destroyed). This means that such a detection event heralds the entanglement of the atomic ensembles. It also means that the creation of the single quantum of excitation and its storage in a memory are merged into a single operation.

Once pairs of memories have become entangled, entanglement can be propagated as shown in the lower part of figure 1.3. Bright resonant *read* pulses simultaneously illuminate two memories, so that if one atomic excitation is present in an ensemble, it will be transferred back into state $|g\rangle$ with a high probability while emitting a photon in so-called *field 2*. Field 2 photons from different memories are brought to interfere on a $50 : 50$ beam splitter. After the beam splitter, it is again impossible to tell from which ensemble came a single photon. So the detection of one (and only one) photon at the output of the beam splitter projects the two remaining memories onto an entangled state in which they share a single delocalized atomic excitation. In the absence of such an event, the process failed and must be repeated.

The presence of entanglement storage at each step of the protocol ensures that the time required to generate long distance entanglement scales polynomially in the total distance.

Critical to the DLCZ protocol is the use of ensemble of atoms, in which the collective enhancement effect (see section 2.2.3) ensures the high quality of the light-matter entanglement. Since its proposal, the memory part of the DLCZ protocol has known numerous lab demonstrations, although the entanglement swapping operation remains a tricky part [82]. The memory part of the protocol has been realized with an efficiency and a memory time reaching respectively 73% and 3 ms [97].

Although the fact that the quantum signal generation and its storage are merged in a single step is an attractive feature of the DLCZ protocol, its probabilistic nature also has some serious drawbacks. Indeed, in order to generate high purity single photons, the success probability must be very low. In addition to the low count rate itself, this makes the whole process more sensitive to any experimental imperfection such as signal contamination by scattered light or detectors' dark counts. For this reason, the development of quantum memories as described in section 1.3.1 where the generation of the quantum signal and its subsequent storage are distinct procedures is still a meaningful goal.

1.3.5 State of the art

Let us finish this introductive chapter with a brief overview of the state of the art in quantum memories, focusing on quantum memories based on EIT in cold atomic ensembles, which are the type of memories studied in the rest of this manuscript. Many review articles can give a much more detailed account such as [98–100].

The first experimental demonstrations of light storage using EIT date back to 2001 with an experiment in an ultra cold atom cloud (Bose-Einstein Condensate) [81] and another in a warm atomic vapor [84]. They were followed the year after by the demonstration of an EIT memory in a rare earth doped crystal [89]. In these papers, the stored optical signals were bright pulses of light so that the *quantumness* of the memory could not be assessed. Furthermore, memory lifetime and storage efficiencies were limited.

The first *really quantum* memories were produced in 2005 and were used to store single photons. Again, two independant groups did the same storage experiment, one in a cold atomic sample [101], the other in a warm atomic vapor [102]. It was checked that after a few microseconds of storage, the single photon character of the signal was preserved.

From there on, experimentalists strived either to push further the *quantumness* of
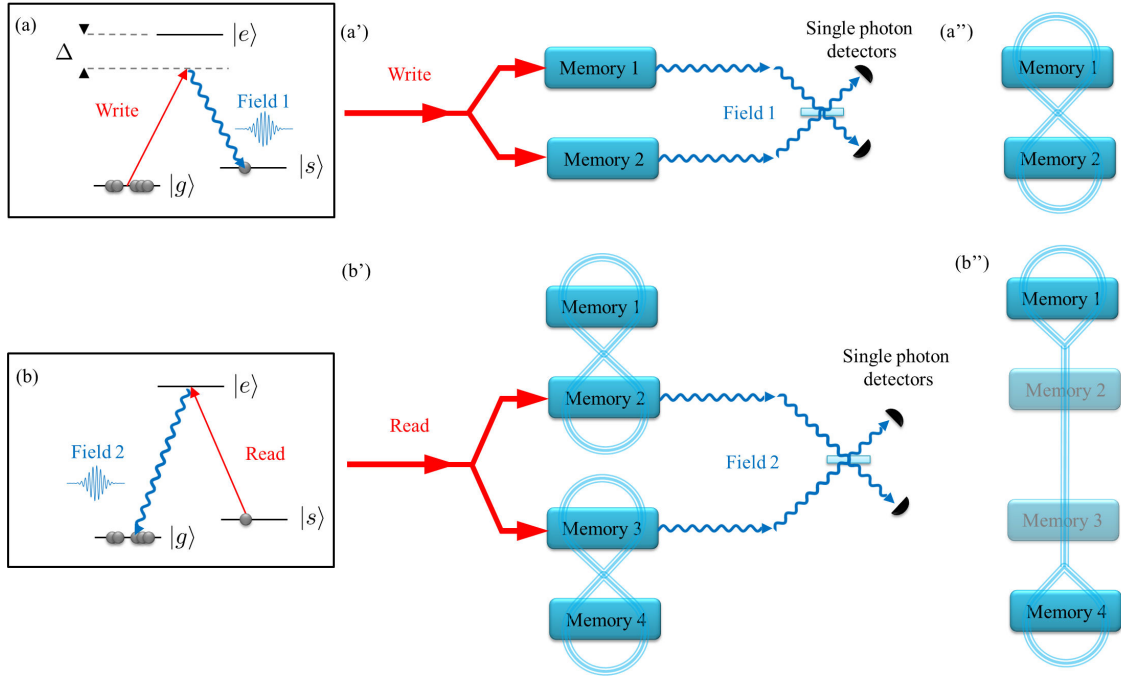
Figure 1.3: **The DLCZ protocol.** Upper part: generation of entangled single excitations stored inside quantum memories. (a) Atomic level scheme in the memories. (a') The probablistic creation of a single excitation into two memories by the weak off-resonant *write* pulse, followed by the detection of a single heralding photon after a beam splitter projects the quantum memories onto (a") an entangled state. Lower part: entanglement swapping between adjacent pairs of entangled memories. Initially, memories 1 and 2 are entangled and so are memories 3 and 4. (b) and (b') A bright resonant *read* pulse shined at memories 2 and 3 deterministically returns any atomic excitation back into state $|g\rangle$ while generating single photons in *field 2*. The paths of field 2 photons are brought together on a beam splitter after which it is impossible to tell where a photon came from. If a single photon is detected, then the procedure is successful and leaves memories 1 and 4 entangled (b"). Mathematically, the entanglement swapping operation is a projection of the four particle wavefunction $(|\mathbf{0}\rangle_1|\mathbf{1}\rangle_2 + |\mathbf{1}\rangle_1|\mathbf{0}\rangle_2) \otimes (|\mathbf{0}\rangle_3|\mathbf{1}\rangle_4 + |\mathbf{1}\rangle_3|\mathbf{0}\rangle_4)$ on the two particle state $|\mathbf{0}\rangle_2|\mathbf{1}\rangle_3 + |\mathbf{1}\rangle_2|\mathbf{0}\rangle_3$, resulting in the generation of the state: $|\mathbf{0}\rangle_1|\mathbf{1}\rangle_4 + |\mathbf{1}\rangle_1|\mathbf{0}\rangle_4$ in which excitations in memories 1 and 4 have become entangled although they have never interacted before!

the memories, or to improve their figures of merit. On the way towards the greatest quantumness, EIT in cold atomic ensembles was used to store entangled photon pairs in 2008 [103] as well as squeezed vacuum pulses [104, 105]. More recently, it was used to store a quantum bit encoded in the polarization of a single photon with memory times hitting the millisecond range [106–108]. On the way towards better and better figures of merit, recent experiments performed on classical signals have been reported with storage times above 16 seconds [109] or with efficiencies reaching 78% [110]. Using the DLCZ protocol, storage efficiencies of 73% have also been observed [97], as well as storage times of one tenth of a second [111]. The (spatially) multimode nature of these storage media have also been discussed in [112] and probed experimentally by Inoue et al. [113, 114] using the DLCZ protocol, and more recently by Veissier et al. [5], Nicolas et al. [6] using EIT. This

	Qubit storage	Multimode capacity	Fidelity F	Efficiency η	memory time τ
EIT	✓	✓(3) [114]	98.6% [108] to 100% [107]	78% [110]	16 s [109]
GEM	todo	✓(20) [115]	todo	80% (cold atoms) [83] 87% (warm atoms) [116]	20 µs [115]
DLCZ	✓	✓(3) [113, 114]	none	73% [97]	100 ms [111]
AFC (crystals)	✓	✓(1060) [119]	> 99% [92–94]	56% [117]	20 µs [118]

Table 1.1: **Summary of the best achievements in quantum memories for a selection of systems.** For all four systems, record-breaking values come from different experiments and have not been observed simultaneously yet. Note that coherence times exceeding one second have been reported in experiments with rare-earth-doped crystal [120].

demonstration constitutes a major part of this thesis and is reported in details in chapter 3.

Table 1.1 compares the best reported figures of merit of different memory media and protocols. Electromagnetically Induced Transparency in cold atoms appears to be a very promising way to implement quantum memories due to its potential high efficiencies, long lifetimes and high fidelities. EIT memories also have a certain multimode capacity in the spatial domain and have been employed sucessfully for the storage of complex quantum states (single-photon qubits, squeezed vacuum, entangled pairs, ...). Of course, these nice figures of merit have not been achieved simultaneoulsy yet, and this is why research must go on.

1.4 Conclusion

In this chapter, we have drawn a panorama of the research on quantum memories and put them in perspective with quantum information science and especially with quantum communications.

- In future quantum communication networks, **quantum repeaters** will be based on **quantum memories for light**.

- Critical parameters estimating the quality of a potential quantum memory include mainly the **fidelity** of the storage, the memory **lifetime**, its **efficiency** and **multimode capacity**.

- No ideal quantum memory candidate has revealed itself yet, but many systems are being investigated and improvements are going on at a high pace with new record-breaking experiments every few months.

In the remaining of this manuscript, we shall report on some experiments done in our lab with two quantum memory candidates. Both quantum memory candidates are implemented using the Electromagnetically Induced Transparency (EIT) protocol in ensembles of cold atoms (or occasionnally the DLCZ protocol).

In odrer to understand the memory protocol, the next chapter is dedicated to EIT and its application to light slowing and trapping.

Chapter 2

EIT, slow and stopped light for quantum memories

Contents

In this thesis, we implement quantum memories in large ensembles of cold atoms using the phenomenon known as Electromagnetically Induced Transparency (EIT). Historically, EIT-based stopped light in atomic ensembles is the first procedure proposed and used to realize a quantum memory ([81, 101]), and it remains today one of the most promising avenues towards quantum memories.

In this chapter, we explain the general functionning of EIT-based quantum memories and present the experimental setup that we use to implement it in the lab.

2.1   Electromagnetically Induced Transparency and slow light

EIT occurs in some media when a light beam that should normally be absorbed is instead
transmitted due to a quantum interference with another light beam, usually called the
control beam. Light propagating in an EIT medium experiences an extremely reduced
(and tunable at will) group velocity. To store a light pulse using EIT, its group velocity is
adiabadically reduced to zero while it propagates inside the medium. This process transfers
the quantum state of the stored light pulse into an atomic coherence.

2.1.1   Linear susceptibility in EIT systems

To understand how EIT quantum memories work, let us first have a look at the response
of such a medium to a probe (signal) beam undergoing EIT.

The model is a three-level atom in a Λ configuration with states $\{|g\rangle, |s\rangle, |e\rangle\}$ as depicted
in figure 2.1. It is initially in state $|g\rangle$. State $|e\rangle$ has a spontaneous decay rate Γ into states
$|g\rangle$ and $|e\rangle$. The reader can refer to appendix A.1 for a more detailed explanation and for
the details of the calculation.

The signal field is close to resonance with the $|g\rangle \leftrightarrow |e\rangle$ transition. We note ω the signal
beam frequency and δ its detuning. EIT for the signal field is engineered by a control field
on resonance with the $|s\rangle \leftrightarrow |e\rangle$ transition (frequency ω_c). In situations where the control
can be off resonance, it is common to use δ as the *two-photon detuning*, but here this will
make no difference. The strength of the light-matter interaction for both fields is described
by their Rabi frequencies Ω_s (signal) and Ω_c (control).
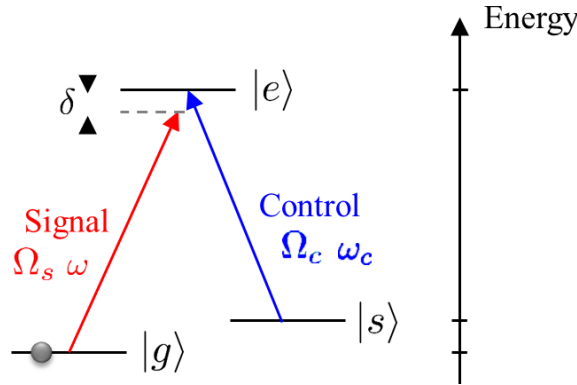
Figure 2.1: **Atomic levels and light fields scheme for EIT.** The signal field is close
to resonance with the $|g\rangle \leftrightarrow |e\rangle$ transition (frequency ω, detuning δ, Rabi frequency Ω_s).
The transmission properties of the atom (initially in state $|g\rangle$) are modified by the control
field, which is on resonance with the $|s\rangle \leftrightarrow |e\rangle$ transition (frequency ω_c, Rabi frequency
Ω_c). Excited state $|e\rangle$ has a spontaneous decay rate Γ.

In the absence of the control field, the signal experiences maximum absorption at
resonance ($\delta = 0$), and the absorption profile around resonance exhibits a Lorentzian
shape with a full width at half maximum equal to Γ.

For simplicity, we chose to neglect the decoherence term γ_{gs} between gound levels $|g\rangle$
and $|s\rangle$. The action of a dielectric material on a propagating light wave is described by the
susceptibility χ, which appears in the wave equation in the presence of matter:

$$\nabla^2 \vec{E} - (1 + \chi)\frac{1}{c^2}\frac{\partial^2}{\partial t^2}\vec{E} = 0 \tag{2.1}$$

With the given notations, the linear susceptibility per atom is given by:

$$\chi(\delta) = \kappa \frac{\mathrm{i}\delta}{\mathrm{i}\left(\delta^2 - \frac{\Omega_c^2}{4}\right) + \frac{\delta\Gamma}{2}} \tag{2.2}$$

Where $\kappa = d_{eg}^2/2\epsilon_0\hbar$. The real part of χ gives the dispersion (phase-shifting) coefficient while the imaginary part provides the absorption coefficient.

In the moderate control field regime defined by $\Omega_c < \frac{\Gamma}{2}$, the poles of $\chi(\delta)$ are imaginary, which allows to re-write the absorption resulting from equation (2.2) as:

$$A_{EIT}(\delta) = \frac{C_+}{\delta^2 + \delta_+^2} + \frac{C_-}{\delta^2 + \delta_-^2} \tag{2.3}$$

The expressions of C_+, C_-, δ_+ and δ_- are given in appendix A.2. This is the "pure EIT"
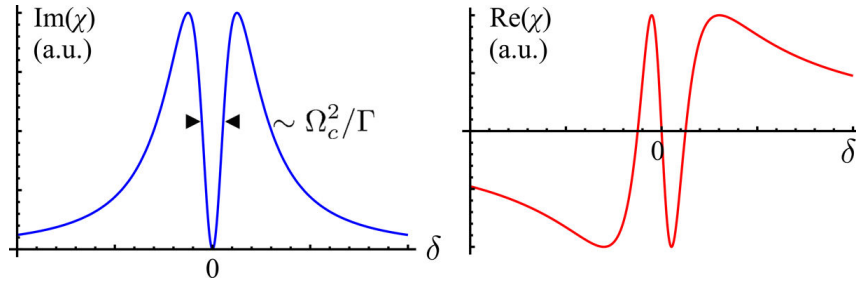
Figure 2.2: **Absorption and dispersion profiles in an EIT medium.** Imaginary (left side, blue curve) and real (right side, red curve) components of the susceptibility $\chi(\delta)$ given by equation (2.2) as a function of the signal's detuning δ. Both are zero at zero detuning, meaning perfect transparency for a resonant signal. The group velocity however, which is linked to $\frac{\mathrm{d}}{\mathrm{d}\delta}\mathrm{Re}(\chi(\delta))$ is extremely reduced in this region as explained in section 2.1.2. The plot is made for $\Omega_c = \Gamma/2$.

region, where the absorption profile looks like the unperturbed (Lorentzian) resonance in which a narrow "transparency window" of width Ω_c^2/Γ has been opened. Figure 2.2 shows the theoretical shape of $\chi(\delta)$ as defined by equation (2.2).

As the power of the control field Ω_c^2 increases, the transparency window becomes wider and wider until the two halves of the absorption spectrum become two well separated resonances. In the limit of very intense control field, the absorption profile looks like two distinct resonances of width $\Gamma/2$ separated by Ω_c, a phenomenon also known as the Autler-Townes splitting.

Recently, the distinction between EIT and Autler-Townes splitting (ATS) has raised some discussions [4, 121, 122]. This was due in part to the fact that EIT alone can lead to quantum memories while ATS alone cannot. In the model presented here, the two phenomena appear as different behaviors of a single system that depend on the value of one parameter. But there are other systems which can exhibit ATS without EIT [121, 123, 124], in particular in the presence of large decoherence (γ_{sg}). Our group has investigated experimentally the transition between the two behaviors in [4] in the well-controlled system that we use to implement a quantum memory. Figure 2.3 shows how the absorption

profile evolves with increasing values of Ω_c (see section 2.3 or Giner [125], Veissier [126] for experimental details).

This study was reported in [4] and in the PhD dissertations by Giner [125] and Veissier [126]. It was found that in the weak control field region (which is relevant for the implementation of quantum memories), the EIT model of equations (2.2) and (2.3) fits very well to the experimental data. With increasing values of Ω_c however, the simple three level model breaks down as the more intricate structure of the atoms begins to play a significant role [123]. In the region $\Omega_c \lesssim \Gamma$ which is relevant for quantum memories however, this will not be an issue.
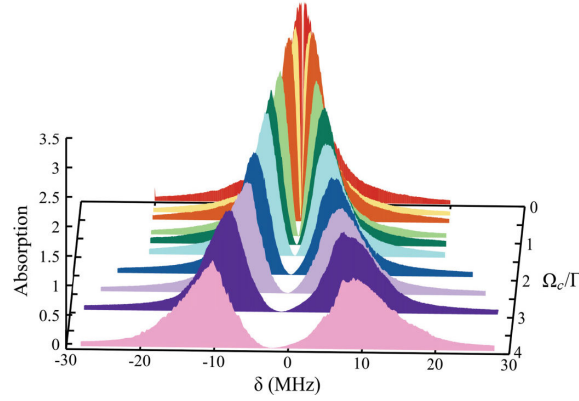
Figure 2.3: **Experimental absorption profiles for various values of the control Rabi frequency Ω_c.** The vertical axis shows the absorption coefficient (or more precisely the optical depth as defined in equation (2.6)), the left-right horizontal axis gives the detuning δ of the signal and the back-front horizontal axis the (dimensionless) power of the control field Ω_c/Γ (where $\Gamma = 2\pi \times 5.2\,\text{MHz}$). As the power of the control field increases, the transparency window broadens until the atomic resonance is finally split into well separated peaks. However, the complex detailed structure of the atoms used in the experiment prevents the formation of two nice resonances as in a naive ATS model. In these measurements, the convention for naming the ground states $|g\rangle$ and $|s\rangle$ of ^{133}Cs was the opposite of the one that will be used for the quantum memory implementation in section 2.3 but this is merely a matter of definition. Credits: Giner et al. [4].

Let us now turn to the consequence of EIT that is relevant for quantum memory implementation: the slow light effect. For this, we consider an *ensemble* of atoms of density n_0 and length L, so that the susceptibility experienced by the signal field is now given by: $n_0 \chi(\delta)$.

2.1.2   Slow light in an EIT medium

Even if the susceptibility in equation (2.2) is zero at exact resonance (meaning that a resonant pulse can propagate without absorption), there is a strong light-matter coupling. This coupling manifests itself as a spectacular slow light effect.

The group velocity v_g of a wave packet of frequency ω and wave vector k is given by: $1/v_g = \mathrm{d}k/\mathrm{d}\omega$. The wave vector $k(\omega)$ (or $k(\delta)$) is derived from the propagation equation (2.1): $k(\omega)^2 = \frac{\omega^2}{c^2}(1 + \text{Re}(\chi(\omega)))$. In the vicinity of resonance, this leads to:

$$v_g = \frac{c}{1 + \frac{1}{2}\omega\frac{\mathrm{d}}{\mathrm{d}\delta}\mathrm{Re}(\chi(\delta))} \tag{2.4}$$

Yet it can be seen from figure 2.2 that the dispersion is extremely steep in the vicinity of the resonance. At the linear order in δ, from equation (A.16), we have: $\mathrm{Re}(\chi(\delta)) \sim -\kappa\delta/\delta_+\delta_- \sim 4\kappa\delta/\Omega_c^2$. So if the power of the control field is decreased towards zero, then the group velocity of a signal pulse can be made arbitrarily small, according to:

$$v_g \underset{\delta\to 0}{\sim} \frac{c}{1 + 2\frac{n_0\kappa\omega}{\Omega_c^2}} \tag{2.5}$$

In this equation and from now on, we take into account the fact that we're considering an *ensemble* of atoms through the replacement: $\kappa \to n_0\,\kappa$.

It is useful to introduce the *optical depth* (OD) of the atomic ensemble, which is defined as the absorption of a resonant ($\delta = 0$) signal in the absence of control field by the whole length of the ensemble in logarithmic units[1]:

$$d_0 = 4\frac{n_0\omega\kappa L}{c\Gamma} \tag{2.6}$$

In terms of the OD, the group velocity of equation (2.5) can be rewritten as:

$$\frac{c}{1 + \frac{d_0\Gamma c}{2L\Omega_c^2}} \tag{2.7}$$

In practice, the most spectacular experimental demonstration of this ultra slow light effect was done by Hau et al. [80] in 1999. They measured a signal group velocity of $17\ \mathrm{ms}^{-1}$ in a Bose Einstein condensate of sodium atoms.

The slow light effect can be seen as the working principle of EIT-based quantum memories as will be detailed in the next section.

2.2 EIT quantum memory in an ensemble of atoms

In this section, we consider the realization of a quantum memory inside an ensemble of atoms described by the EIT model introduced in the previous section.

2.2.1 Stopping light in an EIT medium

The working principle of an EIT quantum memory can be explained following the steps of figure 1.2:

- In step (a), the memory is initialized. An ensemble of three-level atoms with the Λ structure of figure 2.1 is prepared with all atoms in state $|g\rangle$. A control beam of Rabi frequency $\Omega_c \sim \Gamma$ is shined on them, so that a signal beam would experience an atomic susceptibility $\chi(\delta)$ as given in equation (2.2). Then, a signal pulse of duration τ_s and free space length $l_s = c \cdot \tau_s$ impinges on the atomic ensemble.

---

[1]Following the tradition in atomic physics, the optical density is defined here in the *natural* base e. Safety goggle manufacturers use base 10 OD instead.

- Between steps (a) and (b), the signal pulse enters into the atomic ensemble. There, it propagates without absorption at a reduced group velocity v_g depending on the value of Ω_c. For absorption to be completely suppressed, the signal bandwidth, given roughly by $1/\tau_s$, must fit entirely inside the transparency window, which means $\Omega_c > 1/\tau_s$. As it gets slower, the signal pulse is also spatially compressed by a ratio equal to the slowing factor v_g/c. Thanks to this huge reduction in size, a signal pulse measuring several hundred meters in free space can fit inside an atomic ensemble of a few millimeters!

- From equation (2.5), it appears that v_g can be made zero by switching off the control beam. When Ω_c approaches 0, v_g scales linearly with the power of the control beam (Ω_c^2): $v_g \sim 2c\Omega_c^2/\kappa n_0\omega$. If this happens while the signal pulse is still inside the atomic ensemble, it remains "trapped" there until v_g is finally made non-zero again. Since this also closes the transparency window, one may have doubts about how the signal can be trapped in a medium which is not any more transparent for it. This apparent riddle is solved by the fact that there is no more *light* in "stopped" light : as v_g is reduced to zero, the signal is turned entirely into atomic coherence, which is of course not concerned with transparency issues. For each photon in the signal field, one atom is transferred from state $|g\rangle$ to state $|s\rangle$. This is formalized by the concept of dark state polaritons (see section 2.2.2 and Fleischhauer and Lukin [127, 128], Lukin [129], Fleischhauer et al. [130] for details).

- In step (b), the signal remains trapped inside the atomic ensemble as long as the control beam remains off. In reality, the amplitude of the stored signal decreases on a timescale set by the coherence time of the memory τ.

- In step (c), the hand-pressing-a-button stands for switching the control beam back on, reestablishing a non-zero group velocity v_g for the signal, which can thus propagate again inside the atomic ensemble and finally leave it.

In this description of the memory protocol, it becomes clear that the power of the control beam Ω_c^2 is at the center of a trade-off governing the efficiency of the storage. For a given signal, this power must be **large enough** for the signal spectrum of width $\sim 1/\tau_s$ to fit in the transparency window, but it must also be **small enough** for the signal spatial extension (compressed to $\sim \tau_s \cdot v_g$) to fit inside the atomic ensemble. On one hand, if Ω_c is too small, the high-frequency components of the signal will be out of the transparency window and they will be absorbed: the memory will act as a frequency filter removing the signal sharp rising and falling edges. This not only changes the signal shape but also causes loss, i.e. it lowers the efficiency η. On the other hand, if Ω_c is too large, then the signal pulse length will remain too long to fit inside the ensemble and some of it will leak out of the memory medium and won't be stored, also lowering η.

The first condition (large Ω_c) translates into $\tau_s\Omega_c > 1$ – which importantly does not depend on n_0. The second condition (small Ω_c) translates into $\tau_s\Omega_c^2 < L\kappa\omega n_0/c = \frac{d_0\Gamma}{4}$. It results from these conditions that in order to maximize the efficiency of an EIT memory, one has to chose the *smallest* Ω_c value that allows the transparency window to cover the entire signal bandwidth, and use an ensemble as dense and as long as possible. The **optical density** appears to be the name of the game enabling both conditions to be satisfied (if and only if it is large enough). Let us inderline that the inclusion of a non-zero dephasing term γ_{gs} between levels $|g\rangle$ and $|s\rangle$ in the model of section 2.1 sets a limit to the transparency that can be achieved [86, 123]. The resonant ($\delta = 0$) single-atom absorption coefficient

at finite control power is no longer zero but given by $\kappa\gamma_{gs}/(\frac{\Omega_c^2}{4} + \frac{\Gamma\gamma_{gs}}{2})$. Since non-zero absorption means reduced efficiency for the memory, it is crucial to choose a medium in which the dephasing between levels $|g\rangle$ and $|s\rangle$ is as small as possible.

2.2.2 Dark state polariton description

An alternative and insightful point of view on slow and stopped light in EIT media was introduced by Fleischhauer and Lukin [127] under the stage name of Dark-State Polaritons. The *dark state* arises as an eigenstate of the atomic hamiltonian (in the rotating frame) given in (A.9) at resonance ($\delta = 0$):

$$\hat{H}_{\mathrm{RWA}} = \begin{pmatrix} 0 & 0 & \Omega_s \\ 0 & 0 & \Omega_c \\ \Omega_s & \Omega_c & 0 \end{pmatrix} \tag{2.8}$$

It has three eigenstates:

$$|\Psi_0\rangle = \frac{1}{\sqrt{\Omega_s^2 + \Omega_c^2}} \left(\Omega_c|g\rangle - \Omega_s|s\rangle\right) \qquad \text{with eigenvalue: } 0$$

$$|\Psi_\pm\rangle = \frac{1}{\sqrt{2}} \left(|e\rangle \pm \frac{1}{\sqrt{\Omega_s^2 + \Omega_c^2}} \left(\Omega_s|g\rangle + \Omega_c|s\rangle\right)\right) \qquad \text{with eigenvalues: } \pm\sqrt{\Omega_s^2 + \Omega_c^2}$$

The state $|\Psi_0\rangle$ does not contain the excited state $|e\rangle$ so it cannot decay radiatively. That's why it's called the *dark* state. If the signal and control are out of resonance by the same amount, then the fraction of the excited state $|e\rangle$ contained in the bright states $|\Psi_\pm\rangle$ is modified, but the dark state $|\Psi_0\rangle$ is unchanged. The proportions of states $|g\rangle$ and $|s\rangle$ in the dark state depend on the relative intensities of the control and signal beams. This dependence of $|\Psi_0\rangle$ on Ω_s^2/Ω_c^2 leads to an alternative description of the memory process.

Consider a single atom prepared in the EIT conditions and let us switch to a quantum description of the signal beam. In the begining, the signal is in the vacuum state $|0\rangle$ (so that $\Omega_s = 0$) and the control beam has a non-zero Rabi frequency Ω_c. Consequenlty, the atom is initially in eigenstate $|\Psi_0\rangle = |g\rangle$. Let one signal photon $|1\rangle$ encounter the atom. This translates into an increase of Ω_s to a non-zero value, so that the atomic eigenstate is slightly modified into $|\Psi_0\rangle = \frac{1}{\sqrt{\Omega_s^2 + \Omega_c^2}} \left(\Omega_c|g\rangle - \Omega_s|s\rangle\right) \sim |g\rangle$. As required by the memory protocol, the control power Ω_c^2 is then decreased. If the variation is adiabatic [2], the atom will remain in the same eigenstate $|\Psi_0\rangle$ while $|\Psi_0\rangle$ evolves from almost $|g\rangle$ to exactly $|s\rangle$ when Ω_c reaches zero. The atom has been transferred from $|g\rangle$ to $|s\rangle$! If one has an atomic *ensemble* and multiple signal photons, then for each one of them, one single atom is tranferred from $|g\rangle$ to $|s\rangle$. And for each of these atomic transfers, one photon is emitted into the control beam, as required for energy conservation.

What happens to the signal photons becomes more evident if we notice the following. As the atomic state inside the ensemble is modified by the EIT process (atoms are promoted from $|g\rangle$ to some other state $|\Psi_0\rangle \neq |g\rangle$), what is *really* propagating inside the ensemble at

---

[2]In fact, it has been argued by Liu et al. [81], Matsko et al. [131] that the adiabatic condition is unecessary in the case of EIT light storage: even in the case of a rapid (instantaneous) switch-off of the control beam, the atomic state follows instantly and no additionnal absorption is caused. For this reason, in practice all EIT light storage experiment use the fastest possible switch, on the order of a few nanoseconds.

velocity v_g (equation (2.4)) is a mixed state of (signal) electric field and atomic coherence (or spin wave).

The state of such a light-matter superposition has been shown to be [130]:

$$\Psi(z,t) = \frac{\Omega_c}{\sqrt{\Omega_c^2 + g^2 n_0}} E_s(z,t) - \frac{g\sqrt{n_0}}{\sqrt{\Omega_c^2 + g^2 n_0}} \sqrt{n_0}\hat{\rho}_{sg}(z,t) \qquad (2.9)$$

In which $E_s(z,t)$ stands for the signal electric field envelope, $\hat{\rho}_{sg}(z,t)$ for the local average atomic coherence between states $|s\rangle$ and $|g\rangle$, and the signal Rabi frequency Ω_s has been replaced by the single-photon coupling strength $\Omega_s^2 \to g^2 n_0$. In this expression, the relative proportions of photonic and atomic components are given by the same coefficients that gave the ratio between states $|g\rangle$ and $|s\rangle$ in the dark state $|\Psi_0\rangle$ (equation (2.9)). Without entering into details, Fleischhauer and Lukin [127, 128] have used a fully quantum description to prove that the field Ψ has a bosonic behavior and its excitations are multi-atomic analogous of the dark state $|\Psi_0\rangle$ (equation (2.9)) called **dark state polaritons** that propagate with the group velocity given by equation (2.4). It also appears that a polariton with zero group velocity (at $\Omega_c = 0$) has lost all its photonic part and consists solely of a (stationnary) spin wave.

2.2.3   The role of the ensemble: collective enhancement

The EIT susceptibility of equation (2.2) has been derived for a single atom and spatial features of the signal and control beams such as their directions and shapes have not been considered. But as has been already argued in section 2.2.1, the interaction strength with a single atom is far too weak to perform efficient light slowing and stopping [3]. Besides, if we were to implement a quantum memory with a single atom in free space, then the re-emission of the stored photon would have no reason to happen in the signal's own spatial mode. Fortunately, the use of an extended ensemble of atoms automatically solves this problem, thanks to a phenomenon known as collective enhancement. In short, when a signal pulse is stored as an atomic spin state $|s\rangle$ inside an ensemble, *every* atom participates in the absorption, and each one of them retains a phase that reflects the spatial interference of the control and signal fields. When the control field is turned back on after storage, the emission is forced in the mode which results from maximal constructive interference between the control and the stored excitation in a fashion that reminds of holography. Some authors have therefore named ensemble-based quantum memories "quantum holograms" [112].

The state of the ensemble is better described by so-called collective states, in which a single atomic excitation is delocalized over the entire ensemble:

$$\begin{aligned}
|\underline{g}\rangle &= |g_1, g_2, \cdots g_N\rangle \\
|\underline{s}\rangle &= \frac{1}{\sqrt{N}} \sum_{1 \le i \le N} |g_1, g_2, \cdots g_{i-1}, s_i, g_{i+1}, \cdots g_N\rangle \\
|\underline{e}\rangle &= \frac{1}{\sqrt{N}} \sum_{1 \le i \le N} |g_1, g_2, \cdots g_{i-1}, e_i, g_{i+1}, \cdots g_N\rangle
\end{aligned} \qquad (2.10)$$

---

[3]An alternative way to enhance the light matter coupling and to maximize memory re-emission into the desired mode is to put the atom in a cavity which is resonant with the signal beam. However, this cavity has to be stabilized and this brings in additionnal complexities. Moreover, a single atom in a cavity remains intrinsically a *singlemode* quantum interface. It must be noted that the two techniques (the use of an ensemble and a resonant cavity) can be (and have been) combined such as shown in a recent DLCZ experiment [97].

Where the sum runs over all N atoms inside the ensemble. In addition to the *single-excitation* states $|\underline{s}\rangle$ and $|\underline{e}\rangle$, multiply excited states can be defined:

$$|\underline{ss}\rangle = \frac{1}{\sqrt{N(N-1)}} \sum_{1 \le i < j \le N} |g_1, \cdots s_i \cdots s_j \cdots g_N\rangle \qquad (2.11)$$

Similar definitions go for states with higher excitation numbers, and for the $|e\rangle$ state as well. As long as the number of excitations is small enough compared to the total number of atoms, the states $|\underline{s}\rangle, |\underline{ss}\rangle, ...$ behave as Fock states. They are the dark state polaritons (see previous section) in the purely atomic case ($\Omega_c = 0$). When a signal pulse $\sum_n a_n |n\rangle$ is stored in the ensemble via EIT, it is mapped onto the atoms as $\sum_n a_n |\underline{s_n}\rangle$ (where $|\underline{s_0}\rangle = |\underline{g}\rangle$, $|\underline{s_1}\rangle = |\underline{s}\rangle$, $|\underline{s_2}\rangle = |\underline{ss}\rangle$ and so on).

Collective enhancement arises from a subtlety that was hidden in equation (2.10). During the spin-flip process, the atom i at position $\vec{r}_i$ absorbs a signal photon of wave vector $\vec{k}_s$ and simultaneously emits a control photon of wave vector $\vec{k}_c$, so it comes in the superposition (2.10) with a phase factor $e^{i(\vec{k}_s - \vec{k}_c) \cdot \vec{r}_i}$. In the memory readout, it absorbs a control photon of wave vector $\vec{k}'_c$ and re-emits a signal photon of wave vector $\vec{k}_{\text{out}}$. The ensemble is returned in the collective state $\left(\frac{1}{\sqrt{N}} \sum_{1 \le i \le N} e^{i(\vec{k}_s - \vec{k}_c + \vec{k}'_c - \vec{k}_{\text{out}}) \cdot \vec{r}_i} \right) |\underline{g}\rangle$. The global factor before $|\underline{g}\rangle$ gives the square root of the probability amplitude of this process. It is significant if and only if $\vec{k}_{\text{out}} = \vec{k}_s - \vec{k}_c + \vec{k}'_c$. If one has two independent control beams, this allows to control at will the direction of the retrieved photon. In practice, for reasons that will be explained in section 2.2.5, it is desirable to have the smallest possible angle between the signal and control beams. In our case, we adopt what is known as the forward configuration by chosing a single control beam $\vec{k}'_c = \vec{k}_c$. This causes the photon to be re-emitted in in the same spatial mode and direction as the signal ($\vec{k}_{\text{out}} = \vec{k}_s$). The amplitude of each term in equation (2.10) also varies depending on the intensity distribution of the signal and control beams but this leaves the present discussion unaltered.

In addition to the collective enhancement effect, the ensemble nature of the storage medium provides it with an intrinsic multimode capacity that will be used extensively in chapter 3 where we will demonstrate the storage of various superpositions of spatial modes [6].

2.2.4   A glance beyond the simple model

Let us now address briefly some questions that arise at the boundaries of the model presented heretofore.

- **Is it still EIT when there is no more control field ?** The derivation given in appendix A.1 is done perturbatively in the case of a strong control field and a weak signal. But when the control field is switched off, it necessarily becomes less intense than the signal, casting doubt on the validity of the perturbative approach. The dark state polariton picture of section 2.2.2 provides an answer by showing that signal photons progressively disappear as a light pulse is slowed down, so that the signal can still be considered as perturbatively small relative to the control. The question could also be formulated equivalently as: *how to fit a signal pulse's spectrum inside a shrinking EIT bandwidth ?* Fleischhauer and Lukin [127, 128] argued that the time variation of the dispersion curve also modifies the signal's spectrum. As the signal pulse is dynamically slowed down, its spectrum is gradually compressed. If

the signal spectrum initially fits inside the transparency window, then this property is conserved while the control field power is decreased.

- **The multilevel structure of real atoms.** Real atoms have more complex level structures than ideal Λ ones used in the model of section 2.1. In the cesium atom for example (which we use in our experiments) the levels $|g\rangle$ and $|s\rangle$ are split respectively into 9 and 7 different Zeeman sublevels. The excited state $|e\rangle$ is also split in multiple sublevels. Moreover, adjacent levels not directly involved in the main EIT process may perturb it. This effect is especially important if the atoms are hot, leading to large Doppler broadening, or if the power of the control field Ω_c is too important (much larger than Γ) as shown in [4]. In the last years, our group had studied the effect of multiple levels in coherent processes [124, 132]. A detailed theoretical model has been given by Sheremet et al. [123].

  As such, the multilevel atomic structure is not a problem for EIT or for memories. It merely causes atoms in different sublevels to act as several independant three-level Λ systems. In each of these subsystems, both the signal and control beam may have different Rabi frequencies, depending on the state magnetic moment and on the light polarization. As long as Ω_c satisfies the conditions for efficient memory given in section 2.2.1 in all the subsystems, the EIT memory works just as well. The multilevel structure becomes a trouble if the different Λ subsystems have different energy splittings as will be seen in the next section.

- **Off resonant EIT and Raman quantum memories.** EIT also exists in the case of a non resonant control beam ($\omega_c \neq \omega_{es}$) in which case the perfect transparency ("off-resonant EIT") occurs at the exact two photon resonance ($\omega - \omega_c = \omega_{gs}$), just next to a stimulated Raman absorption line (see [86]). Off-resonant EIT causes slow light in the same way as in the resonant case and can lead to quantum memories with various control detuning ([85, 86]). The linear susceptibility in Raman configuration is shown in figure 2.4. It is given by:

$$\chi(\delta) = \frac{i\gamma_{sg} + \delta}{\delta^2 + i\delta\left(\frac{\Gamma}{2} + \gamma_{sg}\right) + \delta\Delta_c + i\Delta_c\frac{\Gamma}{2} - \gamma_{sg}\frac{\Gamma}{2} - \frac{\Omega_c^2}{4}} \tag{2.12}$$

  The derivation for this can be found for example in the PhD dissertation by Scherman [86], Cviklinski [133].

  All experiments reported in the rest of this manuscript have used resonant EIT only. It was diagnosed that one of the mechanisms limiting the storage efficiency is a residual absorption of the signal caused, e.g. by a mismatch of the control and signal beams, as well as a limited transparency. In experiments performed after this manuscript was under completion, Dr. Valentina Parigi and Dr. Christophe Arnold showed that switching to a slightly off-resonant EIT configuration (or Raman configuration) allowed to mitigate this residual absorption and to significantly increase the storage efficiency.

After having explained the basic functionning of EIT quantum memories, we now turn our attention to mechanisms governing a very important parameter: the memory time τ_m.
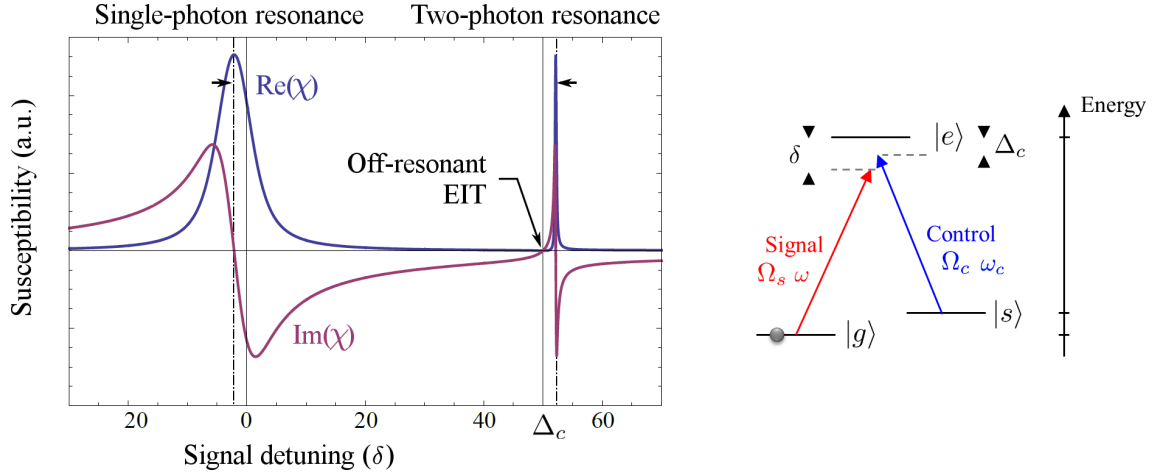
Figure 2.4: **Level scheme (right) and linear susceptibility (left) in off-resonant EIT (or Raman) configuration.** Credits: Scherman [86].

2.2.5 Inhomogeneous broadening and decoherence: the dark side of using an ensemble

Using ensemble of atoms enables for a strong light-matter coupling, gives rise to collective enhancement and directional re-emission of the signal and provides us with a multimode storage medium. But it also opens a back door to the enemy of quantum memories: decoherence. Inhomogeneous broadening in an ensemble of atoms induces specific decoherence mechanisms that are of course absent in the single-atom EIT model.

In short, inhomogeneities will cause different atoms (at different positions or in different velocity classes or in different internal sublevels) to evolve with uncorrelated individual phase factors. Since the re-emission process happens as a collective in-phase emission from all the atoms, an uncontroled dephasing will oppose to this beautiful collective re-emission.

It has been stressed in section 2.2.3 that in the superposition state of equation (2.10), different atoms come with different *static* phases. They reflect the interference pattern of the signal and control beams, and are responsible for the maximization of the signal re-emission *in the desired mode*. But any inhomogeneity in the atomic eigenfrequencies ω_{gs} will result in different atoms in equation (2.10) also coming with different *dynamic* phases: phases that will evolve in time at different rates! Now in this case, when the control pulse is reapplied on the atomic ensemble to retrieve the stored signal, atoms will have dephased and the collective re-emission will be decreased.

In the collective state (2.10), let now atom number i evolve with a phase $\Phi_i(\tau)$ over a time τ. Then at time τ, the collective state has changed to:

$$|\underline{s}(\tau)\rangle = \frac{1}{\sqrt{N}} \sum_{1 \leq i \leq N} e^{i\Phi_i(\tau)} |g_1, \cdots g_{i-1}, s_i, g_{i+1}, \cdots g_N\rangle \tag{2.13}$$

But the probability to retrieve the signal in the correct mode (i.e. the memory efficiency) is still given by the same interference condition with the control beam. The efficiency thus scales with time as:

$$\eta(\tau) = |\langle \underline{s}(0)|\underline{s}(\tau)\rangle|^2$$

$$= \left| \frac{1}{N} \sum_{1 \leq i,j \leq N} e^{i\Phi_i(\tau)} \langle g_1, \cdots, g_{j-1}, s_j, g_{j+1}, \cdots, g_N | g_1, \cdots, g_{i-1}, s_i, g_{i+1}, \cdots, g_N \rangle \right|^2$$

$$= \left| \frac{1}{N} \sum_{1 \leq i \leq N} e^{i\Phi_i(\tau)} \right|^2 \tag{2.14}$$

Taking the continous limit, this expression turns into:

$$\boxed{\eta(\tau) = \left| \int d\Phi_\tau \, n(\Phi_\tau) e^{i\Phi_\tau} \right|^2} \tag{2.15}$$

Where $n(\Phi_\tau)$ is the distribution of the individual phases at time τ.

Inside a cold atom setup, three main sources of inhomogeneous broadening exist, as will be now detailed:

- **Magnetic field inhomogeneities.** The states $|g\rangle$ and $|s\rangle$ are in fact two manifolds of magnetic sublevels labelled $|m_F\rangle$, $m_F = -F \cdots + F$ as depicted in figure 2.6. In the presence of a non-zero magnetic field of projection B along the quantization axis, these sublevels are shifted by $\delta\omega_{gs} = \mu_B \, g_F \, m_F \, B$ (μ_B is the Bohr magneton, g_F the Landé factor of state $|F\rangle = |g\rangle$ or $|s\rangle$ and m_F the index of the magnetic sublevel). If moreover the magnetic field is not constant in space, an atom in state m_F at position z will evolve with a phase:

$$\Phi_{i,m_F}(\tau, z) = \mu_B g_F m_F B(z)\tau/\hbar \tag{2.16}$$

The efficiency given by equation (2.15) becomes an integral over space. Noting $n_0^{m_F}(z)$ is the local density of atoms in the m_F sublevel, we obtain:

$$\eta(\tau) = \left| \sum_{m_F = -F \cdots +F} \int dz \, n_0^{m_F}(z) e^{i\mu_B g_F m_F B(z)\tau/\hbar} \right|^2 \tag{2.17}$$

Taking a gaussian atomic spatial distribution $n_0^{m_F}(z) = \frac{2}{L\sqrt{\pi}} e^{-4z^2/L^2}$ (as expected in a magneto-optical trap with a cloud of length L), a first order approximation (gradient) to $B(z)$ and a single m_F sublevel with $\mu_B g_F m_F B(z) = \alpha_{m_F} \cdot z$ we have:

$$\eta(\tau) = \left| \int_{\mathbb{R}} dz \, e^{-\frac{4z^2}{L^2}} e^{i\alpha_{m_F} z\tau} \right|^2 \propto e^{-L^2 \alpha_{m_F}^2 \tau^2/8} \tag{2.18}$$

i.e. a gaussian decay with a memory time:

$$\boxed{\tau_m = 2\sqrt{2}/L\alpha_{m_F}} \tag{2.19}$$

Assuming the following parameters: $L = 2$ mm, $\mu_B \cdot g_F = 350$ kHz/G and taking m_F to be the maximum difference $\Delta m_F = 16$ between magnetic levels in ^{133}Cs (see
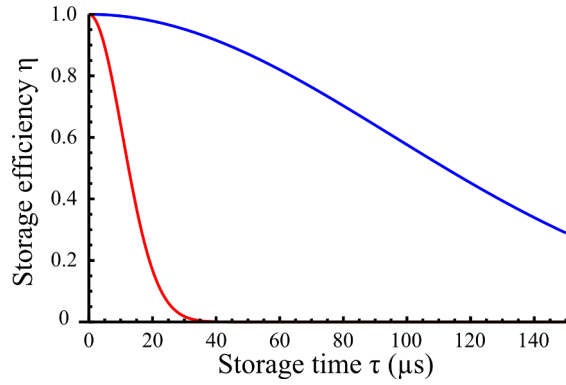
Figure 2.5: **Expected decay of the memory efficiency with time caused by various decoherence mechanisms.** The blue curve refers to magnetic field inhomogeneities as given by equation (2.19). This estimation is done with the following experimental parameters: $L = 2$ mm, $\Delta B \sim \pm 5$ mG, and $m_F \to \Delta m_F = 16$ and for the tabulated value of $\mu_B \cdot g_F = 350$ kHz/G [134]. Their measurement will be described in section 2.3.2. The resulting memory time is $\tau_m \sim 50$ µs. The red curve shows the expected decay resulting from the thermal motion of the atoms in the presence of an angle α between the signal and control beams. It appears to put a much more stringent limitation on the storage time. It has been obtained from equation (2.20) using parameters: $\lambda = 852$ nm, $\alpha = 1.8°$, $T = 800$ µK yielding a decay time $\tau_m \sim 15$ µs.

insert in figure 2.6), we obtain a theoretical memory time on the order of 50 µs as shown in figure 2.5.

A more realistic model should take into account the populations $n_0^{m_F}(z)$ of the various m_F sublevels as well as the *relative* dephasing between levels from the $|g\rangle$ and $|s\rangle$ manifolds, not only one m_F sublevel of $|s\rangle$ as done here. However, the simple formula (2.19) gets all the physics of the process and gives the correct order of magnitude for the memory time τ_m.

This Zeemann dephasing model was introduced by [135] in order to explain the extremely short memory times in the pioneering DLCZ photon-pairs generation experiments that have been performed at Caltech in a magneto-optical trap.

- **Thermal atomic motion.** Atomic motion also causes dephasing, because if an atom moves during the storage, then it will not have the correct phase factor for its new position when the control beam will be re-applied for memory readout. This effect will be all the more important as the phase between the signal and control beams will have changed between the two atomic positions. It therefore depends on the angle α between the two beams.

  More precisely, if the *i-th* atom is transferred from $|g\rangle$ to $|s\rangle$ at position $\vec{r}_i$ and then back from $|s\rangle$ to $|g\rangle$ at position $\vec{r'}_i$, then it aquires a phase factor equal to: $\Phi_i = (\vec{k}_c - \vec{k}_s) \cdot (\vec{r}_i - \vec{r'}_i)$. If the atom displacement results from thermal motion, then it can be more efficiently parametrized using the atom velocity $\vec{v}_i$, so that we can write: $\Phi_i(\tau) = (\vec{k}_c - \vec{k}_s) \cdot \vec{v}_i \tau$. The integral in equation (2.15) becomes an integral over the atomic velocity. In a Maxwell-Boltzmann distribution $\propto e^{-mv^2/2k_BT}$, such as expected in a magneto-optical trap, this leads to:

$$\eta(\tau) = \left| \int_{\mathbb{R}}^{3} \mathrm{d}^3\vec{v}\, \mathrm{e}^{-\frac{mv^2}{2k_BT}} \mathrm{e}^{i(\vec{k}_c - \vec{k}_s)\cdot\vec{v}_i\tau} \right|^2 \propto \mathrm{e}^{-2\delta k^2\tau^2 k_BT/m} \tag{2.20}$$

$m = 2.207 \times 10^{-25}$ kg denotes the mass of a ^{133}Cs atom, k_B the Boltzmann constant, and the wave-vector difference along the signal axis is given by $\delta k = 2\pi\sin(\alpha)/\lambda$. Again, the efficiency decays in time as a gaussian with a time constant:

$$\boxed{\tau_m = \frac{\lambda}{2\pi\sin(\alpha)\sqrt{2k_bT/m}}} \tag{2.21}$$

This can ben qualitatively understood as the time required for an atom moving at the most probable velocity to travel a distance equal to the width of an interference fringe between the signal and control. With $\alpha \sim 1.8°$ as used in our setup and assuming a typical magneto-optical trap temperature equal to the ^{133}Cs Doppler temperature $T_D = 125$ μK we estimate a limit on the memory time τ_m on the order of 35 μs. Given our good cancellation of magnetic field gradients, this is already a stronger constraint than the 50 μs expected from magnetic field inhomogeneities. Moreover, a much higher temperature than T_D has been measured in our setup ($T \sim 0.8$ mK) leading to a still smaller $\tau_m \sim 15$ μs (2.3.2). The expected decay curve is shown in figure 2.5.

- **Differential light shift in dipole traps.** In the rest of this chapter and in the next one, our quantum memory medium will be a cloud of atoms freely falling from a magneto-optical trap (MOT), so we won't be concerned with light shifts. However, in setups involving atoms in dipole traps – such as will be considered briefly in chapter 4 – inhomogeneous light shifts caused by the trapping light are an additionnal cause of decoherence.

  Indeed, in the presence of an off-resonance laser field $\vec{E}_0(\vec{x})\mathrm{e}^{\mathrm{i}\omega t}$, an energy level is subjected to a light shift that proportionnal to the spatially varying intensity $\vec{E}_0^2(\vec{x})$ (and also depends on the squared amplitudes of all (allowed) transitions and on the laser frequency ω) [136]. Except in some very special cases, different levels are shifted differently. In particular, the energy difference between $|g\rangle$ and $|e\rangle$ will vary proportionnally to $\vec{E}_0^2(\vec{x})$, causing an inhomogeneous broadening of the EIT optical transitions as soon as $\vec{E}_0(\vec{x})$ is not constant over the whole atomic sample.

  In certain atoms the light shifts on different levels compensate each other exactly at so-called magic wavelengths. Such is the case of the ^{133}Cs atom, and this property will be an important asset in the experiment of chapter 4.

> The two previous sections have given an overview of the theoretical tools required to describe and understand the slow light effect and its application to optical quantum memories. The parameters playing a key role in EIT quantum memories have been identified:
>
> - **Light slowing and the trade-off governing the control Rabi frequency Ω_c.** The control power must be small enough for efficient light slowing and large enough for the transparency window to encompass the signal whole spectrum. **Increasing the optical depth (OD) d_0** of the atomic ensemble allows to satisfy both criteria.
>
> - **Inhomogeneous broadening** in extended atomic media must be tightly controlled since it leads to decoherence and hence to a reduction of the expected memory time. Especially worrisome mechanisms are the **dephasing of Zeeman sublevels in inhomogeneous magnetic fields** and the **thermal motion of atoms** combined with a non-collinear signal and control configuration.
>
> In the next section, we will describe how this theoretical model can be realized in practice in an ensemble of magneto-optically trapped cold cesium atoms.

2.3   Implementation in a cold atomic ensemble

In the previous sections, we have given the basic theory underlying the functioning of EIT and EIT-based quantum memories in atomic ensembles, and we have described the physical mechanisms accounting for the quality of the memory. In this section, we will now describe our experimental implementation of such a cold-atom-based EIT quantum memory.

2.3.1   Preparation of the memory medium in a magneto-optical trap

As previously mentionned, our memory medium is provided by a cloud of cold cesium atoms. Alkali atoms have the advantage of being easy to manipulate by laser cooling and trapping techniques, they have very small homogeneous dephasing rates γ_{gs} and a strong interaction with light on optical transitions that are suitable for EIT. In addition, ^{133}Cs has two magic wavelengths, allowing it to be used in dipole traps that are exempt of light shift induced broadening, something we'll take advantage of in chapter 4.

The atoms are cooled and trapped in a magneto-optical trap (MOT). Most of the technical details of the setup used in this work have been already described extensively by Giner [125], so only the most essential parts are given in the following. The ^{133}Cs level scheme is shown in figure 2.6 with the various beams used for atomic cooling and trapping (MOT generation), for atomic probing and for memory implementation.

Atoms are provided by dispensers [4] placed about 15 cm below the MOT itself. A pressure below 10^{-9} Torr $\sim 10^{-12}$ bar is maintained by a 40 L/s ion pump [5]. The MOT is generated by three pairs of one-inch-wide retro-reflected beams. As indicated on figure 2.6, the trapping laser (T) is close to (10 MHz below) the $|6S_{1/2}, F = 4\rangle \rightarrow |6P_{3/2}, F' = 5\rangle$

---

[4]By SAES Getters
[5]Model Starcell VacIon Plus 40 by Agilent
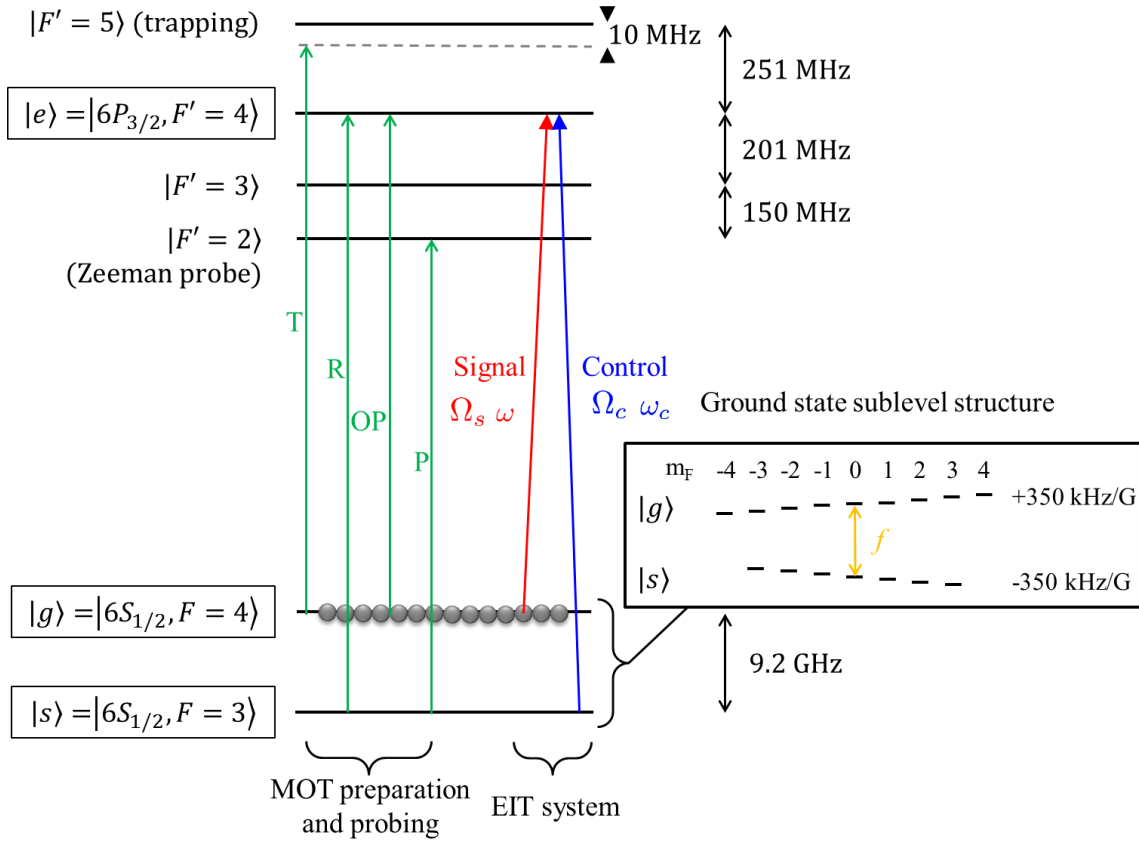
Figure 2.6: ^{133}Cs **levels and laser beams used for MOT preparation and probing (green arrows) and EIT subsystem (red and blue arrows).** Vertical energy splittings are not to scale. Atoms are prepared in the $|g\rangle = |6S_{1/2}, F = 4\rangle$ hyperfine ground state. All optical transitions are part of the D2 line $|6S_{1/2}\rangle \to |6P_{3/2}\rangle$ of wavelength $\lambda \sim 852$ nm. Levels $|g\rangle$, $|e\rangle = |6P_{3/2}, F' = 4\rangle$ and $|s\rangle = |6S_{1/2}, F = 3\rangle$ involved in EIT have been highlighted. Light beams on the left (green arrows) are involved in the MOT preparation: T: Trapping, R: Repumper, OP: Optical pumping (not used in the experiment of chapter 3), P: Zeeman probe (see 2.3.2). Light beams on the left (same color code as in figure 2.1) are used to implement EIT. All lasers are provided by external cavity diode lasers except the signal that comes from a CW Ti:Sapph laser. Signal and control are locked in phase and frequency at the ^{133}Cs hyperfine splitting. Appart from the control-signal locking, all lasers are locked on an atomic reference via saturated absorption spectroscopy. The insert shows the Zeeman sublevel structure of the two ground states $|g\rangle$ and $|s\rangle$ and their first order magnetic splitting coefficients $\mu_B \cdot g_F$. The orange arrow symbolizes the microwave field of variable frequency f used to probe the Zeeman structure and the magnetic field percieved by the atoms (section 2.3.2).

transition ands the repumper laser (R) is resonant to the $|6S_{1/2}, F = 3\rangle \to |6P_{3/2}, F' = 4\rangle$ transition. They are generated by extended cavity diodes lasers that were built by former PhD student members of the group after an original design by the SYRTE at the Observatoire de Paris [137]. Commercial versions of these lasers are now available. The fabrication of the diode lasers that we used is described in details in the PhD dissertations by Scherman [86] and Giner [125]. They were frequency-locked on atomic lines by saturated

absorption spectroscopy, yielding a (locked) laser linewidth of 400 kHz [86]. The lasers are brought to the MOT vacuum chamber by optical fibers. They are timed using single-pass acousto-optic modulators. The power used in the three trapping beams and in the two repumping beams is on the order of 3×25 mW and 2×2 mW respectively. A pair of coils close to the anti-Helmholtz configuration generate a magnetic field gradient on the order of 20 G/cm along their common axis. The shape and position of the resulting MOT (see the right panel in figure 2.7) can be slightly adjusted by changing the direction of the T and R beams. It has a typical length $L = 2$ mm and a diameter on the order of 1 mm.

Since the MOT preparation involves powerful magnetic field gradients and since magnetic inhomogeneities are a source of decoherence (see section 2.2.5), the trap is turned off during the actual experiment so that the atoms are freely falling. The MOT is regenerated every 15 ms during a 11.5 ms phase in which trapping and repumping beams are on as well as the magnetic gradient. It is followed by a 3.5 ms phase used for the experiments in which the magnetic gradient and the T and R beams are progressively turned off. The timing sequence is shown in figure 2.7. In order to get rid of the magnetic gradient as fast as possible a custom switching circuit has been specially fabricated by the lab's electronic facility [125] [6]. Non-magnetic material has been used whenever possible, so as to limit the influence of eddy currents. In particular, the MOT chamber itself is made out of glass. Trapping and Repumping beams are also switched off, albeit a little bit later than the magnetic field. Repumper is switched off last so as to ensure that all atoms are prepared in level $|g\rangle$ as required for EIT. All EIT and memory measurements were performed between 2 and 3 millisecond after the magnetic field was switched off. This caused us to work at a lower optical density than what shorter times could permit, but it was a necessary compromise to ensure that we worked at zero magnetic field.

The **optical depth** in the signal path d_0 has been measured at various times using a weak probe beam (optical power on the order of a few hundreds of nanowatts so as to remain well below the saturation intensity) in the same spatial mode as the signal. The probe beam had the same frequency as the Trapping beam: about $2 \times \Gamma$ or 10 MHz below the $|6S_{1/2}, F = 4\rangle \rightarrow |6P_{3/2}, F' = 5\rangle$ transition. In order to get the value of d_0 (at resonance on the signal transition $|g\rangle = |6S_{1/2}, F = 4\rangle \rightarrow |e\rangle = |6P_{3/2}, F' = 4\rangle$), the logarithm of the ratio of the output to input powers is corrected to compensate for the different transition strengths and for the probe detuning.

$$d_0 = \frac{S_{44'}}{S_{45'}} \left(1 + \frac{4\delta^2}{\Gamma^2} \right) \text{Log} \left(\frac{I(L)}{I(0)} \right) \tag{2.22}$$

where the S_{ij} are the relative transition strength factors between levels $|i\rangle$ and $|j\rangle$, δ is the probe detuning and $I(0)$ and $I(L)$ are the probe intensities before and after traversing the cloud's length. This gives a typical value $d_0 \sim 15$ when the memory experiment starts which decreases with time due to the cloud expanding and falling as displayed in figure 2.7.

Inside this atomic cloud, we use the following ^{133}Cs levels to implement EIT:

$$\boxed{\begin{aligned} |g\rangle &= |6S_{1/2}, F = 4\rangle & \text{(ground state)} \\ |s\rangle &= |6S_{1/2}, F = 3\rangle & \text{(storage state)} \\ |e\rangle &= |6P_{3/2}, F' = 4\rangle & \text{(excited state)} \end{aligned}} \tag{2.23}$$

---

[6]Faster switching circuits have been reported in Gradient Echo Memory experiments [83]
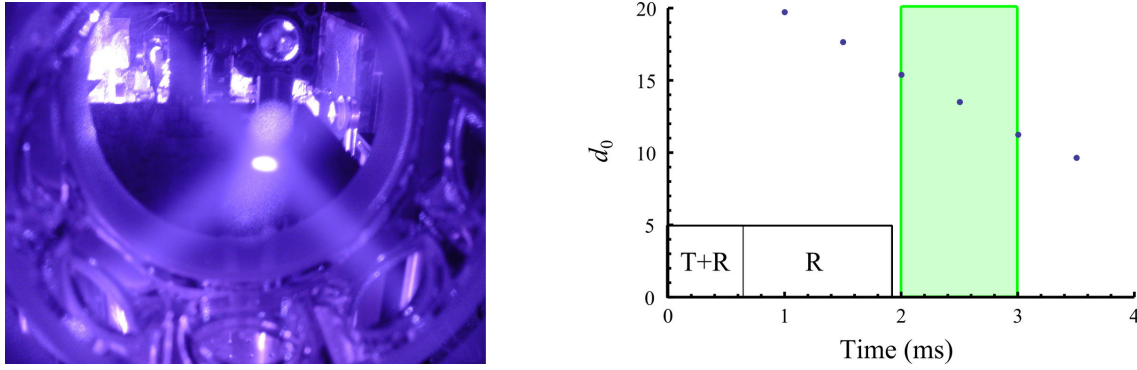
Figure 2.7: **Right: One of the first image of our MOT. Left: Decrease of the optical depth d_0 after the switch-off of the magnetic gradient.** The picture on the right was taken with a standard CCD camera after removing the infrared filter. The three pairs of trapping beams are clearly visible as well as the atom cloud in the center. (Credits: Giner [125], Veissier [126]). On the left panel, the blue dots show the measured optical depth d_0 at various times after the switch-off of the magnetic field. The 1 ms-long period used for EIT and quantum memory experiments is highlighted in green. It results from a compromise between a good extinction of residual magnetic fields (eddy currents) and a sufficient OD. The time origin is the instant when we send the command to switch off the magnetic gradient. The trapping (T) and repumping (R) lasers stay on a little longer to ensure all atoms are prepared in level $|g\rangle$ as shown by the black boxes.

But before moving to EIT and stopped light measurements, let us turn our attention to the decoherence sources mentionned in section 2.2.5.

2.3.2　Measure and control of decoherence sources

In a cold atom setup such as the one we just described, we need to investigate inhomogeneous broadening mechanisms resulting from two origins: magnetic field inhomogeneities and thermal atomic motion.

2.3.a　Magnetic field fluctuations

We have mentionned in 2.2.5 that magnetic inhomogeneities constitute a major source of decoherence in EIT-based quantum memories. For this reason, the use of magnetic material has been avoided whenever possible (the MOT is prepared in a vacuum chamber made out of glass and the stands for the coils are made out of plastic) and the whole experiment is surrounded by three pairs of coils used to compensate stray magnetic fields.

In order to get the most sensitive measurement, the magnetic field is measured directly by the observation of the splitting of the magnetic levels of the atoms inside the cloud after the trapping gradient has been turned off. The magnetic field measurement results from a two-step process iterated over a given frequency range:

- In a fist step, a microwave pulse of very precise frequency $f \sim 9.2\,\mathrm{GHz}$ (near the hyperfine ground state splitting) is sent on the atoms. It is generated by a high precision RF generator [7] and shined on the atoms using a linear antenna. It drives a

---

[7]SMB100A by Rhode & Schwarz.

magnetic transition (Rabi oscillation) between levels $|F = 4, m_F\rangle$ and $|F = 3, m'_F\rangle$ if and only if the microwave frequency matches the transition frequency between these levels.

- In a second step, the optical depth is probed in level $|s\rangle = |6S_{1/2}, F = 3\rangle$ with a laser beam resonant with the $|6S_{1/2}, F = 3\rangle \rightarrow |6P_{3/2}, F' = 2\rangle$ transition (beam "P" in figure 2.6), giving a measure of how many atoms have been transferred during the first step.

This process is repeated over mutliple MOT realizations while the microwave frequency f is scanned. Each time f meets a particular transition frequency, a peak appears in the probe absorption. A typical spectrum is displayed in figure 2.8.

Magnetic transitions must of course comply with the selection rules imposing that only transitions with $\Delta m_F = 0$, ± 1 are allowed. This leads to a total of 21 possible transitions: 7 π and 14 σ transitions. Out of them, six pairs of σ transitions are degenerate as the Zeeman splitting constant is equal in magnitude and opposite in sign for manifolds $|F = 4\rangle$ and $|F = 3\rangle$. This leaves a total of fifteen distinguishable transitions. Consequently, we obtain spectra exhibiting 15 equally spaced peaks such as shown in figure 2.8. The distance between the peaks gives the constant part of the magnetic field and the width of the extremal peaks provides a measure of the field's inhomogeneity across the atomic ensemble.
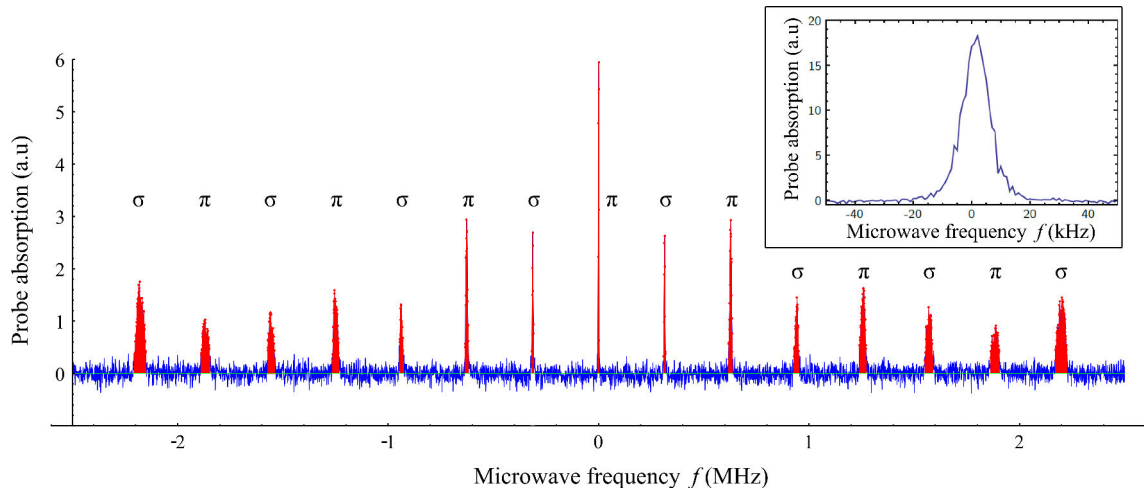
Figure 2.8: **Zeeman spectroscopy used to determine the magnetic field.** The vertical axis gives the probe absorption and the horizontal axis is the microwave detuning f. In this measurement, there was a constant bias field causing a neat separation of the different peaks. A strong gradient can also be seen as the peaks get larger and larger as their m_F quantum number increases in absolute value (from the middle to the sides). The Zeeman peaks are colored in red and the nature of the transition (π or σ) is indicated for each peak. The measured background is shown in blue its mean value in green. Insert: absorption profile after magnetic field compensation. All peaks are now gathered within ± 10 kHz, which corresponds to a total magnetic gradient of about 4 mG across the whole ensemble. Typical magnetic field fluctuations caused the peaks to move within ± 25 kHz.

Without compensation, a typical splitting of about 200 kHz between adjacent peaks is observed, corresponding to a constant magnetic field of about ~ 0.6 Gauss resulting from

Earth's field plus some additionnal parasitic sources in the lab. When the compensation coils are on and their bias current is optimized [8], all the peaks can be brought inside a ± 10 kHz (best case) to ± 25 kHz (worst case) wide window, which corresponds to a maximum magnetic gradient of 4 to 10 milligauss across the whole ensemble. If no other mechanism entered into the game, we should be able to compensate (linearly varying) magnetic inhomogeneities well enough to merge all the Zeeman peaks into a single peak of the same width as the central ($m_F = 0 \to m_F = 0$) peak which is on the order of one kilohertz (see figure 2.9). In practice, we typically achieved a ± 20 kHz residual spread, and we observed fluctuations around this value from one run to another. The origin of these remaining fluctuations remains unclear at the present time and they set the limit to the precision of the magnetic field cancelling that we can achieve. The insert in figure 2.8 shows a typical Zeeman profile after compensating the magnetic field. From equation (2.19) we expect a decoherence time of $\tau_m \sim 50$ µs.

Even if the previous analysis is enough to measure and reasonably control the magnetic field inhomogeneities, we should be able to extract more information from the Zeeman spectroscopy signals. Indeed, via the measurement of the number of transferred atoms in each peak, one could determine the population in each magnetic sublevel by solving a linear system as we'll now explain.

To do so properly, we have take a closer look at how all the various transitions (some of which happen in the same time) affect the probe absorption. π transitions are easier to model because they are not degenerate. If the microwave pulse is sent on the atoms over a time t, the populations P_4 and P_3 of levels $|F = 4, m_F\rangle$ and $|F = 3, m_F\rangle$ undergo Rabi oscillations according to:

$$P_4(t) = P_4(t = 0) \left(\cos^2\left(\tilde{\Omega}t\right) + \left(\frac{\delta f}{\tilde{\Omega}}\right)^2 \sin^2\left(\tilde{\Omega}t\right) \right)$$
$$P_3(t) = P_4(t = 0) \left(\frac{\Omega}{\tilde{\Omega}}\right)^2 \sin^2\left(\tilde{\Omega}t\right)$$

$$(2.24)$$

where $\tilde{\Omega} = \sqrt{\Omega^2 + (\delta f)^2/4}$ and Ω are the off- and on-resonance Rabi frequencies of the considered transition and δf is the detuning of the microwave frequency to this particular transition. $\tilde{\Omega}$ and Ω depend on the Clebsch-Gordan coefficient of the transition and on the microwave polarization and power. The absorption of the probe beam is then proportionnal to $P_3(t)$ and to the square of the Clebsch-Gordan coefficient of the specific $|F = 3, m_F\rangle \to |F' = 2, m'_F\rangle$ probing transitions (taking the probe polarization into account).

From equation (2.24), we see that the combination of microwave pulse power and duration must be optimized so that all Zeeman transitions give rise to easily understandable peaks. Figure 2.9 (a) shows the theoretical evolution of a single peak described by $P_3(t)$ as the microwave pulse duration t increases. Zooms on the central peak recorded for various microsave pulse durations t (2.9 (b) and (c)) show an excellent agreement with the predicted shape. A good combination of microwave pulse duration and power should allow for all the peaks to resemble curve (b). In our case, this led to a power of 27 dB_c and a pulse duration $t = 500$ µs. Changing the orientation of the antenna modifies the microwave polarization seen by the atomic ensemble and hence modifies the ratio between the π and σ transitions. It was chosen so that both of them were visible.

---

[8]We can control independantly the current in all six coils, so in principle we can compensate both the constant and the linearly varying parts of the magnetic field.
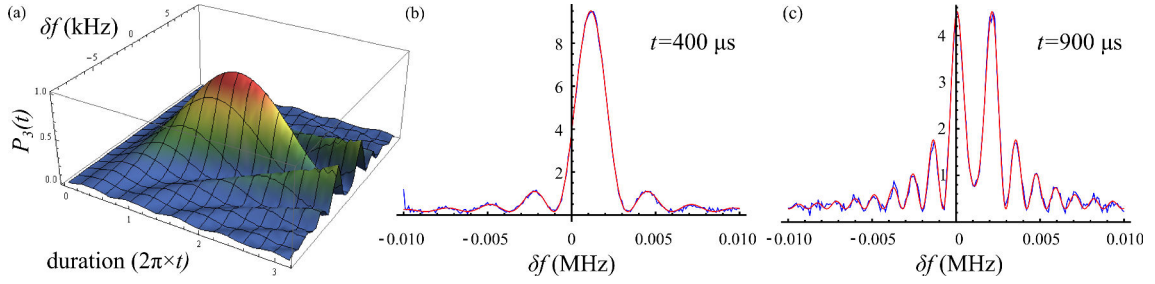
Figure 2.9: **Zeeman spectroscopy: zoom on a single peak.** (a) Theoretical evolution of a single peak calculated from equation (2.24). Experimental zooms on the central Zeeman peak for microwave pulse durations $t = 400\,\mu s$ (b) and $t = 900\,\mu s$ (c). The data (blue) shows an excellent agreement with the model (red). The slight offset of the center of the curves relative to zero detuning reflects the calibration defect of the microwave generator.

The populations in each of the m_F sublevels with $m_F = -3 \cdots +3$ could be extracted by computing the area under each π transition peak and normalizing it by both the (square of the) Clebsch-Gordan coefficient of the corresponding probe ($|F = 3\rangle \rightarrow |F' = 2\rangle$) transition and the transfer coefficient extracted from equation (2.24). The populations in the remaining $m_F = \pm 4$ sublevels could be extracted from the extremal (non-degenerate) σ transitions with an analogous normalization.

Unfortunately, the (small) flucutations of the magnetic field over time and the time it takes to record a full spectrum such as in figure 2.8 make this beautiful analysis break down. The scanning is so slow (up to half a minute if one wants a good enough resolution) that the peaks have time enough to move into and out of the resonance condition, so that it is not possible to extract a quantitative information from the scans. However, it *does* give a *qualitative* indication of the population of the various $|m_F\rangle$ sublevels, as well as a *quantitative measurement* of the magnetic field which was its primary goal.

As another way to get rid of the decoherence caused by the magnetic inhomogeneities, we tried to optically pump all atoms to the single $m_F = 0$ sublevel, which is insensitive to magnetic field.

To this end, an additionnal pair of coils was used to induce a moderate constant bias magnetic field of about one Gauss, thus defining the quantization axis along the signal path. A collimated, linearly polarized pump beam (beam "OP" in figure 2.6), resonant with the $|g\rangle = |6S_{1/2}, F = 4\rangle$ to $|6P_{3/2}, F = 4\rangle$ was sent from the both sides of the chamber to induce π transitions (it was sent simultaneously from both sides to avoid pushing the atoms away to one side). The pump was started after the atoms were released from the trap and before the time at which the memory measurements would take place. A copropagating and identically polarized repumper beam was mixed with the pump beam in order to prevent the atoms from escaping into level $|s\rangle$. The Clebsch-Gordan coefficient for the $|F = 4, m_F = 0\rangle$ to $|F' = 4, m_F = 0\rangle$ transition being zero, all atoms should accumulate in the "dark" sublevel $|m_F = 0\rangle$.

The effect of this procedure on the Zeeman spectra was clearly visible as can be seen on figure 2.10. However, before all atoms could reach the target level, losses started to dominate and the cloud OD dropped dramatically. We tried variously detuned OP beams, various OP and R powers and various pumping durations but could not reach a satisfying
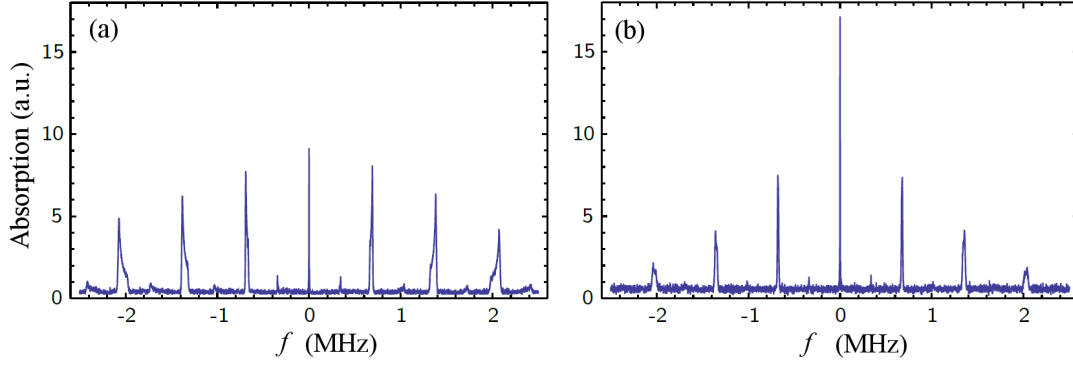
Figure 2.10: **Optical pumping trials.** Zeeman spectroscopic scan (a) without and (b) with optical pumping beams. Some of the population has been transferred from adjacent sublevels to the sublevel $|m_F = 0\rangle$ (whose peak has risen up), but the overall optical density is also lower. When either the pumping power or time get higher, the central peak does not gain any more but the OD continues to decrease. Credits: Veissier [126].

level of atomic transfer to the sublevel $m_F = 0$ while not losing completely the optical density. Several factors may be responsible for the limited efficiency of our optical pumping trials. The main ones are the size of the $|g\rangle = |6S_{1/2}, F = 4\rangle$ manifold (because of which so many optical pumping cycles are necessary before the atoms are caught in the dark state) and the high OD of the cloud (because of which the pump beams do not easily access the center of the cloud unless their power be raised too high which in turn causes heating and losses) as well as the cloud temperature (see next). For these reasons, and because the magnetic field was not the main source of decoherence, optical pumping was not used in the subsequent experiments nor was it used in the qubit storage experiment of chapter 3.

Beyond working to establish a more effective optical pumping, another possibility to get rid of some of the magnetic field fluctuations would be to sychronize the experiment on the room power source. This track is being investigated for the nanofiber-based setup that will be described in chapter 4.

As mentionned in 2.2.5, the remaining magnetic field inhomogeneities measured in our setup lead to an expected memory time on the order of a few tens of microseconds.

$$\boxed{\tau_m \sim 50\ \mu s \qquad \text{(magnetic inhomogeneities)}}$$

The other important parameter governing the memory decay time is the temperature of the atomic ensemble which we will now consider.

2.3.b   MOT temperature

The temperature of our cloud was extracted from absorption profile measurements as shown in figure 2.11 after the magnetic field was cancelled down to less than $\sim \pm 5$ mG, inducing an overall inhomogeneous broadening of less than $\sim \pm 25$ kHz in the worst case which is completely neglegible regarding the natural lineshape Γ.

In the absence of Doppler broadening, the natural linewidth of the D2 line is $\Gamma \sim$ 5.234 MHz [134]. In the presence of Doppler broadening, the absorption profile is described

by a Voigt function, which is the convolution of a gaussian function of width given by the Doppler broadening with a Lorentzian of width Γ.
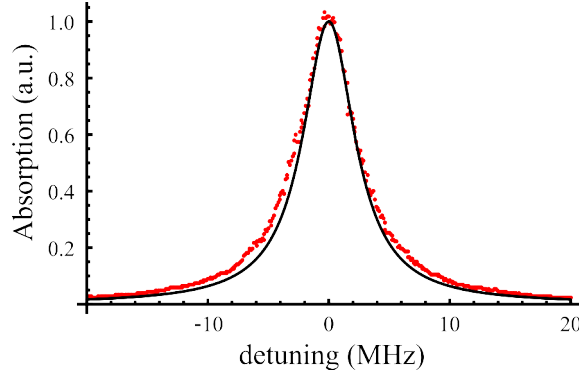

Figure 2.11: **Absorption profile of the signal in the MOT.** The red dots are the actual measurements and the black line is the theoretical Lorentzian shape. For technical reasons, the atoms were first transferred from $|g\rangle$ to $|s\rangle$ for this particular measurement, but this doesn't affect the linewidth (each atom is expected to absorb only two photons on average in this transfer process, so the possible induced heating is much smaller than the temperature scales that are expected). The small but measurable discrepancy between the ideal and observed linewidths is a signature of the temperature of the cloud. A fitting of these data to a Voigt profile provided an estimate of $T \sim 0.8$ mK. Credits: Giner [125].

We measured a temperature around 0.8 mK. With an angular separation of $1.8 \pm 0.2°$, this sets a theoretical limit of $\tau_m \sim 15$ μs on the memory time (see equation (2.20)). So in the present state of the setup, the MOT temperature constitutes the main limitation on the memory time.

$$\boxed{\tau_m \sim 15 \text{ μs} \qquad \text{(thermal dephasing)}}$$

After the completion of the work reported in this manuscript, additionnal work was led by Dr. Valentina Parigi and Dr. Christophe Arnold regarding the cooling of the atomic cloud. The inclusion of a phase of Sisyphus cooling after the magnetic gradient switch-off allows to reach lower temperatures and holds much promise regarding the memory time.

After this characterization of the memory medium, we now expose how the signal and control beams are generated for the EIT and quantum memory experiments.

2.3.3 Signal generation

The signal beam is generated by a continuous wave titanium-sapphire laser operating at $\lambda = 852.12$ nm. It is locked on the atomic transition $|g\rangle = |6S_{1/2}, F = 4\rangle \rightarrow |e\rangle = |6P_{3/2}, F' = 4\rangle$ line via saturated absorption spectroscopy and has a linewidth on the order of 10 kHz. It is focused inside the MOT to a $w_{0s} \sim 50$ μm waist where it overlaps with the (wider) control beam as depicted in figure 2.12. Signal and control propagate with a relative angle of $\alpha \sim 1.8 \pm 0.2°$. To achieve this tight angle, the signal is reflected on the edge of a mirror which has been cut in order to let the control pass without being diffracted). The control frequency is locked in phase with the signal by mixing parts of the two beams and measuring their beat note. In the atomic cloud, the beams have linear

orthogonal polarizations correponding to the simultaneous (and equiprobable) driving of σ^+ and σ^- transitions. This polarization configuration allows to form all possible EIT subsystems within the atomic structure of ^{133}Cs (2.6 and A.3), so that no part of the signal should find a way to be absorbed without interacting with the control.

In order to probe the functionning of the memory in the quantum regime, we prepare brief signal pulses with cascaded acousto-optic modulators. The mean photon number in the pulses is adjusted with neutral density filters. If it is low enough and the pulses are detected by a photon counting device such as an avalanche photodiode, then the signal is a good approximation to the Fock state $|1\rangle$ after postselection over positive detection events.

The signal pulses are also modulated in time to have a smooth shape. Sharp edges in a photon temporal mode broaden its spectrum and increase the risk that it won't fit into the EIT window as discussed in section 2.2.1. Ideally, because of time-reversal symmetry, the best timeshape a photon could have in order to maximize its absorption by a single quantum emitter would be the exact time-reverse shape of the spontaneously emitted photons, which would be a rising exponential followed by a sharp falling edge. In practice, our pulses have a gaussian rising edge followed by a sharp falling one. Their half-maximum length (duration) is $\tau_s \sim 350$ ns.

Since the signal will be detected at the single-photon level with an avalanche photodiode, we need to isolate it from any possible external noise (parasitic light) sources, as we will now describe.

2.3.4 Filtering the single-photon signal pulses

The separation of the signal from parasitic light sources is a very strong requirement for single-photon level memory operation. The MOT trapping and repumping lights are off during the memory measurement and the experimental setup has been enclosed behind a black curtain. The main parasitic light source is the control beam, which has to overlap with the signal inside the atomic cloud as shown in figure 2.12.

The typical control power used in the quantum memory experiments was between $10\,\mu$W and $20\,\mu$W. At $\lambda = 852$ nm, this represents some 4.3 to 8.6×10^{13} photons per second. As a comparison, the intrinsic dark noise of our single-photon detectors (avalanche photodiodes SPCM-AQR-14-FC by Perkin Elmer) is around 100 Hz. To get a smaller contribution from the control than from the detector intrinsic noise, an attenuation of the control by ~ 120 dB is required.

Theoretically, the angular separation between the signal and control beams should be more than enough (by far!) to guarantee a sufficient level of filtering. The angle between the two beams is $\alpha \sim 1.8 \pm 0.2°$ – which is much larger than the sum of the beams divergences. They overlap at their waists (inside the MOT) where they have respective radii of $w_{s0} \sim 50\,\mu$m (signal) and $w_{c0} \sim 200\,\mu$m (control). The signal is mode-matched to and coupled into a singlemode fiber after leaving the vacuum chamber. The fiber is then directed to a single-photon detector. The total distance between the center of the atomic cloud and the fiber coupler is on the order of 75 cm.

At a distance $d = 25$ cm after the cloud center, the beams encounter a lens ($f' = 250$ mm) that recollimates the signal and prepares it for being injected into the fiber. At this point, the spatial separation between the beams centers is already 7.8 ± 0.9 mm, while their radii are respectively 1.35 mm (signal) and 0.4 mm (control). We can get an upper bound to the control-signal overlap at a distance d from the cloud center by integrating a
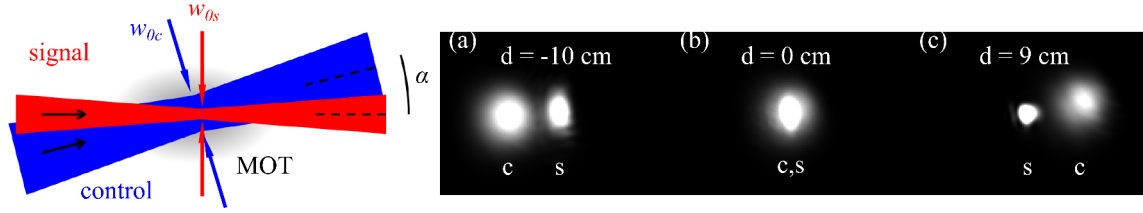
Figure 2.12: **Signal and control beam paths.** The outline on the left shows the way the signal and control beams overlap inside the MOT. The angle α between them has been purposfully exagerated. The pictures on the right show the beams (s: signal, c: control) (a) 10 cm before the position of the MOT, (b) inside the MOT, and (c) 9 cm after the MOT.

gaussian function of width equal to the control width on an interval of length equal to the signal diameter (roughly four times $w_s(d)$). This, in turn, should give an upper bound to the leakage of the control inside the signal mode. At $d = 25$ cm, the attenuation is already $\sim 1500 \pm 500$ dB. Since this estimation does not take into account the precise shape of the signal, it is a very conservative bound, and we should expect a significantly higher attenuation. Nor does it take into account the losses on the various optical elements or the non-unit efficiency of the single-photon detectors. It is considerably higher than the required level of filtering. Figure 2.13 shows the theoretical evolution of the signal and control beam profiles from the center of the MOT to the first lens.
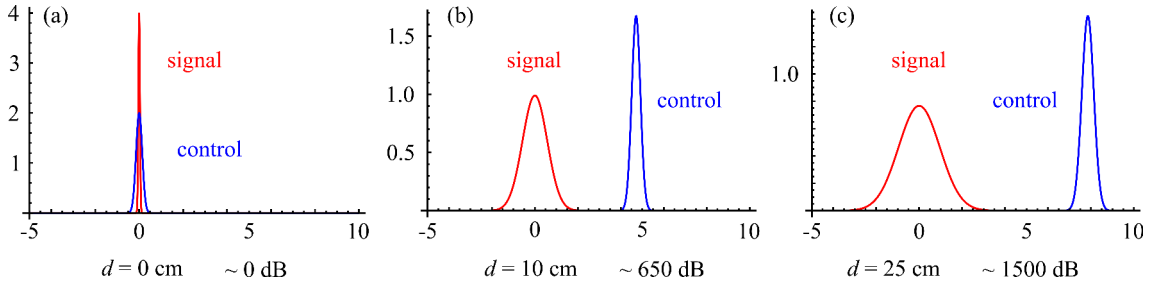
Figure 2.13: **Theoretical overlap between the control (blue) and signal (red) beams.** (a) At the cloud center, (b) 10 cm after the cloud center, and (c) 25 cm after the cloud center (i.e. at the position of the recollimating lens). The overlap of the beams is maximum in (a). It decreases fast with the propagation distance and is already below -650 dB at position (b) and -1500 dB at position (c).

In reality, the control leakage proved to be much more important than estimated by this method, with an overall attenuation of 100 dB. In addition to the angular filtering, we took advantage of the fact that the signal and control had linear orthogonal polarizations to further filter the control with a Glan-Taylor prism. Far from gaining 40 dB in control attenuation as we would expect for well polarized beams, we gained only a factor 10. So, we attribute the remaining control leakage to unpolarized reflections on the vacuum chamber surfaces and possibly other optical surfaces. The noise remaining after filtering is reported in table 2.1.

In conclusion, the noise level in our setup is mainly determined by the leakage of the control into the signal beam. An overall noise rate on the order of 1 kHz was achieved essentially through the angular separation of the beams. As we will see in the next chapter,

Source	Rate
APD dark counts	~ 80 Hz
MOT scattering	~ 200 Hz
Control leakage (at 15 µW)	~ 800 Hz

Table 2.1: **Experimentally measured sources noise.** The noise is given as the corresponding average rate of single-photon detection events on the APD. Each noise source has been measured independently from the others (except for the APD dark count rate).

this enabled us to characterize the quantumness of our memory when we probed it with weak coherent pulses containing down to 0.4 photon on average. In the next section, we will describe the EIT and preliminary quantum memory measurements, and compare them to the expectations from the last sections. This will open the way to the multimode storage experiments reported in chapter 3.

2.4 EIT and stopped light measurements

The control beam, which is responsible for EIT, has been introduced in the last two sections and in figure 2.12. As the result of an experimentally determined compromise between light slowing and transparency, its power was set to ~ 15 µW, which corresponds to a Rabi frequency $\Omega_c \sim 1.3\,\Gamma$ (given its gaussian TEM_{00} shape with a waist radius of $w_{0c} = 200$ µm).

The control-induced transparency was measured with moderate power (i.e. non single-photon) signal pulses[9]. The frequency difference in the locking of the control and signal was adjusted to maximize transparency, as was the overlap between the beams shown in figure 2.12. Typical transparency measured in these conditions was $\sim 45\%$ (at zero signal detuning, i.e. $\delta = 0$). This has to be compared with the absorption the signal would normally undergo in the absence of the control beam. At 2 ms (after the magnetic field switch-off), where the memory experiment period starts and where the transparency measurements were made, the optical depth is $d_0 \sim 15$, which means the transmission should be: $\mathrm{e}^{-15} \sim 3 \times 10^{-5}$ % !

In order to measure the light slowing effect and to confirm the transparency measurements, we went to the single-photon regime with 350 ns short and few-photon signal pulses such as described in 2.3.3. From equations (2.5) and (2.6), we expect the group velocity in our atomic ensemble to be:

$$v_g = \frac{c}{1 + \frac{d_0 \Gamma c}{2L\Omega_c^2}} \sim 3.3 \times 10^{-5} c \tag{2.25}$$

This amounts to compressing a pulse of length $l_s = 90$ m in vacuum to no more than 3 mm. However impressive it be, it is still longer than the atom cloud itelf ($L \sim 2$ mm), so we expect that the signal slowing won't be sufficient to trap all of it inside the memory. Shorter pulses wouldn't help however because we would then be limited by the fact that their sepectrum wouldn't fit in the EIT window anymore as explained in section 2.2.1. Only an increase of the optical density d_0 could allow to circumvent this issue.

---

[9]The signal power was in the nanowatt range (so as to respect the weak signal beam approximation of section 2.1) and the pulses had a duration of ten to twenty microseconds.

And indeed, this is what we observe when we switch off and on the control beam (performing the memory protocol described in 2.2.1). A fraction 8% of the total pulse energy leaks out of the memory before the control has been fully turned off, a fraction $15 \pm 2\%$ is stored and retrieved at a later time and the rest is lost. The ratio between the leaking and stopped parts of the signal reflects the ratio between the ensemble length L and the signal length when compressed by the slow light effect.
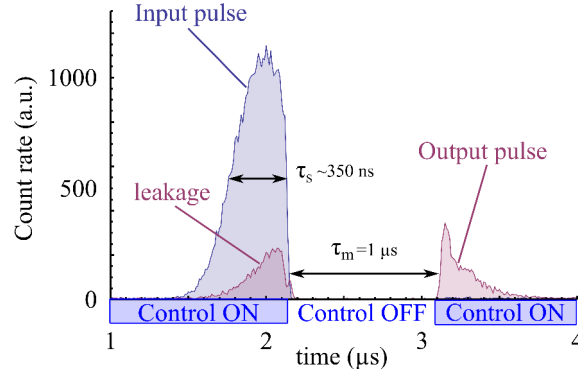

Figure 2.14: **Typical outcome of a quantum memory experiment.** The curves show the average single-photon count rates versus time. The input pulse (reference) is displayed in bluish purple. It is recorded when no atoms are present. The signal has a half-gaussian time shape of FWHM 350 ns. In this experiment, the mean photon number has been set to 0.6 per pulse. The output pulse is displayed in reddish purple. Since the pulse contraction induced by the group velocity reduction is not enough for the whole pulse to fit inside the ensemble's length L, part of it leaks out before the control is turned off. Part of it (representing a storage efficiency of $\sim 15\%$) is stored and retrieved when the control beam is turned back on. The storage time τ_m can be varied. It is 1 μs in this example. Reference and outcome photons are detected on an avalanche photodiode (Model SPCM-AQR-14-FC by Perkin-Elmer) and the experiment is repeated many times (in this case 10^6 times) in order to have a good statistics and to reconstruct correctly the temporal profile of the photons. The background noise is mainly due to the control beam. The ON/OFF state of the control beam, which governs the memory protocol, is indicated below the time axis. Its power was 15 μW, corresponding to $\Omega_c \sim 1.3 \times \Gamma$.

The remaining losses (since 15% and 8% do not add up to the expected 45% transparency that was measured with longer and stronger signal pulses) are expected to be caused by some remaining absorption process possibly linked to the presence of absorbing atoms on the edges of the storage window (atoms that do not see the control well enough due to spatial misposition or spectral shifting). Although this has been investigated only after the main results of the next chapter were obtained, we believe that moving from resonant EIT to off-resonant EIT will contribute to mitigate this issue.

A typical memory experiment is shown in figure 2.14. When performing the few-photon memory experiments, we also noticed the importance of the temporal shaping of the signal. If the signal shape is replaced by a square pulse for example, then we see high-frequency sidebands on the edges of the signal that do not feel the slow light effect and simply leak out of the memory without being stored.

Least, by varying the time at which the control field si turned back on, we can measure the memory decay time τ_m. The measured decay ~ 15 μW confirms our expectations from

the 800 µK temperature measurements of section 2.3.2. More details on the experimental measure of the efficiency decay time will be given in the next chapter.

2.5 Conclusion

In this chapter, we have described the Electromagnetically Induced Transparancy phenomenon and its application to quantum memories in atomic ensembles. We have taken care to emphasize the elements underlying the quality of an EIT-based quantum memory, and we have discussed the limiting mechanisms that are relevant for our experimental implementation.

We have then described how we realized the EIT conditions in the lab with a cold ensemble of magneto-optically trapped ^{133}Cs atoms. Coherently with the previously discussed model, we have characterized the parameters responsible for the performance of the quantum memory.

MOT experimental parameters:

- **MOT repetition rate:** 15 ms
  MOT buildup time: 11.5 ms
  MOT free expansion time: 3.5 ms
  Usefull time slot for EIT quantum memory: from 2 ms to 3 ms after magnetic field switch-off

- **MOT physical and optical properties:**
  Length: $L \sim 2$ mm
  Optical depth ($|F = 4\rangle \rightarrow |F' = 4\rangle$): $d_0 = 15$ (at 2 ms after magnetic field switch-off)
  Temperature: $T \sim 800$ µK
  Magnetic field spread: $\Delta B \sim \pm 5$ mG

- ^{133}Cs **levels used for EIT:**

$$|g\rangle = |6S_{1/2}, F = 4\rangle \quad \text{(ground state)}$$
$$|s\rangle = |6S_{1/2}, F = 3\rangle \quad \text{(storage state)}$$
$$|e\rangle = |6P_{3/2}, F' = 4\rangle \quad \text{(excited state)}$$

Quantum memory characteristics:

- The **memory time** is currently limited by the atomic temperature and the angle between the signal and control beams to a value $\tau_m \sim 15\ \mu s$.

- Current limitation on the **memory efficiency** $\eta \sim 15 \pm 2\%$ is the result of the compromise governing the control power. The Rabi frequency $\Omega_c \sim 1.3\ \Gamma$ was chosen to ensure a good enough **transparency** (45% at resonance) and an (almost) sufficient **group velocity reduction** (by a factor over 10^5). Residual absorption during the re-emission of the signal is also strongly suspected to play negatively against η.

Perspectives:

- The lowering of the cloud's temperature with the goal of extending the memory time is currently under development in the group.

- The improvement of the memory efficiency by adopting a slightly off-resonance (Raman) EIT configuration is also being explored and has given promising preliminary results: with a signal detuning on the order of $\delta \sim 2 \times \Gamma \sim 2\pi \times 10$ MHz, the memory's efficiency has been reliably increased to $\eta \sim 25 \pm 2\%$. The reason for the improvement is that the off-resonant signal suffers less from residual absorption during re-emission. These two last upgrades are being endeavored thanks to the work of Dr. Valentina Parigi and Dr. Christophe Arnold.

- In addition, the realization of a higher OD atomic cloud using an elongated "dark and compressed" MOT is under investigation in the course of the PhD work by Pierre Vernaz-Gris within a partnership with the Autralian National University.

- The next chapter will be devoted to the question of the memory **multimode capacity**, through the demonstration of the storage of multiple transverse modes in the quantum regime and the storage of a qubit encoded in the Orbital Angular Momentum (OAM) state of the signal.

Chapter 3

Storage of a Qubit encoded in orbital angular momentum

Contents

Introduction

In the previous chapter, we have described EIT-based slow light media and given a description of our cold-atom implementation of such a system. We have given its main properties and detailed how it can be used to implement a quantum memory. We have seen that, being an *ensemble-based* quantum memory medium, it is subject to specific inhomogeneous broadening mechanisms (magnetic field fluctuations and thermal Doppler broadening) leading to decoherence effects that have to be mitigated. However, this ensemble-based approach also provides our quantum memory system with an advantageous property, namely a genuine *multimode capability*. This has to be contrasted to quantum memories based on single quantum emitters that are intrinsically singlemode.

In this chapter, we focus on this multimode nature by showing that our memory can reliably store quantum states of light in different spatial modes. Prior to our study, image storage using EIT in atomic gases had already been demonstrated in the classical regime [138, 139]. Delayed heralded single-photon emission had also been shown to exhibit spatial mode entanglement in DLCZ-like experiments [113, 114].

For our study, we chose to work with so-called Laguerre-Gaussian beams, also known as *twisted beams*, whose main feature is to exhibit a quantized *orbital angular momentum*. Over the past ten years, the orbital angular momentum of light has known a growing interest in the scientific community. It is in particular considered an attractive degree of freedom for quantum information encoding due to its unbounded Hilbert space structure [140, 141].

In our work, we extended the spatial mode storage to the quantum regime by storing pulses at the single-photon level in different Laguerre-Gaussian modes [5]. Then, we worked on the quantum storage of Laguerre-Gaussian modes superpositions, i.e. orbital angular momentum encoded Qubits. The fidelity of the storage is high enough to establish the quantum nature of the process, as reported in [6].

It is noteworthy that the subject of the quantum storage of light's spatial modes has attracted interest in different teams at the very same time. Work on Laguerre-Gaussian modes storage have been reported simultaneously by a group in Hefei [142].

The first section introduces Laguerre-Gaussian beams and the orbital angular momentum of light. The second and third sections describe respectively our experimental generation and the measurement of orbital-angular-momentum-carrying light beams. The fourth section integrates these experimental capabilities with the quantum memory of chapter 2.

3.1   Transverse Modes

In this first section, we introduce the transverse modes of a light beam with a focus on light orbital angular momentum which we'll use afterwards for quantum information encoding.

3.1.1   Laguerre-Gaussian modes and light orbital angular momentum

3.1.a   Laguerre-Gaussian modes

Our study was focused on a set of modes known as *Laguerre-Gaussian modes* (LG). They appear as a complete orthonormal set of solutions to the paraxial wave propagation equation:

$$2\mathrm{i}k\frac{\partial}{\partial z} + \frac{\partial^2}{\partial x^2} + \frac{\partial^2}{\partial y^2} = 0 \tag{3.1}$$

Solving this equation yields a family of functions that give the envelope of the electric field of a light beam propagating with a mean wave-vector $\vec{k}$ along coordinate z. Assuming a polar symmetry in the transverse (x,y) or (r,θ) plane, we obtain:

$$\mathrm{LG}_p^l(r, \theta, z) = \mathcal{E}_0 K_{lp} \frac{w_0}{w(z)} \left(\frac{r\sqrt{2}}{w(z)} \right)^{|l|} \mathrm{e}^{il\theta} \mathrm{e}^{-(r/w(z))^2} \mathrm{L}_p^{|l|} \left(\frac{2r^2}{w(z)^2} \right) \mathrm{e}^{ikr^2/2R(z)} \mathrm{e}^{i(2p+|l|+1)\zeta(z)}$$

$$\tag{3.2}$$

where $\mathcal{E}_0$ is the electric field amplitude, $K_{lp} = \sqrt{\frac{2}{\pi}\frac{p!}{(l+p)!}}$ is a normalization constant, and $\mathrm{L}_p^{|l|}$ are the generalized Laguerre polynomials. The parameters $w(z) = w_0\sqrt{1 + (z/z_R)^2}$, $z_R = \pi w_0^2/\lambda$, $R(z) = z\left(1 + (z_R/z)^2\right)$, and $\zeta(z) = \mathrm{arctg}(z/z_R)$ are respectively the radius, Rayleigh length, radius of curvature and Gouy phase for a beam of waist w_0 and wavelength $\lambda = 2\pi/k$. The electric field itself is obtained by multiplying $\mathrm{LG}_p^l(r, \theta, z)$ by the plane-wave component $\mathrm{e}^{i(\omega t - kz)}$.

In contrast to the standard $\mathrm{TEM}_{00} = \mathrm{LG}_{p=0}^{l=0}$ mode, the higher-order Laguerre-Gaussian modes exhibit some specific features. They have a rotating phase profile $\mathrm{e}^{il\theta}$ with a singularity at the origin. Due to this rotating phase, the local Poynting vector has a non-vanishing component along the orthoradial direction and the beam thus possesses an *orbital angular momentum* (OAM) around its propagation axis. The orbital angular momentum carried by each photon in such a mode is equal to the index $l \in \mathbb{Z}$ (in $\hbar$ units) which is also equal to the circulation of the phase around the axis divided by 2π [1]. As the LG modes are eigenfunctions of the propagation equation (3.1), their transverse shape, and hence the OAM of the photons is preserved. This makes the OAM number l a relevant quantum number for information encoding. As required for the smoothness of the electric field amplitude, the phase singularity is associated with an intensity nulling in $r = 0$ as the $2|l|$-th power of the radial coordinate $(\frac{r\sqrt{2}}{w(z)})^{2|l|}$. This feature gives the LG modes their characteristic doughnut-shaped intensity profiles.
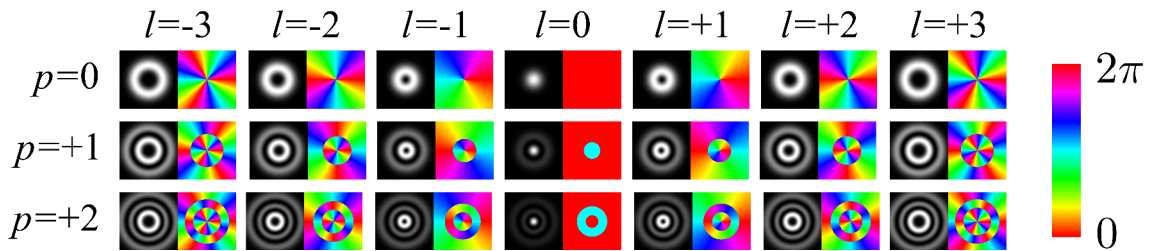
Figure 3.1: **Intensity and phase profiles of the first modes of the Laguerre-Gaussian family**. Azimuthal index l increases from left to right and radial index p increases from top to bottom. The phase is displayed in hue colors as shown on the right. The $l = 0$, $p = 0$ mode corresponds to the fundamental TEM_{00} mode.

---

[1]This was first realized by Allen et al. [143] when they computed the total OAM carried by a LG beam of given intensity and divided this value by the photon flux in such a beam.

The other index, $p \in \mathbb{N}$, describes the radial shape of the beam. With each additional p unit, the amplitude has an additional sign change along the radius and the intensity an additional zero-value ring. This number has a less straightforward interpretation than the orbital index l and has therefore been subject to less scientific investigation hitherto [144, 145]. It appears only as the index of the generalized Laguerre polynomial, which is of degree p. In the rest of this work, we consider only $p = 0$ modes for which:

$$\mathrm{L}_{p=0}^{|l|} = \mathrm{constant} \quad \forall l \in \mathbb{N} \tag{3.3}$$

and which have (at most) one single bright ring. Figure 3.1 shows the intensity and phase profiles of the first LG beams.

3.1.b   Interference with a gaussian beam

A straightforward and widely used method to measure a beam phase pattern is to look at its interference with a plane wave (or a gaussian TEM_{00} beam). Depending on the details of the beams (curvature and propagation direction), the interference of a LG beam with a TEM_{00} beam gives rise to two characteristic patterns: the spirale and the fork. We will use this method to check the phase patterns of our experimentally generated beams in section 3.2.2.

The spirale results from the interference of a plane wave with a rotating-phase wave of different curvature radius R. Taking only the relevant factors into account, the intensity in the (r,θ) plane is given by:

$$
\begin{aligned}
I(r,\theta) \propto |1 + \mathrm{e}^{\mathrm{i}\left(\frac{kr^2}{2R} + l\theta\right)}|^2 &= |1 + \cos\left(\frac{kr^2}{2R} + l\theta\right) + \mathrm{i}\sin\left(\frac{kr^2}{2R} + l\theta\right)|^2 \\
&= \left(1 + \cos\left(\frac{kr^2}{2R} + l\theta\right)\right)^2 + \sin^2\left(\frac{kr^2}{2R} + l\theta\right) \\
&= 2\left[1 + \cos\left(\frac{kr^2}{2R} + l\theta\right)\right]
\end{aligned}
\tag{3.4}
$$

The fork results from the interference of a plane wave with a rotating-phase wave of same curvature radius but with a different transverse mean momentum k_x. Mixing polar (r,θ) and cartesian (x,y) coordinates for simplicity and taking only the relevant factors into account, the intensity in the transverse plane is given by:

$$
\begin{aligned}
I(x,y) \propto |1 + \mathrm{e}^{\mathrm{i}(k_x x + l\theta)}|^2 &= |1 + \cos\left(k_x x + l\theta\right) + \mathrm{i}\sin\left(k_x x + l\theta\right)|^2 \\
&= \left(1 + \cos\left(k_x x + l\theta\right)\right)^2 + \sin^2\left(k_x x + l\theta\right) \\
&= 2\left[1 + \cos\left(k_x x + l\theta\right)\right]
\end{aligned}
\tag{3.5}
$$

The resulting interference patterns are shown in figure 3.2.

3.1.c   Hermite-Gaussian modes

Solving the paraxial equation assuming cartesian symmetry yields another well-known familiy of light beams: the Hermite-Gaussian (HG) modes, defined by the following amplitude profile:

$$\mathrm{HG}_{n,m}(x,y,z) = \mathcal{E}_0 K'_{nm} \frac{w_0}{w(z)} \mathrm{H}_n\left(\frac{\sqrt{2}x}{w(z)}\right) \mathrm{H}_m\left(\frac{\sqrt{2}y}{w(z)}\right) \mathrm{e}^{-\frac{x^2+y^2}{w(z)^2}} \mathrm{e}^{\mathrm{i}k\frac{x^2+y^2}{2R(z)}} \mathrm{e}^{\mathrm{i}(n+m+1)\zeta(z)} \tag{3.6}$$
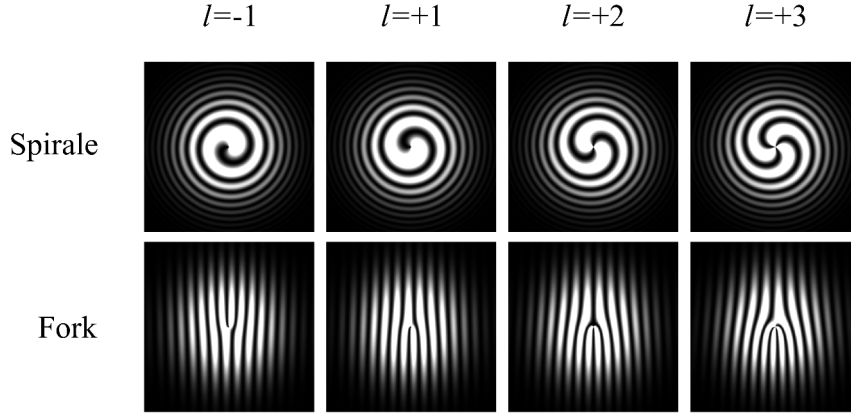
Figure 3.2: **Theoretical spirale (top line) and fork (bottom line) interference patterns**. The interferences are computed for various values of the OAM quantum number l and with a gaussian envelope, which was not explicitly written in equations (3.4) and (3.5). The winding direction of the spirale indicates the sign of l and the number of bright fringes gives the value of $|l|$. The upwards or downwards pointing of the fork gives the sign of l and the number of branches in the fork gives the value of $|l|$.

where $K'_{nm} = \frac{1}{\sqrt{2^{n+m+1}\pi n! m!}}$ is a normalization constant and H_n is the Hermite polynomial of order n. The indices $n, m \in \mathbb{N}$ give the number of phase flips along the x and y directions. In the following, we will use only the first order modes with indiced $n, m = 0$ or 1, corresponding to:

$$\begin{aligned} H_0(x) &= 1 \\ H_1(x) &= x \end{aligned} \tag{3.7}$$

Each phase flip is also associated with a zero of the intensity to ensure the smoothness of the electric field. The intensity patterns of the first HG modes are displayed in figure 3.3. HG and LG modes can be turned into one another by linear combination. Such LG mode superpositions will be required in the next sections in order to describe some possible states of an OAM-encoded quantum bit.

In the next section, we will show how we use the l number as a degree of freedom to implement a qubit.

3.1.2 Quantum information using OAM

The orbital angular momentum of light is considered an attractive degree of freedom for quantum information encoding because it evolves in a discrete infinite-dimensional Hilbert space [146]. Using high-dimensional encoding has been shown to increase the security of quantum cryptography protocols [147], while also increasing the information transmission rate. This prospect has boosted the interest in OAM quantum information encoding. In this section, we describe how to implement a qubit using the OAM degree of freedom.

For a proof-of-principle that the quantum memory described in section 2.3 can store multiple spatial modes in parallel, we considered a two-dimensional subspace of all possible transverse modes spanned by the two modes $\mathrm{LG}_{p=0}^{l=\pm1}$. A single photon in this subspace with a given polarization and temporal shape defines a qubit. The logical basis states are

$$n{=}1 \qquad n{=}2 \qquad n{=}3 \qquad n{=}4 \qquad n{=}5$$
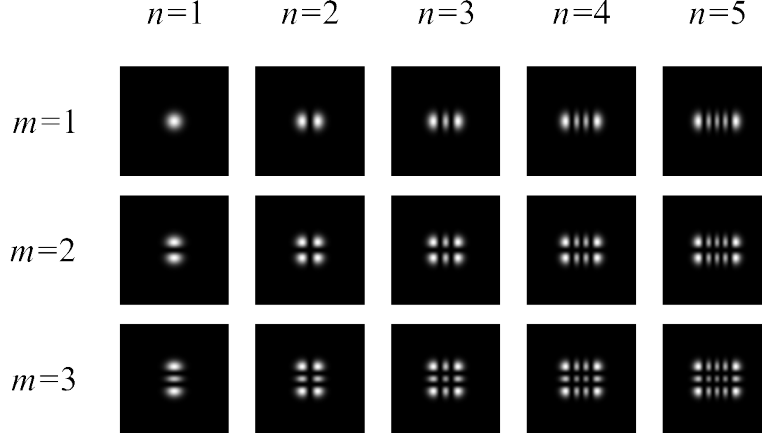
Figure 3.3: **Theoretical intensity profiles of the first modes of the Hermite-Gaussian family**. The phase is piecewise constant with a π jump at every dark line. The indicex n (resp. m) give the number of bright spots (or lines of bright spots) in the horizontal (resp. vertical) direction.

defined as:

$$\begin{aligned}
|\mathbf{0}\rangle &= |l = +1\rangle = |\mathrm{R}\rangle \\
|\mathbf{1}\rangle &= |l = -1\rangle = |\mathrm{L}\rangle
\end{aligned} \tag{3.8}$$

where the letters R and L refer to the right or left helicity of the photon wavefront. In addition to the logical basis states, it will be useful to define four additionnal states as equal-weight superpositions of $|\mathrm{R}\rangle$ and $|\mathrm{L}\rangle$:

$$\begin{aligned}
|\mathrm{H}\rangle &= (|\mathrm{R}\rangle + |\mathrm{L}\rangle)/\sqrt{2} \\
|\mathrm{D}\rangle &= (|\mathrm{R}\rangle + \mathrm{i}|\mathrm{L}\rangle)/\sqrt{2} \\
|\mathrm{V}\rangle &= (|\mathrm{R}\rangle - |\mathrm{L}\rangle)/\sqrt{2} \\
|\mathrm{A}\rangle &= (|\mathrm{R}\rangle - \mathrm{i}|\mathrm{L}\rangle)/\sqrt{2}
\end{aligned} \tag{3.9}$$

Their corresponding spatial modes are Hermite-Gaussian modes. Indeed, it can be checked that the superposition of two first order ($l = \pm 1$) LG modes with a relative phase ϕ gives a two-lobed HG mode, the orientation of which is given by $\phi/2$. Dropping all irrelevant factors from equation (3.2), we have:

$$\begin{aligned}
\mathrm{LG}_{p=0}^{l=+1} + \mathrm{e}^{\mathrm{i}\phi}\mathrm{LG}_{p=0}^{l=-1} &\propto \frac{r\sqrt{2}}{w}\mathrm{e}^{\mathrm{i}\theta} + \frac{r\sqrt{2}}{w}\mathrm{e}^{\mathrm{i}\phi}\mathrm{e}^{-\mathrm{i}\theta} \\
&= \frac{r\sqrt{2}}{w}\mathrm{e}^{\mathrm{i}\phi/2}\left[\mathrm{e}^{\mathrm{i}\left(\theta - \frac{\phi}{2}\right)} + \mathrm{e}^{-\mathrm{i}\left(\theta - \frac{\phi}{2}\right)}\right] \\
&\propto \frac{r\sqrt{2}}{w}\cos\left(\theta - \frac{\phi}{2}\right)
\end{aligned} \tag{3.10}$$

The last line shows that the amplitude of such a superposition varies linearly with a spatial cartesian coordinate rotated by $\phi/2$ with respect to the x axis as illustrated in figure 3.4. The letters H, D, V and A used to label these states refer to the (horizontal, diagonal, vertical or anti-diagonal) orientation of the two bright lobes of the corresponding HG

mode. If one denotes $\alpha_{\rm d}$ the angle made by the dark line with the horizontal axis in such a superposition (as will be done later in this chapter), then from equation (3.10), we have:

$$\alpha_{\rm d} = {(\phi - \pi)}/{2} \tag{3.11}$$

Let us note that from equation (3.2), the modes supporting the logical basis states of the qubit $|{\rm R}\rangle$ and $|{\rm L}\rangle$ evolve with the same Gouy phase factor $e^{2i\zeta(z)}$, which is twice the Gouy phase of a TEM$_{00}$ beam. Therefore, the $|{\rm R}\rangle$ and $|{\rm L}\rangle$ components in a superposition state will not dephase as a result of the propagation. In particular, the $|{\rm H}\rangle$, $|{\rm D}\rangle$, $|{\rm V}\rangle$ and $|{\rm A}\rangle$ states propagate without deformation, which is also a consequence of them being eigenmodes of the paraxial equation (3.1). If one wishes to use a larger fraction of the OAM Hilbert space and keep this enjoyable property, one needs to include $p \neq 0$ modes as well in order to keep $2p + |l|$ constant. Otherwise, superposition modes will be affected by the propagation. One can of course get rid of this issue if one looks at the beams only at mutually conjugated positions.
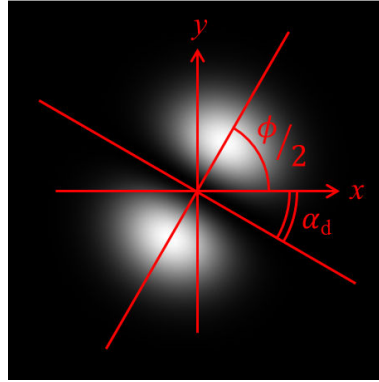
Figure 3.4: **Intensity profile of the superposition of two LG modes.** As explained in equation (3.10), the superposition $\mathrm{LG}_{p=0}^{l=+1} + e^{i\phi}\mathrm{LG}_{p=0}^{l=-1}$ results in a HG mode rotated by $\phi/2$ in the transverse plane. The image has been drawn for $\phi = 2\pi/3$ so the axis of the HG mode makes a $\pi/3$ angle with the horizontal axis x. The dark line in the middle (across which the phase jumps from 0 to π) is characterized by the angle $\alpha_{\rm d} = {(\phi - \pi)}/{2}$ as given by equation (3.11).

A quantum bit can be efficiently represented using the so-called *Bloch sphere* [12]. The most general expression of a quantum bit in a pure state can be written as:

$$\begin{aligned}
|\Psi\rangle &= \alpha|\mathbf{0}\rangle + \beta|\mathbf{1}\rangle \\
&= a|\mathbf{0}\rangle + be^{\mathrm{i}\phi}|\mathbf{1}\rangle \\
&= \cos(\vartheta/2)|\mathbf{0}\rangle + \sin(\vartheta/2)e^{\mathrm{i}\phi}|\mathbf{1}\rangle
\end{aligned} \tag{3.12}$$

with $|\alpha|^2 + |\beta|^2 = 1$, or $a, b \in \mathbb{R}$ and $\phi \in [0, 2\pi[$, or $\mathrm{tg}(\vartheta/2) = {b}/{a} \Rightarrow \vartheta \in [0, \pi[$. The angles ϑ and ϕ completely characterize $|\Psi\rangle$, and they also correspond to the position of a point on the unit sphere expressed in spherical coordinates. So a state $|\Psi\rangle$ can be represented as a point on the surface of the unit sphere as shown in figure 3.5. The poles of the sphere correspond to the logical basis states $|\mathbf{0}\rangle = |{\rm R}\rangle$ and $|\mathbf{1}\rangle = |{\rm L}\rangle$, which are the LG modes in our implementation. The equatorial plane of the Bloch sphere is spanned by the HG

Figure 3.5: **Bloch sphere for the qubit basis** $\{|\mathbf{0}\rangle, |\mathbf{1}\rangle\} = \{|\mathrm{R}\rangle, |\mathrm{L}\rangle\}$, and representation of the phase and amplitude profiles of relevant basis modes. Using the notations of equation 3.12: $|\Psi\rangle = a|\mathrm{R}\rangle + be^{\mathrm{i}\phi}|\mathrm{L}\rangle$, the azimuthal angle ϕ inside the equatorial plane is the relative phase between the $|\mathrm{R}\rangle$ and $|\mathrm{L}\rangle$ components, and the polar angle is equal to $\vartheta = 2\mathrm{arctg}(b/a)$.
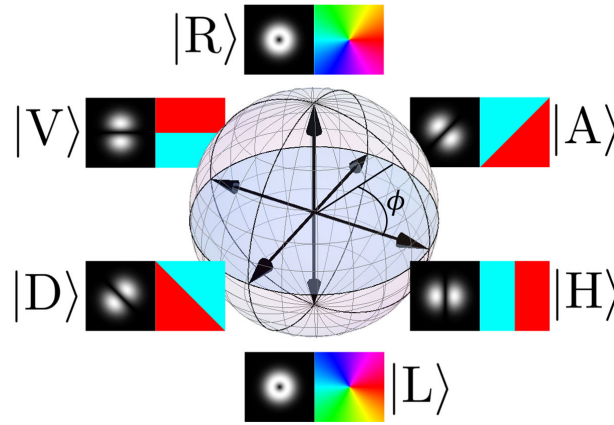
modes of equation (3.9) and the angle ϕ in the sphere is precisely the angle ϕ between the two components $|\mathbf{0}\rangle$ and $|\mathbf{1}\rangle$ of the qubit.

Now that we have theoretically presented the LG modes and how to use them to implement an OAM qubit, we turn to their experimental generation and manipulation in the lab.

3.2 Experimental generation of an OAM Qubit

Our OAM qubit is defined as a linearly polarized signal pulse at the single-photon level in which the information is encoded through the value of the orbital angular momentum quantum number l. This section describes how we produced such a qubit.

3.2.1 Generating transverse modes with a spatial light modulator

The standard light ressource in any optics lab being a gaussian TEM_{00} beam, higher order LG (or HG) beams have to be produced out of it. Many techniques have been developed over the years to achieve such a goal. A review of these techniques can be found for example in [140]. We decided to work with a *spatial light modulator* (SLM) because it offers a maximal versatility and ease-of-use, in that it allows to switch straightforwardly from one mode to another one.

A spatial light modulator is a liquid-crystal screen with voltage-adressed pixels. The one we used had a 792×600 resolution with $20 \times 20 \ \mu\mathrm{m}^2$ wide pixels for a useful surface of 1.2×1.6 cm ^{2}. Liquid crystals (LC) being birefringent, a (linearly) polarized light beam passing through LC will be phase-shifted by a quantity depending on the angle between its polarization and the LC orientation. The voltage applied to a pixel governs the orientation of the LC and thus the dephasing imposed to the beam at this position. The light is reflected on a mirror behind the liquid crystals so it passes twice through them. This process is shown schematically in figure 3.6. A picture of the SLM is shown in figure 3.7.

---

[2] Model LCOS-SLM X10468 by Hamamatsu.

The SLM is controlled by a computer with which it is interfaced as an additionnal screen. The desired phase patterns are coded and sent to the SLM as grayscale pictures. Example of such phase pictures (or holograms) are shown in figures 3.9 and 3.10.

Since the back mirror of the SLM is not perfectly flat, it induces aberrations that must be corrected. To this end, a calibration phase pattern is provided by the manufacturer. This phase pattern is added to the desired one before it is sent to the device. The importance of this calibration is illustrated in figure 3.8.

The amount of phase modulation obtained for a given voltage depends on the wavelength of the incident light. By using all the allowed dynamic range of the device, we had a phase modulation amplitude above 2π at our wavelength of $\lambda = 852$ nm. The device is thus factory calibrated (as a function of the wavelength) in such a way that it interprets 0 to 255 grayscale levels as a 0 to 2π phase shift. Phase modulation by more than 2π can be reached by taking the modulo of the phase by 2π in a process that ressembles the construction of a Fresnel lens.

In order to explore the possibilities of the SLM and to show its good functionning, we generated arbitrary intensity patterns in the far field of the SLM (observed at the focal plane of a lens). The SLM allows to control the phase of a beam in a given plane, but the intensity distribution there is given by the beam illuminating it. In such conditions, it is not possible to obtain an arbitrary distribution of both amplitude and phase at the output [148]. However, if we leave aside the phase in the output plane, for any intensity pattern in the output plane, it is possible to find a phase distribution in the plane of the SLM which will produce this intensity distribution. An iterative algorithm [149] allows to find the corresponding phase pattern. Its principle is illustrated in figure 3.9 together with an example of generated phase pattern (or hologram) and the image obtained experimentally when this phase pattern is fed to the SLM.

Even if this procedure allows to obtain an arbitrary intensity distribution in the far-field, it is not very useful for our needs, since we are deeply concerned with the production of specific phase patterns.

To produce LG and HG beams, we simply impose the phase that these beams should have. The corresponding holograms are shown in figure 3.10. For a LG beam, we impose the rotating phase pattern: $e^{\pm i\phi}$, and for a HG beam, we use a phase-flip pattern. In the next section, we will discuss the quality (i.e. mode purity) of the beams generated by this method.

3.2.2 Quality of the experimentally generated modes

The mode production by phase-only modulation cannot perform a 100 % efficient mode conversion as the intensity pattern in the SLM plane is still that of a TEM_{00} mode. Since we illuminate the SLM with a collimated beam (of radius w_0), the electric field amplitude in the plane of the SLM has the following envelope:

$$
\begin{aligned}
& e^{i\phi}e^{-r^2/w_0^2} && \text{for a } \text{LG}^{l=+1} \\
& \text{sgn}(x)e^{-\frac{x^2+y^2}{w_0^2}} && \text{for a } \text{HG}_{\text{H}}
\end{aligned}
\tag{3.13}
$$

where $\text{sgn}(x) = x/|x|$ designates the sign function. These expressions can be expanded onto the LG or HG bases. The (square of the) coefficients of the various modes in these decompositions give their proportions inside the SLM output defined by equation (3.13).
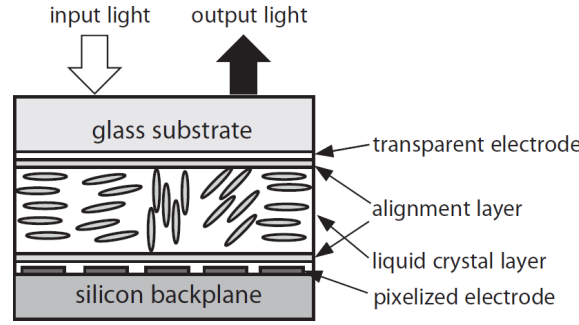
Figure 3.6: **Principle of a liquid crystal SLM.** Credits: Hamamatsu.
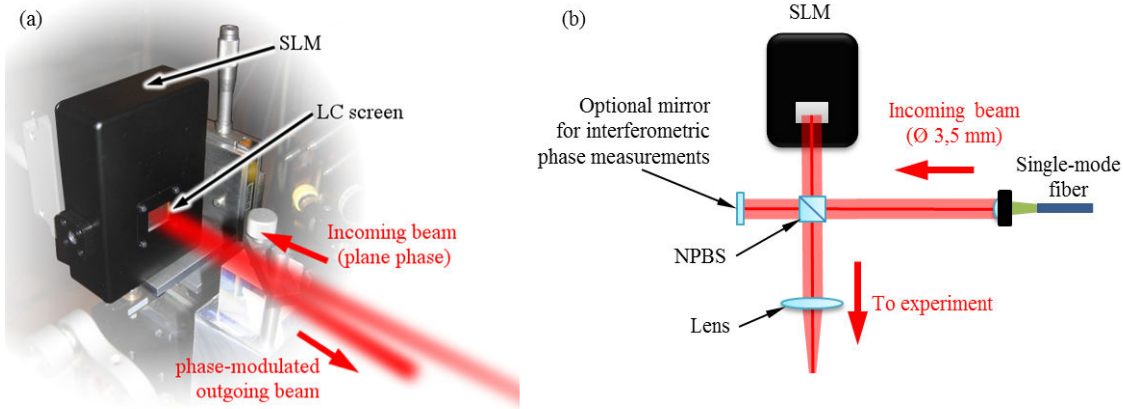
Figure 3.7: **The SLM on the optical table.** (a) Picture of the SLM. (b) Diagram of the setup. The light beam is brought to the SLM via a single-mode optical fiber to ensure a good mode quality. It is expanded to a $1/e^2$ diameter of 7.8 mm with a commercial beam expander (Thorlabs F810APC-842) so that it illuminates a large enough area on the SLM without being cut by the edges of the SLM screen. A non-polarizing beam splitter (NPBS) separates the beam into two paths, one directed towards the SLM and one directed towards an optional mirror. It enables to check the phase pattern of the modulated beams by means of interference as explained in section 3.1.b.
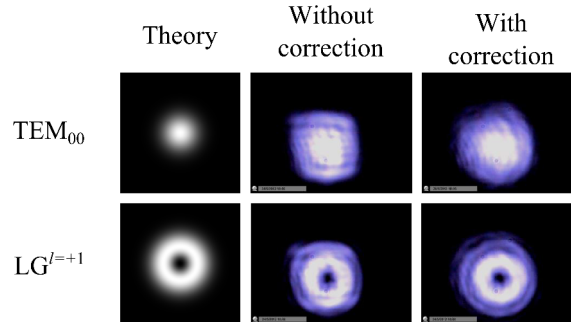
Figure 3.8: **The importance of correcting for the planeity defects of the SLM back mirror.** Theoretical and experimentally achieved beam shapes for two different target beams. Top line: TEM_{00} beam, bottom line: $LG_{p=0}^{l=1}$. We are closer to the ideal mode shapes when using the SLM calibration phase pattern (right colunm) than with the uncalibrated SLM (middle column).
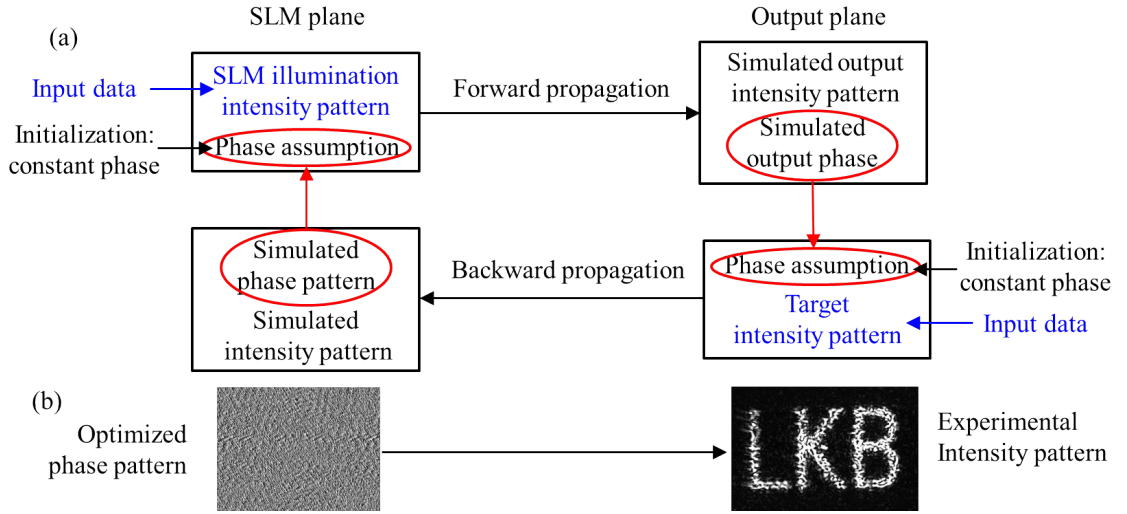
Figure 3.9: **Example of the implementation of the *Gerchberg-Saxton algorithm.***
(a) Principle of the algorithm. The amplitude pattern is propagated forward and backward between the SLM and output planes. At each position, the simulated phase pattern provides the phase assumption for the next step, while the intensity assumption is given by the SLM illumination pattern in the SLM plane and by the target intensity pattern in the output plane. By successive iterations, the simulated phase pattern in the plane of the SLM converges towards one that will produce the target intensity in the output plane. (b) Example of a hologram generated after 50 iterations (left). The phase is coded in grayscale, black meaning 0 and white meaning 2π. Intensity pattern recorded with a CCD camera in the focal plane of a lens when the SLM is fed with this hologram (right).
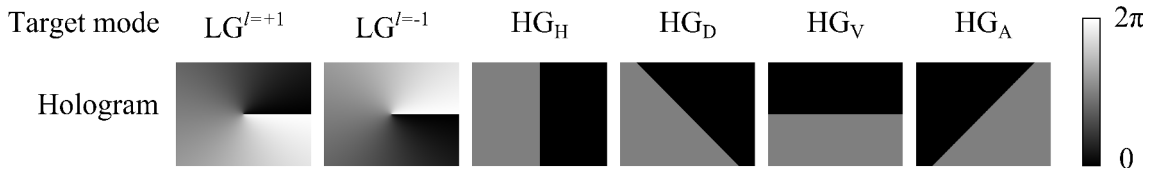
Figure 3.10: **Holograms used to generate LG and HG beams.** The phase is encoded in grayscale as indicated on the right.

For the LG beam generation, the coefficients are given by:

$$C_{l,p} = \int \int \mathrm{LG}_p^l(r, \theta, z = 0)\, \mathrm{e}^{-r^2/w_0^2}\, \mathrm{e}^{\mathrm{i}\phi}\, r \mathrm{d}r \mathrm{d}\theta \qquad (3.14)$$

Of course, the rotating phase pattern in the output beam is the correct one, as it is imposed by the SLM. Consequently, only $l = +1$ modes will be populated, which is also visible in equation (3.14) as the vanishing of the integral over θ for any value of $l \neq 1$. This can be interpreted physically as the fact that the OAM state is well defined – which is what matters for our OAM information encoding. However, different p modes are produced – in fact infinitely many. Numerically computing the integrals in equation (3.14) gives the proportions of the various p modes. We find (see table 3.1) that about 78% of the energy is contained in the $p = 0$ mode.

Since modes with a different p index acquire different Gouy phases as a result of their

propagation, their superposition (defined by equation (3.13)) is not propagation invariant. Close to the SLM, the intensity pattern is dominated by the TEM_{00} envelope of the illuminating beam. As the distance increases, a hole appears in the center as a consequence of the phase singularity $e^{i\phi}$: the beam acquires a doughnut-like shape that is characteristic of LG modes. Additional intensity rings surround the central bright ring. These are the consequence of the presence of higher-order p modes. When the focus is approached, they become less and less visible because they have a stronger diffraction than the $\text{LG}_{p=0}^{l=+1}$ mode. Figure 3.11 shows the observed evolution of the beam as it moves further and further away from the plane of the SLM.

p	**0**	1	2	3	4	5	6	7	8	9
$C_{l=1,p}$	**78.5%**	9.8%	3.7%	1.9%	1.2%	0.8%	0.6%	0.4%	0.3%	0.2%

Table 3.1: **Theoretical overlap of the SLM output with the first LG modes** computed from equation (3.14) when using a rotating phase hologram such as in the top line of equation (3.13) or shown in figure 3.10. The coefficient of the target $\text{LG}^{l=+1}$ mode is written in bold font.
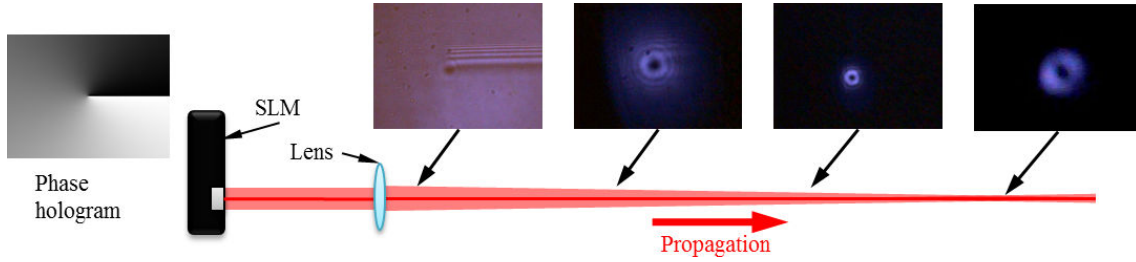
Figure 3.11: **Evolution of the beam after being reflected on the SLM.** The rotating phase hologram $e^{i\phi}$ is displayed on the leftmost part of the figure. Starting from a gaussian illumination beam, about 78% of the energy is transfered to a $\text{LG}_{p=0}^{l=+1}$ mode. The remaining energy populates the various $\text{LG}_{p>0}^{l=+1}$ modes according to the distribution given in table 3.1. As it propagates away from the SLM the beam shape changes from a TEM_{00} envelope (a horizontal dark line is visible: it is a consequence of the imperfections in the phase jump from 0 to 2π when the hologram is displayed on the SLM) to a doughnut shaped mode surrounded by dim additionnal rings. When we near the focus (rightmost image), the additional rings originating from the higher order p modes are no more visible. A very little astigmatism is responsible for the mode being slightly deformed at the focus [150]. Pictures are taken at different scales.

The same modal decomposition goes for HG modes. The "*flipped mode*" defined by the bottom line in equation (3.13) is not a pure HG mode but it can be decomposed on the HG basis. Taking the example of the HG_H mode, the coefficients in this decomposition are given by:

$$C_{n,m} = \int \int \text{HG}_{n,m}(x,y) \, \text{sgn}(x) \, e^{-(x^2+y^2)/w_0^2} \mathrm{d}x\mathrm{d}y \qquad (3.15)$$

Once again, the phase structure is imposed by the SLM and it cannot deviate from it. For HG modes, this translates into the fact that the produced mode has the correct symmetry: in the case of a horizontal HG, only (horizontal) $\text{HG}_{n\in 2\mathbb{N}+1,m=0}$ modes will be populated. In terms of LG mode basis, this means that the produced beam can be written as a

superposition of a $l = +1$ component and a $l = -1$ component with a relative phase factor equal to the desired phase ϕ (ϕ being 0 in the case of a horizontal HG beam). The two "pure-l" components however each contain multiple p modes. A difference between the HG and the LG case is that the overlap of the flipped mode with the target HG_H computed by evaluating the integral in equation (3.15) is only 64%. The first (squared) $C_{n,m}$ coefficients are given in table 3.2. This smaller overlap also translates in the apparition of more

n	0	**1**	2	3	4	5	6	7	8	9
$C_{n,m=0}$	0%	**63.7%**	0%	10.6%	0%	4.8%	0%	2.8%	0%	1.9%

Table 3.2: **Theoretical overlap of the SLM output with the first HG modes** computed from equation (3.15) when using a phase-flip hologram such as in the bottom line of equation (3.13) or shown in figure 3.10. The coefficient of the target $HG_H = HG_{n=1,m=0}$ mode is written in bold font. The $HG_{0,0}$ mode is equal to the TEM_{00} mode. All modes with the wrong parity are absent from the decomposition. The convergence of the coefficients towards zero is slower than in the LG case (table 3.1).

pronounced "higher-order wings" in the exprimentally generated HG beams.

In order to produce better quality HG (and possibly LG) modes, we tried to perform a *pseudo-amplitude modulation* with the SLM [151]. The principle is to add to the phase hologram a blazed diffraction grating, i.e. a saw-tooth phase profile. If the depth of the saw-tooth grating is 2π, then (ideally) all the incoming light is diffracted in the first order. This is indeed equivalent to adding a linear phase to the beam, which just changes its transverse momentum (or propagation direction). If the depth of the grating is *smaller than* 2π, then part of the light will be diffracted in the first order and part will be reflected back in the zero-th order. This process is illustrated in figure 3.12. Changing locally the phase depth of the grating thus allows in principle to modulate the intensity pattern inside the first diffraction order. Adding a custom phase profile to the grating allows in principle to generate an arbitrary phase and intensity pattern in the first order [151]. However, this is also a lossy process because a *single* phase-modulation step cannot perform a unitary manipulation of transverse modes [148].

In the end, however, the pseudo-modulation technique was much more lossy than the "brute force" (phase-flip) method and the required level of control over the shape of the mode made it difficult to combine this mode generation method with our detection setup (see next section). So we used the straightforward phase-only modulated holograms of figure 3.10.
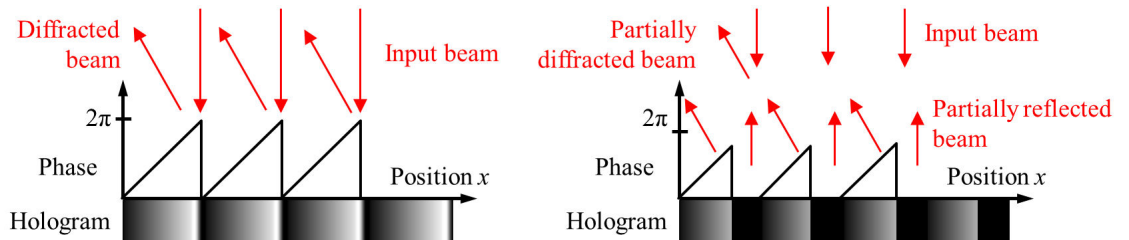
Figure 3.12: **Principle of amplitude pseudo-modulation with a SLM and a saw-tooth phase grating.** Left: a blazed diffraction grating with a depth of 2π diffracts all the light into the first order. Right: by modulating the depth of the grating, a customizable percentage of the light can be sent to the first diffraction order or left in the zero-th order.

We verified the phase pattern of all the beams by interfering them with a reference wave using the optional mirror shown in figure 3.7. For LG modes, we observed both the fork and the spirale shapes. For HG modes, we observed straight interference fringes that are shifted by half an interfringe across the phase-flip line. These observations confirmed that the phase patterns of the SLM output is correctly defined by the holograms shown in figure 3.10. Since we only encode information in the OAM l quantum number and leave aside the p degree of freedom, we were not sensitive to the limited mode conversion efficiency.
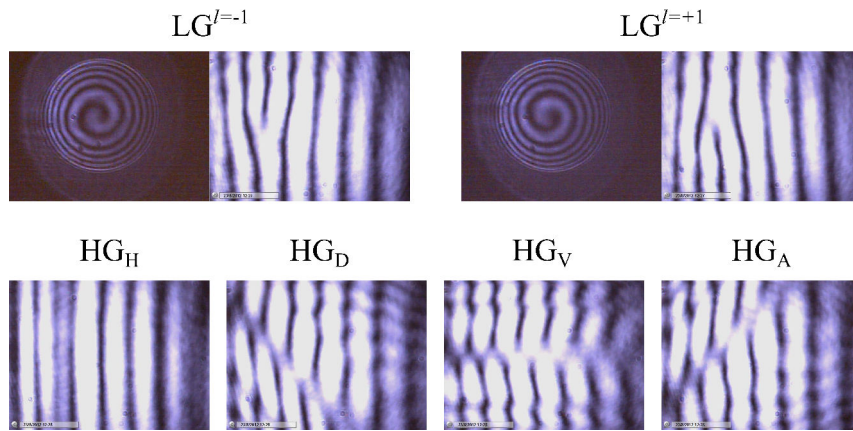
Figure 3.13: **Interferometric observation of the phase of the beams.** Top line: LG modes, bottom line: HG modes.

Summary: LG modes and OAM qubit

- In the two previous sections, we have introduced the **LG** and **HG** families of spatial **transverse modes**, we have detailed how to generate these beams experimentally with a **spatial light modulator**. We have described how the OAM state of a single-photon can encode a qubit.

- Since our goal is to interface these OAM qubits with our quantum memory (chapter 2), we prepared weak coherent signal pulses and spatially shaped them to one of the six modes $|R\rangle$, $|L\rangle$, $|V\rangle$, $|D\rangle$, $|H\rangle$, $|A\rangle$ using the SLM as described in 3.2. The pulses were additionaly time shaped to a half-gaussian profile of FWHM 350 ns as described in section 2.3.3. Their average photon number can be customized by neutral density filters. It is typically lower than one photon per pulse.

- The efficiency of the mode generation with the SLM is limited to 78% for LG modes and 64% for HG modes. However, this will not prove detrimental in the quantum memory experiment because:

    ○ the OAM structure of the beams – which carries the information in our encoding – is correct,

    ○ we use a *projective* detection setup as will be described in the next section, so we simply do not detect the higher-order modes.

The non-perfect efficiency of the beam generation thus merely causes a lower count rate as will be explained at the end of section 3.3.c.

The next section will present in details the setup we developed in order to measure the state of the qubit by projecting it onto any of the states $|R\rangle$, $|L\rangle$, $|H\rangle$, $|D\rangle$, $|V\rangle$ and $|A\rangle$, as required for quantum state tomography.

3.3 Quantum state tomography of OAM qubits

This section exposes the setup we developed to perform the quantum state tomography of the OAM-encoded qubits. A certain amount of work was dedicated to the measurement of the relative phase between different pure-OAM components.

3.3.1 Qubit tomography

In this section, we introduce the tools necessary to understand the characterization of a qubit, i.e. a two-dimensional quantum system evolving in a Hilbert space spanned by the two basis vectors denoted $|0\rangle$ and $|1\rangle$. For a pure state, the qubit can be written as in equation 3.12: $|\Psi\rangle = \alpha|0\rangle + \beta|1\rangle$.

The tomography of such superposition states require measurements performed in a complete set of mutually unbiased bases, i.e. three linearly independent ones [152]. In addition to the logical basis $\{|0\rangle, |1\rangle\}$, two additional mutually unbiased bases can be defined as the superpositions: $\{|\pm\rangle = |0\rangle \pm |1\rangle\}$ and $\{|\pm i\rangle = |0\rangle \pm i|1\rangle\}$ [3]. Measuring the

---

[3]The correspondence with the notations of equation (3.9) is $|+\rangle = |H\rangle$, $|-\rangle = |V\rangle$, $|+i\rangle = |D\rangle$ and $|-i\rangle = |A\rangle$.

qubit in the logical basis will yield the values of $|\alpha|^2$ and $|\beta|^2$ and measurements in the two superposition bases will provide the relative phase between the coefficients α and β. This sequence of measurement actually allows to perform the reconstruction of the density matrix of any mixed state, which in the general case can be expressed as :

$$\hat{\rho} = \frac{1}{2}\left(\hat{\mathbb{I}} + \sum_{i=1}^{3} S_i \hat{\sigma}_i\right) = \frac{1}{2}\begin{pmatrix} 1 + S_1 & S_2 - i\,S3 \\ S_2 + i\,S3 & 1 - S_1 \end{pmatrix} \tag{3.16}$$

where the $\hat{\sigma}_i$ are the Pauli matrices and the coefficients $S_i = \mathrm{Tr}(\hat{\rho}\hat{\sigma}_i)$ are usually called Stokes parameters in analogy with the polarization states terminology. The S_i coefficients indicate the relative weights of either state in the each basis. Indeed, they can written as $S_1 = p_{|\mathbf{0}\rangle} - p_{|\mathbf{1}\rangle}$, $S_2 = p_{|+\rangle} - p_{|-\rangle}$ and $S_3 = p_{|+\mathrm{i}\rangle} - p_{|-\mathrm{i}\rangle}$, where $p_{|\Psi\rangle}$ is the probability to measure the qubit in the state $|\Psi\rangle$.

If the qubit is in a pure state as in equation 3.12, then

$$\hat{\rho} = |\Psi\rangle\langle\Psi| = \alpha^2|\mathbf{0}\rangle\langle\mathbf{0}| + \beta^2|\mathbf{1}\rangle\langle\mathbf{1}| + \alpha\beta^*|\mathbf{0}\rangle\langle\mathbf{1}| + \beta\alpha^*|\mathbf{1}\rangle\langle\mathbf{0}| \ ,$$

and the Stokes parameters can be easily related to the α and β coefficients:

$$S_1 = |\alpha|^2 - |\beta|^2 \qquad S_2 = 2\mathrm{Re}(\alpha\beta^*) \qquad S_3 = -2\mathrm{Im}(\alpha\beta^*).$$

The quantum state tomography of a qubit requires to measure the various probabilities p_i, i.e. to project the qubit over different (mutually unbiased) bases. In the case of the OAM-encoding presented in section 3.1.2, this means projecting the qubit over the Laguerre-Gaussian modes $\mathrm{LG}^{l=+1}$ and $\mathrm{LG}^{l=-1}$ and over the Hermite-Gaussian modes $\mathrm{HG_H}$, $\mathrm{HG_D}$, $\mathrm{HG_V}$ and $\mathrm{HG_A}$. How these projections are realized experimentally is the subject of the next sections.

3.3.2 How to detect the OAM state of a single-photon ?

The determination of the OAM state of a bright beam of light can be done by standard imaging and wavefront measurements (either using interferometry or a microlens array, or any equivalent commercially available technique). These techniques intrinsically require many photons. Measuring the OAM state at the single-photon level asks thus for other methods. The different techniques developed so far can be classified into two categories:

- **Projective-based techniques.** In these methods, the photons are projected onto an OAM eigenstate before being detected. The mode projectors are typically made of a hologram that converts an input mode with non-zero l value into a $\mathrm{TEM_{00}}$ mode followed by a spatial filter (pinhole or single-mode fiber). The holograms can be either fixed [153] or dynamically programmed with a spatial light modulator [154], they can be either intensity [155] or phase holograms [153], they can diffract the light to all directions or be optimized for a single output direction. In any case, the projector only selects one mode and photons in other modes are lost.

- **Mode-sorting techniques.** Here, the propagation direction of the photons is changed depending on their OAM value. This feature overcomes the problem of losses inherent to mode projection. However, these methods are often more challenging than the previous ones. Among them, one can cite a Mach-Zehnder interferometer in the arms of which Dove prisms have been inserted [156]. Another method that has

seen significant developments in the few past years relies on a log-polar coordinate interpolation realized with two phase-modulating elements. The radial and polar coordinates r, θ in one plane are mapped one by one onto the cartesian x and y coordinates in a subsequent plane. This approach was first implemented with two spatial light modulators [157] then with fixed refractive optics [158–160]. It is also possible to take benefit from the fact that any unitary manipulation of transverse modes (and hence mode sorting) can be achieved by multiple phase modulation steps separated by optical Fourier transforms [161].

In our work, we employed a *projective-based* method using *fixed holograms* as in [153] to discriminate between LG modes because of the high distinction ratio and the great simplicity of this method. To discriminate between HG modes (or equivalently to measure the phase ϕ between the $|R\rangle$ and $|L\rangle$ components in a superposition state), we first thought of combining this mode-projection technique with the projective *slit-wheel method* introduced in [162]. It consists in sending the beam through a cache with multiple apertures corresponding to the number of expected bright spots in the HG mode (in our case: two diametrally opposed slits for two bright spots). By rotating the cache, one should in principle be able to record a sinusoidal intensity modulation behind the cache if the input mode is a coherent superposition of $LG^{l=+1}$ and $LG^{l=-1}$, and a constant intensity in the case of an incoherent superposition. However, the two projective techniques (OAM mode conversion and slit-wheel) do not go along very well together, so we went for a mode sorting interferometric design instead. This also has the advantage to ressemble very much the quantum tomography of (more conventional) polarization-encoded qubits – with some additional losses however.

The aborted slit-wheel method trial is reported in the appendix A.4 while the next section describes the setup we finally resorted to. The possibility to extend this OAM measurement setup to higher-dimensional OAM Hilbert spaces is also discussed in appendix A.5.

3.3.3 Interferometric setup for quantum state tomography of OAM qubits

3.3.a Interferometer and mode projectors

The apparatus is schematized in figure 3.15. The incoming state is first split using a non-polarizing beam splitter. Each of the subsequent paths includes a *mode projector* onto an OAM eigenstate. These mode projectors are based on the combination of a *fixed hologram* and a *single-mode fiber* [153]. A blazed fork phase-hologram diffracts the light and performs OAM addition or subtraction depending on its orientation as illustrated in figure 3.14. Thus, on one path, the mode $LG^{l=+1}$ is converted into a mode $LG^{l=0} = TEM_{00}$, which is then efficiently coupled to the single-mode fiber, while any other mode is converted into a Laguerre-Gaussian beam with a non-vanishing l value and hence not coupled to the subsequent fiber. There are two such paths, denoted R and L, that are arranged to project the incoming signal onto the $|R\rangle$ and $|L\rangle$ states respectively. The diffraction efficiency of the holograms is 80% and the coupling efficiency to the single-mode fiber is also around 80%, leading to an overall transmission of about 65%. The rejection of the other mode was measured to be 23 dB in the worst case and up to 37 dB in the best case. Typical value was 25 dB. The mode transformation performed by the holograms will be shown in table 3.5 when we will present the procedure for the alignment of the setup.
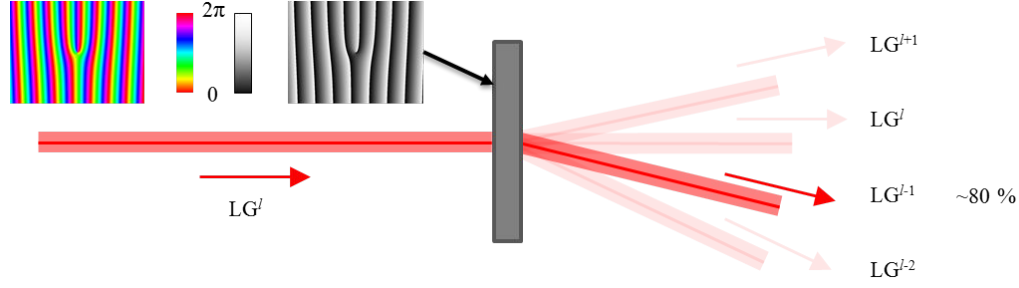
Figure 3.14: **Principle of OAM addition and mode conversion with a blazed fork hologram.** The phase pattern of the hologram is given in hue colors and in grayscale. An impinging light beam in a given LG mode with OAM number l is diffracted by the hologram. Light in diffraction order i is added i units of orbital angular momentum. Thanks to the waw-tooth structure of the hologram, most of the power (about 80%) goes to the first order for which $\Delta l = -1$. Spatial filtering of the first diffraction order by a pinhole or a single-mode fiber thus selects the $LG^{l=+1}$ component of the input beam.
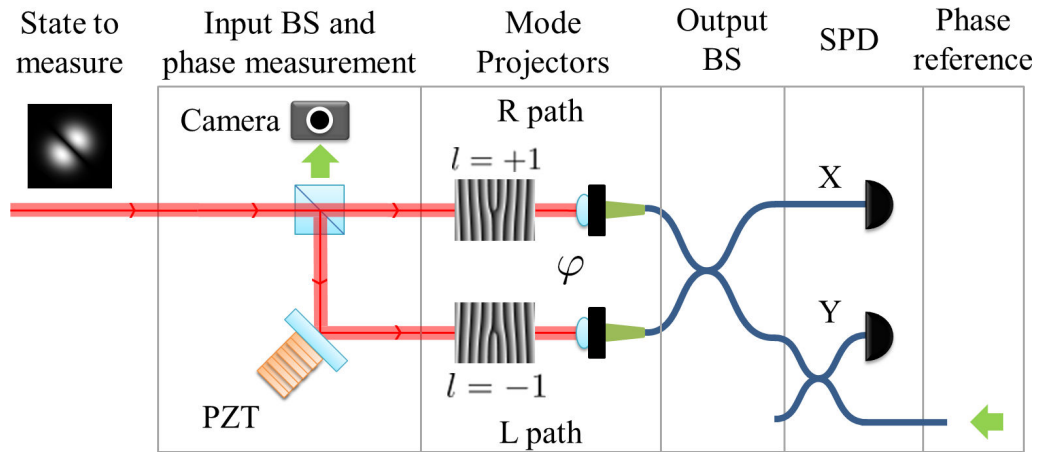
Figure 3.15: **Experimental setup for OAM qubit tomography.** The state to be characterized enters a two-path interferometer, where each path includes a mode projector based on a blazed fork hologram (phase pattern shown) and a single-mode fiber. Depending on the orientation of the hologram's fork, one unit of OAM is added or subtracted from the light that is diffracted on it. Hologram labelled $l = +1$ in path R converts a $LG^{l=+1}$ mode into a TEM_{00} one and hologram $l = -1$ in path L converts a $LG^{l=-1}$ mode into a TEM_{00} one. The beams are then coupled into single-mode fibers that act as spatial filters for the TEM_{00} mode, hence selecting only one OAM component in each path. The fibers are then recombined at a fibered beam splitter with two outputs labelled X and Y, where single-photon detectors (SPD) are located. A phase reference beam, symbolized by the green arrows, is injected backwards and detected by a digital camera at the input beam splitter in order to measure the phase φ of the interferometer. The value of φ defines the measurement basis.

As shown in figure 3.15, the two paths are then recombined via a fiber beam splitter with two outputs labelled X and Y. The difference in propagation length along the two arms of the interferometer causes a phase shift denoted φ. If the input is in a Laguerre-Gaussian mode $|R\rangle$ or $|L\rangle$, then only one of the interferometer arm will contain light, and this light will be equally distributed over X and Y regardless of φ. In contrast, if the input is in a superposition state, then there is a non-zero amplitude in both arms and these amplitudes will interfere. The probabilities to detect light at either outputs X or Y will vary sinusoidally with φ.

More specifically, let us take the example of a pure state $|\Psi\rangle = a|R\rangle + be^{i\phi}|L\rangle$ $(a, b \in \mathbb{R})$ entering the device. Up to a global attenuation factor, it will be transformed into:

$$\left[(a + be^{i(\phi+\varphi)})|X\rangle + (a + be^{-i(\phi+\varphi)})|Y\rangle \right] \tag{3.17}$$

where we have assumed the mode projectors have perfect transmission of their target mode and perfect rejection of all other modes. The number of events detected at the output X for instance will thus be proportional to

$$P = a^2 + b^2 + 2ab\cos(\phi + \varphi). \tag{3.18}$$

These events corresponds to the projection of the incoming state on the state $|R\rangle + e^{i\varphi}|L\rangle$. By choosing φ, any projection basis in the equatorial plane of the Bloch sphere can thus be chosen.

	L path blocked	R path blocked	Full interferometer			
			$\varphi = 0$	$\varphi = \pi/2$	$\varphi = \pi$	$\varphi = 3\pi/2$
Output X	$|R\rangle$	$|L\rangle$	$|H\rangle$	$|A\rangle$	$|V\rangle$	$|D\rangle$
Output Y	$|R\rangle$	$|L\rangle$	$|V\rangle$	$|D\rangle$	$|H\rangle$	$|A\rangle$

Table 3.3: **Mode projection in output X and Y as a function of the configuration of the interferometer.** The relative phase φ defines the projection basis in the equatorial plane of the Bloch sphere. Blocking one of the more projector path turns the measurement basis to the logical (LG) basis.

In summary, the interferometer acts as a mode-sorter in a given Hermite-Gaussian basis: it directs one mode towards output X and the orthogonal mode to output Y. The basis in which this mode sorting occurs depends on the value of the phase φ. For instance, for $\varphi = 0$, all photons in the $|H\rangle$ state will be directed towards output X while photons in state $|V\rangle$ will be directed towards output Y. In the same way, for $\varphi = \pi/2$, the incoming photons are projected on the basis vectors $|A\rangle$ (output X) and $|D\rangle$ (output Y). Finally, if one of the paths is blocked, then the device will act as a projector onto the OAM eigenstate $|R\rangle$ or $|L\rangle$, as a function of the non-blocked path. In this case, the detectors at X and Y receive the same signal, which is proportional to the a or b coefficient of the qubit decomposition (equation (3.12)). Therefore, when the device is properly calibrated (as will be explained in section 3.3.c), it can be regarded as a black box performing state projection and yielding photon counts in the outputs X and Y as summarized in Table 3.3.

We now turn to the control of the interferometric phase φ.

3.3.b Variation and measurement of the interferometer phase

In order to change the projection basis, one mirror inside the interferometer is mounted on a piezoelectric transducer, thus allowing to vary φ. In the following, we explain how to

access this phase using backwards-propagating reference light.

Phase-reference beam.   Thermal and mechanical drifts continuously change the inter-ferometer phase φ on a scale of a few degrees in a few seconds. To access this phase, an auxiliary phase-reference beam is injected backwards into the interferometer (green arrows in figure 3.15). At the input beam splitter, the reference light from paths R and L recom-bines. While it propagates backwards, the reference beam crosses the two holograms. The TEM$_{00}$ modes emerging out of the fibers are converted into a $|\mathrm{L}\rangle$ mode in the R path, and into a $|\mathrm{R}\rangle$ mode in the L path. These modes are superposed at the input beam splitter with a phase difference that is precisely equal to the interferometer phase φ. As a result, we get the superposition $\left(|\mathrm{R}\rangle + \mathrm{e}^{\mathrm{i}\varphi}|\mathrm{L}\rangle\right)$. As shown in equations (3.10) and (3.11), the equal-weight superposition of LG$^{l=+1}$ and LG$^{l=-1}$ modes with a relative phase φ results in a rotated Hermite-Gaussian mode, consisting of two bright spots of opposite phase separated by a dark line. The dark line makes an angle

$$\alpha_{\mathrm{d}} = (\varphi - \pi)/2 \tag{3.19}$$

with the horizontal axis. Measuring this angle enables to access the interferometer phase. The phase reference beam is recorded at a rate of about 10 images per second by a digital camera at the input-BS.

   We now detail how to analyze the images taken by the digital camera to efficiently extract the value of φ.

Image analysis routine.   In a preparational step, all images are enhanced by applying a median filter (to reduce high-frequency noise and dead pixels) and a midtone stretching filter (to increase the contrast in the middle intensity region and to reduce variations in the high- and low-intensity regions).

   When φ varies, the dark line in the intensity pattern of the phase reference beam rotates around the beam axis, according to equation 3.19. First, the center around which the dark line rotates has to be determined. For this purpose, many images for different values of φ are required, covering roughly uniformly the whole range of $\varphi \in [0, 2\pi[$ (corresponding to the range of $[0, \pi[$ for the angle α_{d} of the dark line). Averaging them results in a ring-shaped image, as shown in table 3.4, to which a doughnut-like distribution is fitted. The fit provides two parameters: the position of the center and the radius of interest. As long as the alignment of the reference path is not changed, these values remain valid for all images. Consequently, this initial procedure has to be performed only once for a measurement series: either during the calibration, if a real-time analysis of the phase is desired, or using a part of the stored images, if post-processing is performed.

   The following analysis of the individual images is illustrated in figure 3.16. The center is used as the origin of polar coordinates (r,θ), while the radius of interest defines the area that will be analyzed.

- This circular area is first divided into N angular bins ("pie slices"), where N has to be divisible by 8 so that there will be angle bins corresponding to each of the four $|\mathrm{H}\rangle$, $|\mathrm{D}\rangle$, $|\mathrm{V}\rangle$ and $|\mathrm{A}\rangle$ modes [4]. In our experiments, a typical value of N was 120.

---

[4]The angular coordinate $\theta \in [0, 2\pi[$ is divided into N angle bins, so the angle value of each bin is $\theta_k = 2k\pi/N$, with $k \in [\![0, N-1]\!]$. The angle bin θ_k matching the dark-line angle α_{d} of mode $|\mathrm{D}\rangle$ is equal to $\theta_k = \alpha_{\mathrm{d}} = \pi/4$, which implies $N = 8k$.
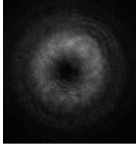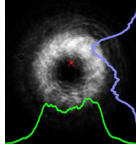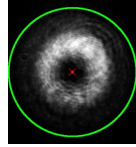
Image without enhancement	Enhanced image & projections	Fitted center

Table 3.4: **Illustration of the steps involved in determining the center of symmetry of the images.** The image displayed in the first column is the average of a few hundred phase-reference pictures. After treating it with the median filtering and midtone stretching operations explained in the text, the second image is obtained. Their difference shows the importance of the image processing; without it, the background would be strong enough to shift the center out of its actual position. In the second image, the projections of the intensity onto x and y axes are shown. They are used to obtain the starting values for the fit: the first-order momenta give an estimated center position (indicated with a red dot), the second-order momenta a starting value for the width of the ring. The last column shows the fit output: the obtained center is depicted in red and the circle with the radius of interest in green.

- For each angular bin k, the average intensity $I(\theta_k)$ is calculated. The first half of this data $(0 - 180°)$ is plotted in figure 3.16c as open red circles. We could now fit a sinusoidal function to $I(\theta_k)$ to determine α_d. However, since we have to process many images and since fits are computationally expensive, we choose the following straight-forward calculation instead.

- Since we are only interested in an axis and not a direction, we "fold" our angle bins: The intensities of each two opposing bins, i.e. lying 180° appart, is added. This leaves us with only $N/2$ bins.

- The dark line should be along the axis of least intensity, but also orthogonal to the axis with most intensity. To account at once for both conditions, we substract from the intensity of each bin the intensity of the (unique) bin at 90° from it. These last two steps also overcome slight image asymmetries and participate in the algorithm robustness against beam misalignment.

- Some fluctuations always remain in the intensity distribution. Therefore, the data is smoothed. The processed intensity $\tilde{I}(\theta_k)$ of bin k is calculated as the average over a 45° wide sector centered around that bin. The data $\tilde{I}$ is shown in figure 3.16c as blue dots.

- The angle of the bin with the smallest $\tilde{I}$ is the angle α_d of the dark axis, giving us the interferometer phase φ via equation 3.19.

Algorithm stability. Since the alignment of the beams from the Left and Right paths is subjected to experimental imperfections, the image analysis routine has been tested against computer-generated images presenting various simulated defects. For this, we numerically
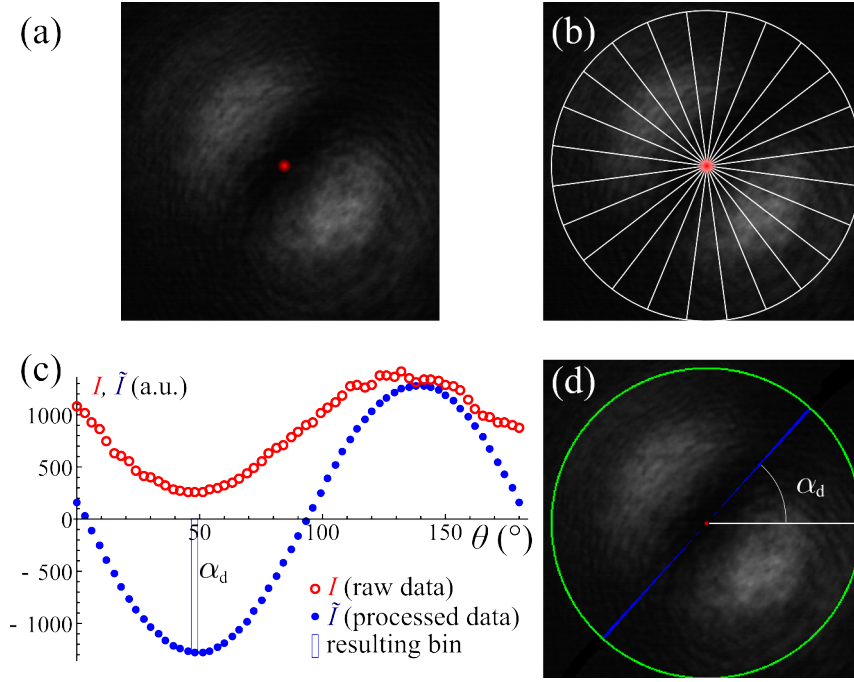
Figure 3.16: **Determination of the dark-line angle α_d.** (a) Around the fitted center (indicated by a red spot), the image is split (b) in equally-weighted angular bins. On this figure, only 24 angular bins are shown for clarity, but $N = 120$ bins are actually used in the real analysis. For each of them, the intensity I is computed. Half of these values (for θ between 0 and 180°) are shown in the plot (c) as red open circles, as a function of the bin angle θ_k. The intensity values are processed as explained in the text to obtain the folded and averaged intensity values $\tilde{I}$. These are plotted as blue dots. In this example, the smallest value of $\tilde{I}$ was found in the 48° angle bin, which is marked by a blue box and corresponds to the angle α_d of the dark axis. In panel (d), the pixels belonging to this angular bin are colored in blue to mark the dark axis, and the area of interest is indicated by the green circle. The original image size was 330×330 pixels.

generated superpositions of Laguerre-Gaussian beams with either positional or angular misalignment. Example of such test images are given in figure 3.17. The test beams have a more pronounced deformation than the experimentally observed phase reference beam. Yet, the image analysis routine gives the correct output for all of them: the phase ϕ that was put in the theoretical expression of the mode superposition.

Timing and noise issues.   The reference light is running backwards through the interferometer setup, but a tiny fraction of it is scattered towards the single-photon detectors at the outputs. To avoid any danger for the detectors and reduce potential noise, we wanted a very low power for the reference beam. The power chosen (~ 2 nW) and the camera exposure time (~ 100 ms) finally resulted from a compromise between the reduction of this noise source and the recording of an image within a time shorter than the typical phase drift.

At this low power level, the detectors' count rate due to the scattered reference light (10^6 Hertz) is already close to saturation. During the actual signal measurements, we
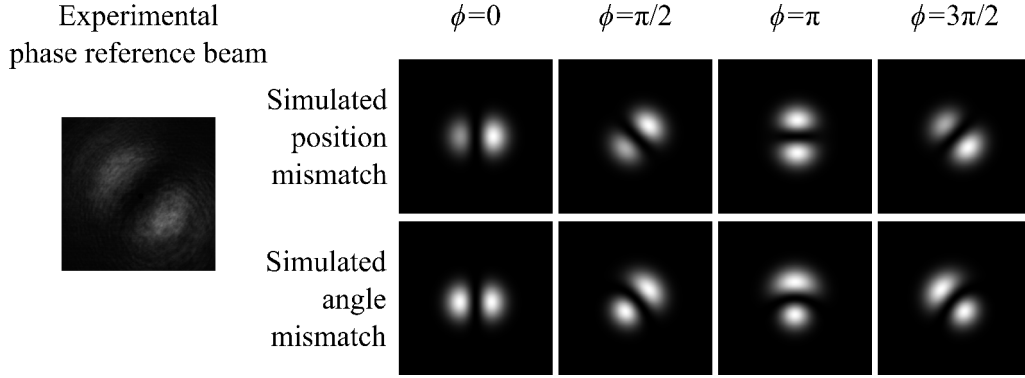
Figure 3.17: **Test of the robustness of the image analysis routine on a sample of test pictures.** On the left of the figure is the experimental reference beam as it is seen on the camera for a certain value of φ. It is in fact the same image as in figure 3.16 for which our image analysis routine found $\varphi = 48°$. On the right of the figure, we show a selection of simulated deformed beams. The beams were computed as the sum of two ideal LG beams (defined by equation (3.2)) with a relative phase ϕ. In the top line, we simulated the effect of a small mismatch in the position of the center of the beams. In the bottom line, we simulated the effect of a small angle between the beams. Both defects yield a deformed HG mode in which one lobe is brighter than the other. This asymetry is also present in the experimental reference beam on the left, but it is less pronounced than in the displayed simulations. When the simulated images were fed to the image analysis routine, the output was the correct ϕ value indicated above the pictures.

therefore interrupt the reference beam using acousto-optic modulators (AOMs). This interruption is short compared to the duration of the experimental cycle, which is in turn much shorter than the exposure time of the reference camera, so this has no influence on the reference image acquisition. In addition, we switched off (gated) the single-photon detectors while the reference light was on.

Even in this configuration, we still noted an influence of the reference light on the background counts within the measurement window: when the reference light was completely blocked, the dark count rate was at about 80 Hz. With the reference light switched on as described above, the dark noise increased to $200 - 250$ Hz within the measurement window. Using mechanical shutters, we excluded light leaking through the AOMs as the reason. The dark count rate of the detector decreased over tens of milliseconds after the reference beam was turned off. Phenomenologically, the decay might be described by a stretched-exponential function [163]. This behaviour has already been observed in other experiments, e.g. [164], and it might be explained by delayed afterpulses of the avalanche photodiodes [165].

Polarization and wavelength of the phase reference beam. We show now that it is highly desirable to use the same polarization and the same wavelength for the reference light as for the signal.

First, the polarization maintaining fibers and the fibered beam splitter, but also dielectric mirrors, are indeed birefringent, so the interferometer phase experienced by the signal and by the reference beam will differ if they have different polarizations. Furthermore, the birefringence changes with the mechanical stress of the fibers as with the temperature

drifts, thus this difference will not stay constant.

Second, if the two optical paths differ geometrically by ΔL, two beams at different wavelengths will accumulate different interferometer phases. The variation of the measured interferometer phase around a certain wavelength $\lambda = c/\nu$ can be easily calculated as:

$$(\mathrm{d}\varphi/\mathrm{d}\nu) \approx 12°/(\mathrm{cm\,GHz}) \times \Delta L \; , \tag{3.20}$$

where ν is the light frequency. So with a path difference ΔL on the order of a few centimeters, a difference by a few hundreds of MHz in the light providing the phase reference beam is already enough to change the inferred value of φ by several tens of degrees.

Finally, dispersion can also play a significant role since a part of the interferometer is fibred. In a single-mode fibre, the change of the effective refractive index is dominated by the dispersion of the material [166]. We can thus estimate the dispersion $\mathrm{d}n/\mathrm{d}\nu$ of our silica fibres to be on the order of $10^{-3}/100\,\mathrm{nm}$ for our fibres [167]. In a perfectly symmetrical situation, the first-order contribution of dispersion vanishes. However, even if the optical path lengths are precisely equal, there might be a difference in their composition in terms of free-space and fibred lengths. Let us call this difference in fibre length ΔL_{fib}. With this, we find:

$$(\mathrm{d}\varphi/\mathrm{d}\nu) \approx -0.1°/(\mathrm{cm\,GHz}) \times \Delta L_{fib} \; . \tag{3.21}$$

This effect will be smaller than the previous one for typical configurations, but can still play a role if signal and reference are separated by several GHz.

If the frequencies of signal and reference are different, but stay constant, these two contributions lead, first, to a constant offset that could be determined, and second, to a different change of the phase when varying the path length. The latter difference is proportional to the relative wavelength difference and can thus in many cases be neglected for close wavelengths. As soon as the frequencies vary however, especially with respect to each other, the correlation between signal and reference interferometer phase will be lost. We therefore avoided these problems by using light from the same source as those used for the signal state to be measured.

In this section, we have presented a detailed description of our OAM detection setup, and discussed the relevant issues relative to the phase reference. The next section gives a detailed calibration procedure, together with the main figures of merit that have been measured thoroughly.

3.3.c   Calibration procedure and benchmarking

The detection setup presented here is very sensitive to the incoming beam position on the hologram dislocation and to its direction. The required fine tuning allows to calibrate and assess the performance of the setup.

Optimizing couplings and limiting cross-talk.   The goal of the alignment procedure is twofold. First, we look for an optimal coupling of the respective LG mode into the fiber of the respective path. Second, we want a good rejection of all the other modes, as demanded by the mode selection requirement. The alignment is performed using classical bright beams aligned with the signal to be analyzed later, their path being defined by the same single-mode fiber. The spatial light modulator described in section 3.2 enables to send various spatial modes into the detection setup.

In a first step, the position of the holograms is set. For this purpose, we use the fact that the intensity distribution in the far field of the hologram depends strongly on the relative position between the incoming beam and the hologram center. This distribution is observed with a camera placed after the hologram. Sending in a $LG^{l=+1}$ mode, we can thus optimize the observed intensity distribution to be close to a TEM_{00} profile in the R path. In the same way, the position of the L path hologram is optimized by sending in a $LG^{l=-1}$ mode. The mode conversion performed when the holograms are well centered is shown in table 3.5. Even a small deviation of the hologram by a few micrometers become clearly visible. Then, the coupling into the fibers is optimized. Using two mirrors behind each of the holograms, we are able to adapt the mode exiting the hologram by maximizing the coupling efficiency up to 80%.
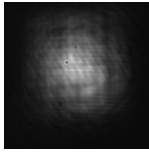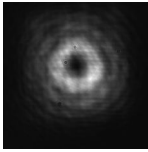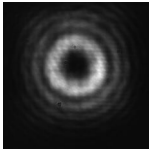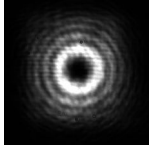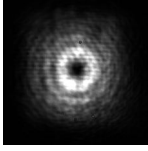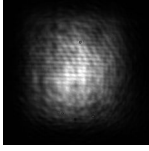
Mode at input	$LG^{l=+1}$	TEM_{00}	$LG^{l=-1}$
R path			
L path			

Table 3.5: **Mode conversion performed by the holograms.** After finely tuning the position of the hologram center, the impinging mode $LG^{l=+1}$ (resp. $LG^{l=-1}$) is converted into a TEM_{00} mode in the far field of the R path (resp. L path), while other modes are converted to higher l-valued modes with doughnut shapes.

The next stage consists in sending a TEM_{00} mode and use the same mirrors to now minimize its coupling. The rejection pattern of the setup is more pronounced than the acceptance and thus allows a better approach to the optimal point. Finally, a random search in the region around the found optimum allows to do some fine tuning. Here, all 6 degrees of freedom (2 transversal positions of the hologram and 4 directions for the 2 mirrors) are slightly varied while switching between the coupled mode and the unwanted modes (such as TEM_{00}). This way, the ratio η_{others}/η_{LG} is minimized (where η_{Λ} is the coupling efficiency of a mode Λ into the single-mode fiber), while the coupling η_{LG} of the matching mode is kept at or close to the maximum.

Each path is then characterized by measuring the coupling for different LG modes sent into the setup. In the R path for example, we record the transmission of the mode corresponding to that path ($LG^{l=+1}$), the two neighbors in the l number ($LG^{l=+2}$ and $LG^{l=0} = TEM_{00}$), and the mode corresponding to the other path ($LG^{l=-1}$). We typically obtain an average rejection of 17 dB for the next neighbors (2% transmission), while the suppression for the opposite mode (with $\Delta l = 2$) is 25 ± 3 dB [5] . An example of detailed coupling figure of merit is given in table 3.6.

---

[5]In fact, one of the hologram had a tiny scratch on its surface, leading to a lower efficiency.

Mode	R path	Lpath
$LG^{l=-2}$	0.1 %	2.8%
$LG^{l=-1}$	0.5 %	**77.8 %**
$LG^{l=0}$	0.1 %	1.7 %
$LG^{l=+1}$	**82.3 %**	0.03%
$LG^{l=+2}$	5.7%	0.04 %

Table 3.6: **Coupling efficiency in both paths for various input Laguerre-Gaussian modes.**

Calibration of φ. An additional characterization is performed by sending classical beams carrying the four Hermite-Gaussian modes HG_V, HG_D, HG_H and HG_A. Theoretically, all four modes should lead to the same power of coupled light into both fibers. However, we observed that the power balance is not strictly mode-independent. Most of this imbalance can be explained by the imperfect mode filtering given in table 3.6. In path R for example, 82 % transmission for mode $LG^{l=+1}$ and 0.5 % for mode $LG^{l=-1}$ make up for a ± 6 % fluctuation in transmission between different HG modes. These mode selective losses decrease the count rate and can additionnaly lead to a reduction of the fringe visibility, leading in turn to a decrease in the maximal measurable fidelity.

Finally, the fiber beam splitter is installed, the phase reference beam is injected as described in 3.3.b and the interferometer phase slowly scanned. Sending again the modes HG_V, HG_D, HG_H and HG_A, we measure the power in outputs X and Y correlate their values to the interferometer phase φ obtained from the reference. The resulting fringes allow to check first for a good fringe visibility (typical values above 93 %) and second for the correct phase relation between signal and reference. Figure 3.18 illustrates this process. As seen before, the power detected at the output X should exhibit a sinusoidal dependence in $\varphi = 2\alpha + \pi$ (equation (3.11)). The condition for minimum power, i.e. $\varphi = \phi + \pi \leftrightarrow 2\alpha = \phi$ resulting from equation 3.17, allows to deduce the value of ϕ from the position of the resulting fringes. We checked that this was indeed the case and found good agreement within $\pm 3°$ which corresponds to our phase discretization.

The setup thus enables to accurately project an input state on various target modes. We will finally discuss the detection efficiency of the setup.

Detection power efficiency. The overall power efficiency of the device comes from the limited transmission of various components:

- **Input-BS and filtering:** $\sim 50\%$. The combination of the 50/50 beam splitter at the input and the subsequent mode selection causes a 50 % fraction of the signal to go "into the wrong path" no matter what the input mode. This fraction is filtered out and lost.

- **Hologram diffraction efficiency and other optics:** $\sim 80\%$.

- **Fiber coupling efficiency:** $\sim 80\%$.

- **Beam splitter for phase reference:** $\sim 25\%$ losses if we take in to account data from both output X and Y. In order to inject the phase reference into the interferometer, an additional fiber beam splitter is inserted between output Y and the single photon detector, causing to lose part of the signal. In principle, if it has a
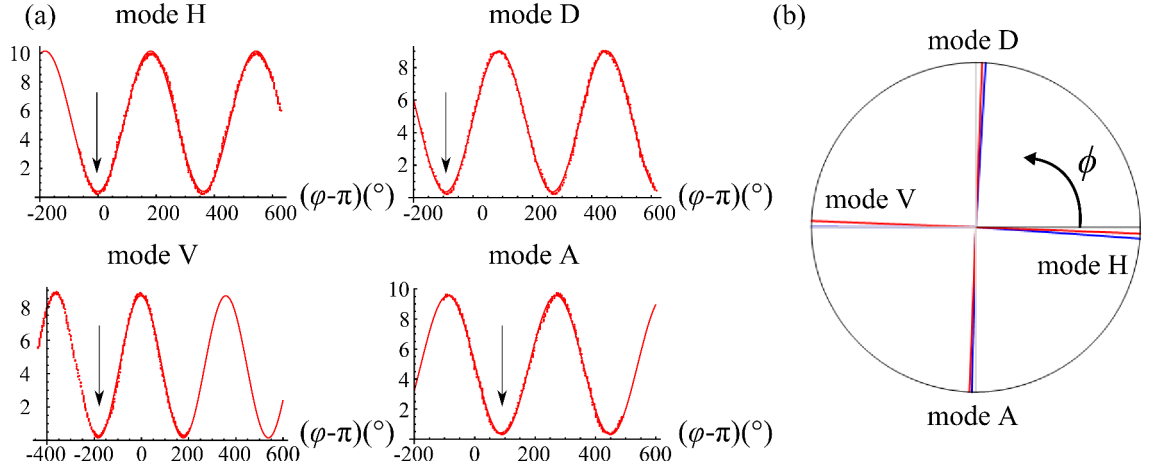
Figure 3.18: **Calibration of the interferometer phase φ.** (a) Fringes measured during the calibration procedure. Different HG beams (with a power on the order of a fraction of milliwatt) were used for this measurement. The vertical axis reprensents the power transmimtted to output X and the horizontal axis represents the interferometer phase $\varphi - \pi$ measured using the phase reference beam and the image analysis routine as explained in the text. As expected, the fringe shifts horizontally in $\pi/2$ steps as the various modes are sent (i.e. when the phase ϕ between the R and L components of the superposition (3.10) is changed). The position of the extrema (indicated by black arrows) indicates where we have: $\phi + \varphi \equiv \pi \pmod{2\pi}$. (b) From this measurement, we locate the four HG modes on the equator of the Bloch sphere (seen from top, so that ϕ increases counterclockwise). The fringe positions (black arrows) measured in (a) are shown as blue lines. The red lines show their average position: is the cross whose arms are the closest possible to the blue lines while enforcing $90°$ between its arms. In this particular example, the fringe visibility reaches $93\pm2\%$, and the inferred ϕ values were respectively $-0.1°$, $86.5°$, $176.1°$ and $268.6°$ for the modes H, D, V and A. The average deviation from the ideal ϕ values is $2.2 \pm 1.6°$.

power transmission factor T, then a fraction T of the signal in the Y path will be lost. Even if the amount of photons in the Y path itself may vary depending on the input state and on the device configuration (or *which fraction of the light inside the interferometer exits at output Y ?*), the average losses induced by the phase reference injection are T/2, in our case 25% with a 50:50 beam splitter [6]. In some situations, for simplicity, we simply do not look at output Y and only take into acount measurements in output X. In this case, the output-BS itself induces 50% losses (and the beam splitter for phase-reference beam injection does not play a role anymore).

From all these parameters, we extract the detection efficiency:

$$
\boxed{\begin{array}{c} 24\% \pm 3\% \\ \text{or } 16\% \text{ if we only consider output X} \end{array}} \tag{3.22}
$$

Note that for HG modes measured in the equatorial plane of the Bloch sphere, this is only the *mean* efficiency. Since we expect a fringe, if we look at output X only, then the detection efficiency will be double at the fringe maximum, and close to zero at the fringe minimum.

Moreover, in our implementation, the power efficiency for the HG modes was slightly lower than for the LG modes. This was due not to the detection setup itself but to the imperfections of the HG mode generation as indicated in 3.2.2. Only 64% of the total beam energy is carried by $LG^{l=+1}$ and $LG^{l=-1}$ modes. The rest of the power is carried by higher order $p > 0$ modes that are not not coupled into our mode projectors. Even if these effective losses depend on the input mode, they do not degrade the quality of the tomography (the visibility of the fringe recorded when φ is scanned and then the fidelity), because the two modes of a given basis experience the same transmission.

Additionnaly, when we will perform measurements in the single-photon regime (as will be described in the next section) the setup transmission given by equation 3.22 has to be multiplied by the quantum efficiency of the single-photon detectors, which was around 45% in our case.

Effects of imperfections on the measured fidelity. The various imperfections can lead to mistaking one mode for another. This effect can be quantitatively estimated as an upper bound on the fidelity that can be obtained when measuring an ideal input state. This in turn gives an estimate of the error we make when we derive the fidelity of an experimental mode to a target mode from measurements with our device.

The fidelity of HG states at the entrance is especially sensitive to a reduced visibility V, setting a limit of $F_{\max} = 1/2(1 + V)$. The reduced visibility can originate from a contamination by background noise, imperfect mode filtering or mode-dependent fiber-coupling. An imbalance of $\pm\Delta$ in the fiber coupling of orthogonal HG modes will decrease the visibility of the fringe by approximately $\Delta^2/2$. A 93% fringe visibility as in figure 3.18 leads to a maximum fidelity of 97% [7]. A visibility extrapolated to 97% if background noise is subtracted allows to reach close to 99% fidelities.

---

[6]Greater splitting ratios, such as 90:10 or even 99:1 would reduce these losses as well as the detection efficiency fluctuations.

[7]For technical reasons, the contamination with reference light is much stronger during the calibration than during the APD measurements.

A shift in the interferometer calibration (figure 3.18) by an angle ϵ will decrease the maximum fidelity by an amount ϵ^2. For ϵ as large as 5°, the fidelity decreases by less than a percent. As can be seen from figure 3.18, this phase shift was quite easily controled to better than 3°.

For LG modes at the entrance, no fringe should be present in the ideal case when scanning φ. Therefore, their fidelity is insensitive to visibility reduction. However, a small relative leakage ϵ of mode L in path R (and vice versa) leads to a spurious fringe with a visibility $2\sqrt{\epsilon}$ and to a decrease of the maximum fidelity to $1 - \epsilon$. With a leakage of less than -25 dB, the resulting error on the fidelity is limited to a fraction of a percent.

> When we proceeded to the quantum memory experiments, this calibration procedure was repeated everyday. Since the memory measurements lasted sometimes up to several hours, we checked that the calibration was stable over these timescales. In particular, for every set of quantum memory measurements, the calibration procedure was first performed before the memory experiment series and then checked after the memory series was completed. Everytime, the calibration had remained unaltered, even after several hours.

The next subsection will give examples of the full tomography of some OAM-encoded qubits using the setup we've just described.

3.3.4   Example of OAM tomography in the single-photon regime

In this subsection, the detection setup is regarded as a black-box, yielding photon counts at the different outputs according to the interferometer configuration as described in table 3.3. For simplicity, the forecoming analysis will be done only with data from Output X unless stated otherwise.

The data presented here is the measurement of the *input pulse* (reference) at a mean photon-number equal to 0.6 photon per pulse. The signal is a weak coherent state with a half-gaussian temporal mode of FWHM 350 ns as described in section 2.3.3. With the setup in the HG bases configuration (i.e. measuring the fringe), three million measurements were made for each of the HG input modes, while one million measurements were performed for the LG input modes, giving respectively about 50000 and 17000 measurement per 6° phase bin. In the configurations for measuring in the LG basis (i.e. with a blocked arm in the interferometer), one million measurements were performed for each of the two basis states, irrespective of the input state.

The measured count rates for input modes $|R\rangle$, $|L\rangle$, $|H\rangle$ and $|D\rangle$ at outputs X and Y are given in appendix A.6. The corresponding Stokes parameters and the fidelity to ideal states are given in table A.5 (using output X data only for simplicity). From these measurements, the density matrix of the input states can be reconstructed using the formulae given in section 3.3.1 (see equation (3.16)):

$$\boxed{\begin{aligned} S_1 &= p_{|\mathbf{0}\rangle} - p_{|\mathbf{1}\rangle} \\ S_2 &= p_{|+\rangle} - p_{|-\rangle} \\ S_3 &= p_{|+\mathrm{i}\rangle} - p_{|-\mathrm{i}\rangle} \end{aligned}} \tag{3.23}$$

where $p_{|\Psi\rangle}$ is the probability to measure the qubit in the state $|\Psi\rangle$. In table 3.7, we give the density matrix parameters resulting from these calculations. In figure 3.19, we give a more graphical view of these data for the two modes $|R\rangle$ and $|V\rangle$ (see legend for details).

Mode	S_1	S_2	S_3	S^2	F
$|R\rangle$	0.99	0.01	-0.09	0.99	99.2 %
$|L\rangle$	-0.97	0.0	-0.14	0.96	98.3 %
$|H\rangle$	0.15	0.95	-0.17	0.95	97.6 %
$|D\rangle$	-0.07	0.11	0.98	0.98	99.0 %
$|V\rangle$	0.15	-0.95	-0.09	0.93	97.4 %
$|A\rangle$	0.32	-0.15	-0.92	0.97	95.8 %

Table 3.7: **Stokes parameters and state fidelities** extracted from the analysis of coherent pulses with a mean photon-number slightly below 0.6. The $S^2 = S_1^2 + S_2^2 + S_3^2$ parameter measures the purity of the state. In this particular example, the recontruction of mode $|A\rangle$ suffers from the coupling imbalance between paths R and L and from our imperfect mode preparation. The fidelity of the other modes is mostly limited by the background noise, which hasn't been subtracted here. The error bar on the fidelities is on the order of 0.5 percentage points. For simplicity, data from Output X only has been used here, but data from Output Y yields identical results.

After computing the density matrix $\hat{\rho}$ of a given state from the count rate measurements described thereabove, we can measure the state resemblance to a target state $|\Psi\rangle$ by computing the fidelity:

$$\boxed{F = \langle\Psi|\hat{\rho}|\Psi\rangle} \tag{3.24}$$

In the data presented here, no noise has been subtracted. We can estimate our **Signal-to-Noise Ratio** (SNR) from the count rate and background noise. First, let us discuss the SNR for the measurements in the HG bases (fringe):

- The measured average signal rate $\bar{n}_{Sig}$ (i.e., the rate at the average height of the fringes) was 0.03 clicks/measurement.

- The background noise originated from the APD dark noise (about 200 Hz as discussed in section 3.3) and the light beams (mainly the control) required for the quantum memory operation as discussed in section 2.3.4. With about 1 kHz, they constitute the major background contribution. Even though the signal pulses have a FWHM of 350 ns, we recorded single-photon detection events over their whole length, which is 800 ns in order to capture their whole timeshape. This gives a background rate of about $\bar{n}_{Bg} = 10^{-3}$ background events per measurement, leading to a SNR on the order of 30 ($\bar{n}_{Bg}/\bar{n}_{Sig} = 3.3\%$).

- While the total number of measurements is in the millions, the number of *events* in a single bin is much smaller, thus a significant Poissonian fluctuation can be expected. The angular bins at different φ values were only roughly equally covered by measurements, showing a standard deviation of up to 35%. The average numbers of detection events per bin were 557 (4.2% statistical errors) for the LG input states and 1400 (2.7% statistical errors) for the HG input states.

If we include the statistical errors in the SNR, the SNR for measurements in the HG bases is thus about 17 in average. For the measurements in the LG basis (where one arm of the interferometer is blocked), the train of thought is the same, but the numbers are slightly different, leading to a SNR of about 14 for this measurement. In summary, we can state a typical SNR value of about 15 for the whole state characterization (HG and LG bases).

In summary, this section has shown the reliability of our setup for OAM qubit tomography. Its performances can be summarized by the following parameters:

- Cross-talk suppression (in LG basis): ~ 25 dB,

- Precision in phase measurement: better than $3°$,

- Detection efficiency: 16% (output X only, not counting the APD quantum efficiency.)

- Stability: calibration remains unchanged over several hours of continous operation.

In the next section, we will use this detection setup to demonstrate the quantum storage of the OAM-encoded qubits defined in section 3.1.2 inside the quantum memory presented in chapter 2.

3.4   A quantum memory for OAM encoded Qubits

Thanks to the experimental tools for LG modes manipulation that have been presented
in the previous sections, we first demonstrated the storage of LG modes at the single-
photon level. Then, we demonstrated the quantum storage of an OAM-encoded qubit.
Importantly, we measured the memory decay time and verified that the storage fidelity
validated the quantumness benchmarks.

3.4.1   EIT optical memory and OAM preservation

In a first experiment [5], we showed that our quantum memory can store weak coherent
pulses with different spatial (LG) modes, and that the OAM of the stored pulses is preserved
in the process. These measurements involved only the mode projectors and did not require
the interferometric phase measurement.

   LG (and HG) coherent pulses at the single-photon level have been stored and retrieved
out of the memory, showing that the OAM quantum number l is conserved. A selection
of memory curves with 0.6 photon per pulse is displayed in figure 3.20 (see caption for
details). The six modes $LG^{l=+1}$, $LG^{l=-1}$, HG_V, HG_D, HG_H and HG_A were stored with
the same efficiency ($\eta = 16\% \pm 2\%$ measured after a 1 µs storage time) as a gaussian
TEM_{00} mode.

3.4.2   memory decay time for stored LG modes

The memory decay time has been studied with LG and HG modes by varying the readout
time. The different spatial modes exhibitied a similar characteristic memory decay time.
The decay of the memory efficiency can be fitted by a gaussian function as predicted in
section 2.2.5 (seefigure 3.21). The characteristic time of this gaussian fit is $\tau_m = 15$ µs,
which corresponds to the motional dephasing estimated in section 2.3.2.

3.4.3   Full characterization of the quantum storage

3.4.a   Full Qubit tomography and quantum storage

The study of the OAM preservation in subsection 3.4.1 is not enough to draw a conclusion
regarding the quantum nature of the memory process. Indeed, a two-way OAM mode
sorter (or even a two-way OAM mode projector) and classical detectors combined with a
light source and a SLM could be enough to reproduce the behavior reported in figure 3.20.
In a quantum cryptography hacking scheme, this would be called an *intercept-and-resend
attack* [168].

   In order to prove that the storage in indeed *coherent*, we must show that not only
the $|R\rangle$ and $|L\rangle$ components of a qubit are preserved (as done in section 3.4.1) but also
that the *phase* ϕ between them is identical before and after the memory. It is to this
end that we developed the interferometric setup that was described extensively in section
3.3.a. Figure 3.22 shows a sketch of the entire experiment, from the signal generation to
the qubit measurement setup with the quantum memory inbetween.

   The preservation of the phase ϕ during the storage process is illustrated in figure 3.23.
It shows how the count rates at the output of the detection setup for HG input qubits are
modulated when φ is varied from 0 to 2π. Such modulation is of course (almost) absent
when the qubit is in a $|R\rangle$ or $|L\rangle$ state as can be seen in figure 3.19. The presence of the
fringe indicates that the state is in a *coherent* superposition of states $|R\rangle$ and $|L\rangle$. The

horizontal position of the fringe gives the value of the phase ϕ between the $|R\rangle$ and $|L\rangle$ components of the qubit. This is just the same as in the calibration process illustrated by figure 3.18, except we are now measuring less-than-single-photon pulses instead of bright beams. The overall count rate decreases by 85% after storage as a consequence of the $\eta = 15\%$ efficiency of the memory. As a consequence, the visibility of the fringes also decreases because the signal-to-noise ratio is reduced by the same factor. Nevertheless, the fringes are still highly visible after storage, proving that the coherence of the $|R\rangle$ and $|L\rangle$ components has been preserved during storage.

In order to make this assertion quantitative, we perform the full qubit tomography, as explained in section 3.3.1. We compute the Stokes parameters and reconstruct the state density matrix. Then, we compare this density matrix to the target density matrix and quantify their resemblance by computing the fidelity. In table 3.8 and in figure 3.24, we illustrate this process for a set of measurements for which the mean photon number per pulse was $\bar{n} = 0.6$ and the memory time $\tau = 1$ μs. Table 3.8 gives the fidelities of the states after they have been stored and recalled from the memory. The mean fidelity without background noise correction is $F_{\text{mean,raw}} = 92.5\%$. It is $F_{\text{mean,cor}} = 98.1\%$ if we subtract the background noise from the count rates.

But even now, the question remains: *was it truly quantum ?* [8] If we were probing our memory with true single-photons, the fidelities presented in table 3.8 would leave no doubt as to the "quantumness" of the memory. But in order to answer the question in a satisfactory manner for qubits implemented with weak coherent states, a more detailed analysis is required as will be presented in the next subsection.

3.4.b Weak-coherent-state qubits and quantum storage

It is known that the best guess that one can do with classical measurements of the quantum state of a two-dimensional single quantum system yields an average fidelity of 2/3. When a classical observer has n identical copies of such a two-dimensional quantum system, the best guess he can make allows him to reconstruct the state with the following fidelity value (see [169] for a derivation):

$$F_{\text{max}}(n) = \frac{n+1}{n+2} \tag{3.25}$$

Consequently, if a classical observer measures a weak coherent state $|\alpha\rangle$ with $\bar{n} = \alpha^2$ photons on average, he can in principle guess the system state with a fidelity bounded by:

$$F_{\text{max}}(\bar{n}) = \frac{1}{1 - e^{-\bar{n}}} \sum_{n \in \mathbb{N}^*} \frac{n+1}{n+2} \frac{e^{-\bar{n}} \bar{n}^n}{n!} \tag{3.26}$$

In this expression the first factor $^1/(1 - e^{-\bar{n}})$ reflects the fact that events where no photon is detected do not contribute to the observer's guess and the sum over all possible photon numbers n is the average of the maximal fidelities $F_{\text{max}}(n)$ weighted by the poissonian photon number distribution.

However, in a quantum cryptography scenario, this is still too optimistic. Indeed, it assumes that the classical observer (which is in fact a *quantum hacker* in this case) will *always* perform a measure-and-resend-attack, which means we are comparing the classical observer to a *unit efficiency* memory. But since our quantum memory has a 15% efficiency,

---

[8]Could not a classical measurement scheme mimic the memory behavior with the same efficiency η and fidelity F ?

a potential quantum hacker must be allowed a similar level of losses if we are to make a fair comparison. The strategy developed by Specht et al. [66] and Gündoğan et al. [93] allows a classical observer to draw the maximal advantage from such a lower-than-unity efficiency. If the quantum hacker knows the average photon number $\bar{n}$ and if he is allowed a (known) loss percentage $1 - \eta$, then he can find a threshold value $N_{\text{thresh}}(\bar{n}, \eta)$ such that he will perform the intercept-and-resend attack if and only if the *actual* number of photons inside the pulse is greated than $N_{\text{thresh}}(\bar{n}, \eta)$, and induce losses otherwise. This way, he takes a maximal advantage of the higher $F_{\text{max}}(n)$ for large n, given a specific allowed loss percentage $1 - \eta$. With this strategy, a purely classical measurement [9] can reach a maximum fidelity given by:

$$F_{\text{max}}(\bar{n}, \eta) = \frac{\frac{N_{\text{thresh}}(\bar{n}, \eta)+1}{N_{\text{thresh}}(\bar{n}, \eta)+2}\, p(\bar{n}, \eta) \;+\; \sum_{n > N_{\text{thresh}}(\bar{n}, \eta)} \frac{n+1}{n+2}\frac{\mathrm{e}^{-\bar{n}}\,\bar{n}^n}{n!}}{p(\bar{n}, \eta) \;+\; \sum_{n > N_{\text{thresh}}(\bar{n}, \eta)} \frac{\mathrm{e}^{-\bar{n}}\,\bar{n}^n}{n!}} \qquad (3.27)$$

where $p(\bar{n}, \eta)$ is the probability to perform a measurement-and-resend attack if the number of photons in precisely $N_{\text{thresh}}(\bar{n}, \eta)$. The numerator of equation (3.27) is the sum of the $F_{\text{max}}(n) = \frac{n+1}{n+2}$ maximal fidelities weighted by the photon number probability distribution if the observer *does* perform a measurement, i.e. if $n \geq N_{\text{thresh}}(\bar{n}, \eta)$. The denominator reflects the fact that the observer induces losses in all other cases. The $p(\bar{n}, \eta)$ and $N_{\text{thresh}}(\bar{n}, \eta)$ functions are computed in the following way. $N_{\text{thresh}}(\bar{n}, \eta)$ is the smallest integer satisfying $1 - \sum_{n=0}^{N_{\text{thresh}}} \frac{\mathrm{e}^{-\bar{n}}\,\bar{n}^n}{n!} \leq (1 - \mathrm{e}^{-\bar{n}})\eta$ and p is equal to $p = (1 - \mathrm{e}^{-\bar{n}})\eta - \sum_{n > N_{\text{thresh}}} \frac{\mathrm{e}^{-\bar{n}}\,\bar{n}^n}{n!}$.

In order to compare the output of our quantum memory to the maximal classically achievable fidelity defined by equation (3.27), we performed quantum memory experiments for a wide range of mean number of photons per pulse $\bar{n}$. The results are plotted in figure 3.25. For almost all the photon numbers we worked with, we beat the classical threshold by several standard deviations, even if the fidelity is computed without background subtraction. At too low $\bar{n}$, the signal-to-noise ratio is too small to achieve a high enough fidelity and at too high $\bar{n}$, the classical limit reaches unity, which can of course not be beaten.

A single data point in figure 3.25 results from the integration of many measurements. In the following lines, we give an idea of all the steps required to such an end.

---

[9]As it is done in quantum security proofs, the procedure described here for maximizing the classically achievable fidelity is *in principle feasible*, in that it is not forbidden by known physical rules, but it is completely out-of-reach of the current technology.

Steps required for a single data point in figure 3.25

- **MOT preparation.** In particular: magnetic field cancelation and EIT optimization.

- **OAM detection setup calibration.** As described in section 3.3.c.

- **Choice of $\bar{n}$ and τ values.**

- **Quantum memory experiments.** Qubits with an average photon number $\bar{n}$ are prepared in all the six $|R\rangle$, $|L\rangle$, $|H\rangle$, $|D\rangle$, $|V\rangle$ and $|A\rangle$ states. Each state is sent to the memory where it is stored for a time τ, before it is read out and detected. Each state is measured both in the LG basis (by blocking alternatively the R and L path of the detection setup) and in the HG bases (by scanning φ). At the lowest photon number, up to 15×10^6 measurements were performed in the equatorial plane of the Bloch sphere for each input state. Critical for this measurement was the stability of the detection setup over long timescales. All the measurements are then repeated with the memory turned off (no MOT) in order to get a reference (i.e. to characterize the input pulse without storage).

- **Data treatment.** The memory parameters $\eta(\tau)$ and $F(\tau)$ are computed for each qubit state and then averaged.

3.5   Conclusion

This chapter has presented the interfacing of non-trivial spatial modes and light angular momentum with the quantum memory presented in chapter 2. Our experimental tools for manipulating such spatial modes have been discussed in detail.

More advanced OAM mode sorting techniques like the one developed by Lavery et al. [158] and Mirhosseini et al. [160], and mode more advanced generation techniques such a the unitary programmable mode converter developed by Morizur [148], could enable to use efficiently a much greater span of the OAM Hilbert space.

- In this chapter, we have proven the **multimode nature** of our cold-atom-based quantum memory by storing and retrieving **multiple spatial modes**.

- We have seen theoretically and experimentally how to implement **quantum bits** using a 2-dimensional subspace of the **orbital angular momentum** Hilbert space, and we have presented a detailed method for characterizing them.

- The quantum memory benchmarking parameters $\eta \sim 15\%$ and $\tau_m \sim 15\ \mu s$ were shown to be the same for all the investigated spatial modes. Based on the size of our ensemble and on the $\sqrt{l}$ scaling of the LG modes, we can conjecture that this figure of merit will remain true for about 100 stored LG modes.

- We have compared the fidelity of the storage process to the maximal classically achievable fidelity and solidly established the *quantum nature* of the storage.

One of the limitations of the current memory implementation is the MOT temperature which limits the memory time τ_m as has already been noted in chapter 2. Even if the MOT temperature is dramatically reduced and if the influence of the magnetic field can be mitigated, the fact that the atoms are freely falling will ultimately limit the memory time to a fraction of a millisecond. Moreover, the free-space implementation can increase the difficulty to collect the photons emitted from the memory. Permanently trapped atoms can allow to beat these limitations.

The next chapter will present our first efforts towards a new light matter interface which answers these issues (at the expense of the spatially multimode property) by trapping cold atoms in the vicinity of a nano-waveguide made of an elongated optical fiber.
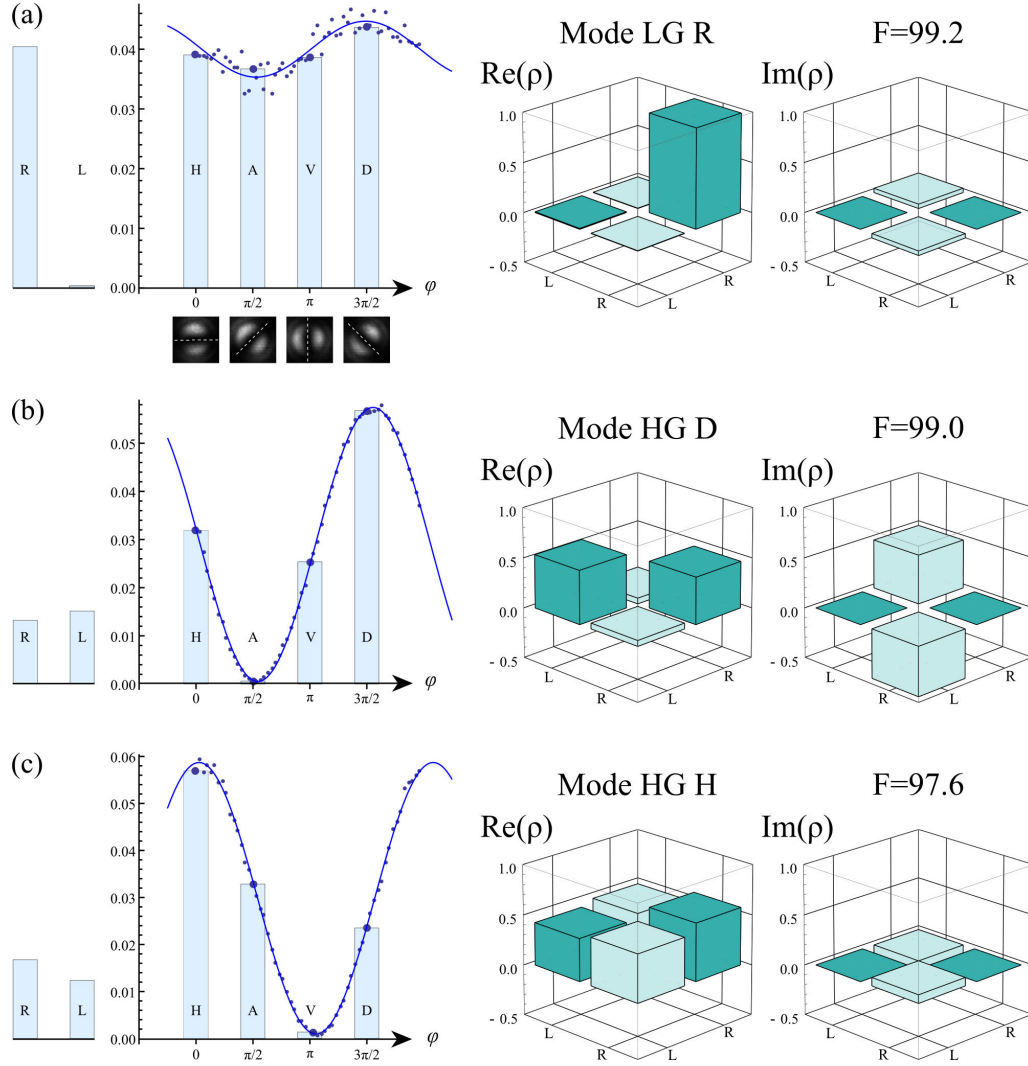
Figure 3.19: **Measurement of different input qubit states** with a mean photon number equal to 0.6. Panels (a), (b) and (c) respectively correspond to the $|R\rangle$, $|D\rangle$ and $|H\rangle$ modes. The bar diagrams show the count rates (average number of detected photons per experimental trial) recorded at output X for various device configurations, corresponding to projections of the qubit over the states $|R\rangle$, $|L\rangle$, $|H\rangle$, $|A\rangle$, $|V\rangle$ and $|D\rangle$. Typical images of the phase reference beam are shown below the axes in (a), corresponding to $\varphi = 0$, $\pi/2$, π and $3\pi/2$. The superimposed fringes (dots : experimental data, solid line : sinusoidal fit) show the variation of the count rates when the interferometer phase φ is scanned. In (a), the spurious modulation of the count rate as a function of φ comes from the small power leakage ϵ of the mode $|R\rangle$ in the Left path, as explained at the end of the last section. In (b) and (c) for the equal-weight superpositions $|D\rangle$ and $|H\rangle$, the count rates in both Laguerre-Gaussian configurations is nealry the same, up to the poissonian error in the photon number statistics, and the visibility recorded when scanning φ is high. It is not exactly unity because no background subtraction has been performed. The reconstructed density matrices are given next to the figure as well as the fidelity with the ideal target state. The error bar on the fidelities is on the order of 0.5 percentage points.
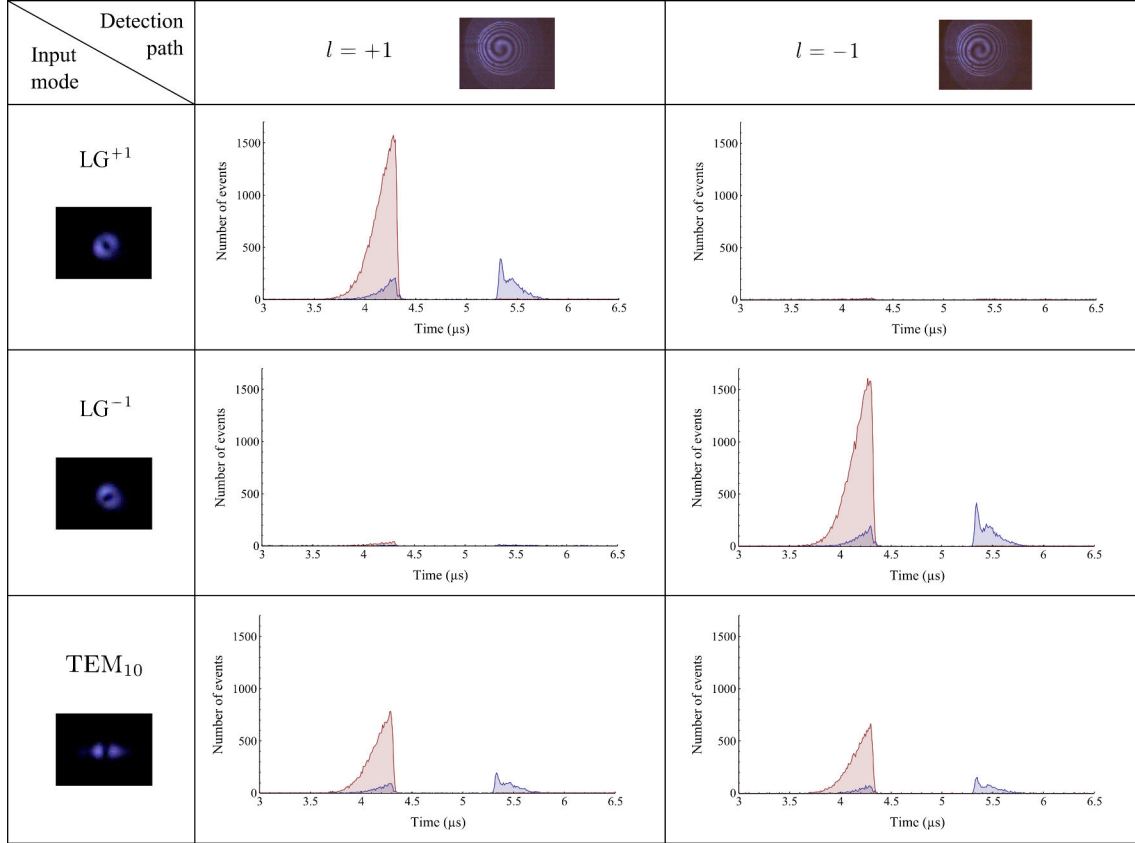
Figure 3.20: **Preservation of the OAM number l during storage and retrieval** of $LG^{l=+1}$, $LG^{l=-1}$, and HG_{10} modes at the single-photon level. The number of counts is represented as a function of time. Pink lines represent the incoming signal pulses recorded without memory operation and blue lines correspond to memory output. The early detection events show the leakage of the signal, while the later ones correspond to the readout of the memory (memory time: 1 µs). Each curve results from 5.10^5 repetitions of the experiment. The low level of cross-talk in the pink curves (input state measurements) shows that the detection setup disciminates well between $LG^{l=+1}$ and $LG^{l=-1}$ modes. Note that the residual leakage of the $LG^{l=-1}$ mode in the R path is more important than the leakage of the $LG^{l=+1}$ mode in the L path, which is coherent with the values given in table 3.6. The low level of cross-talk in the blue curves (memory readout state measurements) shows that the memory preserves the l-number of the stored photons.
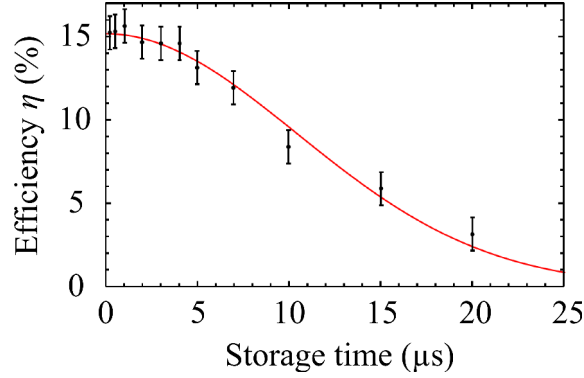
Figure 3.21: **Measurement of the time decay of the memory efficiency.** The experimental points show the memory efficiency $\eta(\tau)$ (vertical axis) as a function of the storage time τ (horizontal axis). Following the model given in section 2.2.5, a gaussian shape is fitted to the data, providing a characeristic decay time of 15 µs. The data presented in this figure results from the storage of $\mathrm{LG}^{l=-1}$ pulses with mean photon number 0.6. The memory parameters are identical to the ones given at the end of chapter 2: a control beam power on the order of $\Omega_c \sim 1.3 \times \Gamma$, leading to a group velocity $\sim 3 \times 10^{-5}c$ and a pulse compression to a length of 3 mm. The measured 15 µs memory decay time corresponds to a thermal-dephasing-limited memory whose characteristic time is given by $\lambda/(2\pi \sin(\alpha)\sqrt{2k_B T/m})$, with $T \sim 1$ mK and $\alpha \sim 1.8°$.
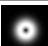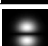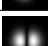
Input mode		Raw fidelity	Corrected fidelity
$|R\rangle$		$95.1 \pm 0.5\%$	$99.3 \pm 0.5\%$
$|L\rangle$		$90.0 \pm 0.8\%$	$97.7 \pm 0.6\%$
$|V\rangle$		$90.3 \pm 1.1\%$	$98.8 \pm 0.5\%$
$|D\rangle$		$94.0 \pm 0.9\%$	$98.7 \pm 0.5\%$
$|H\rangle$		$94.7 \pm 0.9\%$	$98.1 \pm 0.5\%$
$|A\rangle$		$90.6 \pm 1.1\%$	$96.2 \pm 0.8\%$

Table 3.8: **State fidelities.** Fidelities of the readout states for six input qubits without and with background noise subtraction. The mean photon number per pulse is $\bar{n} = 0.6$. Errors were estimated assuming Poissonian statistics and taking into account the phase binning and residual error on the calibration of the interferometer. The mean fidelity is $F_{\mathrm{mean,raw}} = 92.5\%$ without background correction and $F_{\mathrm{mean,cor}} = 98.1\%$ with background subtraction. These after-storage fidelities may be compared to the before-storage fidelities reported in table 3.7 for the same set of experimental parameters and at the same photon number: since the corrected fidelity is almost the same as before (up to a 0.5% uncertainty), the lower F values can be attributed to a lower SNR caused only by the decrease in the count rate for an identical background noise.
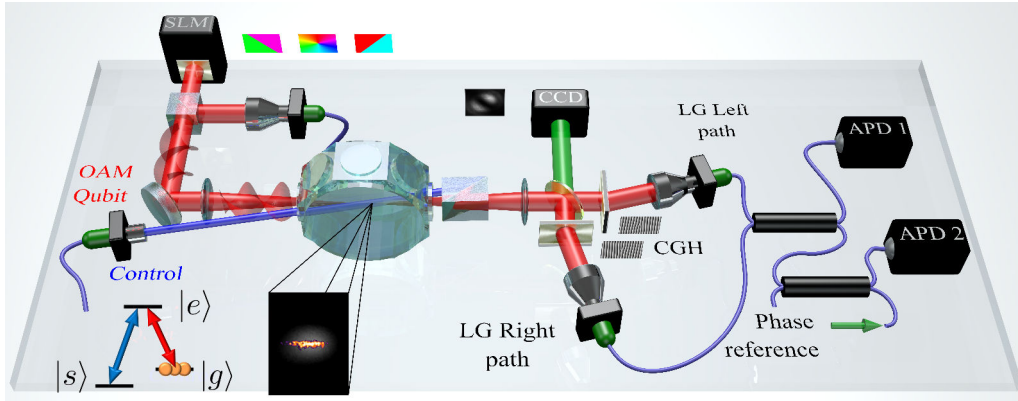
Figure 3.22: **Experimental setup for quantum storage and analysis of OAM qubits.** An orbital angular momentum photonic qubit encoded with a spatial light modulator (SLM) is coherently mapped into a large atomic ensemble of cold cesium atoms and retrieved on demand at a later time. The control and OAM qubit beams have linear orthogonal polarizations, copropagate with an angle of 1.8° and are separated after the memory interface by a Glan-Taylor polarizing beam splitter. To fully reconstruct the density matrix of the retrieved qubits, the photons enter into a two-path interferometer, where each path includes a mode projector based on a blazed-fork computer-generated hologram (CGH) and a single-mode fiber. The two paths are arranged in a way to project the photons respectively into the $|L\rangle$ (LG Left path) and $|R\rangle$ (LG Right path) qubits states. Events are detected at the output of a fiber beam splitter by single-photon counting modules (APD 1 and APD 2). The relative phase φ between the two paths is scanned and experimentally determined by sending a phase-reference beam backward and analyzing its spatial structure at the input of the interferometer via a CCD camera. The zoom in inset shows a false color image of the atomic ensemble.
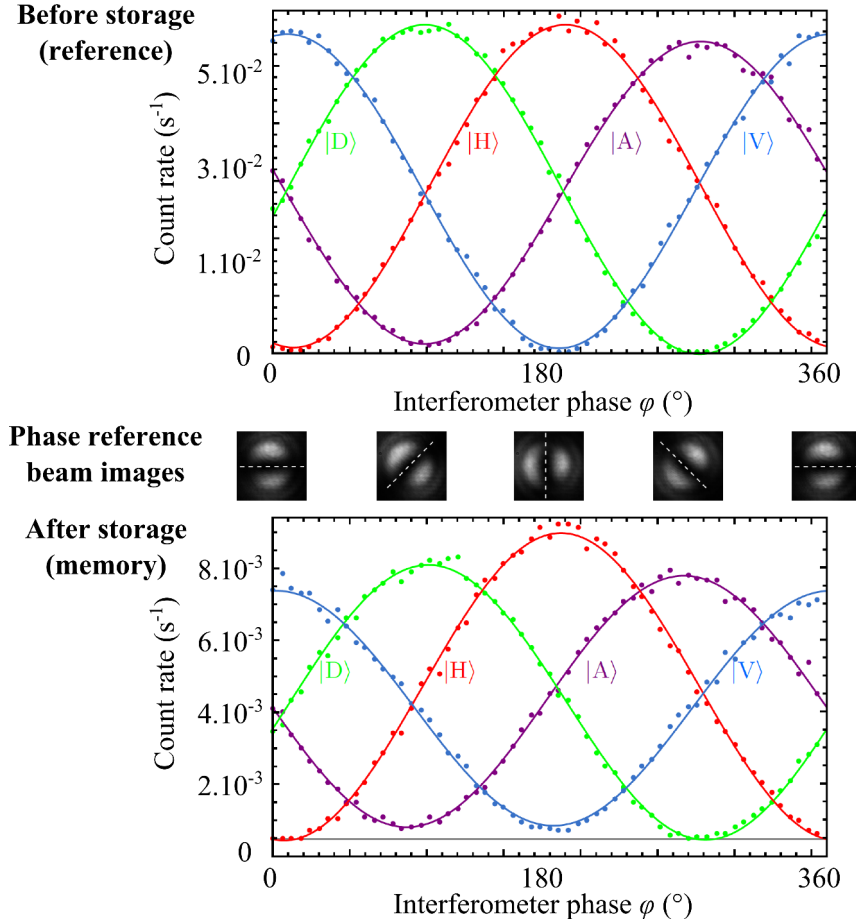
Figure 3.23: **Fringes before (top) and after (bottom) quantum storage.** Qubits in four different HG states ($|H\rangle$, $|D\rangle$, $|H\rangle$ and $|A\rangle$) are sent into and recalled from the memory with a 15% efficiency after a 1 µs storage. The interferometer phase φ is scanned slowly and measured while the experiment is performed. Plotting the count rates at the output of the detection setup as a function of φ reveals a series of fringes, proving that the measured state is a *coherent* superposition of $|R\rangle$ and $|L\rangle$ states. Although the visibility of the fringes slightly decreases after the memory readout as a result of the signal-to-noise ratio being reduced by the memory efficiency, the coherent nature of the superposition states recalled from the memory is clearly visible. This is particularly true if we compare the bottom of the fringes to the (independently measured) background noise level indicated by the gray line. The solid lines are sinusoidal fits to the data. Output X only is displayed in the figure for clarity. Output Y gives similar but with opposite phases. Images in the middle show a few of the phase reference pictures that were taken in order to measure φ.

$\mathrm{Re}(\rho)$ $\qquad$ $\mathrm{Im}(\rho)$
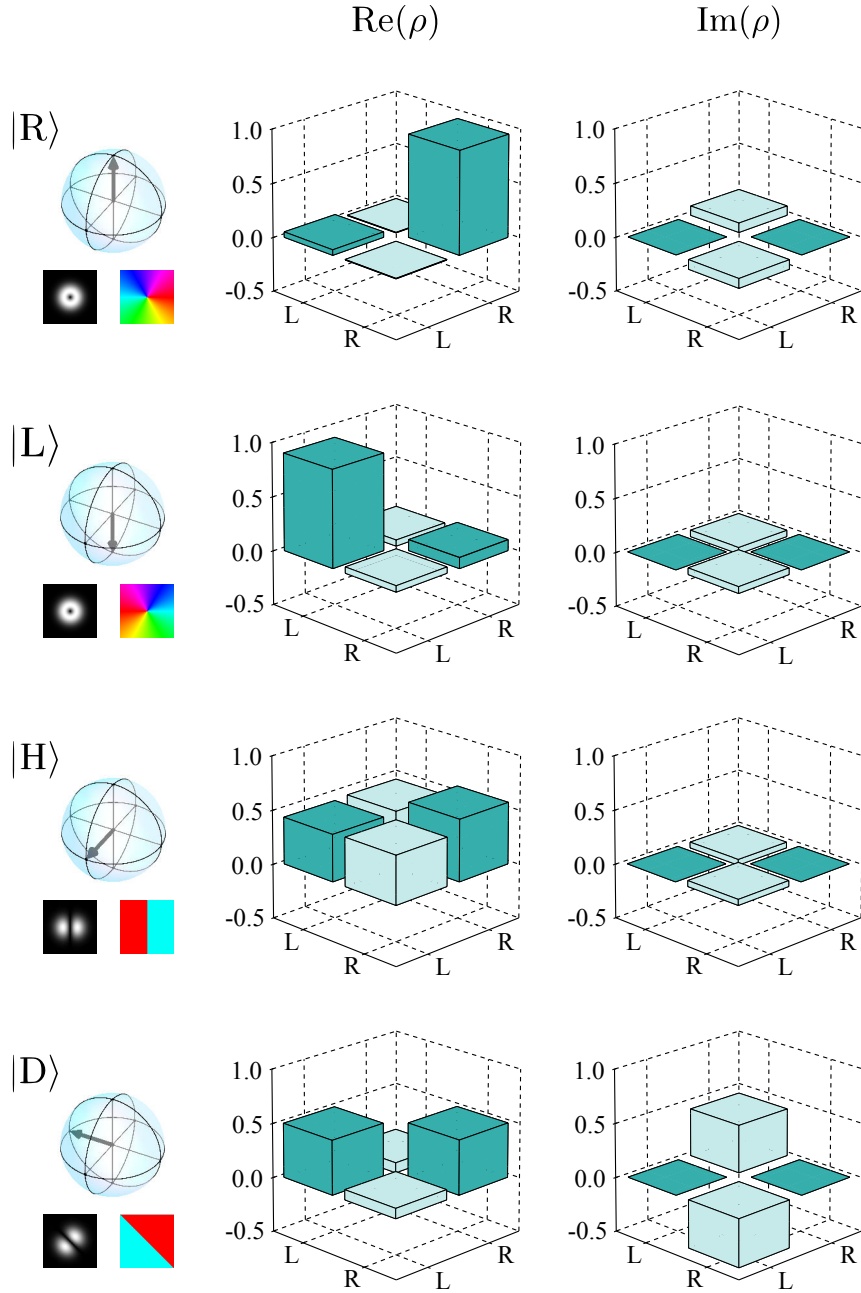
Figure 3.24: **Quantum tomography of OAM qubits after memory readout.** Reconstructed density matrices for the four input states $|\mathrm{R}\rangle$, $|\mathrm{L}\rangle$, $|\mathrm{H}\rangle = (|\mathrm{R}\rangle + |\mathrm{L}\rangle)/\sqrt{2}$ and $|\mathrm{D}\rangle = (|\mathrm{R}\rangle + \mathrm{i}|\mathrm{L}\rangle)/\sqrt{2}$. The mean number of photons per pulse is here $\bar{n} = 0.6$, and the storage time is 1 µs. No background correction has been applied. The first column displays the location of the state on the Bloch sphere, the phase pattern imprinted by the SLM and the associated spatial mode's (theoretical) intensity pattern. The associated state fidelities are given in table 3.8: respectively 95.1%, 90.0%, 94.7% and 94.0%.
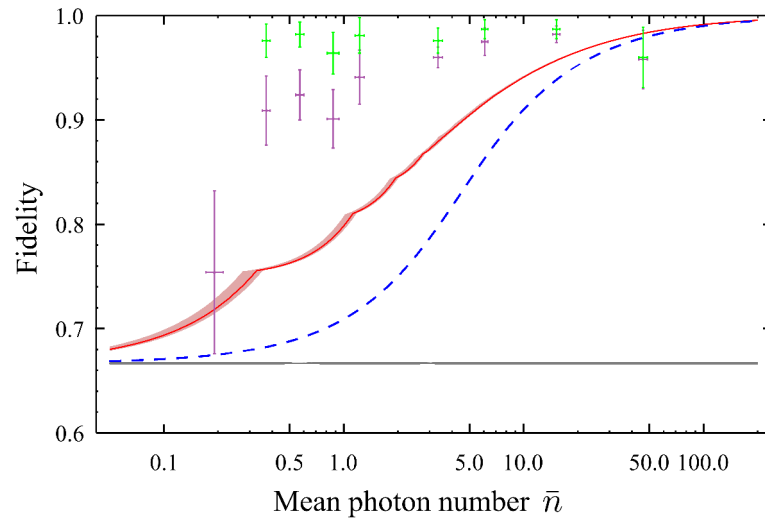
Figure 3.25: **Average fidelities of the retrieved qubits after quantum storage.** The state fidelity after storage, averaged over the six input qubits, is given as a function of the mean photon-number per pulse $\bar{n}$. The purple points correspond to the raw data while the green ones are corrected from background noise. The blue dotted line gives the classical limit for a memory with unity storage and readout efficiency (equation (3.26)) and the red line shows the classical limit for the actual efficiency of our memory device (equation (3.27)). The pink shaded area represents the uncertainty on the efficiency. Vertical and horizontal error bars indicate respectively standard deviation on the fidelity measurements and on the mean photon number.

Chapter 4

Towards a nanofiber-based light-matter interface

Contents

Introduction

In the two previous chapters, we have presented the implementation and the characterization of a free-space cold-atom-based optical quantum memory. The last chapter was in particular devoted to demonstrating the intrinsic spatial multimode nature of the memory and using this feature to store and recall OAM-encoded quantum bits. However, this system suffers from several imperfections, such as the temperature not being low enough, the optical depth too limited, and the fact that the atoms will eventually fall because the magneto-optical trap must be turned off during the memory operation. Moreover in free-space light-matter interfaces, the collection of photons emitted from the memory may be an additionnal trouble, especially in delayed single-photon generation experiments such as the DLCZ protocol.

These issues could potentially be more efficiently handled in a recently-proposed design in which neutral atoms are loaded in a dipole trap in the vicinity of a *nanofiber*. A nanofiber is an optical fiber which has been tapered down to a subwavelength diameter. If the angle of the taper region is small enough, then the transition is adiabatic [170] and the fiber can still guide the light even at very low diameters, but a significant fraction of the guided power travels in the form of an evanescent field around the nanofiber. The evanescent field in such systems has been used in various research applications, such as evanescent coupling to and photon collection from microdevices [171]. Since the light in the evanescent field is very tightly confined, its corresponding electric field is huge. Atoms located in its vicinity will interact strongly with it, which means light-matter interfaces with high optical depth can be realized. The evanescent field can also be used to hold the atoms for a long time around the nanofiber by means of a suitably designed dipole trap. Following the initial proposal by Balykin et al. [172] in 2004, two research teams, led by Arno Rauschenbeutel in Mainz and Jeff Kimble in Caltech, started to develop such systems with the goal of studying one-dimensional many-body physics or light-matter interaction at the quantum level in cavity QED context. Motivated by the promises of such systems to realize high-efficiency light-matter quantum interfaces, which has not been demonstrated heretofore, our group started to investigate them around 2012.
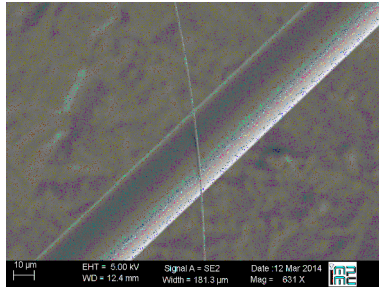
Figure 4.1: **SEM image of a nanofiber.** On this picture, a nanofiber of diameter ~ 400 nm lies on top of another fiber of larger diameter. Scanning electron microscopy allowed to characterize the nanofibers by measureing their diameter at various positions. Credits: UPMC.

In this chapter, we will describe the first steps we took towards this new plateform for light-matter interfacing.

4.1 Nanofibers as a light-matter interface

It is a very remarkable feature that a waveguide can be made of a refractive structure with dimensions smaller than the light wavelength. Yet, the field of nanofiber fabrication and applications has been booming over the last decade (see for example [173] or [174] for topical reviews). In this section, we introduce the concept of a nanofiber and describe how the propagation of light in such structures can be utilized to create an efficient light-matter interface based on dipole trapping and evanescent coupling.

4.1.1 Light propagation in a nanofiber-based waveguide

This subsection describes the way light can be guided in nano-waveguides, i.e. waveguides whose transverse dimensions (defined by the radius ρ) are smaller than the wavelength of the guided light λ.

The description of light propagation is similar to that in standard step-index optical fibers (figure 4.2). The standard theory of conventional optical waveguides is exposed in details in [175]. The fiber is modeled as a medium with a core index n_{Co} and a cladding index n_{Cl}. Thus, the index profile of the waveguide is defined stepwise by: $n(r) = n_{\mathrm{Co}}$ if $r < \rho$ and $n(r) = n_{\mathrm{Cl}}$ if $r > \rho$. In conventional fibers, both indices are very close to the mean silica index. In a nanofiber, the cladding is replaced by the vacuum, so that $n_{\mathrm{Cl}} = 1$ and $n_{\mathrm{Co}} \sim 1.5$.
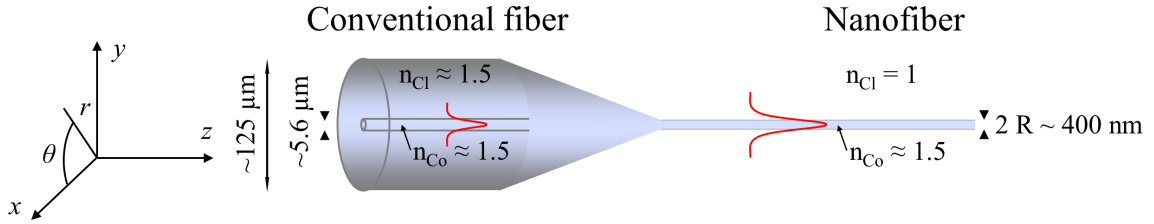
Figure 4.2: **Sketch of a conventional fiber and a nanofiber** with a transition region inbetween. On the left, conventional fibers (for light at $\lambda = 852$ nm) are made of a ~ 5.6 μm diameter core surrounded by a 125 μm diameter cladding, both made out of silica. A very small difference in their refraction indices n_{Co} and n_{Cl} is enough to confine the light in the core. The red bell-shaped curve shows how the guided light remains inside the core with an moderate evanescent field extending through the cladding. On the right, the fiber has been tapered into a nanofiber with a subwavelength diameter of $2R \sim 400$ nm. The silica from the cladding fills the equivalent of the core, while vacuum provides the equivalent of the cladding. Light is still guided in such a system, but due to the smaller core diameter, a much larger proportion of the light energy now travels inside the evanescent part of the field.

The electric field of a guided mode propagating towards increasing z values is expressed as:

$$\vec{E}(r, \theta, z, t) = \vec{e}(r, \theta) e^{i(\omega t - \beta z)} \tag{4.1}$$

where the propagation constant β plays an analogous role to the wavevector k in vacuum and must satisfy: $k n_{\mathrm{Cl}} < \beta < k n_{\mathrm{Co}}$. Solving Maxwell's equation in cylindrical coordinates, the amplitude $\vec{e}$ can be separated in a radial part, which is given by combinations of Bessel functions, and an azimuthal part which is a periodic function of θ. A major difference with free-space modes such as the ones we manipulated in the previous chapter, is that the guided modes have a non-vanishing component along the z direction, i.e. a longitudinal component. This characteristic feature of beyond-paraxial-approximation beams has been utilized very recently to engineer spin-orbit coupling in photons and directional light emission [176, 177]. Using an adimensional radial parameter R, this longitudinal component is given by:

$$
\begin{aligned}
e_z &= \frac{J_\nu(UR)}{J_\nu(U)} f_\nu(\theta) && \text{for } 0 < R < 1 \\
e_z &= \frac{K_\nu(WR)}{K_\nu(W)} f_\nu(\theta) && \text{for } R > 1
\end{aligned} \tag{4.2}
$$

where $f_\nu(\theta)$ can be either $\cos(\nu\theta)$ (so-called *even modes*) or $\sin(\nu\theta)$ (*odd modes*), and where J_ν and K_ν are respectively Bessel functions of the first kind and modified Bessel functions of the second kind. The parameters U and W give the (inverse of the) characteristic length in the transverse direction, and are given by:

$$R = \frac{r}{\rho} \qquad\qquad \text{dimensionless radius}$$
$$V = k\rho\sqrt{n_{\text{Co}}^2 - n_{\text{Cl}}^2}$$
$$U = \rho\sqrt{(kn_{\text{Co}})^2 - \beta^2} \qquad \text{inverse of the characteristic length in the core}$$
$$W = \rho\sqrt{\beta^2 - (kn_{\text{Cl}})^2} \qquad \text{inverse of the characteristic length in the cladding}$$

(4.3)

Depending on the value of $\nu \in \mathbb{N}$ in equation (4.2), three different kinds of modes can be defined:

- For $\nu = 0$ and if f_ν is a sine function, then the z component of the electric field vanishes. These modes are called **transverse electric** modes or TE$_{0m}$ modes.

- For $\nu = 0$ and if f_ν is a cosine function, then the z component of the magnetic field vanishes. They are the **transverse magnetic** TM$_{0m}$ modes.

- For $\nu > 1$, we have the so-called HE$_{\nu m}$ and EH$_{\nu m}$ **hybrid modes**.

The index 0 or $\nu \in \mathbb{N}^*$ is related to the azimuthal dependence of the mode and the index $m \in \mathbb{N}^*$ is related to the value of β. Indeed, β cannot be arbitrary: it is given by the continuity equation for the θ component of the electric field. Depending on the value of the V parameter, it may have several solutions, or a single one. In the case of a single-mode fiber, which corresponds roughly to $V < 2.405$, there is only one possible β value, which corresponds to the HE$_{11}$ mode.

Interestingly, all the light energy does not propagate inside the core. The decay of the electric field out of the cladding follows an exponential profile that can be approximated by:

$$K_\nu(WR) \sim \sqrt{\frac{\pi}{2WR}}\mathrm{e}^{-WR} \qquad \text{as } R \to +\infty \tag{4.4}$$

So if the nanofiber radius ρ is small enough, a significant proportion of the beam energy can be located *around* the nanofiber in the form of an evanescent field.

It is this evanescent field that holds much promise for light-matter interfacing. Indeed, light is tightly confined over large distances, yet a large part of its energy is located in vacuum where it can be interfaced with neutral atoms. A very interesting proposal consists in taking advantage of the different decay lengths $1/W$ of the different wavelengths to create a two-color dipole trap that can hold atoms in the vicinity of the nanofiber for long times while they remain adressable by another beam propagating inside the fiber.The principle of the two-color dipole trap, first proposed by Balykin et al. [172] is briefly explained in the next section.

4.1.2   A two-color dipole trap in the evanescent field of the nanofiber

The variation of the decay length $1/W$ with the wavelength cannot be seen directly from equation (4.3) because the propagation parameter β itself is a non-trivial function of λ.

Moreover, β is given by a transcendental equation and has thus no simple analytical form. From numerically solving the equation for $1/W$, one finds that it has the type of dependence one would normally expect in such a case: shorter wavelengths decay more rapidly than longer ones.

This allows for a very beautiful two-color trapping scheme first proposed by Balykin et al. [172]. A red-detuned laser propagating inside the nanofiber creates a long-range attractive dipole potential. To avoid atoms getting adsorbed on the surface, a phenomenon which can be modeled by the inclusion of a Van der Waals potential (following an attractive short-range inverse-power law), a blue-detuned laser is added to the first one. Since the "Blue" laser evanescent field decays more rapidly than the "Red" one, one can find a combination of laser intensities that creates a repulsive potential barrier followed by an attractive potential well. Cold atoms can thus be trapped in the vicinity of the nanofiber by the Red laser, while adsorbing on the surface is prevented by the Blue one. Figure 4.3 shows a qualitative plot of the possible dipole potential.

Such an architecture offers a radial confinement of the atoms, and possibly an azimuthal confinement if the polarizations of the red- and blue-detuned lasers are well chosen (linear orthogonal). By employing two red-detuned beams, a standing wave is created in the nanofiber, resulting in a periodic trapping potential along the z direction with individual trapping sites separated by half a red wavelength.
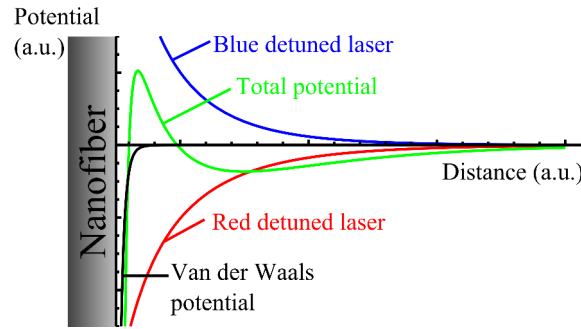
Figure 4.3: **Qualitative plot of the potential for a two-color dipole trap** such as proposed by Balykin et al. [172]. The red and blue curves give the dipole potential (square of the electric field) of the red- (attractive) and blue- (repulsive) detuned lasers. The black curve is a model of the Van Der Waals forces responsible for surface adsorption and the total potential is shown in green.

Such trapping architectures have been realized recently in several research groups for various purposes [178–180]. One early realization in such systems was that the dipole potential led to inhomogeneous light shifts as briefly introduced in section 2.2.5. In particular, Le Kien et al. [181] realized that in general, the inhomogeneous light shifts caused by the different trapping lasers will cause different magnetic sublevels $|m_F\rangle$ to be inhomogeneously shifted, as if under the influence of an external magnetic field gradient. For quantum information applications such as EIT quantum memories introduced in chapter 2, such inhomogeneous broadening mechanisms should be avoided. Schneeweiss et al. [182] partially solved the issue by introducing a well-controlled external magnetic field in their experimental setup.

Another solution, proposed by Le Kien et al. [183], is to make use of so-called *"magic wavelengths"* for the red- and blue-detuned trapping beams, i.e. wavelengths for which the light shifts exactly cancel. Not all neutral atoms can be trapped with magic wavelengths,

but the case of ^{133}Cs is a favorable one. This approach was endeavored by Kimble's group as reported in [179, 184]. The tabulated magic wavelengths are [183]:

$$
\boxed{\begin{aligned}
\lambda_{\mathrm{Blue}} &\sim 685 \text{ nm} \\
\lambda_{\mathrm{Red}} &\sim 935 \text{ nm}
\end{aligned}}
\tag{4.5}
$$

Due to its simplicity of principle, we decided to follow the magic-wavelength approach to realize our own *state insensitive* dipole trap.

In addition, Lacroûte et al. [179] proposed to use parallel (instead of orthogonal) linear polarizations for the red- and blue-detuned lasers, arguing that this would lower the requirements on the laser power for a given trapping potential depth. This however, would lead to an increased light shift that is not compensated for by the magic wavelengths. To overcome this additionnal shift, they propose to use yet another blue-detuned laser, propagating in the opposite direction to the first blue-detuned laser. In order to avoid forming a standing wave, slightly different frequencies (i.e. with Δf in the tens of gigahertz range) should be used for the two blue-detuned lasers.
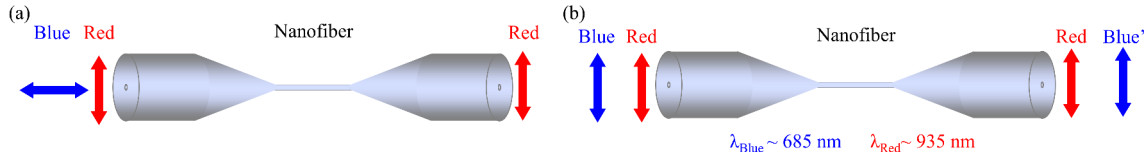
Figure 4.4: **Possible trapping schemes.** (a) Trapping scheme by Le Kien et al. [181] uses two Red lasers to create a standing wave and an orthogonally polarized Blue laser. Wavelengths are arbitrary but a carefully controlled magnetic field is required to compensate for differential light shifts. (b) Trapping scheme by Lacroûte et al. [179] uses two identical-frequency Red lasers and two identically polarized, slightly detuned Blue lasers. The usage of magic wavelengths guarantees a state-independant potential exempt of inhomogeneous differential light shifts. The goal of our group is to implement scheme (b) for quantum memory applications.

This results in a total of four dipole trapping beams, all having the same linear polarization. Two counter-propagating identical-frequency red-detuned lasers at $\lambda \sim 935$ nm create an attractive standing-wave potential and two counter-propagating blue-detuned lasers at $\lambda \sim 685$ nm separated in frequency by a few tens of gigahertz produce a repulsive shell around the nanofiber that prevents the atoms from adsorbing on the nanofiber and compensate for light shifts. The required power is estimated to be about 2×0.95 mW for the red-detuned laser and about 2×16 mW for the blue-detuned one [179] (from here on labeled "Red" and "Blue"). Figure 4.4 shows the proposed laser configuration inside the nanofiber.

The next sections will describe our experimental progress towards the realization of such a nanofiber-based light-matter interface.

4.2   Setting up the experiment

4.2.1   Nanofiber fabrication

The first step towards the contruction of a nanofiber-based light-matter interface was to develop our own nanofiber fabrication stage. We used the so-called flame pulling technique

(which was reviewed recently by Ward et al. [185] and independantly by Hoffman et al. [186]), which consists in tapering a standard optical fiber by holding it on top of a flame (so as to bring it a little below silica metling temperature or $\sim 1100\,°C$) and pulling on it on both sides. The elongation of the fiber due to the pulling and the matter conservation lead to the production of a taper region of constant diameter (the length of which is determined by the length of fiber which is exposed to the flame) connected to the untapered parts of the fiber by exponentially narrowing profiles. The transmission is monitored in real time and gives valuable information on where to stop the pulling process. Indeed, as the fiber gets thinner and thinner with the pulling process, it comes to a point where it does not satisfy the monomode condition anymore and multiple modes become populated. The interference of the different modes as the propagation length is continuously changed gives rise to a beating of characteristic frequency. At some point, the nanofiber region reaches a new singlemode condition. The disappearance of the beating notes in the transmitted power is thus a signature that the tapered region satisfies the singlemode condition once again. If the angle of the tapered region is small enough [170], then the fundamental HE_{11} mode of the untapered region couples with high efficiency to the fundamental HE_{11} mode of the subwavelength-diameter region. A very critical parameter for this process to be successful is the absolute property of the fiber being elongated and of the whole pulling unit. Indeed, a single speck of dust is enough to make the fiber burn if it comes in contact with the evanescent field in the tapered region.

Baptiste Gouraud was in charge of this project, which resulted in the reliable production of optical nanofibers with $> 95\%$ transmissions. SEM images recorded at UPMC, such as shown in figure 4.1, confirmed that taper diameters on the order of 400 nm and taper lengths of several millimeters were reached. All these results will be presented in much greater details in Baptiste's PhD dissertation.

The rest of this section describes the laser and vacuum setup developed for cold-atom trapping.

4.2.2 Preparing the free-space MOT

The first step was to prepare a free-space MOT similar to the one that was presented in section 2.3. It is intended to provide the cold-atom source required to load the future dipole trap.

The design was basically the same with a few upgrades allowing for a greater ease-of-use and reproducibility. The atomic levels and corresponding laser frequencies used for the MOT generation are identical to the ones that were presented in figure 2.6. Here follows a list of the main changes in the laser and vacuum system design.

We resorted to **commercial versions** of the interference-filter-based extended cavity **diode lasers** developed at the SYRTE [136] [1]. As in the previous implementation, they are stabilized by saturated absorption spectroscopy. For a greater stability and reliability of the MOT laser system, we are currently looking to replace the analogue lock-in-amplifiers for the laser frequency stabilization by **digital locking loops** with auto-relock function. Olivier Morin, Anna Lejeannic and Kun Huang have made signigicant progress towards such an end.

A noteworthy change in the optical layout of the lasers was the systematic inclusion of ***double-pass*** **acousto-optic modulators** (AOM) for the laser timing, and the inclusion

---

[1] Commercialized by Radian Dyes and Laserlabs.

of a **more versatile control electronics**. Double-passing instead of single-passing the AOM necessarily decreases the overall diffraction efficiency [2], but is also allows to shift the laser frequency without the need to re-align the setup. These changes should permit to have a **direct computer control of the laser detunings**. Also in constast with the previous design, the MOT beam collimators and retro-reflectors have been fixed directly on the vacuum chamber in order to optimize space and reduce mechanical vibrations.
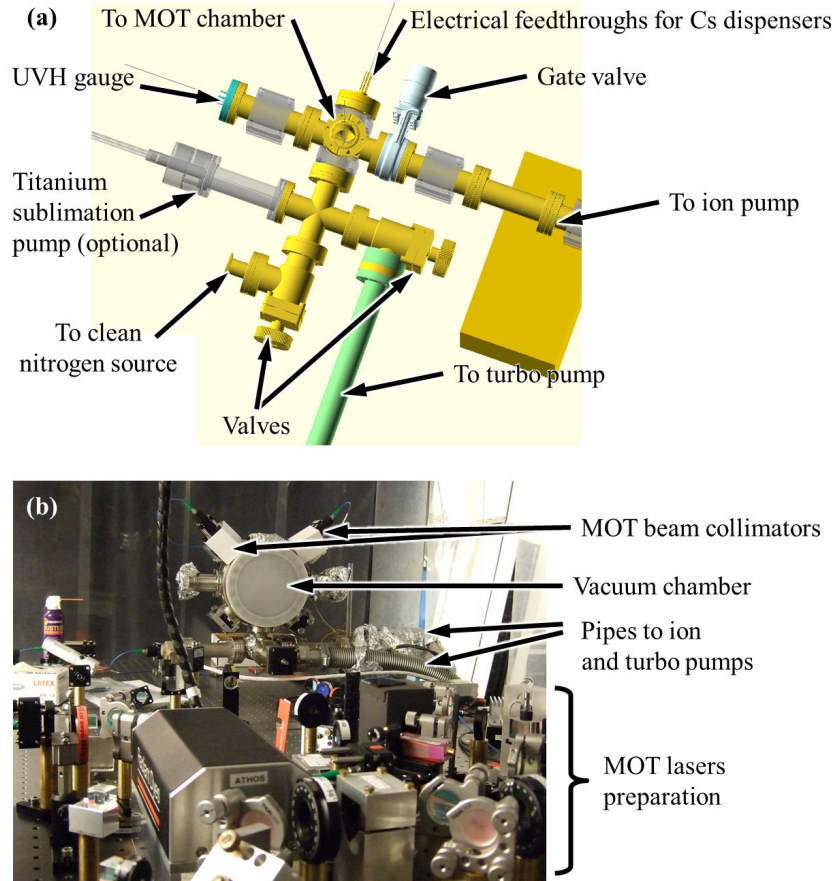
Figure 4.5: **Vacuum system plan and setup under construction.** (a) Plan of the (floor-level of the) vacuum system. The MOT chamber itself (not displayed) is fixed above the plane of the drawing. (b) picture of the system during construction. Part of the laser table for the free-space MOT generation is visible in the foreground. Behind it, the vacuum chamber is still partially covered in its protective covers. Two MOT collimators and their associated retroreflectors are attached to the chamber. They are fed by polarization-maintaining optical fibers coming from the laser table. Behind the black curtain lies the nanofiber fabrication stage.

Least, we dropped the all-glass chamber design and switched back to a more classical metallic vacuum chamber with detachable glass windows. This allows to have a more direct access to the core of the chamber in order to install the nanofiber inside of it. We

---

[2]Still, we achieved overall efficiencies ranging from about 50% to up to 75% depending on the mode quality at the output of the diode. Even if the diode outputs have been reshaped using anamorphic prisms and cylindrical lenses, some diodes just have lower-quality output spatial modes than others.

use the same 40 L/s ion pump[3] as in the previous experiment. The cesium atoms are provided by the same dispensers by SAES Getters. As we expect that we may need to open the chamber on a more regular basis than in the previous experiment (to replace the nanofiber), we installed a three-way airlock allowing to connect the chamber alternatively to a clean nitrogen source for venting, a turbo pump for mid-vacuum generation or only to the ion pump. The plans for this vacuum system and a picture of the early stages of its construction are shown in figure 4.5.

Laser diodes for the dipole trap. The Red and Blue light beams for the dipole trap are provided by three DL100 pro diode lasers by TOPTICA. They are labeled A, B and C. Without wavelength tuning, diode A provides ~ 76 mW of Red light at 936.75 nm, diode B provides ~ 16.5 mW of Blue light at 686.16 nm and diode C ~ 21.7 mW of Blue light at 686.12 nm, as summarized in table 4.1.

Laser diode	Available power (mW)	Wavelength (nm)
A (Red)	76	936.75
B (Blue)	16.5	686.16
C (Blue')	21.7	686.12

Table 4.1: **Power and wavelength of the free-running laser sources for the magic wavelength dipole trap.**

However, the first experimental demonstrations did not involve the dipole trap yet. They will be presented in the next subsection.

4.2.3 MOT-nanofiber interfacing.

The second milestone in this long-term project was the insertion of a low-loss subwavelength-diameter optical fiber inside the vacuum chamber and its first interfacing with the magneto-optical trap.

Insertion of the nanofiber in the vacuum chamber. The position of the nanofiber in the vacuum chamber is schematized in figure 4.6. Inserting the nanofiber in its final position requires to open the large lateral window and to insert the two ends of the nanofiber through ultra-high vacuum compatible feedthrouhgs.

The nanofiber fabrication and the MOT chamber opening are done in parallel. An extreme level of cleanliness is required. Since the fiber is to be inserted in an ultra-high vacuum (UHV) environment, it is cleaned several times with propanol over the entire length that is to be inserted in vacuuum. The fiber transmission is monitored continuously throughout the various stages of the procedure. To this end, the piece of fiber being tapered[4] is connectorized at both ends with universal bare fiber terminators and ceramic ferrules[5]. On each side of the few-centimeter-long part which is used for the tapering, one meter of bare fiber length is cleaned and reserved for later insertion in vacuum. From one side, a 780 nm wavelength laser[6] is injected into the fiber while it is detected by a

---

[3]Equipped with the same μ-metal shielding.
[4]SM800, core diameter 5.6 µm, cladding diameter 125 µm by Thorlabs
[5]BFTU and Senki FC/PC 126 µm, 3 mm Single Mode Connector by Thorlabs.
[6]S1FC780PM by Thorlabs.

commercial photodiode on the other side. During the tapering process, the measurement of this probe light gives information relative to both the overall transmission of the nanofiber (regardless of the light wavelength) and to its diameter (through the observation of mode beating).

After the tapering is complete, the flame used in this process is removed and the fiber is glued on a steel holder using a low degasing (UHV compatible) glue. The glue is fixed by UV illumination. Then, the fiber and its holder are moved into the vacuum chamber. Extreme care must be taken during this step in order to avoid breaking the fiber or contaminating it with dust. Transmission is still being recorded. The lose ends of the fiber (still attached to the laser source and photodiode for transmission monitoring) need to be fed through UHV airtight feedthroughs to the exterior of the chamber. Home-made bored cone-shaped Teflon feedthroughs were designed at the lab in teamwork with Kevin Makles from the group of Antoine Heidmann. The fiber is fed through the hole in the middle of the cone, which is then screwed on a UHV flange with a Swagelok nut. The tightening of the Swagelok nut compresses the Teflon feedthrough in such a way that the ensemble becomes completely airtight. This method has been tested with a helium leak detector and was found robust down to the limit sensitivity of the detector (roughly below 10^{-10} Torr).
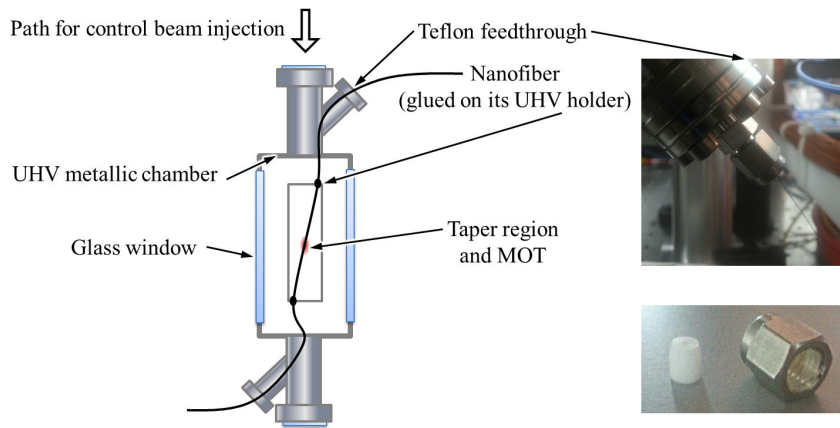
Figure 4.6: **Drawing of the nanofiber inside the vacuum chamber.** The nanofiber passes through two home-made Teflon feedthroughs able to maintain a vacuum below 10^{-9} Torr. It is glued on a steel-made holder with UHV compatible glue. It makes a 15° angle with the axis of the vacuum chamber. A control beam for EIT or DLCZ experiments will be injected in the chamber along this axis. The MOT is superposed with the subwavelength part of the nanofiber in the middle of the chamber. The pictures on the right show the feedthroughs used to fit the nanofiber inside the vacuum chamber. Bottom: home-made Teflon cone with a 130 µm diameter hole, and swagelok nut. Top: Whole assembly with the nanofiber inserted in the chamber.

At this point, it becomes necessary to remove the bare-fiber terminator and ferrule from the fiber lose end in order to feed it through the UHV flange. Since we do not have a sufficient precision to guarantee that a fiber coupling will remain identical after removing and re-installing its detachable ferrule, we first remove the ferrule on the side which is connected to the photodiode[7]. A UHV-clean Teflon pipe was used to guide the fiber lose end through the UHV flange before it is inserted in the Teflon feedthrough. Then, the

---

[7]The photodiode alignment is far less sensitive than a fiber-to-fiber coupling as on the side of the light

fiber end is re-functionalized with a fiber connector and we check the power transmission before tightening the swagelok nut. This way, we check that this step, which necessarily induces some mechanical strain on the fiber, does not degrade its overall transmission. In a last step, we repeat this operation on the other lose end of the fiber (the one that is connected to the monitoring light source). Disconnecting and reconnecting it is the largest source of uncertainty in our fiber insertion protocol. Even with this uncertainty, an overall transmission over 95% was achieved, the reference for 100% transmission being taken before the tapering process started.

This fiber has been in the vacuum chamber for five months now, and has been successfully interfaced with the cold atom cloud as will now be presented.

Collection of the MOT fluorescence into the nanofiber. In a first time, the MOT was superimposed on the tapered part of the fiber by playing with the fine alignment knobs of the MOT beams and on the coil current offset while monitoring the MOT position with a camera. By turning on and off the MOT beams and recording the transmitted power in the nanofiber in the absence of other light sources, we could measure that a small fraction of the MOT scattered light was collected in the nanofiber. Optimizing this MOT fluorescence collection is thus a good way to maximize the overlap of the MOT with the nanofiber.
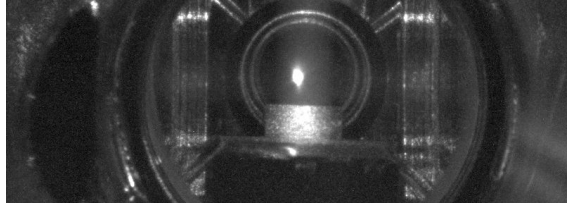
Figure 4.7: **An early image of the MOT inside the nanofiber chamber.**

In-fiber optical density measurements. In a second time, by turning off the MOT trapping beams and magnetic field in a similar fashion as in the previous experiment (chapters 2 and 3) and by sending a resonant probe beam on the $|F = 4\rangle \rightarrow |F' = 4\rangle$ transition, an optical depth of a few units has been measured. A major difference with the previous experiment however, was that the power of the probe had to to be *much weaker* for this measurement. Several phenomena contribute to this difference. First, the light being so tightly confined in the vicinity of the nanofiber, the electric field and hence the light-matter coupling strength for a given optical power is much higher (as a comparison, the signal path in the previous experiment had a 50 µm radius while the field in the present experiment is concentrated in a small fraction of a micrometer). Also because the field is concentrated over very small regions, less atoms are present in the interaction zone for an identical atomic density. Standard commercial photodiodes did not have the required combination of dynamic range and response time, so we used a custom-design fast and amplified photodiode by our electronic facility.

Typical values of optical depth around $d_0 \sim 5 \pm 1$ were measured routinely. This is still low enough to allow for direct on-resonance measurements on the signal transition $|F = 4\rangle \rightarrow |F' = 4\rangle$, at the further expense of the probe beam power (because using a non-cycling transition means we need to use very little power in order to avoid population

---

source injection.

transfer mechanisms). This OD value is still much lower than in the previous experiment (chapters 2 and 3), but let us underline that this was measured in the absence of further (Sisyphus) cooling mechanism and without loading the dipole trap ($d_0 \sim 100$ is targeted). We expect this figure of merit to increase to much higher values when we will load the dipole trap. Still this is enough to perform a proof-of-principle that the system is well suited for the implementation of a light-matter interface at the quantum level.

Before presenting the very first EIT results and the quantum interfacing of the nanofiber with the atoms, the next section will describe an important aspect of the still-to-be-completed dipole trapping scheme: the separation of the single-photon level signal from the milliwatt-level dipole-trap light.

4.3   Spectral filtering

4.3.1   Position of the problem and possible solutions

In this experiment, the signal light at 852 nm will ultimately propagate in the nanofiber together with the intense light at 685 nm and 935 nm that generate the dipole trap. Since we will want to detect single-photon signal pulses, it is crucial to be able to separate it from the dipole trap wavelengths with an amazingly high extinction ratio. Indeed, as indicated in section 4.1.2, up to about fifteen milliwatts of dipole trap light will be sent through the fiber.

In the free-space experiment for comparison, the main source of background noise was the leakage of a tiny fraction of the fifteen microwatt control beam. Although the wavelengths of the signal and noise were much closer in this case, the angular separation of the beams and some polarization filtering were enough to keep the induced noise at a reasonable level.

To get an idea of the orders of magnitude, a power P = 15 mW of light at $\lambda = 685$ nm represents a flux of N = $P\lambda/(hc) \sim 5 \times 10^{16}$ photons per second. For ~ 1 mW of the Red magic light, we get about one order of magnitude less. So if we target about the same noise level as in the previous experiment, we need an attenuation factor on the order of 140 dB.

To reach such a high attenuation (for which a standard dielectric dichroic mirror would be pointless) several solutions have been considered:

- **Volume Bragg Gratings (VGB)**. Also referenced by [179], these volume holograms have been specially developped by Optigrate to achieve a very narrow high reflectivity window centered arround 852 nm, while other wavelengths are transmitted – allowing to combine the signal with the trapping light. The rejection of the undesired wavelengths is on the order of 70 to 90 dB. For a review on VBG, see [187].

- **Interference filters (IF)** are another commercially available solution providing a narrow high transmission window arround 852 nm and up to 60 dB of broadband attenuation elsewhere. They are also less sensitive to the angle of incidence but do not allow for a simple design to combine signal and dipole-trap beams.

- **Fiber Bragg Gratings (FBG)**. Bragg gratings inscribed in fiber components were an attractive option because they held the promise of integration in a completely

fibered device. However, their performances are limited by the quality of the circula-
tors they have to be used in conjunction with. At 852 nm, the commercially available
circulators could not compete with either of the two previous solutions. The cross
talk of the circulator itself would have limited the attenuation of the unwanted wave-
lengths to less than 40 dB.

So in our experiment, we chose to work with a combination of volume Bragg gratings
(see figure 4.8) and interference filters.
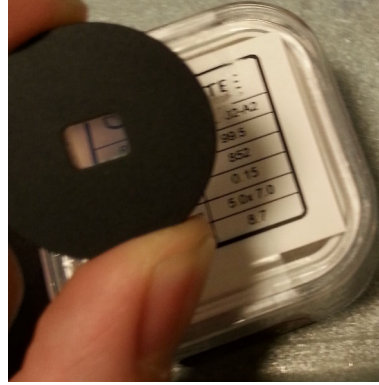
Figure 4.8: **Picture of a VBG in its holder.** The active area is 5 mm $\times$ 7 mm wide and
the grating is 8 mm thick. Specified input and output angles are respectively $2 \pm 1°$ and
$-8 \pm 1°$.

4.3.2   Alignment and characterization of the filtering setup

In figure 4.9, we show a schematic view of the filtering setup (an alternative version using
one VBG and one IF is shown in figure 4.10). The alignment is done as follows.

In a first stage, the light coming from the nanofiber collimator is matched to the first
VBG with a pair of ultrabroadband mirrors. The angle of the first VBG is carefully
adjusted while monitoring the transmission of light at 852 nm. It is finely tuned until min-
imum transmission is reached. It is checked that both magic wavelengths are transmitted
and that "close to nothing" of them is reflected (the reflected power at these wavelengths is
out of the reach of a standard lab powermeter). In addition to the angle of incidence, the
wavefront's flatness is a crucial parameter. The second VBG is aligned following the same
procedure as the first. The power efficiency of the combined two VBG is around 93%.

In a second stage, the filtered signal is coupled into a fiber with another pair of mirrors.
In the first implementation, the fiber coupling efficiency was limited to $\sim 36\%$ due to an
imperfect mode matching. This is expected to be improved significantly as soon as we will
make use of a more adequate lensing system at fiber output. The filtering quality of the
setup is then measured by monitoring the power in this signal fiber when injecting Red
and Blue magic light from the nanofiber collimator.

For a first test, the light was detected with a highly sensitive photodetector (Thorlabs
PDF10A) which has a sensitivity of 0.6 V/pW over a wide wavelength range. Doing the
test with 4 mW of either wavelength, the leakage was below the detector's sensitivity. So
the precision was limited by the noise measured on the oscilloscope in the absence of light:
about 20 mV which corresponds to a maximum power of 30 fW. This means that the
achieved filtering is better than 110 dB at both magic wavelengths.

Figure 4.9: **The spectral filtering setup using VBG only.** The first VBG reflects only the light at 852 nm and transmits the Red and Blue magic wavelengths. A second VBG enhances the attenuation of the Red and Blue light in the signal path. The tight angle in the beam direction ($\sim 10°$) is imposed by the design of the VBG. The signal collimator collects the filtered light at 852 nm. Behind the first VBG, a dichroic mirror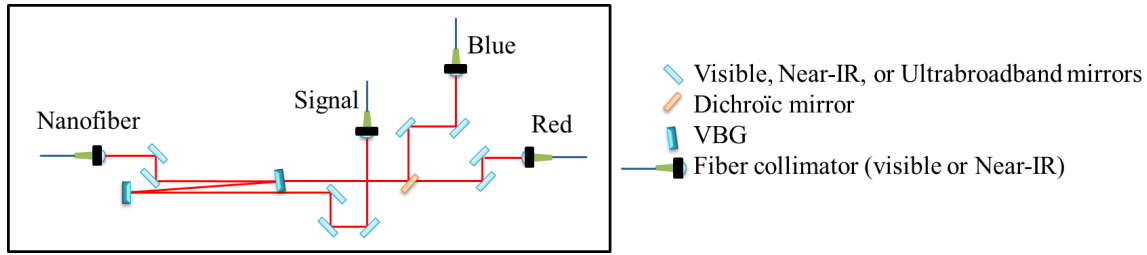 (HR@685+HT@935) separates the Red and Blue light. Of course, this works in both directions and so it allows both to inject the Red and Blue magic light as well as a probe into the nanofiber, and to separate the probe from the beams being injected into or leaving the nanofiber.

In order to measure the real filtering quality of the setup, a further characterization has been performed with an avalanche photodiode, yielding attenuation factors around 128 dB at 685 nm and 120 dB at 935 nm. This is close to but a little lower than the target values. It should be noted that this measurement was done with a coarse filtering of the background emission of the laser diodes A, B and C (see next section), so it gives only a lower bound to the real attenuation factor. We expect that if we properly remove the diode laser background emission, then the targeted attenuation factor of 140 dB will be reached.

Apart from the improvement of the suppression of the laser diode's background emission, efforts to reach the desired filtering level can include a perfecting of the phasefront's planeity and the addition of an IF after the VBG.

In a third stage, a dichroic mirror[8] is installed after the first VBG to separate the Red and Blue light beams (which are still being injected from the nanofiber collimator). Each one of them is coupled into its specific collimator. We measured the VBG's transmission to be 72% for the Blue and 94% for the Red. The dichroic mirror causes neglectible losses on both beams ($< 0.5\%$ on Blue and $\sim 1.5\%$ on Red).

In a last step, we reverse the direction of light propagation and inject the Red and Blue light from their respective collimators into the nanofiber collimator. Thus, it is checked that the injection of the trapping light into the nanofiber can be efficiently done with this setup as expected from time reversal symmetry of the previous alignment procedure. Indeed, within a few percents uncertainty, the coupling is the same in both directions, namely $\sim 40\%$ for the Blue and $\sim 50\%$ for the Red. These values include the limited transmission of the VBG.

The interference filters have been tested in a simpler setup. The IF was simply put between a photodetector and a collimated laser beam emerging from an optical fiber. The transmission of the IF at 852 nm was found to be above 96%. Their measured isolation was above 53 dB at 935 nm and 57 dB at 685 nm, but this was measured without a proper filtering of the diode background emission.

---

[8]Custom design by Altechna.
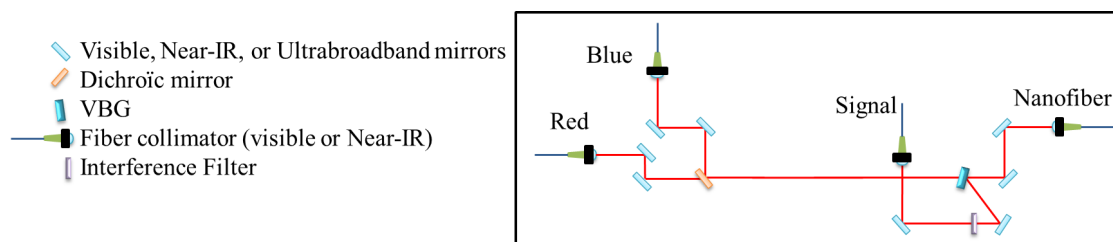
Figure 4.10: **Alternative spectral filtering setup using one VBG and one IF.**

4.3.3 Leakage due to the background emission of the Red magic diode

While following the alignment procedure described in the previous section, it was noticed that the laser diode at the Red magic wavelength has a relatively high level of background emission at 852 nm (see figure 4.11).

Our first filtering measurements showed a leakage of ~ 0.25 pW per milliwatt of Red light through the pair of VBG units. The corresponding attenuation was below 95 dB which is clearly not enough. Inserting an IF in the filtering path didn't change the attenuation which tended to indicate that this leakeage was close to 852 nm.

We first feared that anti-Stokes scattering in the fibers might be involved. However, the orders of magnitude are incompatible with the amount of observed leakage. Typical anti-Stokes scattering power is 40 pW per kilometer of fiber at 500 mW pump power. With an excitation power 50 times lower and three orders of magnitude less in the fiber length, the fraction of picowatt we observed could not be explained by anti-Stokes scattering.
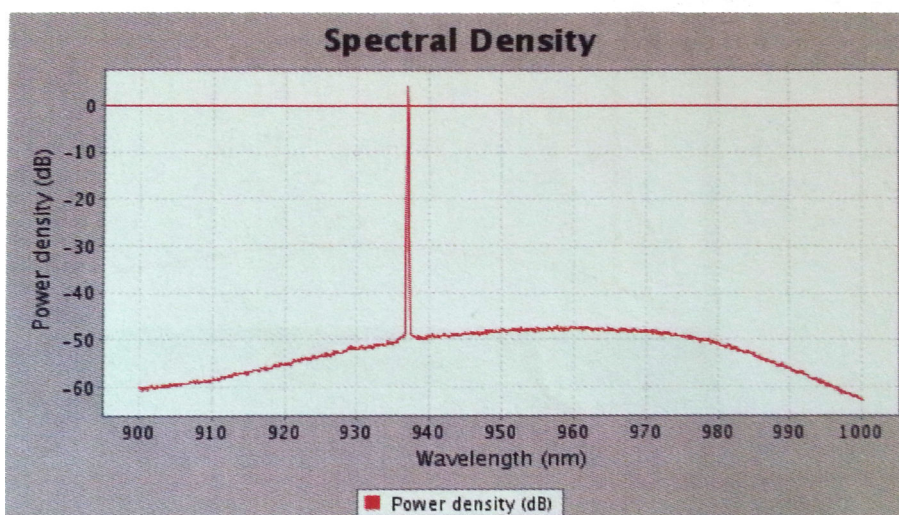
Figure 4.11: **Emission spectrum of laser diode A** providing the trapping light at the Red magic wavelength (685 nm). Reproduced from the factory test sheet by TOPTICA. Although spontaneous emission around 852 nm is expected to be extremely reduced (maybe about 60 dB lower than the laser emission), we still detected parasitic light when spectrally filtering very sharply around 852 nm. The addition of a dichroic mirror at the output of the diode removed most of this parasitic light.

Filtering the output of the Red laser diode with a standard dichroic mirror (R > 99% @ 852 nm, T > 85% @ 917 nm) allowed us to remove most of the parasitic spontaneous emission at 852 nm – and confirmed the origin of the residual leakage! With this purification, we performed the measurements reported in the previous section

We expect that the figure of merit of the filtering setup can be improved by a better purification of the outputs of the magic laser diodes, such as can be done with narrower and higher attenuation filters.

4.3.4 Spectral filtering setup: a short summary

Let us summarize in a few key numbers the outcomes of the testing of the filtering setup of figure 4.9.

Attenuation by two VBG along the signal path		
Wavelength (nm)	Target (dB)	Measured (dB)
685 (Blue)	140	128
935 (Red)	130	124
852 (signal)	0	0.3

Efficiency of the injection into the nanofiber		
Wavelength (nm)	VBG losses	Overall injection efficiency
685 (Blue)	72 %	$\sim 40\%$
935 (Red)	94 %	$\sim 50\%$

IF transmission properties	
Wavelength (nm)	Transmission
685 (Blue)	-57 dB
935 (Red)	-53 dB
852 (signal)	$> 96\%$

> As a summary of this section, our filtering setup is almost up to the specifications. With the minor improvements proposed, it should enable operation at the single-photon level. It has also reveald to us the importance of filtering the magic diode background emission.

4.4   Recent progress and towards optical quantum memories

When I left the lab to start writing this manuscript, we had gone as far as taking the first OD measurements without dipole trap. In this last section, I would like to acknowledge the milestones that Baptiste Gouraud, Dominik Maxein and Olivier Morin have reached since then.

The subsequent measurements were done by directly interfacing the MOT with the nanofiber as done in section 4.2.3 without turning the dipole trap on. Yet, they prove that the setup is suitable for performing of interesting tasks in the quantum realm.

- **Magnetic field measurements.** The same microwave generator and antenna as in section 2.3.2 were used to probe the magnetic field seen by the atoms. A similar set of compensation coils and a controlled current source were built in order to cancel the remaining magnetic fields. For reasons that still need to be elucidated, the best magnetic field cancellation shows a spread of ± 50 kHz, which leads to expect a magnetic field induced memory decay time of $\tau_m = 30$ µs from section 2.2.5.

- **Polarization control inside the nanofiber.** Even with all the precautions taken in the fabrication and vacuum insertion of the nanofiber, some imperfections remain, in the form of dipole scattering sites at the surface of the fiber. Yet, these defects can be utilized to probe the polarization of the light inside the nanofiber as proposed by Vetsch et al. [188], by looking at the light they scatter through a polarizer. This technique allowed to control the polarization of signal probe beam inside the nanofiber.

- **EIT in the nanofiber.** An external control beam has been added as foreseen in figure 4.6, making a 15° angle with the nanofiber axis. An EIT effect reaching a 35% transparency has been measured by using the same laser beams and the same optical phase-and-frequency lock as in section 2.3.

- **First quantum memory signal in the single-photon regime.** Following the first EIT measurements with classical beams, the quantum memory protocol was implemented with signal pulses at the single-photon level. To get rid of the contamination by the control (even though $\alpha \sim 15°$!), the usage of an atomic filter cell was necessary to isolate the low-photon number signal. The first memory experiments show a typical efficiency on the order of $\eta \sim 5\%$, which is currently limited by the low optical depth. Indeed, most of the signal leaks out of the memory before being stopped, as discussed in section 2.2.1. Going to lower temperatures and loading the dipole trap should open the way to higher-performance quantum memory applications.

These recent achievements prove the in-principle feasibility of a quantum light-matter interface with the system we developed.

4.5 Conclusion

In this chapter, we have introduced our new setup for a **nanofiber-based quantum interface**. The principle of a two-color dipole trap and its usage for fibered quantum information tasks were schematically explained. Our experimental progress have shown that we can interface a nanofiber waveguide with a cold atom cloud down to the quantum regime and a quantum memory effect has now been observed, which remains to be improved.

When the full setup will be put together (including the dipole trap), we expect that the figures of merit of this new interface will exceed that of the previous (free-space) implementation. As an important step towards this goal, we have presented the characterization of the filtering setup enabling to isolate the single-photon level quantum signal from the intense dipole trap light.

The group's efforts are currently focused on the possibility to use the nanofiber interface to store and recall heralded single photons emitted from the free space MOT, and to implement the DLCZ protocol inside the nanofiber, making it an *intrinsically fibered single-photon source.*

Conclusion

So we have come to the end of this journey through optical quantum memories, light orbital angular momentum and nanowaveguide-coupled light-matter interfaces.

The foregoing pages have given an introduction to quantum memories and their place within quantum information research. They have included a basic theoretical description of electromagnetically induced transparency in cold atomic ensembles, and its experimental implementation in our lab. The quantum memory resulting from this implementation was benchmarked and compared to the model predictions. Special emphasis was put on the memory efficiency η and lifetime τ_m. The experimental tools to fight against known decoherence mechanisms (thermal motion and magnetic field inhomogeneities) have been presented in detail. We have also detailed the spatial multimode capability of our quantum memory. For this, the Laguerre-Gaussian modes and the associated concept of light orbital angular momentum have been introduced, as well as the method for manipulating them in the lab. A complex detection setup was designed and characterized in order to realize the full quantum tomography of orbital-angular-momentum-encoded qubits. This brings us to what is probably the main result of this thesis:

> **The (first) quantum storage of a quantum bit encoded in the orbital angular momentum state of a weak light pulse at the single-photon level.** The memory was implemented using the EIT protocol in a cold atomic ensemble. Measured storage parameters include the efficiency $\eta \sim 15 \pm 2\%$, the storage lifetime $\tau_m \sim 15$ µs, and the qubit fidelity after storage (without noise correction) $F \sim 92 \pm 1\%$.

At last, we introduced a new class of light-matter interfaces based on the trapping of cold atomic ensembles around nanofibers. Our experimental progress towards the construction and full operation of such a device has been reported, including the characterization of the setup required to separate the single-photon level signal from the yet-to-be-completed two-color dipole trap. First measurements of the atomic cloud optical density using a probe beam propagating inside the nanofiber yield promising perspectives for future quantum memory implementations.

Recent achievements and reasonable prospects for a foreseeable future include:

- The increase of the free-space memory efficiency η by switching to a Raman configuration. Experiments with a signal detuning of $\delta \sim 2 \times \Gamma (2\pi \times 10 \text{ MHz})$ have already shown a memory increase to $\eta \sim 25 \pm 2\%$.

- The inclusion of better cooling mechanisms and the construction of a lower-temperature, higher-density magneto-optical trap will be the next steps. Memory times on the order of hundreds of microseconds should then get within range.

- The storage of other kinds of complex modes such as polarization-OAM hybrid modes is about to be demonstrated soon, while using the higher-efficiency Raman memory configuration.

- The possible scaling of the number of stored orbital angular photonic modes in the memory could be considered afterwards. The current atomic cloud is expected to be able to support several dozens of modes without efficiency loss.

- The further development of the nanofiber-based interface, in particular the inclusion of the fiber-embeded two-color dipole trap, and the demonstration of the system quantum-information-relevant capabilities. Preliminary results have already shown a quantum memory effect with an efficiency ($\eta \sim 5 \pm 1\%$) limited by the currently low optical depth.

The results obtained within this thesis add another tile to the road of quantum information science and technology. While we are still far from meeting the performances that would make a quantum memory useful in a realistic quantum communication scenario, they participate in extending the level of control we have over nature, and in suggesting that quantum-related technologies haven't reached their limit yet. As a former reader of *Alice in Quantumland* [3] and long-time sci-fi fan, I am happy to have been able to get (modestly) involved in this fascinating (though not magical) scientific adventure. It will continue long after I'll have left the group, here at Laboratoire Kastler Brossel and in many other places around the world.

Appendix A

Appendix

A.1 Derivation of the EIT linear susceptibility

The aim of this appendix is to justify the expression of the linear susceptibility in an EIT medium given in equation (2.2).

A.1.1 Model

Let us first present in details the model underlying the calculation.

We consider a single atom in a three-level Λ scheme as depicted in figure A.1. The atom interacts with a control field at angular frequency ω_c on the $|s\rangle \leftrightarrow |e\rangle$ transition and with a signal field at angular frequency ω on the $|g\rangle \leftrightarrow |e\rangle$ transition. [1] The atom is treated quantum mechanically in the basis $\{|g\rangle, |s\rangle, |e\rangle\}$. The light is described classically by the electric fields:

$$
\begin{aligned}
\vec{E}_c &= \vec{E}_{c0}\mathrm{e}^{\mathrm{i}\omega_c t} \qquad \text{(control)} \\
\vec{E}_s &= \vec{E}_{s0}\mathrm{e}^{\mathrm{i}\omega t} \qquad \text{(signal)}
\end{aligned}
\tag{A.1}
$$

For simplicity, the control field is assumed to be on resonance, which means $\hbar\omega_c = \hbar\omega_{se} = E_{|e\rangle} - E_{|s\rangle}$. The signal has a detuning δ defined by: $\omega = \omega_{ge} + \delta$ where $\hbar\omega_{ge} = E_{|e\rangle} - E_{|g\rangle}$.

We neglect any dephasing mechanism other than the one resulting from the decay of state $|e\rangle$. In particular, we neglect the homogeneous dephasing between levels $|s\rangle$ and $|g\rangle$. The decay rate Γ of the excited state results from the contributions of the decay rates in both channels $|e\rangle \to |g\rangle$ and $|e\rangle \to |s\rangle$: $\Gamma = \Gamma_{eg} + \Gamma_{es}$. The relative strength of the two decay rates is given by the square of the ratio of the dipole matrix elements of the transitions.

In our experiments, we use ^{133}Cs atoms with $|g\rangle = |F = 4\rangle$, $|s\rangle = |F = 3\rangle$, and $|e\rangle = |F' = 4\rangle$ on the D2 line so we have $\Gamma_{eg}/\Gamma_{es} \sim 1.09$ [134].

The free atomic hamiltonian in Schrödinger picture in the $\{|g\rangle, |s\rangle, |e\rangle\}$ basis is given by:

---

[1] Because we are concerned with the application of EIT to quantum memory systems, we use the "control" and "signal" terminology from the quantum memory background, which are more commonly refered to as "control" and "probe" in the EIT community.
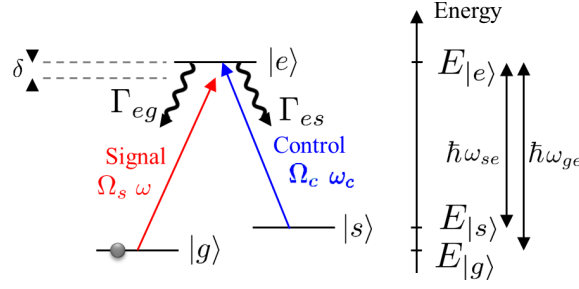
Figure A.1: **Energy levels and light fields involved in EIT.** The atom is initially in state $|g\rangle$. It interacts with a signal field of Rabi frequency Ω_s and of frequency ω close to resonance with the $|g\rangle \leftrightarrow |e\rangle$ transition, and with a control field of Rabi frequency Ω_c and of frequency ω_c at resonance with the $|s\rangle \leftrightarrow |e\rangle$ transition (detuning δ). Excited state $|e\rangle$ decays spontaneously into states $|s\rangle$ and $|g\rangle$ at rates Γ_{es} and Γ_{eg}.

$$\hat{H}_0 = \hbar \begin{pmatrix} 0 & 0 & 0 \\ 0 & \omega_{ge} - \omega_{se} & 0 \\ 0 & 0 & \omega_{ge} \end{pmatrix} \tag{A.2}$$

The energy reference is level $|g\rangle$. Levels $|s\rangle$ and $|e\rangle$ have phases oscillating respectively in the microwave and optical frequency ranges.

The coupling between the light fields and the atom is given by the dipole interaction $\hat{V} = -\hat{\vec{d}} \cdot \vec{E}$, where $\hat{\vec{d}}$ is the atomic electric dipole moment operator. In our model, this translates into:

$$\begin{aligned} \hat{V}(t) = & - \vec{E_{c0}} \cdot \vec{d_{es}} \cos(\omega_c t) \left(|e\rangle\langle s| + |s\rangle\langle e|\right) \\ & - \vec{E_{s0}} \cdot \vec{d_{eg}} \cos(\omega t) \left(|e\rangle\langle g| + |g\rangle\langle e|\right) \end{aligned} \tag{A.3}$$

Using the real expression of the electric fields will allow us to detail the rotating wave approximation in the next section. We merge the dipole strength and the electric field amplitude in a single quantity, the Rabi (angular) frequency defined by:

$$\begin{aligned} \Omega_c &= -\frac{\vec{E_{c0}} \cdot \vec{d_{es}}}{\hbar} \\ \Omega_s &= -\frac{\vec{E_{s0}} \cdot \vec{d_{eg}}}{\hbar} \end{aligned} \tag{A.4}$$

These quantities depend on the polarization of the electric fields and on the spin orientation of the atoms in the levels $|g\rangle$, $|s\rangle$ and $|e\rangle$.

Our aim is to find how the atomic medium reacts to the signal field. This is described by the susceptibility χ, defined at the linear order as the proportionality coefficient between the applied signal field $\vec{E}_s$ and the resulting atomic polarization $\vec{P}$:

$$\vec{P} = \epsilon_0 \chi \vec{E}_s \tag{A.5}$$

If the atom is described by its density matrix $\hat{\rho}$ with a dipole element ρ_{eg} coupled to the signal field $\vec{E}_s$, then the polarization per atom will be given by:

$$\vec{P} = \vec{d}_{eg}\rho_{eg} \tag{A.6}$$

Once χ will be known, the propagation of the signal wave will be deduced from the modified d'Alembert equation (2.1). So all we need to do is to compute coherence term ρ_{eg} of the atomic density matrix.

A.1.2   Derivation of the expression of the linear susceptibility

With the elements introduced in the previous section, the computation of the linear susceptibility will consist in the following steps:

- writing down the full atomic hamiltonian in the rotating frame and proceeding to the rotating wave approximation (RWA).

- Writing down the master equation for the atomic density matrix $\hat{\rho}$ in the rotating frame in the basis $\{|g\rangle, |s\rangle, |e\rangle\}$ (this includes the calculation of the commutator of the density matrix with the hamiltonian and the addition of the Lindblad decoherence terms). This will yield a set of coupled differential equation for the various components of the density matrix.

- Then, assuming that the signal acts a small perturbation on the initial density matrix $\hat{\rho} = |g\rangle\langle g|$, a pair of coupled equations involving the coherences ρ_{sg} and ρ_{eg} are extracted from the steady-state condition to this differential system.

- The expression of ρ_{eg} resulting from it then gives the desired linear susceptibility.

The full atomic hamiltonian is given from equations (A.2) and (A.3):

$$\hat{H} = \hbar \begin{pmatrix} 0 & 0 & 0 \\ 0 & \omega_{ge} - \omega_{se} & 0 \\ 0 & 0 & \omega_{ge} \end{pmatrix} + \hbar\Omega_c \cos(\omega_c t) \begin{pmatrix} 0 & 0 & 0 \\ 0 & 0 & 1 \\ 0 & 1 & 0 \end{pmatrix} + \hbar\Omega_s \cos(\omega t) \begin{pmatrix} 0 & 0 & 1 \\ 0 & 0 & 0 \\ 1 & 0 & 0 \end{pmatrix} \tag{A.7}$$

Moving to the rotating frame, i.e. to the frame rotating at the frequency imposed by the optical fields $\vec{E}_s$ and $\vec{E}_c$, is done by multiplying the atomic state vector by the operator $\hat{U}(t) = \exp(\mathrm{i} \begin{pmatrix} 0 & 0 & 0 \\ 0 & \omega - \omega_{es} & 0 \\ 0 & 0 & \omega \end{pmatrix} t)$. Writing the Schrödinger equation for the rotating state vector gives the expression of the hamiltonian in the rotating frame:

$$\begin{aligned}
\hat{H}_{\mathrm{rot}} = \mathrm{i}\hbar\partial_t \hat{U}(t) + \hat{U}(t)\hat{H}_0\hat{U}^\dagger(t) + \hbar\Omega_c \cos(\omega_c t)\hat{U}(t) \begin{pmatrix} 0 & 0 & 0 \\ 0 & 0 & 1 \\ 0 & 1 & 0 \end{pmatrix} \hat{U}^\dagger(t) \\
+ \hbar\Omega_s \cos(\omega t)\hat{U}(t) \begin{pmatrix} 0 & 0 & 1 \\ 0 & 0 & 0 \\ 1 & 0 & 0 \end{pmatrix} \hat{U}^\dagger(t)
\end{aligned} \tag{A.8}$$

Next, the rotating wave approximation (RWA) is applied. It consists in developing the cosines, computing the matrix products, and neglecting the fast oscillating terms in front

of the slow (constant) ones. Thus, only the positive frequency part of the light couples to the desexcitation terms:

$$\hat{H}_{\text{RWA}} = -\hbar\delta \begin{pmatrix} 0 & 0 & 0 \\ 0 & 1 & 0 \\ 0 & 0 & 1 \end{pmatrix} + \frac{1}{2}\hbar\Omega_c \begin{pmatrix} 0 & 0 & 0 \\ 0 & 0 & 1 \\ 0 & 1 & 0 \end{pmatrix} + \frac{1}{2}\hbar\Omega_s \begin{pmatrix} 0 & 0 & 1 \\ 0 & 0 & 0 \\ 1 & 0 & 0 \end{pmatrix} \tag{A.9}$$

The density matrix in the rotating frame is denoted $\hat{\rho}$. Its evolution is governed by the Lindblad equation:

$$\partial_t \hat{\rho} = \frac{1}{i\hbar}\left[\hat{H}_{\text{RWA}}, \hat{\rho}\right] + \frac{\Gamma_{eg}}{2}\left(2|g\rangle\langle e|\rho|e\rangle\langle g| - |e\rangle\langle e|\rho - \rho|e\rangle\langle e|\right)$$
$$+ \frac{\Gamma_{es}}{2}\left(2|s\rangle\langle e|\rho|e\rangle\langle s| - |e\rangle\langle e|\rho - \rho|e\rangle\langle e|\right) \tag{A.10}$$

Computing all the terms in the equation thereabove yields the following optical Bloch equations:

$$\partial_t \rho_{gg} = -\frac{i}{2}\Omega_s(\rho_{eg} - \rho_{ge}) + \Gamma_{eg}\rho_{ee}$$
$$\partial_t \rho_{ss} = -\frac{i}{2}\Omega_c(\rho_{es} - \rho_{se}) + \Gamma_{es}\rho_{ee}$$
$$\partial_t \rho_{ee} = \frac{i}{2}\Omega_c(\rho_{es} - \rho_{se}) + \frac{i}{2}\Omega_s(\rho_{eg} - \rho_{ge}) - \Gamma\rho_{ee}$$
$$\partial_t \rho_{gs} = -i\delta\rho_{gs} + \frac{i}{2}\Omega_c\rho_{ge} - \frac{i}{2}\Omega_s\rho_{es} \tag{A.11}$$
$$\partial_t \rho_{ge} = -i\delta\rho_{ge} + \frac{i}{2}\Omega_c\rho_{gs} - \frac{i}{2}\Omega_s(\rho_{ee} - \rho_{gg}) + \frac{\Gamma}{2}\rho_{ge}$$
$$\partial_t \rho_{se} = -\frac{i}{2}\Omega_c(\rho_{ee} - \rho_{ss}) - \frac{i}{2}\Omega_s\rho_{sg} + \frac{\Gamma}{2}\rho_{se}$$

Interestingly, the relaxation does not appear in the equation governing the coherence between the two ground levels ρ_{gs}. Of coures, it was a choice on our part not to include a specific γ_{gs} dephasing term, but although the coupling between levels $|g\rangle$ and $|s\rangle$ is mediated by a transition via the excited level $|e\rangle$, there is no influence of the relaxation experienced by $|e\rangle$. The susceptibility is found by looking for a perturbative steady state solution to the optical Bloch equations. The zero order density matrix is assumed to be $\rho \sim \rho_{gg}|g\rangle\langle g|$. Terms of order one are the signal's (angular) Rabi frequency Ω_s as well as all other density matrix coefficients.

With this assumption, the steady state condition for ρ_{gs} and ρ_{ge} gives a linear set of equations:

$$0 = -i\delta\rho_{gs} + \frac{i}{2}\Omega_c\rho_{ge}$$
$$0 = -i\delta\rho_{ge} + \frac{i}{2}\Omega_c\rho_{gs} + \frac{i}{2}\Omega_s - \frac{\Gamma}{2}\rho_{ge} \tag{A.12}$$

From which the coherence term ρ_{eg} can be extracted as desired:

$$\rho_{eg} = \frac{\frac{i}{2}\delta\Omega_s}{\left(i\delta^2 - \frac{\Omega_c^2}{4}\right) + \frac{\Gamma\delta}{2}} \tag{A.13}$$

Then, recalling equations (A.5) and (A.6), the susceptibility (per atom) is expressed as:

$$\chi(\delta) = \frac{d_{eg}^2}{2\epsilon_0\hbar} \frac{\mathrm{i}\delta}{\mathrm{i}\left(\delta^2 - \frac{\Omega_c^2}{4}\right) + \frac{\delta\Gamma}{2}} \tag{A.14}$$

The properties resulting from this expression will be examined in section A.2, but let's first give a dictionary to translate the notations of this manuscript into other author's notations.

A.1.3   Comparison with notation systems from other works

In order to facilitate the comparison with different articles cited in the bibliography, I give here the correspondance with the notations of different authors.

Fleischhauer et al. [130]	This manuscript
γ_{12}	0
Δ_1 , Δ	$-\delta$
δ	$-\delta$
Δ_2	0
γ_{13}	Γ
Ω_p	Ω_s

Table A.1: Correspondance with the notations used in [130]

Anisimov and Kocharovskaya [189]	This manuscript
Δ	0
α	$\Omega_s/2$
Ω	$\Omega_c/2$
γ_{ab}	$\Gamma/2$
Γ_{bc}	0

Table A.2: Correspondance with the notations used in [189]

Scherman [86], Mishina et al. [124]	This manuscript
Δ_s	δ
Ω_{se}^c	Ω_c
Ω_{ge}^s	Ω_s
γ_{sg}	0
γ_{eg}	$\Gamma/2$
Δ_c	0

Table A.3: Correspondance with the notations used in [86, 124]

A.2   EIT linear susceptibility: from EIT to ATS

Let us examine a little bit more the expression of the susceptibility χ given by equation (A.14).

It has poles given by [189]:

$$\tilde{\delta}_{\pm} = \frac{1}{2}\left(\mathrm{i}\frac{\Gamma}{2} \pm \sqrt{\Omega_c^2 - \frac{\Gamma^2}{4}} \right) \tag{A.15}$$

and thus a partial fraction decomposition as:

$$\chi(\delta) = \frac{C_+}{\delta - \tilde{\delta}_+} + \frac{C_-}{\delta - \tilde{\delta}_-} \tag{A.16}$$

with coefficients:

$$C_{\pm} = \pm\kappa\frac{\tilde{\delta}_{\pm}}{\tilde{\delta}_+ - \tilde{\delta}_-} \in \mathbb{R}^{\star\pm} \tag{A.17}$$

where $\kappa = {}^{d_{eg}^2}/_{2\epsilon_0\hbar}$. If $\Omega_c < \Gamma/2$, then from equation A.15, we have: $\tilde{\delta}_{\pm} \in \mathrm{i}\mathbb{R}$ [189]. In this case, the *imaginary* part of the susceptibility, which is the *absorption* coefficient, has a remarkably simple expression: it is the difference between two Lorentzian functions centered on resonance ($\delta = 0$). Defining $\delta_{\pm} = \tilde{\delta}_{\pm}/\mathrm{i}$ to get real quantities, the absorption is written as (recall that C_+ and C_- are real and have opposite signs):

$$A_{\mathrm{EIT}}(\delta) = \frac{C_+\delta_+}{\delta^2 + \delta_+^2} + \frac{C_-\delta_-}{\delta^2 + \delta_-^2} \tag{A.18}$$

This corresponds to the "pure EIT" case. In the low control field region, δ_+ tends towards $\Gamma/2$ and δ_- tends towards Ω_c^2/Γ. So that the first term in equation (A.18) acts as the unperturbed atomic resonance line (a Lorentzian of width Γ) and the second term describes a Lorentzian dip of width Ω_c^2/Γ, defining the transparency window within the resonance.

If $\Omega_c > \Gamma/2$, then of course the partial fraction decomposition (A.16) for χ still holds, but equation (A.18) does not anymore describe the absorption because $\tilde{\delta}_{\pm}$ now have real as well as imaginary parts.

In the limit of very large control field $\Omega_c >> \Gamma/2$, the absorption can be approximated by the sum of two Lorentzian functions of width $\Gamma/2$ (half the unperturbed resonance width) shifted away by approximately $\pm\Omega_c/2$ from the $\delta = 0$ resonance as predicted in the model by Autler and Townes [190].

> For the typical parameters used in memory experiments (15 μW in a control beam with a 200 μm waist), we are a little above the "pure EIT" threshold with $\Omega_c/\Gamma \sim 1.3$.

A.3   Cesium D2 line

$6^2P_{3/2}$

263.8906(24) MHz

12.798 51(82) MHz

251.0916(20) MHz

$g_F = 2/5$
(0.56 MHz/G)

$F = 5$

188.4885(13) MHz

201.2871(11) MHz

$g_F = 4/15$
(0.37 MHz/G)

$F = 4$

339.7128(39) MHz

$g_F = 0$
(0.00 MHz/G)

$F = 3$

151.2247(16) MHz

$g_F = -2/3$
(-0.93 MHz/G)

$F = 2$

852.347 275 82(27) nm
351.725 718 50(11) THz
11 732.307 104 9(37) cm^{-1}
1.454 620 563(35) eV

$6^2S_{1/2}$

4.021 776 399 375 GHz (exact)

$g_F = 1/4$
(0.35 MHz/G)

$F = 4$

9.192 631 770 GHz (exact)

5.170 855 370 625 GHz (exact)

$g_F = -1/4$
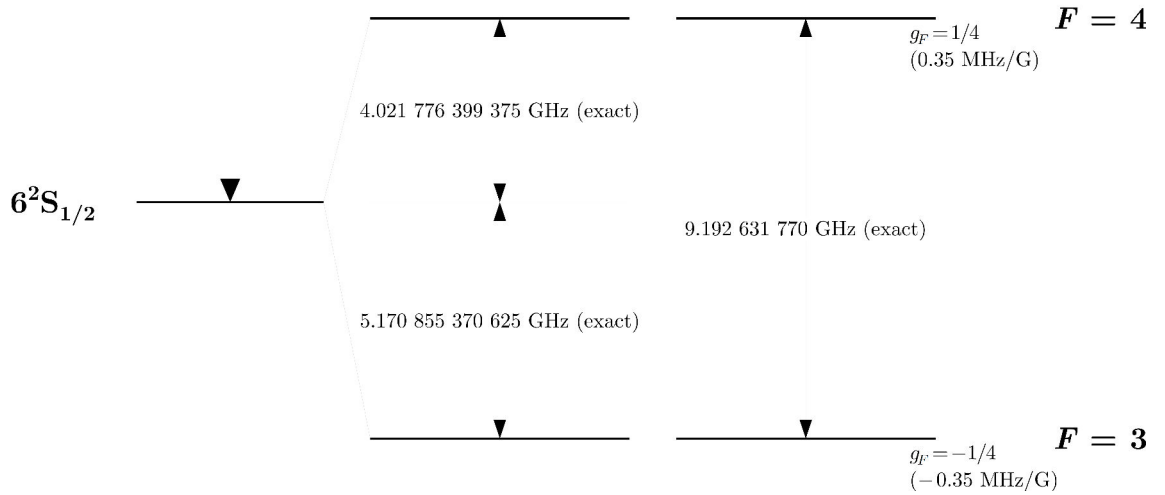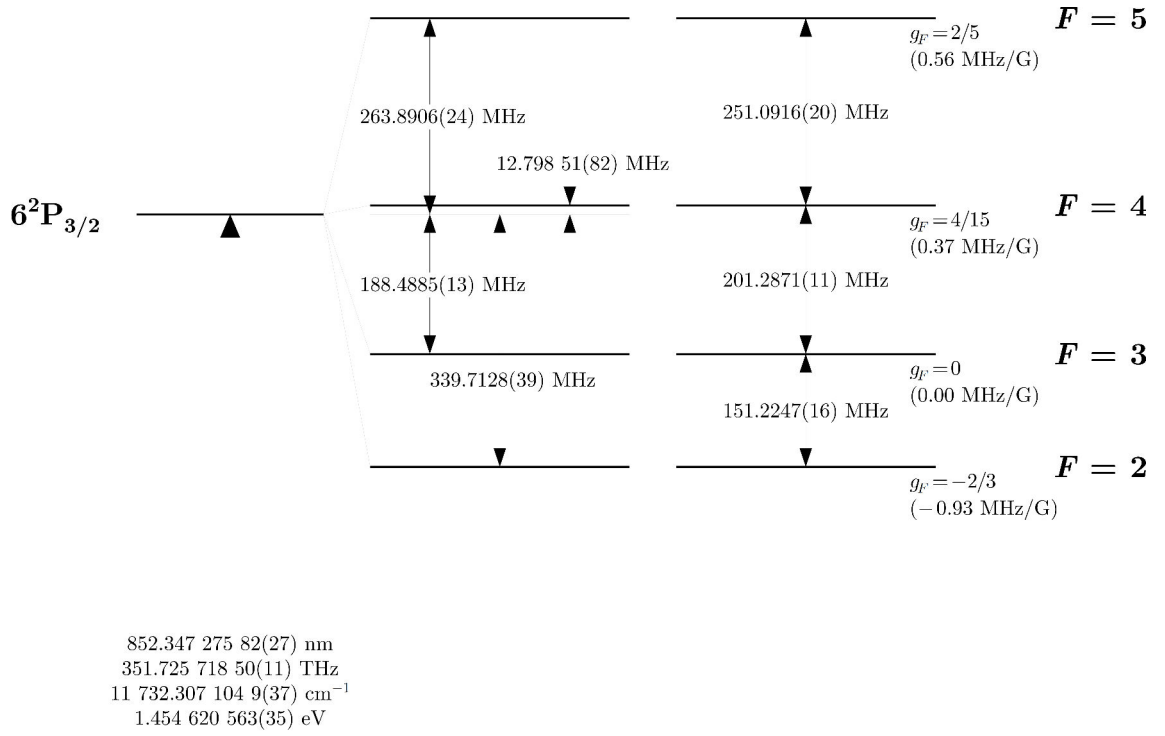(-0.35 MHz/G)

$F = 3$

Figure A.2: ^{133}Cs **D2 line properties.** Credits: Steck [134]

A.4   HG modes discrimination with a slit-wheel

The slit wheel method for HG beam discrimination [162] consists in letting the beam propagate through a cache with a number of transparent angular sectors equal to the number of bright spots in the beam [2]. If the cache is aligned so that the angular position of the bright spots (defined by the phase ϕ between the pure-OAM components of the beam) matches that of the transparent sectors, then a detector behind the cache will record a maximal intensity. Conversely, if the bright spots are aligned with the opaque sectors, then the detector will record a minimal intensity.

This works very well with a bucked detector placed just after the cache that integrates the intensity over the whole beam section. For single-photon regime operation however, we wished to couple the light into single-mode fibers in order to bring it to our APD. So we installed the cache before the input-BS of figure 3.15 and the subsequent OAM mode projectors. Unfortunately, the mode deformation induced by the cache and the subsequent propagation was too strong for the mode projectors to perform efficiently. When we sent HG beams and when we varied the angle of the cache, we observed intensity minima, but we could not record a full sinusoidal fringe as we could expect if we had a bucket detector. This whole process is summarized in figure A.3.
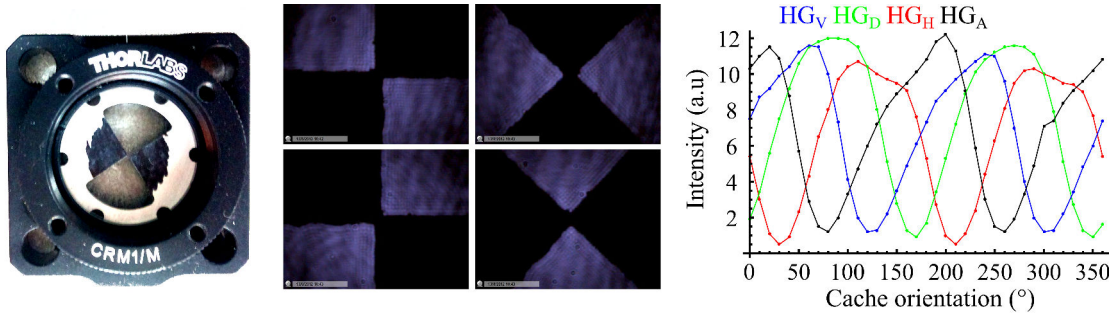
Figure A.3: **Summary of the slit-wheel method trial.** Left: picture of our prototype cache. Midde: images of the cache illuminated with a TEM_{00} beam. The center is well aligned on the beam center and the different positions shown correspond to a projection on the four different HG modes A, H, D and V. Right: power transmitted after the cache *and the LG projection* versus cache orientation for different HG modes. If the minima of the fringes are reasonably well defined, their maxima on the other hand are not at all in agreement with a theoretical sinusoidal behavior. This was due to the fact that we could not use a bucket detector but had to recouple the light into optical fibers instead, using the LG mode projectors described in 3.3.a.

After trying this slit-wheel method, we developed the interferometric device presented in section 3.3.a, which also had the advantage that the results can be more easily interpreted and compared to standard polarization qubit measurements.

---

[2]In fact it works for $LG^{l=+l}$ and $LG^{l=-l}$ superpositions, which happens to be a HG mode in the case of $l = 1$.

A.5   Possibility of higher-dimensional OAM tomography

The OAM tomography setup presented in section 3.3.a is not limited to two-dimensional system analysis and can in principle be extended to higher-dimensional encoding.

To do so, one can introduce additional beam-splitters after the first one. Figure A.4 shows for example an extended setup to perform quantum state tomography in a four-dimensional Hilbert space spanned by the modes $LG^{l=-3}$, $LG^{l=-1}$, $LG^{l=+1}$ and $LG^{l=+3}$. In each of the subsequent paths, a mode projector on a different OAM value is inserted. Keeping an OAM difference $\Delta l = 2$ between different modes ensures a better mode filtering. Fibers at the end of the mode projectors are to be connected to a series of cascading fiber beam-splitters, creating an array of nested interferometers. Alternatively, these nested interferometers could be engraved in photonic circuitry [191, 192], which would also provide greater simplicity and a better phase stability. Similarly to the two-dimensional setup, a phase reference beam is sent backwards. The various unused output ports allow the imaging of the phase reference beams, and the determination of all the relevant phases. The image analysis routine 3.3.b can be directly used to compute the relevant phases between pairs of modes, given the fact that the phase reference is timed in order to image only two-mode superpositions. To do so, mechanical shutters [3] need to be added in the arms of the interferometer array.

One more series of beam splitters would allow quantum tomography in an eight-dimensional space, but it would become challenging and time consuming. Indeed, the addition of more beam-splitters will result in degrading the count rates exponentially in the number of beam splitters (linearly in the number of detected modes). Also the phase measurement and/or stabilization can become a more serious issue if the dimension of Hilbert space increases too much.

Criteria	Current Device	Technique 1	Technique 2
Hilbert space dimension	2	4	15
Losses	75 %	88 %	40 %
Crosstalk Suppression ($\Delta l = 2$)	> 27 dB	> 27 dB	> 30 dB

Table A.4: **Expected performances of two possible extensions of the current device to higher dimensional Hilbert spaces**. Detection efficiency does not take into account the quantum efficiency of the single-photon counters. Technique 1 refers to the multiple input-BS scheme shown in figure A.4 and Technique 2 to the OAM mode sorter scheme shown in figure A.5.

Another way to reach higher-dimensional spaces would be to take advantage of the recently developed OAM mode-sorting techniques [158–160, 193] where OAM states are converted into transverse momentum states. As proposed in figure A.5, the input beam-splitter can indeed be replaced by an OAM mode sorter made out of refractive elements as described in [158] with a separation enhancer [160]. This combination would perform both the separation and mode conversion in the same time, thus largely improving the

---
[3]rise times on the order of ten milliseconds are by far sufficient

detection efficiency and versatility. Indeed, the detection efficiency would remain (almost) constant as the number of detected modes increases. The reduction in the required number of optical elements may also provide a better phase stability.

Table A.4 summarized the performances one can foresee assuming some realistic parameter estimations extracted from [160, 193].

A.6   Example of data table for complete qubit tomography

Mode at input	Config.	X output	Y output
$\vert R\rangle$	L blocked	0.040407	0.018179
	R blocked	0.000309	0.000324
	$\varphi = 0$	0.0390341	0.0186364
	$\varphi = \pi/2$	0.0436709	0.0154430
	$\varphi = \pi$	0.0386111	0.0164444
	$\varphi = 3\pi/2$	0.036705	0.022386
$\vert L\rangle$	L blocked	0.000527	0.000457
	R blocked	0.030068	0.016251
	$\varphi = 0$	0.0306863	0.0164706
	$\varphi = \pi/2$	0.0255	0.020222
	$\varphi = \pi$	0.0307	0.0163
	$\varphi = 3\pi/2$	0.033967	0.015667
$\vert H\rangle$	L blocked	0.016764	0.007461
	R blocked	0.012353	0.006762
	$\varphi = 0$	0.0569388	0.0005357
	$\varphi = \pi/2$	0.0235054	0.0172554
	$\varphi = \pi$	0.0013889	0.0304259
	$\varphi = 3\pi/2$	0.0328398	0.0138835
$\vert D\rangle$	L blocked	0.013232	0.006034
	R blocked	0.015124	0.008112
	$\varphi = 0$	0.0318928	0.0135489
	$\varphi = \pi/2$	0.0567808	0.0006164
	$\varphi = \pi$	0.025389	0.016635
	$\varphi = 3\pi/2$	0.000601	0.0294231

Table A.5: **Photon rates** detected on outputs X and Y for different configurations of the detection setup and for a selection of input qubit modes. As expected, output Y experiences a lower count rate due to the phase reference injection. The mean number of photons per pusle was 0.6. No noise subtraction has been performed. Figure 3.19 displays these data in a more visual way. The Stokes parameters and fidelities given in table 3.7 are computed from the count rates presented here.
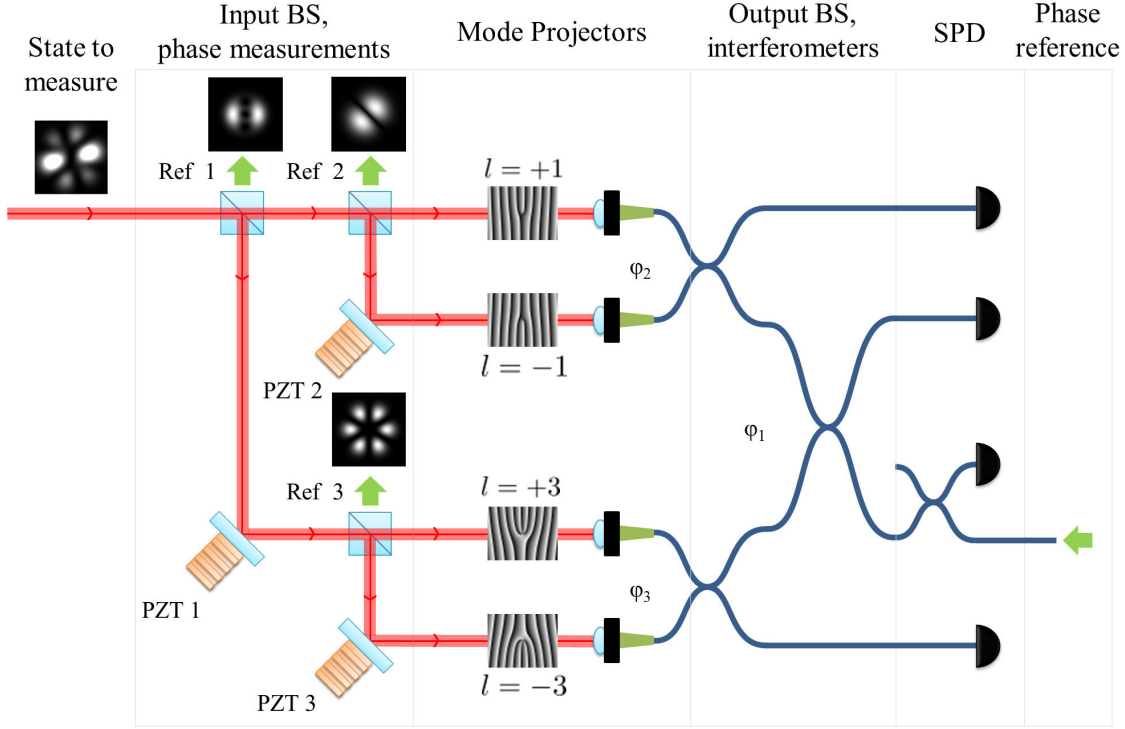
Figure A.4: **Similar setup for quantum state tomography in a four-dimensional Hilbert space** spanned by $|l = -3\rangle$, $|l = -1\rangle$, $|l = +1\rangle$ and $|l = +3\rangle$. The mode to be measured is split between four paths by three cascaded beam-splitters. Each path contains a mode projector based on a fork hologram and a single-mode fiber. The transmitted light (corresponding to different projections on the OAM eigenstates) is brought to interfere in an array of beamsplitters and directed to single-photon detectors (SPD). A phase reference beam (sketched by the green arrows) is injected backwards and detected at the three input beam-splitters. Ref. 1, 2 and 3 denote the outputs of the phase-reference beam allowing to measure the phases $\varphi_{1,2,3}$ respectively. Expected intensity patterns are displayed. In order to get the Ref. 1 intensity pattern (which allows a simple measurement of φ_1), the $l = +1$ and $l = -3$ paths must be blocked, e.g. using fast switching mechanical shutters. The mode displayed at the input, i.e. $|l = +1\rangle + |l = -1\rangle - |l = +3\rangle - \mathrm{i}|l = -3\rangle$, is shown for illustrative purpose.
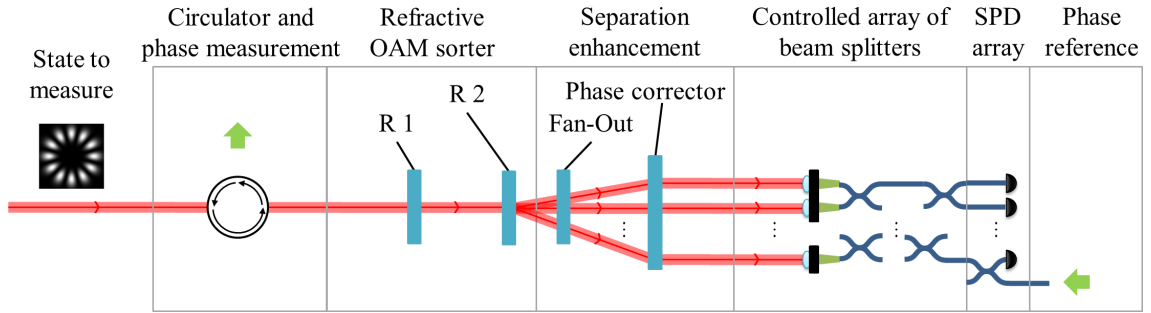
Figure A.5: **A possible alternative implementation** for extending the device to higher-dimensional Hilbert spaces, using mode sorting refractive optics R1 and R2 as developed in [158, 160]. The input beam-splitters and subsequent holograms can be replaced by the combination of a circulator (to separate the signal and the phase reference beam) and an OAM mode sorter made of two refractive elements R1 and R2. The reformatter R1 performs a log-polar to cartesian coordinate mapping and the phase corrector R2 corrects for the different propagation lengths from R1 to R2. These two elements transform copropagating LG beams with different l values into approximate TEM_{00} beams with a propagation direction tilted by an angle proportional to l. The fan-out separation enhancer is a specific periodic phase-only hologram that increases the angular separation between the different modes by decreasing the residual mode-overlap. After being separated and losing their specific spatial shapes, the different OAM components can be brought to interfere in a controlled array of beam-splitters, then directed towards single-photon detectors (SPD). A good timing of the phase reference should be ensured with appropriated shutters inserted in the interferometer array in order to record all the relevant phase differences. The superposition $|l = +6\rangle + |l = -6\rangle$ is shown at the input for illustrative purpose.

Bibliography

[1] Terry Pratchett. *Pyramids*. Corgi, 1989.

[2] Terry Pratchett. *Night Watch*. Corgi, 2002.

[3] Robert Gilmore. *Alice in Quantumland: An Allegory of Quantum Physics*. 1995.

[4] L. Giner, L. Veissier, B. Sparkes, A. S. Sheremet, A. Nicolas, O. S. Mishina, M. Scherman, S. Burks, I. Shomroni, D. V. Kupriyanov, P. K. Lam, E. Giacobino, and J. Laurat1. Experimental investigation of the transition between autler-townes splitting and electromagnetically-induced-transparency models. *Physical Review A*, 87: 013823, 2013.

[5] L. Veissier, A. Nicolas, L. Giner, D. Maxein, A. S. Sheremet, E. Giacobino, and J. Laurat. Reversible optical memory for twisted photons. *Optics Express*, 38:712, 2013.

[6] A. Nicolas, L. Veissier, L. Giner, E. Giacobino, D. Maxein, and J. Laurat. A quantum memory for orbital angular momentum photonic qubits. *Nature Photonics*, 8:234, 2014.

[7] Adrien Nicolas, Lucile Veissier, Elisabeth Giacobino, Dominik Maxein, and Julien Laurat. Quantum state tomography of orbital angular momentum photonic qubits via a projection-based technique. to be submitted, 2014.

[8] Claude Fabre. Atomes et lumière: interaction matière rayonnement, 2010. URL http://hal-sfo.ccsd.cnrs.fr/.

[9] A. Einstein, B. Podolsky, and N. Rosen. Can quantum-mechanical description of physical reality be considered complete? *Physical Review*, 47:777, 1935. doi: 10. 1103/PhysRev.47.777.

[10] L.-M. Duan, M. D. Lukin, J. I. Cirac, and P. Zoller. Long-distance quantum communication with atomic ensembles and linear optics. *Nature*, 414:413, 2001.

[11] P. Zoller, R. Blatt, J. Kempe, A. Sergienko, H. Briegel, L. Kouwenhoven, D. Suter, D. Bruss, S. Kröll, R. Thew, T. Calarco, G. Leuchs, J. Twamley, J.I. Cirac, M. Lewenstein, L. Vandersypen, D. Deutsch, D. Loss, A. Wallraff, J. Eisert, N. Lütkenhaus, G. Wendin, A. Ekert, S. Massar, R. Werner, C. Fabre, J. E. Mooij, A. Winter, N. Gisin, M. B. Plenio, J. Wrachtrup, P. Grangier, E. Polzik, P. Zanardi, M. Grassl, S. Popescu, A. Zeilinger, S. Haroche, G. Rempe, A. Imamoglu, and M. Santha. Quantum information processing and communication: Strategic report on current status, visions and goals for research in europe, February 2013. URL http://qurope.eu/content/Roadmap.

[12] Michael A. Nielsen and Isaac L. Chuang. *Quantum Computation and Quantum Information (Cambridge Series on Information and the Natural Sciences)*. Cambridge University Press, 2000.

[13] Ignacio Cirac and Peter Zoller. Goals and opportunities in quantum simulation. *Nature Physics*, 8:264, 2012.

[14] Immanuel Bloch, Jean Dalibard, and Sylvain Nascimbène. Quantum simulations with ultracold quantum gases. *Nature Physics*, 8:267, 2012.

[15] . URL http://en.wikipedia.org/wiki/Complexity_class.

[16] Peter Shor. Algorithms for quantum computation: Discrete logarithms and factoring. In Los Alamitos IEEE Computer Society Press, editor, *Proceedings of the 35th Annual Symposium on Foundations of Computer Science*, page 124, 1994.

[17] Peter Shor. Polynomial-time algorithms for prime factorization and discrete logarithms on a quantum computer. *SIAM Journal of Computing*, 26:1484, 1997. doi: 10.1137/S0097539795293172.

[18] Lieven M. K. Vandersypen, Matthias Steffen, Gregory Breyta, Costantino S. Yannoni, Mark H. Sherwood, and Isaac L. Chuang. Experimental realization of shor's quantum factoring algorithm using nuclear magnetic resonance. *Nature*, 414:883, 2001.

[19] B. P. Lanyon, T. J. Weinhold, N. K. Langford, M. Barbieri, D. F.V. James, A. Gilchrist, and A. G. White. Experimental demonstration of a compiled version of shor's algorithm with quantum entanglement. *Physical Review Letters*, 99:250505, 2007. doi: 10.1103/PhysRevLett.99.25050510.1103/PhysRevLett.99.250505.

[20] Chao-Yang Lu, Daniel E. Browne, Tao Yang, and Jian-Wei Pan. Demonstration of a compiled version of shor's quantum factoring algorithm using photonic qubits. *Physical Review Letters*, 99:250504, 2007. doi: 10.1103/PhysRevLett.99.250504.

[21] Alberto Politi, Jonathan C. F. Matthews, and Jeremy L. O'Brieny. Shor's quantum factoring algorithm on a photonic chip. *Science*, 325:1221, 2009. doi: 10.1126/science.1173731.

[22] Nanyang Xu, Jing Zhu, Dawei Lu, Xianyi Zhou, Xinhua Peng, and Jiangfeng Du. Quantum factorization of 143 on a dipolar-coupling nuclear magnetic resonance system. *Physical Review Letters*, 108:130501, 2012. doi: 10.1103/PhysRevLett.108.130501.

[23] Lov Kumar Grover. A fast quantum mechanical algorithm for database search. In *Proceedings of the 28th Annual ACM Symposium on the Theory of Computing*, 1996.

[24] Stefanie Barz, Elham Kashefi, Anne Broadbent, Joseph F. Fitzsimons, Anton Zeilinger, and Philip Walther. Experimental demonstration of blind quantum computing. *Science*, 335:303, 2012. doi: 10.1126/science.1214707.

[25] K.-A. Brickman, P. C. Haljan, P. J. Lee, M. Acton, L. Deslauriers, and C. Monroe. Implementation of grover's quantum search algorithm in a scalable system. *Physical Review A*, 72:050306(R), 2005.

[26] Robert Prevedel, Philip Walther, Felix Tiefenbacher, Pascal Böhi, Rainer Kaltenbaek, Thomas Jennewein, and Anton Zeilinger. High-speed linear optics quantum computing using active feed-forward. *Nature*, 445:65, 2007. doi: doi: 10.1038/nature05346.

[27] Aram W. Harrow, Avinatan Hassidim, and Seth Lloyd. Quantum algorithm for linear systems of equations. *Physical Review Letters*, 103:150502, 2009. doi: 10. 1103/PhysRevLett.103.150502.

[28] X.-D. Cai, C. Weedbrook, Z.-E. Su, M.-C. Chen, Mile Gu, M.-J. Zhu, Li Li, Nai-Le Liu, Chao-Yang Lu, and Jian-Wei Pan. Experimental quantum computing to solve systems of linear equations. *Physical Review Letters*, 110:230501, 2013. doi: 10.1103/PhysRevLett.110.230501.

[29] Nathan Wiebe, Daniel Braun, and Seth Lloyd. Quantum algorithm for data fitting. *Physical Review Letters*, 109:050505, 2012. doi: 10.1103/PhysRevLett.109.050505.

[30] Nicola Jones. The quantum company. *Nature*, 498:286, 2013.

[31] Nicolas Gisin and Rob Thew. Quantum communication. *Nature Photonics*, 1:165, 2007.

[32] Jeff H. Kimble. The quantum internet. *Nature*, 453:1023, 2008. doi: 10.1038/ nature07127.

[33] John Steward Bell. On the einstein-podolsky-rosen paradox. *Physics*, 1:195, 1964.

[34] John Steward Bell. *Speakable and unspeakable in quantum mechanics: Collected papers on quantum philosophy.* Cambridge University Press, 1987.

[35] John F. Clauser, Michael A. Horne, Abner Shimony, and Richard A. Holt. Proposed experiment to test local hidden-variable theories. *Physical Review Letters*, 23:880, 1969. doi: 10.1103/PhysRevLett.23.880.

[36] Alain Aspect, Philippe Grangier, and Gérard Roger. Experimental tests of realistic local theories via bell's theorem. *Physical Review Letters*, 47:460, 1981.

[37] C. H. Bennett and G. Brassard. Quantum cryptography: Public key distribution and coin tossing. In *IEEE International Conference on Computers, Systems and Signal Processing*, volume 175, page 8, 1984.

[38] Artur K. Ekert. Quantum cryptography based on bell's theorem. *Physical Review Letters*, 67:661, 1991.

[39] Artur K. Ekert, John G. Rarity, Paul R. Tapster, and G. Massimo Palma. Practical quantum cryptography based on two-photon interferometry. *Physical Review Letters*, 69:1293, 1992.

[40] Charles H. Bennett, Gilles Brassard, and N. David Mermin. Quantum cryptography without bell's theorem. *Physical Review Letters*, 68:557, 1992.

[41] T. C. Ralph. Continuous variable quantum cryptography. *Physical Review A*, 61: 010303(R), 1999. doi: 10.1103/PhysRevA.61.010303.

[42] Mark Hillery. Quantum cryptography with squeezed states. *Physical Review A*, 61: 022309, 2000. doi: 10.1103/PhysRevA.61.022309.

[43] N. J. Cerf, M. Lévy, and G. Van Assche. Quantum distribution of gaussian keys using squeezed states. *Physical Review A*, 63:052311, 2001. doi: 10.1103/PhysRevA. 63.052311.

[44] Frédéric Grosshans and Philippe Grangier. Continuous variable quantum cryptography using coherent states. *Physical Review Letters*, 88:057902, 2002.

[45] Valerio Scarani, Antonio Acín, Grégoire Ribordy, and Nicolas Gisin. Quantum cryptography protocols robust against photon number splitting attacks for weak laser pulses implementations. *Physical Review Letters*, 92:057901, 2004.

[46] W. K. Wootters and W. H. Zurek. A single quantum cannot be cloned. *Nature*, 299: 802, 1982. doi: 10.1038/299802a0.

[47] M. Peev, C. Pacher, R. Alléaume, C. Barreiro, J. Bouda, W. Boxleitner, T. Debuisschert, E. Diamanti, M. Dianati, J. F. Dynes, S. Fasel, S. Fossier, M. Fürst, J.-D. Gautier, O. Gay, N. Gisin, P. Grangier, A. Happe, Y. Hasani, M. Hentschel, H. Hübel, G. Humer, T. Länger, M. Legré, R. Lieger, J. Lodewyck, T. Lorünser, N. Lütkenhaus, A. Marhold, T. Matyus, O. Maurhart, L. Monat, S. Nauerth, J.-B. Page, A. Poppe, E. Querasser, G. Ribordy, S. Robyr, L. Salvail, A. W. Sharpe, A. J. Shields, D. Stucki, M. Suda, C. Tamas, T. Themel, R. T. Thew, Y. Thoma, A. Treiber, P. Trinkler, R. Tualle-Brouri, F. Vannel, N. Walenta, H. Weier, H. Weinfurter, I. Wimberger, Z. L. Yuan, H. Zbinden, and A. Zeilinger. The secoqc quantum key distribution network in vienna. *New Journal of Physics*, 11:075001, 2009.

[48] Abdul Mirza and Francesco Petruccione. Realizing long-term quantum cryptography. *Journal of the Optical Society of America B: Optical Physics*, 27:A185, 2010. doi: 10.1364/JOSAB.27.00A185.

[49] J. Brendel, N. Gisin, W. Tittel, and H. Zbinden. Pulsed energy-time entangled twin-photon source for quantum communication. *Physical Review Letters*, 82:2594, 1999.

[50] R. T. Thew, S. Tanzilli, W. Tittel, H. Zbinden, and N. Gisin. Experimental investigation of the robustness of partially entangled qubits over 11 km. *Physical Review A*, 66:062304, 2002.

[51] Rupert Ursin, Thomas Jennewein, Johannes Kofler, Josep M. Perdigues, Luigi Cacciapuoti, Clovis J. de Matos, Markus Aspelmeyer, Alejandra Valencia, Thomas Scheidl, Alessandro Fedrizzi, Antonio Acin, Cesare Barbieri, Giuseppe Bianco, Caslav Brukner, Jose Capmany, Sergio Cova, Dirk Giggenbach, Walter Leeb, Robert H. Hadfield, Raymond Laflamme, Norbert Lutkenhaus, Gerard Milburn, Momtchil Peev, Timothy Ralph, John Rarity, Renato Renner, Etienne Samain, Nikolaos Solomos, Wolfgang Tittel, Juan P. Torres, Morio Toyoshima, Arturo Ortigosa-Blanch, Valerio Pruneri, Paolo Villoresi, Ian Walmsley, Gregor Weihs, Harald Weinfurter, Marek Zukowski, and Anton Zeilinger. Space-quest: Experiments with quantum entanglement in space. In *IAC Proceedings A2.1.3*, 2008.

[52] Thomas Scheidl, Eric Wille, and Rupert Ursin. Quantum optics experiments to the international space station iss: a proposal. *New Journal of Physics*, 15:043008, 2013. doi: 10.1088/1367-2630/15/4/043008.

[53] D. Stucki, N .Walenta, F. Vannel, R. T. Thew, N. Gisin, H. Zbinden, S. Gray, C. R. Towery, and S. Ten. High rate, long-distance quantum key distribution over 250 km of ultra low loss fibres. *New Journal of Physics*, 11:075003, 2009.

[54] Paul Jouguet, Sébastien Kunz-Jacques, Anthony Leverrier, Philippe Grangier, and Eleni Diamanti. Experimental demonstration of long-distance continuous-variable quantum key distribution. *Nature Photonics*, 7:378, 2013.

[55] H.-J. Briegel, W. Dür, J. I. Cirac, and P. Zoller. Quantum repeaters: The role of imperfect local operations in quantum communication. *Physical Review Letters*, 81: 5932, 1998.

[56] Charles H. Bennett, Gilles Brassard, Claude Crépeau, Richard Jozsa, Asher Peres, and William K. Wootters. Teleporting an unknown quantum state via dual classical and einstein-podolsky-rosen channels. *Physical Review Letters*, 70:1895, 1993. doi: 10.1103/PhysRevLett.70.1895.

[57] Dik Bouwmeester, Jian-Wei Pan, Klaus Mattle, Manfred Eibl, Harald Weinfurter, and Anton Zeilinger. Experimental quantum teleportation. *Nature*, 390:575, 1997.

[58] A. Furusawa, J. L. Sørensen, S. L. Braunstein, C. A. Fuchs, H. J. Kimble, and E. S. Polzik. Unconditional quantum teleportation. *Science*, 282:5389, 1998. doi: 10.1126/science.282.5389.706.

[59] I. Marcikic, H. de Riedmatten, W. Tittel, H. Zbinden, and N. Gisin. Long-distance teleportation of qubits at telecommunication wavelengths. *Nature*, 421:509, 2003.

[60] Jian-Wei Pan, Dik Bouwmeester, Harald Weinfurter, and Anton Zeilinger. Experimental entanglement swapping: Entangling photons that never interacted. *Physical Review Letters*, 80:3891, 1998. doi: 10.1103/PhysRevLett.80.3891.

[61] W. J. Munro, K. A. Harrison, A. M. Stephens, S. J. Devitt, and Kae Nemoto. From quantum multiplexing to high-performance quantum networking. *Nature Photonics*, 4:792, 2010. doi: doi:10.1038/nphoton.2010.213.

[62] Nicolas Sangouard, Christoph Simon, Hugues de Riedmatten, and Nicolas Gisin. Quantum repeaters based on atomic ensembles and linear optics. *Reviews of Modern Physics*, 83:33, 2011. doi: 10.1103/RevModPhys.83.33.

[63] S. Tanzilli, W. Tittel, M. Halder, O. Alibart, P. Baldi, N. Gisin, and H. Zbinden. A photonic quantum information interface. *Nature*, 437:116, 2005. doi: 10.1038/nature04009.

[64] Rikizo Ikuta, Yoshiaki Kusaka, Tsuyoshi Kitano, Hiroshi Kato, Takashi Yamamoto, Masato Koashi, and Nobuyuki. Wide-band quantum interface for visible-to-telecommunication wavelength conversion. *Nature Communications*, 2:537, 2011. doi: 10.1038/ncomms1544.

[65] A. D. Boozer, A. Boca, R. Miller, T. E. Northup, and H. J. Kimble. Reversible state transfer between light and a single trapped atom. *Physical Review Letters*, 98: 193601, 2007.

[66] Holger P. Specht, Christian Nölleke, Andreas Reiserer, Manuel Uphoff, Eden Figueroa, Stephan Ritter, and Gerhard Rempe. A single-atom quantum memory. *Nature*, 473:190, 2011. doi: 10.1038/nature09997.

[67] Stephan Ritter, Christian Nölleke, Carolin Hahn, Andreas Reiserer, Andreas Neuzner, Manuel Uphoff, Martin Mücke, Eden Figueroa, Joerg Bochmann, and Gerhard Rempe. An elementary quantum network of single atoms in optical cavities. *Nature*, 484:195, 2012. doi: 10.1038/nature11023.

[68] Nicolas Sangouard, Romain Dubessy, and Christoph Simon. Quantum repeaters based on single trapped ions. *Physical Review A*, 79:042340, 2009.

[69] L.-M. Duan and C. Monroe. Colloquium: Quantum networks with trapped ions. *Reviews of Modern Physics*, 82:1209, 2010. doi: 10.1103/RevModPhys.82.1209.

[70] C. Langer, R. Ozeri, J. D. Jost, J. Chiaverini, B. DeMarco, A. Ben-Kish, R. B. Blakestad, J. Britton, D. B. Hume, W. M. Itano, D. Leibfried, R. Reichle, T. Rosenband, T. Schaetz, P. O. Schmidt, and D. J. Wineland. Long-lived qubit memory using atomic ions. *Physical Review Letters*, 95:060502, 2005.

[71] S. Olmschenk, D. N. Matsukevich, P. Maunz, D. Hayes, L.-M. Duan, and C. Monroe. Quantum teleportation between distant matter qubits. *Science*, 323:486, 2009. doi: 10.1126/science.1167209.

[72] Christoph Kurz, Michael Schug, Pascal Eich, Jan Huwer, Philipp Müller, and Jürgen Eschner. High-fidelity heralded photon-to-atom quantum state transfer. arXiv e-print, 2013. URL http://arxiv.org/abs/1312.5995.

[73] Philipp Müller and Jürgen Eschner. Single calcium-40 ion as quantum memory for photon polarization: a case study. *Applied Physics B*, 114:303, 2014. doi: 10.1007/s00340-013-5681-1.

[74] E. Togan, Y. Chu, A. S. Trifonov, L. Jiang, J. Maze, L. Childress, M. V. G. Dutt, A. S. Sørensen, P. R. Hemmer, A. S. Zibrov, and M. D. Lukin. Quantum entanglement between an optical photon and a solid-state spin qubit. *Nature*, 466:730, 2010. doi: 10.1038/nature09256.

[75] G. D. Fuchs, G. Burkard, P. V. Klimov, and D. D. Awschalom. A quantum memory intrinsic to single nitrogen–vacancy centres in diamond. *Nature Physics*, 7:789, 2011. doi: 10.1038/NPHYS2026.

[76] P. C. Maurer, G. Kucsko, C. Latta, L. Jiang, N. Y. Yao, S. D. Bennett, F. Pastawski, D. Hunger, N. Chisholm, M. Markham, D. J. Twitchen, J. I.Cirac, and M. D. Lukin. Room-temperature quantum bit memory exceeding one second. *Science*, 336:1283, 2012.

[77] H. Bernien, B. Hensen, W. Pfaff, G. Koolstra, M. S. Blok, L. Robledo, T. H. Taminiau, M. Markham, D. J. Twitchen, L. Childress, and R. Hanson. Heralded

entanglement between solid-state qubits separated by three metres. *Nature*, 497:86, 2013. doi: 10.1038/nature12016.

[78] Kristiaan De Greve, Leo Yu, Peter L. McMahon, Jason S. Pelc, Chandra M. Natarajan, Na Young Kim, Eisuke Abe, Sebastian Maier, Christian Schneider, Martin Kamp, Sven Höfling, Robert H. Hadfield, Alfred Forchel, M. M. Fejer, and Yoshihisa Yamamoto. Quantum-dot spin–photon entanglement via frequency downconversion to telecom wavelength. *Nature*, 491:421, 2012. doi: 10.1038/nature11577.

[79] W. B. Gao, P. Fallahi, E. Togan, J. Miguel-Sanchez, and A. Imamoglu. Observation of entanglement between a quantum dot spin and a single photon. *Nature*, 491:426, 2012. doi: 10.1038/nature11573.

[80] Lene Vestergaard Hau, S. E. Harris, Zachary Dutton, and Cyrus H. Behroozi. Light speed reduction to 17 metres per second in an ultracold atomic gas. *Nature*, 397:594, 1999.

[81] Chien Liu, Zachary Dutton, Cyrus H. Behroozi, and Lene Vestergaard Hau. Observation of coherent optical information storage in an atomic medium using halted light pulses. *Nature*, 409:490, 2001.

[82] Julien Laurat, Chin wen Chou, Hui Deng, Kyung Soo Choi, Daniel Felinto, Hugues de Riedmatten, and H. J. Kimble. Towards experimental entanglement connection with atomic ensembles in the single excitation regime. *New Journal of Physics*, 9: 207, 2007.

[83] B. M. Sparkes, J. Bernu, M. Hosseini, J. Geng, Q. Glorieux, P. A. Altin, P. K. Lam, N. P. Robins, and B. C. Buchler. Gradient echo memory in an ultra-high optical depth cold atomic ensemble. *New Journal of Physics*, 15:085027, 2013. doi: 10.1088/1367-2630/15/8/085027.

[84] D. F. Phillips, A. Fleischhauer, A. Mair, and R. L. Walsworth. Storage of light in atomic vapor. *Physical Review Letters*, 86:783, 2001. doi: 10.1103/PhysRevLett.86. 783.

[85] K. F. Reim, P. Michelberger, K.C. Lee, J. Nunn, N. K. Langford, and I. A. Walmsley. Single-photon-level quantum memory at room temperature. *Physical Review Letters*, 107:053603, 2010. doi: 10.1103/PhysRevLett.107.053603.

[86] Michael Scherman. *Transparence induite électromagnétiquement et mémoires quantiques sur la raie D2 du césium : effet de l'élargissement inhomogène dans une structure atomique multi-niveaux*. PhD thesis, Université Pierre et Marie Curie, 2012.

[87] M. Hosseini, G. Campbell, B. M. Sparkes, P. K. Lam, and B. C. Buchler. Unconditional room-temperature quantum memory. *Nature Physics*, 7:794, 2011.

[88] Brian Julsgaard, Jacob Sherson, J. Ignacio Cirac, Jaromír Fiurášek, and Eugene S. Polzik. Experimental demonstration of quantum memory for light. *Nature*, 432:482, 2004.

[89] A. V. Turukhin, V. S. Sudarshanam, M. S. Shahriar, J. A. Musser, B. S. Ham, and P. R. Hemmer. Observation of ultraslow and stored light pulses in a solid. *Physical Review Letters*, 88:023602, 2002.

[90] A. L. Alexander, J. J. Longdell, M. J. Sellars, and N. B. Manson. Photon echoes produced by switching electric fields. *Physical Review Letters*, 96:043602, 2006. doi: 10.1103/PhysRevLett.96.043602.

[91] Christoph Clausen, Imam Usmani, Félix Bussières, Nicolas Sangouard, Mikael Afzelius, Hugues de Riedmatten, and Nicolas Gisin. Quantum storage of photonic entanglement in a crystal. *Nature*, 469:508, 2001. doi: 10.1038/nature09662.

[92] Mikael Afzelius Christoph Clausen, Félix Bussières and Nicolas Gisin. Quantum storage of heralded polarization qubits in birefringent and anisotropically absorbing materials. *Physical Review Letters*, 108:190503, 2012. doi: 10.1103/PhysRevLett. 108.190503.

[93] Mustafa Gündoğan, Patrick M. Ledingham, Attaallah Almasi, Matteo Cristiani, and Hugues de Riedmatten. Quantum storage of a photonic polarization qubit in a solid. *Physical Review Letters*, 108:190504, 2012. doi: 10.1103/PhysRevLett.108.190504.

[94] Zong-Quan Zhou, Wei-Bin Lin, Ming Yang, Chuan-Feng Li, and Guang-Can Guo. Realization of reliable solid-state quantum memory for photonic polarization qubit. *Physical Review Letters*, 108:190505, 2012.

[95] V. Damon, M. Bonarota, A. Louchet-Chauvet, T. Chanelière, and J.-L. Le Gouët. Revival of silenced echo and quantum memory for light. *New Journal of Physics*, 13: 093031, 2011. doi: 10.1088/1367-2630/13/9/093031.

[96] Khabat Heshami, Charles Santori, Behzad Khanaliloo, Chris Healey, Victor M. Acosta, Paul E. Barclay, and Christoph Simon. Raman quantum memory based on an ensemble of nitrogen-vacancy centers coupled to a microcavity. *Physical Review A*, 89:040301, 2014. doi: 10.1103/PhysRevA.89.040301.

[97] Xiao-Hui Bao, Andreas Reingruber, Peter Dietrich, Jun Rui, Alexander Dück, Thorsten Strassel, Li Li, Nai-Le Liu, Bo Zhao, and Jian-Wei Pan. Efficient and long-lived quantum memory with cold atoms inside a ring cavity. *Nature Physics*, 8: 517, 2012. doi: 10.1038/NPHYS2324.

[98] Alexander I. Lvovsky, Barry C. Sanders, and Wolfgang Tittel. Optical quantum memory. *Nature photonics*, 3:706, 2009. doi: 10.1038/nphoton.2009.231.

[99] C. Simon, M. Afzelius, J. Appel, A. Boyer de la Giroday, S. J. Dewhurst, N. Gisin, C. Y. Hu, F. Jelezko, S. Kröl, J. H. Müller, J. Nunn, E. S. Polzik, J. G. Rarity, H. De Riedmatten, W. Rosenfeld, A. J. Shields, N. Sköld, R. M. Stevenson, R. Thew, I. A. Walmsley, M. C. Weber, H. Weinfurter, J. Wrachtrup, and R. J. Young. Quantum memories: A review based on the european integrated project "qubit applications (qap)". *European Physical Journal D: Atomic, Molecular and Optical Physics*, 58:1, 2012. doi: 10.1140/epjd/e2010-00103-y.

[100] Félix Bussières, Nicolas Sangouard, Mikael Afzelius, Hugues de Riedmatten, Christoph Simon, and Wolfgang Tittel. Prospective applications of optical quantum memories. *Journal of Modern Optics*, 60:1519, 2013.

[101] T. Chanelière, D. N. Matsukevich, S. D. Jenkins, S.-Y. Lan, T. A. B. Kennedy, and A. Kuzmich. Storage and retrieval of single photons transmitted between remote quantum memories. *Nature*, 438:833, 2005.

[102] M. D. Eisaman, A. André, F. Massou, M. Fleischhauer, A. S. Zibrov, and M. D. Lukin. Electromagnetically induced transparency with tunable single-photon pulses. *Nature*, 438:837, 2005.

[103] K. S. Choi, H. Deng, J. Laurat, and H. J. Kimble. Mapping photonic entanglement into and out of a quantum memory. *Nature*, 452:67, 2008. doi: 10.1038/nature06670.

[104] Jürgen Appel, Eden Figueroa, Dmitry Korystov, M. Lobino, and A. I. Lvovsky. Quantum memory for squeezed light. *Physical Review Letters*, 110:093602, 2008.

[105] Kazuhito Honda, Daisuke Akamatsu, Manabu Arikawa, Yoshihiko Yokoi, Keiichirou Akiba, Satoshi Nagatsuka, Takahito Tanimura, Akira Furusawa, and Mikio Kozuma. Storage and retrieval of a squeezed vacuum. *Physical Review Letters*, 100:093601, 2008.

[106] M. Lettner, M. Mücke, S. Riedl, C. Vo, C. Hahn, S. Baur, J. Bochmann, S. Ritter, S. Dürr, and G. Rempe. Remote entanglement between a single atom and a bose-einstein condensate. *Physical Review Letters*, 106:210503, 2011. doi: 10.1103/PhysRevLett.106.210503.

[107] Stefan Riedl, Matthias Lettner, Christoph Vo, Simon Baur, Gerhard Rempe, and Stephan Dürr. Bose-einstein condensate as a quantum memory for a photonic polarization qubit. *Physical Review A*, 85:022318, 2012. doi: 10.1103/PhysRevA.85.022318.

[108] Zhongxiao Xu, Yuelong Wu, Long Tian, Lirong Chen, Zhiying Zhang, Zhihui Yan, Shujing Li, Hai Wang, Changde Xie, and Kunchi Peng. Long lifetime and high-fidelity quantum memory of photonic polarization qubit by lifting zeeman degeneracy. *Physical Review Letters*, 111:240503, 2013.

[109] Y. O. Dudin, L. Li, and A. Kuzmich. Light storage on the time scale of a minute. *Physical Review A*, 87:031801(R), 2013.

[110] Yi-Hsin Chen, Meng-Jung Lee, I-Chung Wang, Shengwang Du, Yong-Fan Chen, Ying-Cheng Chen, and Ite A. Yu. Coherent optical memory with high storage efficiency and large fractional delay. *Physical Review Letters*, 110:083601, 2013.

[111] A. G. Radnaev, Y. O. Dudin, R. Zhao, H. H. Jen, S. D. Jenkins, A. Kuzmich, and T. A. B. Kennedy. A quantum memory with telecom-wavelength conversion. *Nature Physics*, 6:894, 2010. doi: doi:10.1038/nphys1773.

[112] Denis V. Vasilyev, Ivan V. Sokolov, and Eugene S. Polzik. Quantum memory for images: A quantum hologram. *Physical Review A*, 77:020302(R), 2008. doi: 10.1103/PhysRevA.77.020302.

[113] R. Inoue, N. Kanai, T. Yonehara, Y. Miyamoto, M. Koashi, and M. Kozuma. Entanglement of orbital angular momentum states between an ensemble of cold atoms and a photon. *Physical Review A: Atomic, Molecular, and Optical Physics*, 74:053809, 2006. doi: 10.1103/PhysRevA.74.053809.

[114] R. Inoue, T. Yonehara, Y. Miyamoto, M. Koashi, and M. Kozuma. Measuring qutrit-qutrit entanglement of orbital angular momentum states of an atomic ensemble and

a photon. *Physical Review Letters*, 103:110503, 2009. doi: 10.1103/PhysRevLett. 103.110503.

[115] Benjamen M. Sparkes. *Storage and Manipulation of Optical Information Using Gradient Echo Memory in Warm Vapours and Cold Ensembles.* PhD thesis, Australian National University, 2013.

[116] M. Hosseini, B. M. Sparkes, G. Campbell, P.K. Lam, and B.C. Buchler. High efficiency coherent optical memory with warm rubidium vapour. *Nature communications*, 2:174, 2011. doi: 10.1038/ncomms1175.

[117] Mahmood Sabooni, Qian Li, Stefan Kröll, and Lars Rippe. Efficient quantum memory using a weakly absorbing sample. *Physical Review Letters*, 110:133604, 2013. doi: 10.1103/PhysRevLett.110.133604.

[118] Mikael Afzelius, Imam Usmani, Atia Amari, Björn Lauritzen, Andreas Walther, Christoph Simon, Nicolas Sangouard, Jiří Minář, Hugues de Riedmatten, Nicolas Gisin, and Stefan Kröll. Demonstration of atomic frequency comb memory for light with spin-wave storage. *Physical Review Letters*, 104:040503, 2010. doi: 10.1103/PhysRevLett.104.040503.

[119] M. Bonarota, J.-L. Le Gouët, and T. Chanelière. Highly multimode storage in a crystal. *New Journal of Physics*, 13:013013, 2011. doi: 10.1088/1367-2630/13/1/013013.

[120] J. J. Longdell, E. Fraval, M. J. Sellars, and N. B. Manson. Stopped light with storage times greater than one second using electromagnetically induced transparency in a solid. *Physical Review Letters*, 95:063601, 2005. doi: 10.1103/PhysRevLett.95.063601.

[121] Tony Y. Abi-Salloum. Electromagnetically induced transparency and autler-townes splitting: Two similar but distinct phenomena in two categories of three-level atomic systems. *Physical Review A*, 81:053836, 2010.

[122] Petr M. Anisimov, Jonathan P. Dowling, and Barry C. Sanders. Objectively discerning autler-townes splitting from electromagnetically induced transparency. *Physical Review Letters*, 107:163604, 2011.

[123] A. S. Sheremet, L. V. Gerasimov, I. M. Sokolov, D. V. Kupriyanov, O. S. Mishina, E. Giacobino, and J. Laurat. Quantum memory for light via a stimulated off-resonant raman process: Beyond the three-level λ-scheme approximation. *Physical Review A*, 82:033838, 2010.

[124] O. S. Mishina, M. Scherman, P. Lombardi, J. Ortalo, D. Felinto, A. S. Sheremet, A. Bramati, D. V. Kupriyanov, J. Laurat, and E. Giacobino. Electromagnetically induced transparency in an inhomogeneously broadened lambda transition with multiple excited levels. *Physical Review A*, 83:053809, 2011.

[125] Lambert Giner. *Etude de la Transparence Electromagnétiquement Induite dans un ensemble d'atomes froids et application aux mémoires quantiques.* PhD thesis, Université Pierre et Marie Curie, 2013.

[126] Lucile Veissier. *Quantum memory protocols in large cold atomic ensembles.* PhD thesis, Université Pierre et Marie Curie, 2013.

[127] M. Fleischhauer and M. D. Lukin. Dark-state polaritons in electromagnetically induced transparency. *Physical Review Letters*, 84:5094, 2000.

[128] M. Fleischhauer and M. D. Lukin. Quantum memory for photons: Dark-state polaritons. *Physical Review A*, 65:022314, 2001.

[129] M. D. Lukin. Colloquium: Trapping and manipulating photon states in atomic ensembles. *Reviews of Modern Physics*, 75:457, 2003.

[130] Michael Fleischhauer, Atac Imamoglu, and Jonathan P. Marangos. Electromagnetically induced transparency: Optics in coherent media. *Reviews of Modern Physics*, 77:633, 2005.

[131] A. B. Matsko, Y. V. Rostovtsev, O. Kocharovskaya, A. S. Zibrov, and M. O. Scully. Nonadiabatic approach to quantum optical information storage. *Physical Review A*, 64:043809, 2001. doi: 10.1103/PhysRevA.64.043809.

[132] M. Scherman, O. S. Mishina, P. Lombardi, E. Giacobino, and J. Laurat. Enhancing electromagnetically-induced transparency in a multilevel broadened medium. *Optics Express*, 20:4346, 2012.

[133] Jean Cviklinski. *Interface quantique atomes-champs en régime de variable continues.* PhD thesis, Université Pierre et Marie Curie, 2008.

[134] Daniel A. Steck. Cesium d line data, 1998. URL http://steck.us/alkalidata.

[135] D. Felinto, C. W. Chou, H. de Riedmatten, S. V. Polyakov, and H. J. Kimble. Control of decoherence in the generation of photon pairs from atomic ensembles. *Physical Review A*, 72:053809, 2005. doi: 10.1103/PhysRevA.72.053809.

[136] Rudolf Grimm, Matthias Weidemüller, and Yurii B. Ovchinnikov. Optical dipole traps for neutral atoms. In Benjamin Bederson and Herbert Walther, editors, *""*, volume 42 of *Advances In Atomic, Molecular, and Optical Physics*, page 95. Academic Press, 2000. doi: http://dx.doi.org/10.1016/S1049-250X(08)60186-X.

[137] X. Baillard, A. Gauguet, S. Bize, P. Lemonde, P. Laurent, A. Clairon, and P. Rosenbusch. Interference-filter-stabilized external-cavity diode lasers. *Optics Communications*, 266:609, 2006.

[138] R. Pugatch, M. Shuker, O. Firstenberg, A. Ron, and N. Davidson. Topological stability of stored optical vortices. *Physical Review Letters*, 98:203601, 2007. doi: 10.1103/PhysRevLett.98.203601.

[139] D. Moretti, D. Felinto, and J. W. R. Tabosa. Collapses and revivals of stored orbital angular momentum of light in a cold-atom ensemble. *Physical Review A*, 79:023225, 2009. doi: 10.1103/PhysRevA.79.023825.

[140] L. Allen, S.M. Barnett, and M.J. Padgett, editors. *Optical angular momentum.* Optics and Optoelectronics. Institute of Physics Publishing, 2003. ISBN 978-0750309011.

[141] Eleonora Nagali and Fabio Sciarrino. *Manipulation of photonic orbital angular momentum for quantum information processing.* Advanced Photonic Sciences, 2012. URL http://cdn.intechopen.com/pdfs-wm/33195.pdf.

[142] Dong-Sheng Ding, Zhi-Yuan Zhou, Bao-Sen Shi, and Guang-Can Guo. Single-photon-level quantum image memory based on cold atomic ensembles. *Nature Communications*, 4:2527, 2013. doi: 10.1038/ncomms3527.

[143] L. Allen, M. W. Beijersbergen, R. J. C. Spreeuw, and J. P. Woerdman. Orbital angular momentum of light and the transformation of laguerre-gaussian laser modes. *Physical Review A*, 45:8185, 1992. doi: 10.1103/PhysRevA.45.8185.

[144] William N. Plick, Radek Lapkiewicz, Sven Ramelow, and Anton Zeilinger. The forgotten quantum number: A short note on the radial modes of laguerre-gauss beams, 2013. URL http://arxiv.org/abs/1306.6517.

[145] E. Karimi, R. W. Boyd, P. de la Hoz, H. de Guise, J. Řeháček, Z. Hradil, A. Aiello, G. Leuchs, and L. L. Sánchez-Soto. Radial quantum number of laguerre-gauss modes. *Physical Review A*, 89:063813, 2014.

[146] Gabriel Molina-Terriza, Juan P. Torres, and Lluis Torner. Management of the angular momentum of light: Preparation of photons in multidimensional vector states of angular momentum. *Physical Review Letters*, 88:016301, 2001. doi: 10.1103/PhysRevLett.88.013601.

[147] Mohamed Bourennane, Anders Karlsson, Gunnar Björk, Nicolas Gisin, and Nicolas J. Cerf. Quantum key distribution using multilevel encoding: security analysis. *JOURNAL OF PHYSICS A: MATHEMATICAL AND GENERAL*, 35:10065, 2002.

[148] Jean-François Morizur. *Quantum protocols with transverse spatial modes.* PhD thesis, Australian National University and Université Pierre et Marie Curie, 2011.

[149] . URL http://en.wikipedia.org/wiki/Gerchberg-Saxton_algorithm.

[150] M. W. Beijersbergen, L. Allen, H. E. L. O. Van der Veen, and J. P.Woerdman. Astigmatic laser mode converters and transfer of orbital angular momentum. *Optics Communications*, 96:123, 1992.

[151] J. Leach, M. R. Dennis, J. Courtial, and M. J. Padgett. Vortex knots in light. *New Journal of Physics*, 7:55, 2005. doi: 10.1088/1367-2630/7/1/055.

[152] Daniel F. V. James, Paul G. Kwiat, William J. Munro, and Andrew G. White. Measurement of qubits. *Physical Review A*, 64:052312, 2001. doi: 10.1103/PhysRevA.64.052312.

[153] Alois Mair, Alipasha Vaziri, Gregor Weihs, and Anton Zeilinger. Entanglement of the orbital angular momentum states of photons. *Nature*, 412:313, 2001.

[154] Adetunmise C. Dada, Jonathan Leach, Gerald S. Buller, Miles J. Padgett, and Erika Andersson. Experimental high-dimensional two-photon entanglement and violations of generalized bell inequalities. *Nat Phys*, 7:677–680, 2011. doi: 10.1038/nphys1996.

[155] Mikhail V. Vasnetsov, V. V. Slyusar, and Marat S. Soskin. Mode separator for a beam with an off-axis optical vortex. *Quantum Electron.*, 31:464, 2001. doi: 10.1070/ QE2001v031n05ABEH001980.

[156] Jonathan Leach, Miles J. Padgett, Stephen M. Barnett, Sonja Franke-Arnold, and Johannes Courtial. Measuring the orbital angular momentum of a single photon. *Phys. Rev. Lett.*, 88:257901, 2002. doi: 10.1103/PhysRevLett.88.257901.

[157] Gregorius C. G. Berkhout, Martin P. J. Lavery, Johannes Courtial, Marco W. Beijersbergen, , and Miles J. Padgett. Efficient sorting of orbital angular momentum states of light. *Phys. Rev. Lett.*, 105:153601, 2010. doi: 10.1103/PhysRevLett.105.153601.

[158] Martin P. J. Lavery, David J. Robertson, Gregorius C. G. Berkhout, Gordon D. Love, Miles J. Padgett, and Johannes Courtial. Refractive elements for the measurement of the orbital angular momentum of a single photon. *Opt. Express*, 20(3):2110–2115, 2012. doi: 10.1364/OE.20.002110.

[159] Malcolm N. O'Sullivan, Mohammad Mirhosseini, Mehul Malik, and Robert W. Boyd. Near-perfect sorting of orbital angular momentum and angular position states of light. *Opt. Express*, 20(22):24444–24449, 2012. doi: 10.1364/OE.20.024444.

[160] Mohammad Mirhosseini, Mehul Malik, Zhimin Shi, and Robert W. Boyd. Effcient separation of light's orbital angular momentum. *Nature Communications*, 4:2781, 2013. doi: 10.1038/ncomms3781.

[161] Jean-François Morizur, Lachlan Nicholls, Pu Jian, Seiji Armstrong, Nicolas Treps, Boris Hage, Magnus Hsu, Warwick Bowen, Jiri Janousek, and Hans-A. Bachor. Programmable unitary spatial mode manipulation. *JOSA A*, 27:2524–2531, 2010. doi: 10.1364/JOSAA.27.002524.

[162] Robert Fickler, Radek Lapkiewicz, William N. Plick, Mario Krenn, Christoph Schaeff, Sven Ramelow, and Anton Zeilinger. Quantum entanglement of high angular momenta. *Science*, 338:640, 2012.

[163] J. Laherrère and D. Sornette. Stretched exponential distributions in nature and economy: "fat tails" with characteristic scales. *Eur. Phys. J. B*, 2(4):525–539, 1998. doi: 10.1007/s100510050276.

[164] S. Garcia, D. Maxein, L. Hohmann, J. Reichel, and R. Long. Fiber-pigtailed optical tweezer for single-atom trapping and single-photon generation. *Applied Physics Letters*, 103(11):114103, 2013. doi: http://dx.doi.org/10.1063/1.4821160. URL http://scitation.aip.org/content/aip/journal/apl/103/11/10.1063/1.4821160.

[165] Jörg Enderlein and Ingo Gregor. Using fluorescence lifetime for discriminating detector afterpulsing in fluorescence-correlation spectroscopy. *Review of Scientific Instruments*, 76(3):033102, 2005. doi: http://dx.doi.org/10.1063/1.1863399. URL http://scitation.aip.org/content/aip/journal/rsi/76/3/10.1063/1.1863399.

[166] Bahaa E. A. Saleh and Malvin Carl Teich. *Fundamentals of photonics. Chapter 8: Fiber optics.* Wiley series in pure and applied optics. Wiley, New York, 1. [dr.] edition, 1991. ISBN 0-471-83965-5.

[167] I. H. Malitson. Interspecimen comparison of the refractive index of fused silica. *J. Opt. Soc. Am.*, 55(10):1205–1208, Oct 1965. doi: 10.1364/JOSA.55.001205. URL http://www.opticsinfobase.org/abstract.cfm?URI=josa-55-10-1205.

[168] Marcos Curty and Norbert Lütkenhaus. Intercept-resend attacks in the bennett-brassard 1984 quantum-key-distribution protocol with weak coherent pulses. *Physical Review A*, 71:062301, 2005. doi: 10.1103/PhysRevA.71.062301.

[169] S. Massar and S. Popescu. Optimal extraction of information from finite quantum ensembles. *Physical Review Letters*, 74:1259, 1995.

[170] J. D. Love, W. M. Henry, W. J. Stewart, R. J. Black, S. Lacroix, and F. Gonthier. Tapered single-mode fibres and devices. part 1: Adiabaticity criteria. *IEE Proceedings J (Optoelectronics)*, 138:343, 1991. URL http://digital-library.theiet.org/content/journals/10.1049/ip-j.1991.0060.

[171] Yves Cand''ela. *Microcavités de silice : Excitation par fibre des modes de galerie et fonctionnalisation par des nanocristaux de silicium.* PhD thesis, Université Pierre et Marie Curie, 2011.

[172] V. I. Balykin, K. Hakuta, Fam Le Kien, J. Q. Liang, and M. Morinaga. Atom trapping and guiding with a subwavelength-diameter optical fiber. *Physical Review A*, 70:011401(R), 2004.

[173] Brambilla. Optical fibre nanowires and microwires: a review. *Journal of Optics*, 12: 043001, 2010.

[174] M. Morrissey, K. Deasy, M. Frawley, R. Kumar, E. Prel, L. Russell, V. G. Truong, and S. Nic Chormaic. Spectroscopy, manipulation and trapping of neutral atoms, molecules, and other particles using optical nanofibers: A review. *Sensors*, 13:10449, 2013. doi: 10.3390/s130810449.

[175] Allan W. Snyder and John D. Love. *Optical waveguide theory.* "", 1983.

[176] Jan Petersen, Jürgen Volz, and Arno Rauschenbeutel. Chiral nanophotonic waveguide interface based on spin-orbit coupling of light, 2014. URL http://www.arxiv.org/abs/1406:2184.

[177] R. Mitsch, C. Sayrin, B. Albrecht, P. Schneeweiss, and A. Rauschenbeutel. Directional nanophotonic atom–waveguide interface based on spin–orbit interaction of light, 2014. URL http://www.arXiv:1406.0896v2.

[178] E. Vetsch, D. Reitz, G. Sagué, R. Schmidt, S. T. Dawkins, and A. Rauschenbeutel. Optical interface created by laser-cooled atoms trapped in the evanescent field surrounding an optical nanofiber. *Physical Review Letters*, 104:203603, 2010. doi: 10.1103/PhysRevLett.104.203603.

[179] C. Lacroûte, K. S. Choi, A. Goban, D. J. Alton, D. Ding, N. P. Stern, and H. J. Kimble. A state-insensitive, compensated nanofiber trap. *New Journal of Physics*, 14:023056, 2012.

[180] R. Kumar, V. Gokhroo, K. Deasy, A. Maimaiti, C. Phelan, M. Frawley, and S. Nic Chormaic. Interaction of laser-cooled ^{8}7rb with higher order modes of an optical nanofiber, 2013. URL http://arxiv.org/abs/1311.6860.

[181] Fam Le Kien, P. Schneeweiss, and A. Rauschenbeutel. State-dependent potentials in a nanofiber-based two-color trap for cold atoms. *Physical Review A*, 88:033840, 2013.

[182] Philipp Schneeweiss, Fam Le Kien, and Arno Rauschenbeutel. Nanofiber-based atom trap created by combining fictitious and real magnetic fields. *New Journal of Physics*, 16:013014, 2014. doi: doi:10.1088/1367-2630/16/1/013014.

[183] Fam Le Kien, Victor I. Balykin, and Kohzo Hakuta. State-insensitive trapping and guiding of cesium atoms using a two-color evanescent field around a subwavelength-diameter fiber. *Journal of the Physical Society of Japan*, 74:910, 2004.

[184] A. Goban, K. S. Choi, D. J. Alton, D. Ding, C. Lacroûte, M. Pototschnig, T. Thiele, N. P. Stern, and H. J. Kimble. Demonstration of a state-insensitive, compensated nanofiber trap. *Physical Review Letters*, 109:033603, 2012.

[185] J. M. Ward, A. Maimaiti, Vu H. Le, and S. Nic Chormaic. Optical micro- and nanofiber pulling rig, 2014. URL http://arxiv.org/abs/1402.6396.

[186] J. E. Hoffman, S. Ravets, J. A. Grover, P. Solano, P. R. Kordell, J. D. Wong-Campos, L. A. Orozco, and S. L. Rolston. Ultrahigh transmission optical nanofibers. *AIP Advances*, 4:067124, 2014. doi: 10.1063/1.4879799.

[187] Alexei L. Glebov, Oleksiy Mokhun, Alexandra Rapaport, Sébastien Vergnole, Vadim Smirnov, and Leonid B. Glebov. Volume bragg gratings as ultra-narrow and multi-band optical filters. In *Invited paper presented at Photonics Europe 2012 Brussels, Belgium*, 2012.

[188] E. Vetsch, S. T. Dawkins, Rudolf Mitsch, Daniel Reitz, P. Schneeweiss, and Arno Rauschenbeutel. Nanofiber-based optical trapping of cold neutral atoms. *IEEE Journal of Selected Topics in Quantum Electronics*, 18:1763, 2012.

[189] Petr Anisimov and Olga Kocharovskaya. Decaying-dressed-state analysis of a coherently driven three-level , system. *Journal of Modern Optics*, 55:3159, 2008.

[190] S. H. Autler and C. H. Townes. Stark effect in rapidly varying fields. *Physical Review*, 100:703, 1955. doi: 10.1103/PhysRev.100.703.

[191] Peter J. Shadbolt, Maria R. Verde, Alberto Peruzzo, Alberto Politi, Anthony Laing, Mirko Lobino, Jonathan C. F. Matthews, Mark G. Thompson, and Jeremy L. O'Brien. Generating, manipulating and measuring entanglement and mixture with a reconfigurable photonic circuit. *Nat. Photonics*, 6:45–49, 2011. doi: 10.1038/nphoton.2011.283.

[192] Daoxin Dai, Jared Bauters, and John E. Bowers. Passive technologies for future large-scale photonic integrated circuits on silicon: polarization handling, light non-reciprocity and loss reduction. *Light-Sci. Appl.*, 1:e1, 2012. doi: 10.1038/lsa.2012.1.

[193] Mehul Malik, Mohammad Mirhosseini, Martin P. J. Lavery, Jonathan Leach, Miles J. Padgett, and Robert W. Boyd. Direct measurement of a 27-dimensional orbital-angular-momentum state vector. *Nat. Commun.*, 4:3115, 2014. doi: 10.1038/ncomms4115.